U.S. ARMY

# FY23

PROCEEEDINGS OF THE U.S. ARMY COMBAT CAPABILITIES DEVELOPMENT COMMAND CHEMICAL BIOLOGICAL CENTER

# IN-HOUSE LABORATORY INDEPENDENT RESEARCH AND CHEMICAL BIOLOGICAL ADVANCED MATERIALS MANUFACTURING SCIENCES PROGRAMS

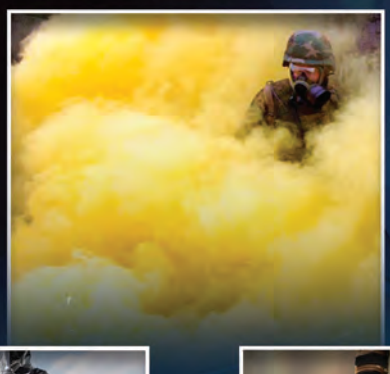

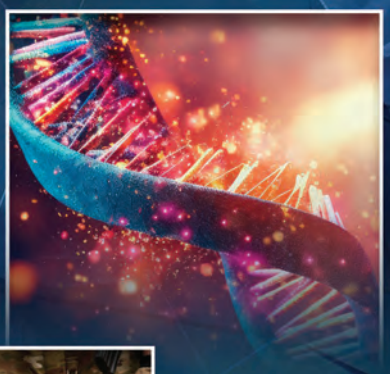

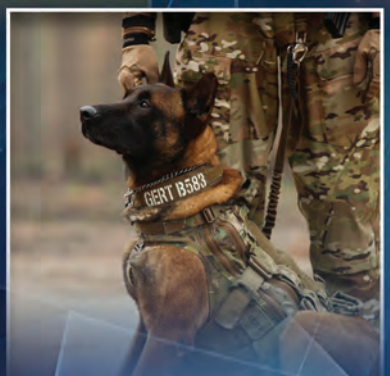


DEVCOM CHEMICAL BIOLOGICAL CENTER

# Message from the In-house Laboratory Independent Research Program Director

I am pleased to present the fifteenth annual edition of the Proceedings of the U.S. Army Combat Capabilities Development Command Chemical Biological Center's (DEVCOM CBC) In-house Laboratory Independent Research (ILIR), Chemical Biological Advanced Materials Manufacturing Science (CBAMMS), and Seedling Programs. As the Senior Research Scientist (ST) for Chemistry and Director of the ILIR and CBAMMS programs, I am proud to lead the Center's Army-funded basic research and innovation programs. These programs offer DEVCOM CBC one of the most significant funding sources to conduct in-house fundamental research towards meeting the needs of the Army.

FY23 saw several successes on the individual and programmatic levels including publications, patent applications, and a project that successfully transitioned to external customer funding. As the needs of the defense community continue to evolve, so too does the focus of the ILIR and CBAMMS programs. Leadership continues to align the funded projects to the Army Modernization Strategy, executing work aligned to Chemical and Biological Sensing, Rational Molecular Synthesis and Nano-system Design, Synthetic Biology, Materials, and Obscuration sciences.

"FY23 saw several successes on the individual and programmatic levels including publications, patent applications, and a project that successfully transitioned to external customer funding."

At the conclusion of FY23, the ILIR and CBAMMS programs hosted another successful Technical Advisory Board (TAB) Review with expert reviewers from across multiple government agencies. For the first time, the TAB Review included a reviewer session that outlined the progress and opportunities DEVCOM CBC experts saw in metal-organic framework technologies. This session was received positively by the reviewer panel who encouraged leadership to conduct a holistic, long-term evaluation of the needs of the Center related to each thrust area. This information could then be distributed to the workforce and help guide future efforts and synergize across research areas. The TAB Review also included a social event that featured posters made by the FY23 Seedling projects, smaller, quick-turn projects that enable DEVCOM CBC scientists to acquire initial data and leverage their initial work to inform a larger research effort.

This report concludes with a technical manuscript from each of the FY23 ILIR, CBAMMS, and Seedling projects that details the advances made during the period of performance. If you have questions regarding the ILIR Program or this report, please contact the DEVCOM CBC Public Affairs Office at usarmy.apg.devcom-cbc.mbx.communications-office@army.mil

Sincerely,
**Patricia (Trish) McDaniel, Ph.D.**
Senior Research Scientist (ST) for Chemistry

# Strategic Mission and Vision

The U.S. Army Combat Capabilities Development Command Chemical Biological Center (DEVCOM CBC) is the primary Department of Defense technical organization for non-medical chemical and biological defense. DEVCOM CBC has the unique ability to advance the mission of the Joint Warfighter and other stakeholders, while leveraging historical expertise, advanced equipment, and state-of-the-art facilities. The Center takes pride in its legacy of solutions born from more than a century of innovation.

## Mission

DEVCOM CBC's mission is to provide innovative chemical, biological, radiological, nuclear, and explosive (CBRNE) defense capabilities to enable the Joint Warfighters' dominance on the battlefield and interagency defense of the homeland. This mission recognizes that the Center's range of influence, while rooted in CB warfare defense, can be applied to all types of challenges in chemistry or biology. The Center's advanced capabilities in synthetic biology and materials science leverage existing core capabilities in biotechnology and decontamination sciences to develop next-generation capabilities that ensure our warfighters are always prepared to operate on the modern and future battlefield.

## Vision

DEVCOM CBC's vision is to be the Army's premier research and engineering center generating CBRNE solutions for the Army, DoD, the Nation, and our Allies. For more than 100 years, the Center has been a distinct asset, providing innovative and economical CB defense technology solutions through scientific and engineering expertise, coupled with our unique facilities and collaboration with partners.

DEVCOM CHEMICAL BIOLOGICAL CENTER

Previous ILIR and CBAMMS funded projects have led to multiple technologies that benefit the warfighter. Here, SFC Johnny Roberts demonstrates how the Dial-A-Threat screening device can analyze a biological agent in 15–30 minutes by warfighters in the field.

The basic science conducted in the ILIR and CBAMMS programs helps to inform translational science efforts. Here, Dr. Danielle Kuhn explains the science that informs how her materials project helps to obscure the asset signatures at a DEVCOM CBC obscurant demonstration.

# DEVCOM CBC Basic Research Project Selection and Evaluation Process

## ILIR and CBAMMS Program Overview

The DoD defines basic research as a "systematic study directed toward greater knowledge or understanding of the fundamental aspects of phenomena and of observable facts without specific applications toward processes or products in mind."[1] To foster and sustain basic research, the DoD created and supports an In-house Laboratory Independent Laboratory (ILIR) program in each DEVCOM center. The Army's Core 6.1 program, which adheres to the guidelines outlined in DoD Instruction 3201.04, dictates that "each DoD component that operates an R&D laboratory or center shall support an ILIR program" and that these laboratories "shall be given wide latitude in the use of ILIR funds…to enable performance of innovative, timely, and promising work without requiring formal and prior approval."[2] Therefore, the purpose of the ILIR program is to identify and fund innovative basic research projects that are high-risk but have high potential payoff for fulfilling future Army capability needs.

The Department of the Army has also established a separate, directed basic research effort for DEVCOM Centers to fund basic research related to their missions and align to the challenges outlined in the Army Modernization Strategy. As such, the Chemical Biological Advanced Manufacturing Material Science (CBAMMS) program funds projects that focus on the fundamental science related to novel material science and signal management through smoke and obscuration.

The ILIR and CBAMMS programs help to foster increased innovation within the Center. They are viewed as a critical part of the Center's efforts to ensure a high level of quality in basic science; to foster innovation in the areas of chemistry and biology; mentor junior investigators in the art and practice of laboratory science; and to explore new technological innovations and phenomenology at the boundaries of chemistry, biology, mathematics, or physics. These projects must also focus on expanding the state-of-the-possible in support of CBRNE defense missions. ILIR and CBAMMS projects receive funding for up to three years and are expected to result in peer-reviewed publications, technical reports, patents, and/or present their findings at local and national scientific gatherings.

## ILIR and CBAMMS Project Selection

Each year, the ILIR and CBAMMS programs solicit the Center's researchers for innovative proposals that correspond to topics highlighted in the DEVCOM CBC Research and Operations (R&O) Directorate's Strategic Roadmap. A panel of external reviewers evaluate and score each proposal on its scientific objective, methodology, investigator qualifications, and the proposed budget. Of these four categories, the scientific objectives and methods are given more weight in the overall score for each project. The panel and program director rank proposals according to merit and written feedback for each project is shared with each PI and guides the Center's ongoing mentoring of researchers. Only proposals deemed basic research by the reviewer panel are considered eligible for funding.

In FY23, ILIR topics included Aerosol Sciences, Chemical and Biological Sensing, Computational Design and Development, Emerging Threats, Panomics and Molecular Toxicology, Rational Molecular Synthesis and Nano-system Design, and Synthetic Biology while the CBAMMS program focused on Materials, Signal Management (Obscuration), and other topics related to surfaces, interfacial dynamics, thin film materials, catalysis, and opto-electronic/sensory technologies. In FY23, fifteen ILIR and CBAMMS proposals were submitted, reviewed, and critiqued by a reviewer panel comprised of scientists from the United States Military Academy, DEVCOM Army Research Laboratory, United States Army Research Office, and DEVCOM Chemical Biological Center.

Of the submitted proposals, three new ILIR projects and two new CBAMMS projects were funded. Additionally, one project continued to receive funding by the Fabrication Advanced Materials/Manufacturing Sciences (FAMMS) campaign with the goal of eventually transitioning to CBAMMS funding in year three of the project. These projects, along with two ILIR and seven CBAMMS continuations, made up the basic science portfolios totaling $3.2M of funding in FY23.

*1 DoD Financial Management Regulation, DoD 7000.14-R, Vol. 2B, Ch. 5*

*2 In-House Laboratory Independent Research Program, DoDI 3201.04, October 15, 2018*

# ILIR and CBAMMS Project Evaluation

Projects selected for funding are reviewed quarterly; these reviews of project performance provide guidance to the program's participants to ensure projects meet significant milestones, that substantive new knowledge is being produced, ensure knowledge is transferred to DEVCOM CBC and the broader scientific community, and to help course-correct when projects experience complications. Each quarterly review features a different focus. Quarter one includes discussions on the project objectives and proposed methods that will be executed throughout the year, quarter two focuses on the data obtained early on, risks, mitigation strategies, or other necessary course corrections, and quarter three focuses on the technical advancements made by each project.

DEVCOM CBC holds an external review in the fourth quarter, known as the Technical Advisory Board (TAB) Review, to assess year-to-date performance of the funded ILIR and CBAMMS projects. Comments and feedback from this review are used to justify continued funding, to course correct individual projects facing substantial roadblocks, and to pause or terminate funding for individual ILIR or CBAMMS projects. The comments and insights provided by the expert panel are used to improve the quality and content of individual research projects, the scientific focus of the ILIR and CBAMMS portfolios, and to guide the overall mission of the programs into the future.

## PROPOSAL SCORING CRITERIA

**Exceptional** (4) Comprehensive and complete in all areas; meets all significant objectives; offers a comprehensive project that exceeds the ILIR vision and is supportable by the proposed approach; has few weaknesses which are easily correctable.

**Acceptable** (3) Meets most of the significant objectives and is responsive to the ILIR vision; offers a feasible technical solution; weaknesses are readily correctable; proposal is complete to the extent that an award could be made in present terms.

**Marginal** (2) Minimally meets ILIR vision and objectives (i.e., offers a project vision that is marginally supported by the proposed approach, and/or claims are not documented or substantiated); significant deficiencies exist.

**Unacceptable** (1) Fails to meet significant characteristics of the ILIR vision and/or objectives stated in the Solicitation; has weaknesses and/or deficiencies that are significant and of such magnitude that they cannot be corrected without extensive discussion/major revision of the proposal.

| | REVIEWERS | | | | | | | |
|---|---|---|---|---|---|---|---|---|
| | 1 | 2 | 3 | 4 | 5 | 6 | 7 | AVG |
| Scientific Objective | 4 | 3 | 4 | 3 | 3 | 4 | 3 | 3.0 |
| Methods and Approach | 4 | 2 | 3 | 2 | 3 | 2 | 2 | 2.6 |
| PI Qualifications | 3 | 3 | 4 | 3 | 3 | 3 | 3 | 3.1 |
| Budget | 3 | 3 | 3 | 1 | 3 | 3 | 3 | 2.7 |
| **Overall Evaluation** | 3.7 | 2.7 | 3.5 | 2.3 | 3.0 | 2.7 | 2.0 | **2.8** |

## FOUR REVIEWERS FROM DIFFERENT FEDERAL DEFENSE ORGANIZATIONS SERVED ON THE FY23 TAB PANEL, INCLUDING:

- **COL F. John Burpo, Ph.D.,** Department Head and Professor, Department of Chemistry and Life Science, United States Military Academy
- **LTC Victor Jaffett, Ph.D.,** Assistant Director, Department of Chemistry and Life Science, United States Military Academy
- **Valerie Martindale, Ph.D.,** Extramural Competency Co-Lead, Biology and Biotechnology Sciences, DEVCOM ARL Army Research Office
- **Rod Kunz, Ph.D.,** Associate Leader, Biological and Chemical Technologies Group, Massachusetts Institute of Technology Lincoln Laboratory


In FY23, the TAB panel was tasked by the program director with producing an unbiased assessment of the content, quality, innovation, accomplishments, and relevance of the R&O basic science programs. Each project was evaluated based on seven areas: (1) scientific objectives, opportunity, and significance, (2) research methodology, (3) connections to the broader community, (4) overall capabilities and metrics, (5) use of PowerPoint, (6) use of time, and (7) overall presentation, with criteria 1–4 weighted as the most important. In FY23, the panel recommended all eligible projects receive continued funding and provided critical feedback to enhance the impact of several of the ongoing projects. Individual scores, portfolio reviews, and the key points from the TAB discussion were all used to generate a report for both project PIs and DEVCOM CBC leadership.

In FY23, the panel felt the funds invested in the portfolios resulted in excellent productivity and that the projects spanned a diverse set of topics important to the Army Modernization Strategy. In particular, the panel remarked that all projects were engaged in high-risk, high-reward work which fulfilled a key tenet of both the ILIR and CBAMMS programs. The presentations also demonstrated the teams receiving funding were productive, sharing large amounts of data and explaining how individual project objectives were being met. Finally, the TAB reviewers were complimentary of the state-of-the-art technologies each project utilized, the quality of the presentations, the multiple, internal DEVCOM CBC collaborations, and the potential for projects to transition to external partners at the conclusion of their ILIR or CBAMMS funding.

While the two portfolios had many strengths, reviewers provided several recommendations and actions to improve both programs. Long-term plans, with input from senior leadership, branch and division leaders, and the workforce could be created to help guide broad efforts by DEVCOM CBC and collaborators to solve the emerging issues faced by the defense community. Identifying these issues and sharing them widely across the Center could lead to synergy between branches, divisions, and subject areas as new technologies are developed. On a similar note, greater communication of the direction of research within the Center could help projects connect to their funding program or broader efforts and better define how their "ultimate success" would benefit the greater scientific community. Finally, reviewers urged all project leaders to invest time and energy at the start of their effort to understand where the experimental and project-wide risks are and identify mitigation strategies that could ensure their project's success.

## Seedling Program Overview

The Seedling program funds smaller, quick-turn (less than one year), "outside-the-box" exploratory basic research projects using funds obtained under the authority of 10 U.S.C § 2363 Funding Laboratory Enhancements Across (X)-4 Categories (FLEX-4). Under FLEX-4, directors of DoD laboratories are directed to use funds to foster basic and applied research, transition novel technologies into operational use, further develop the workforce, and revitalize and recapitalize laboratory infrastructure and equipment. Seedling projects showing promise have the potential to transition to larger ILIR or CBAMMS projects or to external funding sources. Seedling projects also undergo a similar proposal review, selection, and evaluation process as ILIR and CBAMMS projects; however, the Seedling review process is conducted internally at DEVCOM CBC and is more streamlined to fit the lower funding threshold. In FY23, 20 Seedling proposals were received, 10 of which were granted funding to focus on Rational Molecular Synthesis and Nano-system Design, Chemical and Biological Sensing, and Synthetic Biology.

Each TAB Review features a social event with a poster session highlighting projects from the Seedling program. Here, Dr. Stephanie Cole presents her work on a MXene-based biological detection assay to attendees.

## FY23 Basic Research Program Productivity

**22**
Presentation and Proceedings

**4**
Publications

**1**
Project transitioned to customer funding

**1**
Advanced Degree Awarded

# FY23 Basic Research Program Highlights

Dr. Amee Polk (CBAMMS) took part in a collective effort to institute an Educational Partnership Agreement with Johns Hopkins University. The agreement, signed in September 2023, is the most recent example of the Center establishing partnerships with leading academic institutions to support the next generation of scientists gain valuable laboratory experience. The agreement is also designed to streamline collaborations between Johns Hopkins University faculty and DEVCOM CBC scientists.

Dr. Jennifer Lee (CBAMMS) was awarded an “On the Spot Special Act Award” from the Defense Threat Reduction Agency in August 2023. These awards are given for exceptional performances that benefits each agency that takes part in the program. These exceptional performances may include successfully accomplishing projects in addition to normal employee duties, furthering a concept with an immediate benefit to the work unit, or for accomplishing work efficiently and effectively.

# FY23 BASIC RESEARCH PROGRAM PRODUCTIVITY

## 22 Presentations and Proceedings

- Languirand, E.; Collins, M. MOF-Based Janus Micromotor Locomotive Characterization. *Presented at SciX 2022*, Covington, KY, **2–7 October 2022**.
- Gordon, W.O. Surface Science and In Operando Studies of Novel Materials for Chemical Threat Decontamination. Presented at the University of New Hampshire Department of Chemistry, Durham, NH, **25 October 2022**.
- Gordon, W.O. Science for security: Advances in chemical warfare defense. *Presented at the Annual Holiday Party of the Long Island/New York American Chemical Society Subsection*, Long Island, NY, **1 December 2022**.
- Lee, M. A cell-free polymer material platform: DNA-encoded smart materials for sensing and decontamination. *Presented at the Chemical Biological Defense Science and Technology Conference*, Edgewood, MD, **6 December 2022**.
- Browe, M.A. Monte Carlo Simulation of Zirconium-Based Metal-Organic Framework Adsorption. *Presented at the American Physical Society national meeting*, Las Vegas, NV, **5–10 March 2023**.
- Hinkle, A.R. Molecular modeling of toxic industrial chemicals in metal organic framework filtration. *Presented at the American Physical Society national meeting*, Las Vegas, NV, **5–10 March 2023**.
- Garcia, D.C. Cryptographically Protected Bioproduction Strains. *Presented virtually at Vnat 2023 Conference*, **13–15 March 2023**.
- Collins, M.; Languirand, E. Janus metal Organic Framework Micromotors for the Efficient Removal of Chemical Agents. *Presented at the Pittcon Conference and Exposition*, Philadelphia, PA, **18–22 March 2023**.
- Lee, P. Utilizing bioprinting technology to develop a 3D in vitro liver model for predictive toxicology efforts, *Presented at the Society of Toxicology Annual Meeting and Tox Expo*, Nashville, TN, **19–23 March 2023**.
- Lee, M. Cell-free Protein Synthesis for Bio-Functionalized Materials. *Presented at Northwestern University*. Evanston, IL, **29 March 2023**.
- Varady, M.J.; Schenning, C.S.; Peterson, G.W. Mantooth, B.A.; Pearl, T.P. Measurement of MOF-solvent interactions for assessment of compatibility and affinity in polymer matrices. *Presented at the 2023 Spring ACS National Meeting*, Indianapolis, IN, **26–30 March 2023**.
- Kulisiewicz, A.; Tovar, T.; Garibay, S.; Harland, J.; Browe, M.; DeCoste, J. Controlling the heterogeneous catalysis of zirconium clusters bound to modified SBA-15. *Presented at the 2023 American Chemical Society National Meeting*, Indianapolis, IN, **26–30 March 2023**.
- Polk, A. Microstructure and Ignition Properties of Novel Thermites Using NonTraditional Reactive Materials. *Presented at the New Jersey Institute of Technology Symposium*. Newark, NJ, **10–11 April 2023**.
- Buckley, P.E. Project IronDog. *Presented at the Defense Health Agency Military Working Dog Research Symposium*, Fort Belvoir, VA, **18–20 April 2023**.
- Lee, M. Cell-free Protein Synthesis for Bio-Functionalized Materials. *Presented at the University of Minnesota*, Minneapolis, MN, **26 April 2023**.
- Lane, C.; Shroff, S.; Kim, H.; Brasko, B.; Rapp, E.; McKenzie, S.; Rankin, W.; Barnhill, J.; Kovacs, C.J.; Crumbley, A.M.; Love, C.E. Generation of an in-silico analysis tool for identification of polyvalent bacteriophage. *Presented at the United States Military Academy West Point Projects Day Research Symposium*, West Point, NY, **4 May 2023**.
- Buckley, P.E. Project IronDog. *Presented at the Military Working Dog Symposium*, Alpena, MI, **11–15 May 2023**.
- Varady, M.J.; Schenning, C.S.; Thompson, C.B.; Peterson, G.W.; Mantooth, B.A.; Pearl, T.P. Improving Dispersion of Metal-Organic Frameworks in Solution-Cast Polymer Composites: Solvent Selection Guided by Self-Consistent Field Theory and Hansen Solubility Parameters. *Presented at the 2023 DEVCOM Soft Matter Community of Practice workshop*, Aberdeen Proving Ground, MD, **18 May 2023**.
- Buckley, P.E. Beyond Behavior: Identifying Correlates of Olfactory Responses in Military Working Dogs using Physiological Monitoring and Machine Learning. *Presented at the Florida International University K9 SciCon*, Miami, FL, **23–26 May 2023**.
- Antoshak, E.; McDonald, N.D. CRISPR/Cas9 genome editing for customized bacterial outer membranes, *Presented at the 2023 SEED Conference*, Los Angeles, CA, **30 May–2 June 2023**.
- Lee, M. Cell-Free Systems for Materials and Biomanufacturing. *Presented at Metabolic Engineering 11*, Marina Bay Sands, Singapore, **11–15 June 2023**.
- Collins, M.; Languirand, E. Janus Metal Organic Framework Micromotors for the Efficient Removal of Chemical Agents R&O Science Seminar. *Presented at R&O Science Seminar Series*. Aberdeen Proving Ground, MD, **20 July 2023**.

## 4 Publications

- Polk, A.; Chintersingh, K.; Flickinger, M.; Valdes, E.; Gardner, W.; Weihs, T. Effect of composition and process control agents on the microstructure and ignition properties of ball-milled Al-Zr powders. *Pow.* Tech. **2023**, *427*, p 118729.
- Hinkle, A.R.; Browe, M.A.; Iordanov, I.O.; Mantooth, B.A.; Pearl, T.P.; Varady, M.J. Effect of Interfacial Regions and Surface Functional Groups on Chemical Transport in Polymer-Particle Composites. *J. Mater. Chem. C.* **2023**, *127* (23), pp 11231–11239.
- Kulisiewicz, A.M.; Garibay, S.J.; Pozza, G.R.; Browe, M.A.; Sparr, O.; Singh, S.; Kelly, L.A.; DeCoste, J.B. Tunable Photocatalytic Singlet Oxygen Generation by Metal-Organic Frameworks via Functionalization of Pyrene-Containing Linkers. *ACS Appl. Mater. Interfaces.* **2023**, *15* (34), pp 40727–40734.
- Song, F.; Debow, S.; Zhang, T.; Qian, Y.; H-F, Z-C.; Munns K.; Schmidt, S.; Fisher, H.; Brown, J.B.; Su, Y.; Zander, Z.; DeLacy, B.G.; Mirotznik, M.S.; Opila, R.L.; Rao, Y. Interface Catalysts of Ni3Fe1 Layered Double Hydroxide and Titanium Carbide for High-Performance Water Oxidation in Alkaline and Natural Conditions. *J. Phys. Chem.* Lett. **2023**, *14*, pp 5692–5700.

## 1 Project Transitioned to Customer Funding

- In FY23, the project led by Dr. Eric Languirand entitled, "Metal-organic framework micromotors for the efficient removal of chemical agents" secured FY24–25 funding from the Defense Threat Reduction Agency to further explore micromotor decontamination for chemical warfare agents entrained in microscale liquid volumes.

## 1 Advanced Degree Awarded

- Amee Polk of the Obscuration & Nonlethal Engineering Branch and PI of the CBAMMS project entitled, "Microstructure and ignition properties of novel thermites using non-traditional reactive materials" earned a Doctor of Engineering after successfully defending her doctoral dissertation entitled, "Tuning microstructure and reactive properties of titania-based thermites using Al-Zr composite fuels." Dr. Polk's defense took place in August 2023 and her degree was conferred by Johns Hopkins University.


Principal Investigators that participate in the ILIR and CBAMMS programs present their work quarterly to their peers at the Quarter 1 and 2 Reviews, a panel of DEVCOM CBC scientific experts at the Quarter 3 Review, and a panel of extramural senior scientists at the Quarter 4 review, also referred to as the Technical Advisory Board Review. Here, Dr. Eric Languirand presents his work at the TAB Review in September 2023.

# Meet our FY23 Principal Investigators

Our FY23 Principal Investigators (PIs) encompass a diverse group of scientists across the Center's Research and Operations Directorate. Here, biographies of each PI that participated in the FY23 ILIR, CBAMMS, or Seedling programs are alphabetically listed along with their branch and division information.

**Kim Berk**
**Biologist, Applied Synthetic Biology and Olfaction Branch, Sensor Technologies and Biomaterials, CBRNE Assessment Division**
**Seedling Program**

Ms. Kim Berk, a Biologist at DEVCOM CBC, earned a B.S. in Molecular Biology, Biochemistry, and Bioinformatics from Towson University and a M.S. in Biochemistry from the University of Maryland, Baltimore. Following the completion of her master's degree, Ms. Berk worked as a Senior Technician with the Battelle Memorial Institute for approximately one year, before joining Excet, Inc. as a Scientist II. In 2017, Ms. Berk joined DEVCOM CBC and began working in her current role as a Biologist. Ms. Berk conducts research that utilizes synthetic biology to identify potential biowarfare agents in the field.

---

Dr. Casey Bernhards earned her Ph.D. in Biological Sciences in 2014 from Virginia Polytechnic Institute and State University. After graduating, she joined DEVCOM CBC as a National Research Council Postdoctoral Fellow sponsored by the Defense Threat Reduction Agency. She then continued to support DEVCOM CBC as a Senior Scientist with Excet, Inc. before converting to a civilian Research Biologist in 2021. Dr. Bernhards leads projects related to synthetic biology and microbial genetics. Her research focuses on genetically engineering bacteria for beneficial purposes; studying genome engineering tools, such as clustered regularly interspaced short palindromic repeats (CRISPR) gene editing, as emerging threats; and developing cell-free biosensors using engineered genetic circuits.

**Casey Bernhards, Ph.D.**
**Research Biologist, Applied Synthetic Biology and Olfaction Branch, Sensor Technologies and Biomaterials**
**ILIR Program**

---

**Matthew Browe**
**Chemical Engineer, Protective Materials Development Branch, Protection Division**
**CBAMMS and Seedling Programs**

Mr. Matthew Browe received a bachelor's degree in Chemical Engineering from Pennsylvania State University and a master's degree in Chemical Engineering from the University of Delaware in 2011 and 2022, respectively. Mr. Browe began working at DEVCOM CBC as a Chemical Engineer in 2011, focusing on permeation, micro-breakthrough testing, and evaluation of sorbent and barrier materials. His efforts include extensive analysis and data compilation of novel sorbents and metal organic framework (MOF) polymer hybrid films, identifying trends in performance with justification from theory, and materials characterization. Recently, Mr. Browe's research has focused on machine learning and the utilization of Python to develop a regression model that can predict MOF reactivity against toxic chemicals of interest as a function of the physical and chemical properties of a MOF.

**Patricia Buckley, Ph.D.**
**Supervisory Biologist, Deputy Division Chief, Sensor Technologies and Biomaterials Division**
**CBAMMS Program**

Dr. Patricia Buckley earned a B.S. in Biology from James Madison University before studying Biotechnology at Johns Hopkins University, receiving a M.S. in 2000. Dr. Buckley continued her education at the University of Maryland where she earned a Ph.D. in Environmental Pathology in 2013. Currently, Dr. Buckley works as a Supervisory Biologist at DEVCOM CBC where she leads a team that focuses on a variety of topics including the use of cell-free lysates in fieldable sensors and the utilization of Military Working Dogs' olfactory senses in field detection.

---

Dr. Stephanie Cole attended McDaniel College and Johns Hopkins University, earning a B.A. in biology and biochemistry and a Ph.D. in biology, respectively. Following her Ph.D., Dr. Cole began working as a Postdoctoral Research Associate with the National Research Council at DEVCOM CBC. At the conclusion of her time with the National Research Council, Dr. Cole worked at Excet, Inc. for four years as a Senior Scientist I before joining DEVCOM CBC as a Research Biologist.

**Stephanie Cole, Ph.D.**
**Research Biologist, Applied Synthetic Biology and Olfaction Branch, Sensor Technologies and Biomaterials Division**
**Seedling Program**

---

**Shaun Debow**
**Chemical Chemical Engineer, Obscuration & Nonlethal Engineering Branch, Protection Division**
**Seedling Program**

Mr. Shaun Debow attended the University of Iowa, completing B.S. degrees in computer science and chemistry and a M.S. in Chemical and Biological Engineering. Mr. Debow then joined DEVCOM CBC as a General Engineer, where he completed comprehensive courses and training on rocket and warhead design, eventually transitioning to his current role as a Chemical Engineer in 2010. In this capacity, Mr. Debow has served as the DEVCOM CBC chief rocket scientist and liaison to the Tactical Aviation and Ground Munitions Project Office with the Program Executive Office Missiles and Space. Mr. Debow has published many articles and submitted patent applications on materials and decontamination sciences.

---

Dr. Danielle Kuhn attended the State University of New York at Cortland and Binghamton University, studying Chemistry at both institutions, earning a B.S. and Ph.D., respectively. Following her doctoral degree, Dr. Kuhn joined the DEVCOM CBC Smoke and Target Defeat Branch as a National Research Council Postdoctoral Fellow in 2016 and became a civilian Research Chemist in 2018. Currently, Dr. Kuhn is the Team Lead of the Payload Development program. Dr. Kuhn's research has focused on the synthesis of novel materials and evaluating their obscuration ability. Dr. Kuhn's research has led to the publications of several papers and presentations at multiple national conferences and most recently contributed to the discovery of the highest performing obscurant material to date.

**Danielle Kuhn, Ph.D.**
**Research Chemist, Smoke & Target Defeat Branch, Protection Division**
**ILIR Program**

**Ann Kulisiewicz**
**Research Chemist, Protective Materials Development Branch, Protection Division**
**CBAMMS Program**

After earning an M.S. in Inorganic Chemistry from the University of Delaware, Ms. Ann Kulisiewicz began working as a Chemist for Leidos in the CBR Filtration Branch in 2015. Three years later, she transitioned to her current role as a DEVCOM CBC Research Chemist, still within the CBR Filtration Branch. Ms. Kulisiewicz's work focuses on the synthesis, characterization, and testing of MOFs for filtration applications which has led to multiple peer-reviewed journal articles and presentations at the American Chemical Society National Meeting & Exposition.

---

Dr. Eric Languirand attended Towson University and received a B.S. in Forensic Chemistry and Chemistry in 2012. Following his undergraduate studies, Dr. Languirand attended the University of Maryland Baltimore County, earning a Ph.D. in Chemistry in 2017. He developed a nanoimaging device using a surface-enhanced Raman sensor and novel plasmonic sensors and materials, culminating in his contractor appointment to the Chemical Analysis and Physical Properties branch at DEVCOM CBC. In 2019, Dr. Languirand transitioned to his current position as a civilian Research Scientist at DEVCOM CBC where he continues to focus on technology that utilizes applied spectroscopy for chemical characterization.

**Eric Languirand, Ph.D.**
**Research Chemist, Chemical Analysis & Physical Properties Branch, Threat Agent Sciences Division**
**CBAMMS Program**

---

**Jennifer Lee, Ph.D.**
**Chemical Biomedical Engineer, Applied Synthetic Biology and Olfaction Branch**
**Sensor Technologies and Biomaterials Division**
**CBAMMS Program**

Dr. Jennifer Lee, a Biomedical Engineer at DEVCOM CBC, first studied Biomedical Engineering at the University of North Carolina at Chapel Hill, earning a B.S. in 2008. Dr. Lee continued her education at the University of Florida where she earned a Ph.D. in Biomedical Engineering in 2013. Following her doctoral work, Dr. Lee worked as a Postdoctoral Fellow at both the University of Florida and at the National Cancer Institute. In 2021, Dr. Lee joined DEVCOM CBC where she researches cell-free protein synthesis and its incorporation into polymer matrices.

---

Ms. Priscilla Lee attended the University of Maryland, College Park where she earned a B.S. and M.Eng. in Bioengineering. As an undergraduate student, Ms. Lee served as an undergraduate research assistant as an ASPIRE Research Fellow and conducted research as a B.S./M.S. student. In 2023, Ms. Lee began a doctoral program at Johns Hopkins University with a focus on Biomedical Engineering. Ms. Lee was a recipient of the SMART Scholarship as a recruitment scholar before she began her current position as a Biologist at DEVCOM CBC in 2021.

**Priscilla Lee**
**Biologist, Molecular Toxicology Branch, Threat Agent Sciences Division**
**Seedling Program**

**Courtney Love**
**Biologist, BioTechnology Branch, CBRNE Assessment Division**
**ILIR Program**

Ms. Courtney Love studied chemistry at both Wayne State University and the University of Maryland at College Park, earning a B.S. and M.S., respectively. Following her M.S. degree, Ms. Love joined Joint Research and Development, Inc. and worked as a contractor for DEVCOM CBC. As a contractor, Ms. Love engaged with the Defense Threat Reduction Agency regarding chemical warfare agent response promoters and MAGPIX immunoassay development. In the summer of 2021, Ms. Love joined DEVCOM CBC as a Biologist where she has engaged in bacteriophage basic and translational research.

---

Dr. Nathan McDonald attended the University of Delaware, where he studied and conducted research in Biological Sciences. After earning his Ph.D. in 2018, Dr. McDonald continued his training as a National Research Council Postdoctoral Fellow at the Center until 2020 when he transitioned to his current position as a Research Biologist with DEVCOM CBC. Dr. McDonald has multiple publications that detail his research on modifying bacterial antigens for use in detection assay development, emerging threat assessment, and enhanced diagnostic and medical countermeasures. In 2021, Dr. McDonald was awarded a Federation of European Microbiological Societies Congress Attendance grant to attend and present at the American Society for Microbiology/Federation of European Microbiological Societies World Microbe Forum.

**Nathan McDonald, Ph.D.**
**Research Biologist, Biomanufacturing Branch, Sensor Technologies and Biomaterials Division**
**ILIR Program**

---

**Jessica Paradysz, Ph.D.**
**Senior Scientist, Biomanufacturing Branch, Sensor Technologies and Biomaterials Division**
**Seedling Program**

Dr. Jessica Paradysz began her education at Salisbury University where she earned a B.S. in biology. Following her first degree, Dr. Paradysz attended the University of Delaware, ultimately earning both an M.B.A. and Ph.D. in molecular biology and genetics. In 2022, Dr. Paradysz joined Excet, Inc. as a Senior Scientist where she investigates small molecule toxins produced by algae and cyanobacteria and other basic science questions focused on molecular agents.

---

Dr. Dan Phillips received Bachelor of Science degrees in both Physics and Biology from East Tennessee State University in 2010 and his Ph.D. in Molecular Microbiology and Immunology from the University of Maryland, Baltimore in 2016. After completing his first postdoctoral fellowship in synthetic biology and bioelectrochemical systems at the U.S. Naval Research Laboratory, he joined DEVCOM CBC in 2020 as an Oak Ridge Institute for Science and Education Postdoctoral Fellow with Dr. Aleksandr Miklos before becoming a Research Biologist in 2022. In addition to leading this CBAMMS effort to engineer optical materials using biology, he leads device development and integration of biological detection systems on customer-funded efforts.

**Dan Phillips, Ph.D.**
**Research Biologist, Applied Synthetic Biology and Olfaction Branch, Sensor Technologies and Biomaterials Division**
**CBAMMS Program**

**Thomas P. Pearl, Ph.D**
**Research Chemist, Decontamination Sciences Branch, Protection Division**
**CBAMMS Program**

Dr. Thomas P. Pearl is a Research Chemist within the Decontamination Sciences Branch at DEVCOM CBC where he specializes in elucidating contaminant and decontaminant chemical interactions with military-relevant materials that drive mass transport behavior and reactivity. Dr. Pearl studied Physics at Carleton College and Chemistry at the University of Chicago where he earned a B.A. in 1994 and a Ph.D. in 2000, respectively. His areas of expertise include nanoscale and solid-state physics and chemistry with a focus on the properties and behavior of surfaces, interfaces, and thin films. Dr. Pearl has published 20 DEVCOM CBC technical reports and 40 peer reviewed publications.

---

Dr. Amee Polk earned a B.Ch.E. in Chemical Engineering from the University of Delaware followed by a M.S. in Biotechnology and a D.Eng. in Material Science Engineering from Johns Hopkins University. Dr. Polk's training includes ten years of experimental design and development in the field of pyrotechnics and explosives, most of which occurred while employed as a Research Engineer within the Pyrotechnics and Explosives Branch at DEVCOM CBC. Prior to joining DEVCOM CBC, she worked as the lead test engineer for the Large-Scale Chemical Warfare Agent Test Facility. In 2018, Dr. Polk was awarded the Bernard E. Douda Young Scientist Award from the International Pyrotechnics Society and has been granted several patents in the field of pyrotechnics and explosives. She and her research accomplishments were featured in the Johns Hopkins University Material Science in Extreme Environments 2022 annual newsletter and is a member of the International Pyrotechnics Society.

**Amee Polk, Ph.D.**
**Research Chemical Engineer, Obscuration & Nonlethal Engineering Branch, Protection Division**
**CBAMMS Program**

---

**Katherine Rhea**
**Biologist, BioChemistry Branch, CBRNE Assessment Division**
**ILIR Program**

Prior to joining DEVCOM CBC, Ms. Katherine Rhea began her scientific career at the University of Maryland, College Park where she earned a B.S. in Biological Sciences. After graduation in 2011, Ms. Rhea worked as an Environmental Technician/Project Manager with Martel Laboratories JDS, Inc. Ms. Rhea then joined Battelle Eastern Science Technology Center as a Senior Technician where she worked until 2014 when she joined DEVCOM CBC. While at DEVCOM CBC, Ms. Rhea has predominately worked in basic and translational research in cell free protein synthesis and CRISPR technologies. In 2023, Ms. Rhea earned her M.S. in Biotechnology from Johns Hopkins University.

Dr. Kristian Van de Voorde graduated from the University of Southern Mississippi in 2016 with a B.S. in Polymer Science and from the University of Delaware in 2021 with a Ph.D. in Materials Science and Engineering. His research focused on the development of tissue engineered scaffold for regenerative medicine. During this work, Dr. Van de Voorde focused on structure-property relationships from a molecular and processing perspective to readily tune bulk properties to suite specific application. He joined the Respiratory Protection Branch at DEVCOM Chemical Biological Center after graduate school. His current work focuses on exploring structure property relationship in additive manufacturing as well as enabling the development of next generation of protective equipment.

**Kristian Van de Voorde, Ph.D.**
**Chemical Engineer, Protective Materials Development Branch, Protection Division**
**FAMMS and Seedling Programs**

---

**Anne Walker, Ph.D.**
**Chemical Engineer, Protective Materials Development Branch, Protection Division**
**Seedling Program**

Dr. Walker earned both a B.S. in Polymer Science Engineering in 2011 and a Ph.D. in Macromolecular Science and Engineering in 2019 from Case Western Reserve University. Prior to earning her degrees, Dr. Walker worked as an Engineering Aid and Engineering Technician for the United States Air Force Research Laboratory, and transitioned to a Researcher after completing her B.S. In 2019, Dr. Walker joined DEVCOM CBC as a Materials Researcher and, in 2020, to her current position as a Chemical Engineer. As a DEVCOM CBC researcher, Dr. Walker focuses her efforts on transitioning basic science developments into deployable devices and has worked to create an experimental additive manufacturing laboratory that seeks to streamline personal protective equipment research and development processes.

---

Dr. Angela Zeigler earned a B.A. in chemistry from Notre Dame of Maryland University before earning both an M.A. and Ph.D. in chemistry from Johns Hopkins University. Immediately after finishing her doctorate, Dr. Zeigler joined Excet, Inc. as a scientist, working as a contractor for DEVCOM CBC. In 2017, Dr. Zeigler joined DEVCOM CBC where she currently works as a Research Chemist. In her current role, Dr. Zeigler serves as a Principal Investigator in the areas of chemical, biological and radiological detection and aerosol science. She designs and develops concepts for aerosol spectroscopic equipment, particularly involving ultraviolet-visible and infrared wavelength regions. Dr. Zeigler is a subject matter expert in physical chemistry, aerosol research and technology evaluation. She is responsible for managing multiple chemical, biological defense programs related to biological aerosol generation, aerosol threat and background characterization, and collection efficiency testing.

**Angela Zeigler, Ph.D.**
**Research Chemist, Sensors, Signatures, & Aerosol Technologies Branch, Sensor Technologies and Biomaterials Division**
**Seedling Program**

# Table of Contents

The following sections contain manuscripts from each of the funded projects. The ILIR and CBAMMS projects are presented in the order they were evaluated and ranked at the FY23 TAB while the Seedling projects are listed alphabetically by the principal investigator's last name.

## In-house Laboratory Independent Research (ILIR) Projects

## Chemical Biological Advanced Materials Manufacturing Science (CBAMMS) Projects

## 107 Production of an iridescent surface using synthetic biology and a membrane sculpting protein

*Daniel A. Phillips*, John R. Biondo, Cheri M. Hampton, Christian L. Jednorski, Lily McCloskey, Jill B. Harland, Danielle L. Kuhn, Lawrence F. Drummy, Patricia E. Buckley, Aleksandr E. Miklos*

Biology naturally excels at building precise structures at nanometer scales using a variety of biopolymers. In nature, patterning of ordered, high aspect ratio structures can form biomaterials with metamaterial properties, such as structural coloration. Membrane curvature formation mediated by Bin/Amphiphysin/Rvs domain proteins generate high aspect ratio tubule particles with dimensions that could be useful for making a biotemplated obscurant. Here, we build on previous work investigating the in vitro membrane binding and remodeling activity of the Bin/Amphiphysin/Rvs domain-like protein BdpA by using sculpted tubules as templates for plasmonic nanoparticles. The tubule-templated gold nanoparticles changed visible color and shifted the absorbance spectra suggesting this line of investigation may contribute to the development of lightweight, adaptable biological metamaterials and next generation obscurants.

## 117 Controlling the heterogeneous catalysis of zirconium clusters within porous scaffolds

*Ann M. Kulisiewicz*, Sergio J. Garibay, Trenton B. Tovar, Matthew A. Browe*

Catalytic degradation of chemical warfare agents may be achieved with Zr-based MOFs, which are modular materials consisting of a metal node linked by organic struts to form porous, crystalline structures. Hydrolysis activity within these MOFs occurs on the Zr nodes. Therefore, this work sought to better understand the fundamental chemical principles that affect reaction on these Zr nodes. Zr clusters were grafted to silica supports that had been modified with sulfuric acid groups ($SO_3H$-SBA-15) to facilitate binding of the clusters to the support. The results showed that under these conditions, the tethered Zr12 clusters performed selective hydrolysis of DMNP, a nerve agent simulant, while the tethered Zr6 clusters resulted in a mix of hydrolyzed product and undesired product, 4-methylnitrophosphate (4-MNP). Insight into these trends were achieved through computational modeling and characterization of the clusters by powder x-ray diffraction, infrared spectroscopy, and x-ray photoelectron spectroscopy.

## 127 Molecular modeling of toxic industrial chemicals on metal-organic frameworks for next-generation filtration applications

*Matthew A. Browe*, Adam R. Hinkle, Ivan O. Iordanov, Wesley O. Gordon, John Landers, Shivam Parashar, Alex Neimark*

Military personnel are at risk of toxic chemical exposure, often through inhalation. In order to better protect these personnel, this study explores the application of metal-organic frameworks to be used in filtration applications. This work discusses the molecular modeling studies that were performed to determine the ability of a wide variety of zirconium-based metal-organic frameworks to act as filtration media against specific toxic chemicals of interest using Monte Carlo methods and molecular dynamics methods. Specifically, reactive molecular dynamics studies were performed to understand the atomic-level details of the hydrochloric acid (HCl) activation synthesis of MOF-808, where formate modulator groups are removed from the node and ultimately substituted with hydroxyl species. The effect of temperature and HCl concentration on the mechanistic data was explored and discussed

# Seedling Projects

## 139 Simple Modular Aptamer Response Test (SMART)

*Mia Seergae, Aleksandr E. Miklos, Daniel A. Phillips, Elizabeth S. Dhummakupt, Kimberly L. Berk**

Detection and identification of toxins is necessary to safeguard DoD assets, but detection is limited as current capabilities require complex equipment, laboratory space, and trained personnel. This work seeks to minimize this gap by combining an oligo-based fluorescent reporting system with a published qualitative polymerase chain reaction based aptamer detection method. This design employs an isothermal toxin: aptamer competition scheme that would release a barcoded molecular tag (“sensor oligo”) upon the binding of the target toxin to an aptamer, activating a fluorescent reporter system that can be visualized. To date, efforts have shown the system can detect as little as 100 ng of Aflatoxin M1, suggesting this method has potential to improve toxin detection capabilities.

## 145 Reactive molecular dynamics simulations of diisopropyl fluorophosphate on Zirconium metal-organic frameworks

*Matthew A. Browe, Adam R. Hinkle, Ivan O. Iordanov, Adri van Duin*

Reactive force fields, which allow for chemical bonds to be created or dissociated, show how different reactions occur within the system. In this work, the ReaxFF reactive force field method is applied to the interactions between zirconium-based metal-organic frameworks and sarin. Simulations of sarin decomposition on zirconia show very good agreement with quantum calculations. Molecular dynamics simulations show H–F formation and F dissociation for sarin and H–F formation for diisopropyl fluorophosphate. Sarin and diisopropyl fluorophosphate seem to behave very differently, with diisopropyl fluorophosphate being more reactive and unstable. The formation of fluorine clusters and $H_2F$ formation in presence of diisopropyl fluorophosphate is questionable and should be further validated with additional quantum calculations.

## 153 MXene-enabled bacterial DNA extraction for polymerase chain reaction analysis

*Stephanie D. Cole*, Grace E. Rawlett, Shaun M. Debow*

Biological detection assays rely on an initial cell lysis and DNA extraction to free genetic material for analysis. However, current extraction methods are not fieldable due to their requirement for laboratory equipment, multiple steps, or disruptive detergents that interfere with downstream assays. Recently, reports on the antibacterial properties of two dimensional nanomaterials have suggested MXenes disrupt the bacterial membrane and release DNA. This can be achieved with a simple incubation of bacteria with MXenes without the need for specialized equipment. However, using MXenes to extract DNA for detection assays has not yet been reported. Here, we utilized MXenes to extract genetic material from bacterial cells for downstream analysis. Despite detection of free DNA from bacteria lysed by MXenes, qPCR reactions were inhibited by MXenes compared to control assays. Further optimization may mitigate the inhibitory effect of MXenes and advance them as candidates for genomic extraction in biodetection assays.

## 159 MXene electrochemical detoxification of VX

*Shaun Debow*, Stephen P. Harvey, Michael J. Chesebrough, Vanessa L. Funk, Mallory Liebes, Zachary B.S. Zander, Yi Rao*

Electrochemical processes can be used to treat recalcitrant chemicals including nerve agents like VX that have long environmental fates. Electrochemical treatment processes work by applying a current to an electrocatalyst in the presence of a recalcitrant chemical, reacting with the agent or creating reactive species. We sought to increase VX degradation by utilizing electro-Fenton reactions through *in situ* hydrogen peroxide generation using an Oxygen Reduction Reaction catalyst combined with an Oxygen Evolution Reaction catalyst in a dual electrode configuration. Both catalysts were fabricated in-house and based on FeCo-MXene chemistry. VX nerve agent degradation kinetics were similar for both configurations when compared to a single Oxygen Evolution Reaction catalyst for electro chemical advanced oxidation reactions, suggesting additional work is needed to develop more effective decontamination strategies.

## 165 Modeling the lymphatic vessel using microfluidic technology to study immune response *in vitro*

*Priscilla Lee*, Sarfaraz A. Ejazi, Ann Ramierez, Morgan Minyard, Katharina Maisel*

Immune response to toxins of interest is understudied due to the complexity of the immune system. The lymphatic system is a physical component of the immune system that transports cells, toxins, or byproducts throughout the body. Lymphatic vessels are of interest as their function is understudied in vivo and limited by external factors, such as lymphatic fluid flow, in current in vitro models. This study developed a microfluidic device for a lymphatic vessel using additive manufacturing techniques, including computer aided design and biomaterial manufacturing. Lymphatic vessels were constructed and optimized with human lymphatic endothelial cells and collagen hydrogel under static and flow conditions. With the introduction of flow, cells expressed more junction proteins and formed more physiologically relevant cell morphology within the vessel. Rather than relying on a commercially available system, this work developed a platform to assess lymphatic vessels under flow conditions. This model can be used in future toxicity studies, specifically looking at permeability of particles across lymphatic vessels.

# ILIR
# PROJECTS

# Remodeling the bacterial outer membrane for synthetic designer microbes

Erin E. Antoshak[a,b], and Nathan D. McDonald[a]*
[a]U.S. Army Combat Capabilities Development Command Chemical Biological Center, Research & Operations Directorate, 8198 Blackhawk Rd, Aberdeen Proving Ground, MD 21010
[b]Excet Inc., 6225 Brandon Ave, Suite 360, Springfield, VA 22150

## ABSTRACT

Synthetic biology and genome engineering capabilities have facilitated the utilization of bacteria for myriad of applications ranging from medical treatments to biomanufacturing complex molecules. The bacterial outer membrane, specifically the lipopolysaccharide, plays an integral role in the physiology, pathogenesis, and serves as a main target of existing detection assays for Gram-negative bacteria. Here we use CRISPR-Cas9 recombineering to insert *Yersinia pestis* lipid A biosynthesis genes into the genome of an *Escherichia coli* strain expressing the lipid $IV_a$ subunit. We successfully inserted three genes: *kdsD*, *lpxM*, and *lpxP* into the *E. coli* genome and demonstrated their expression via reverse transcription polymerase chain reaction. Despite observing expression of these genes, analytical characterization of the engineered strain's lipid A structure via matrix-assisted laser desorption/ionization time-of-flight mass spectrometry indicated that the *Y. pestis* lipid A was not recapitulated in the *E. coli* background. As synthetic biology and genome engineering technologies advance, novel applications and utilities for the detection and treatments of dangerous pathogens like *Y. pestis* will continue to be developed.

**Keywords:** Lipopolysaccharide, CRISPR-Cas9, genome engineering, lipid A

## 1. INTRODUCTION

A hallmark defining feature of Gram-negative bacteria is the presence of an outer membrane primarily comprised of either lipopolysaccharide (LPS) or lipooligosaccharide (LOS). As the names imply, the LPS and LOS macromolecules contain both a lipid region and carbohydrate chains. The outer membrane molecules can generally be divided into three distinct domains: the lipid A, core oligosaccharide which together make up the LOS (Figure 1A), and finally the repeating carbohydrate O-antigen completing the LPS.[1] Each of the domains has specific and unique structures and properties which contribute to a myriad of phenotypes for individual bacteria. While there are exceptions, one lipid A unit is comprised of a linked D-glucosamine disaccharide backbone which is phosphorylated at positions 1' and 4' of the carbohydrates.[1-3] The backbone is acylated with branching fatty acid chains of varying lengths and substitutions depending on the species. This main unit of lipid A can be further modified by various additions including phosphates, carbohydrates, and other small molecules which can alter the overall charge.[1,3] Together, it is the lipid A unit which is responsible for the endotoxic properties of LPS by activation of the innate immune system via recognition by toll-like receptor 4 (TLR4).[2]

*Yersinia pestis*, the causative agent of the plague, possesses a unique lipid A that undergoes a variety of changes as the organism transitions through its lifecycle and infection stages. The *Y. pestis* lipid A is typical in that it contains a glucosamine carbohydrate backbone like other enterobacteria. Branching from the linked glucosamine residues are a variety of fatty acid acyl chains, the structure and composition of which are dependent on the temperature at which the organism is growing.[4-6] At 37 °C, the temperature encountered during infection, the *Y. pestis* lipid A is tetra-acylated with hydroxymyristate.[6,7] This tetra-acylated lipid A is known as lipid $IV_a$ and is considered the minimal lipid unit required for bacterial survival under laboratory conditions.[8] Furthermore, this lipid $IV_a$ has been shown to be less immunogenic during that contributes to the overall *Y. pestis* pathogenesis during infection.[4-7,9,10] At lower temperatures, 20–28 °C, the *Y. pestis* lipid A is hexa-acylated with the addition of a palmitoleate residue, catalyzed by the enzyme LpxP, and a myristate group catalyzed by the enzyme LpxM (Figure 1B).[5,9,10]

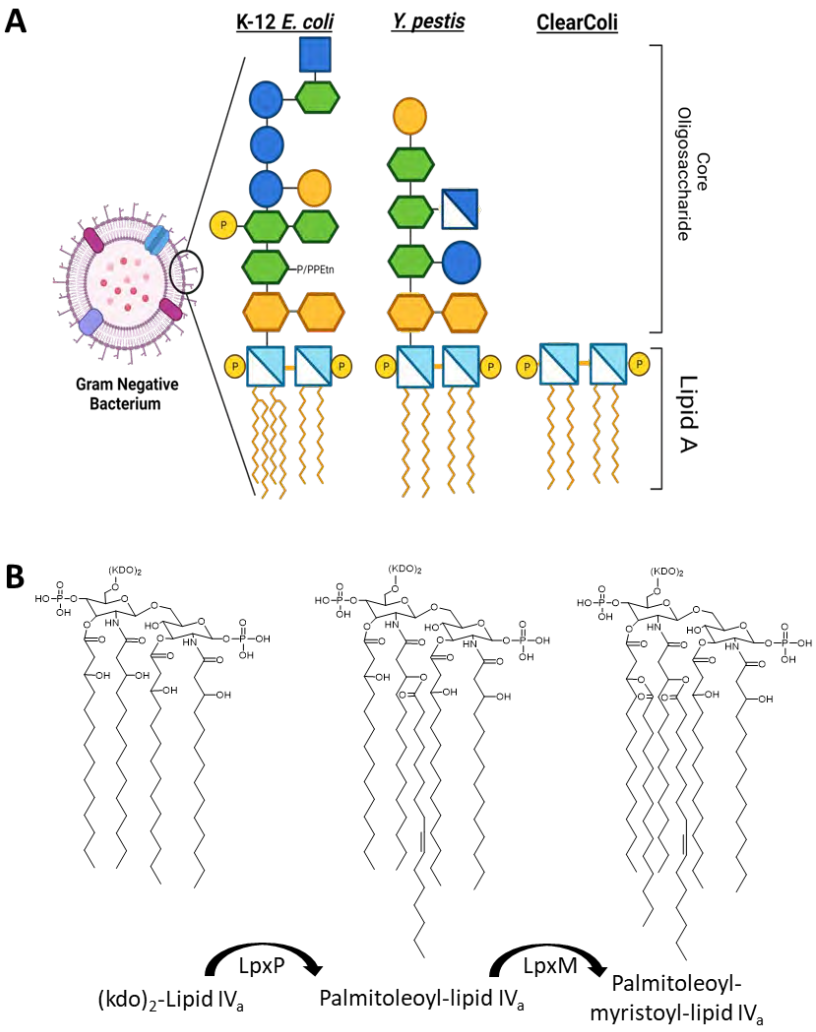


**Figure 1. Representative bacterial outer membrane structures and late acyl transferases biosynthesis. A) Graphical representation of LOS structures from *E. coli* K-12, *Y. pestis* and the mutant *E. coli* strain ClearColi™. B) Function of late acyl transferases LpxP and LpxM.**

Here, we set out to utilize CRISPR-Cas9 recombineering technologies to genetically engineer a commercially available, mutated strain of *E. coli* that expresses lipid $IV_a$ as its outer membrane unit.[8] Using synthetic DNA, we inserted three *Y. pestis* genes involved in lipid A biosynthesis into this *E. coli* scaffold to determine if we could reconstitute the *Y. pestis* lipid A in this strain. Finally, we examine the functionality of two *Y. pestis* lipid A modifying enzymes in the *E. coli* scaffold background, which have been shown to be involved antimicrobial resistance.

## 2. METHODS

### 2.1 Bacterial strains and plasmids

All strains and plasmids used in this study are listed in Table 1. The endotoxin-free *E. coli* (DE3) ClearColi™ electrocompetent cells were purchased through Lucigen. The two plasmid CRISPR-Cas9 system utilized in this work includes a pEcCas (Plasmid #73227) and guide pEcgRNA plasmid (Plasmid #166581) that are available through Addgene and previously described.[11] All strains were grown in Luria Bertani-(LB) Broth (Miller) (Sigma-Aldrich®; St. Louis, MO). Antibiotics were used as needed at the following concentrations: kanamycin (kan) (50 µg/mL) and spectinomycin (spec) (50 µg/mL). All routine culturing was performed at 37 °C with shaking (250 r.p.m.). Expression plasmids for lipid A modifying enzymes were purchased from ATUM.

**Table 1: Strains and plasmids used in this study.**

| Strain or Plasmid | Genotype or phenotype | Reference or source |
|---|---|---|
| pEcCas | pWM119: Cas9, sgRNA (amp->kan) | Addgene #73227[11] |
| pEcgRNA | pTargetF: *ccdB*, Spectinomycin | Addgene #166581[11] |
| pEcgRNA-N20-*lpxM* | Guide RNA vector targeting *lpxM* insertion site in ClearColi™ genome | This study |
| pEcgRNA-N20-*lpxP* | Guide RNA vector targeting *lpxP* insertion site in Clearcoli™ genome | This study |
| pEcgRNA-N20-*kdsD* | Guide RNA vector targeting *kdsD* insertion site in Clearcoli™ genome | This study |
| *Escherichia coli* ClearColi BL21(DE3) | $F^-$ ompT $hsdS_B$ ($r_B^-$ $m_B^-$) gal dcm lon λ(DE3 [lacI lacUV5-T7 gene 1 ind1 sam7 nin5]) msbA148 Δ*gutQ* Δ*kdsD* Δ*lpxL* Δ*lpxM* Δ*pagP* Δ*lpxP* Δ*eptA* | Invitrogen |
| *Escherichia coli* BL21 (DE3) | fhuA2 [lon] ompT gal (λ sBamHIo ΔEcoRI-B int::(lacI::PlacUV5::T7 gene1) i21 Δnin5) [dcm] ΔhsdS | New England BioLabs |
| ClearColi:*lpxM* | Clearcoli™ genome with *Y. pestis lpxM* inserted in the cognate genomic loci | This study |
| ClearColi:*lpxM:lpxP* | Clearcoli™:*lpxM* genome with *Y. pestis lpxP* inserted in the cognate genomic loci | This study |
| ClearColi:*lpxM:lpxP:kdsD* | Clearcoli™:*lpxM:lpxP* genome with *Y. pestis kdsD* inserted in the *gutQ* genomic loci | This study |

## 2.2 Generating repair DNA templates

Donor DNA was supplied as gBlocks™ (Integrated DNA Technologies™; Coralville, IA) constructed to include the gene of interest, N20 sequence, and protospacer adjacent motif (PAM) site indicated in the ClearColi™ sequence. Flanking the gene are ~500 base pair regions homologous to the insertion site. The gBlock™ is used as a template in a polymerase chain reaction (PCR) amplification reaction. The reaction was performed with Phusion® High Fidelity DNA Polymerase (New England Biolabs®; Ipswich, MA) following the NEB Phusion® protocol and utilizing the gBlock primers listed in Table 2. For confirmation, gel electrophoresis was performed of the amplified gBlock™ at 120 V for 30 minutes on a 1 % agarose gel stained with SYBR™ Safe DNA Gel Stain. The amplified DNA was urified using a DNA Clean & Concentrator-100™ kit (Zymo Research®; Irvine, CA).

**Table 2: DNA primers used in this study.**

| Primer ID | Primer Sequence (5' -> 3') |
|---|---|
| 5EC*lpxM*ctrl | ATT AAT TAA CAT CCA TTC GCA GCC G |
| 3EC*lpxM*ctrl | CCT ACA GTT CAA TGA TAG TTC AAC AGA TTT CG |
| Yp_*LpxM*.F | TCG GTT TCA CCC TCT TTC CG |
| Yp_*LpxM*.R | ATT AGC TGG CAT AGG GCG TC |
| *LpxM*_Seq_F | GAA GCG GTT AAT CTG CTG CG |
| *LpxM*_Seq_R | GGA TAA ACC AGC AGG CCG TA |
| *LpxM*_gblock_f | GTG CAC CGG CGT AAC GCC ACT CAAAAA AAG CAC CGA CTC G |
| *LpxM*_gblock_r | TCA TGG TCG CAG CTA CAC CA |
| pTargetF-N20R | ACT AGT ATT ATA CCT AGG ACT GAG |
| 5EClpxPctrl | AGT AGC TGA AAG CAG TCA GC |
| 3EClpxPctrl | AGT AAC TTA CAA GTG TCT CAT ATC GG |
| Yp_*LpxP*.F | TAC AGC GAA GGT TCG CCA AT |
| Yp_*LpxP*.R | ACG CGC ACA ACA AGG TAA AC |
| *LpxP*_Seq_F | TGC AAG ACT GTT GTG TAC GGA |
| *LpxP*_Seq_R | GTA TTT TAC CGT GGG CAT CAC C |
| Kdsd NEW pecgrna n20 F | CAGTCCTAGGTATAATACTAGTCGGAATAGGAACTAAGGAGGGTTTTAGA GCTAGAAATAG |

| Primer ID | Primer Sequence (5' -> 3') |
|---|---|
| Yp_kdsD_screen_F | GAGTCACGCCATATCACTGC |
| CC_gutQ_screen_rev | GTGGCGGAAAGTGAGTTGTT |
| lpxM_Bl21_Screen_F | CGTATCAGCTCTGGTCTGCC |
| lpxM_Yp_Screen_R | CGCGACCTATAAGGCGACAT |
| lpxP_BL21_Screen_F | ATGAGTGCAGCGAGGATCAC |
| lpxP_Yp_Screen_R | AATTAGTGCAGACCTGGGGC |

### 2.3 Guide plasmid construction

The pEcgRNA guide plasmid was constructed to incorporate the targeting single guide RNA by performing inverse PCR with overlapping primers. One primer is specific for each insertion and contains the 20-basepair guide RNA (gRNA)target sequence listed in Table 2. The guide plasmid inverse PCR is followed by Gibson Assembly with NEBuilder® HiFi DNA Assembly Master Mix. Confirmation of the incorporation of the N20 guide region in the plasmid is noted by successful transformation into NEB® 5-alpha Competent *E. coli*. The N20 sequence replaces the selective marker *ccdB* gene. Lastly, the plasmid is isolated by the ZymoPURE Plasmid Miniprep Kit from Zymo Research.

### 2.4 Genome editing with CRISPR-Cas9

First the pEcCas plasmid is electroporated into the ClearColi™ cells in electroporation cuvettes (0.1 cm gap) and pulsed at 1.8 kV. Positive colonies were selected on LB + kan plates. ClearColi™ and subsequent mutant strains containing pEcCas plasmid were made electrocompetent to incorporate the specific pEcgRNA plasmid and donor DNA. The gene editing was conducted as previously described. In brief, the electrocompetent cells were transformed as described above with 100 ng of the specific pEcgRNA and 400 ng of the linear repair template and clones were selected on LB + kan + spec. The successful insertion of each gene of interest was confirmed by colony PCR utilizing the screening primers listed in Table 2.

### 2.5 Plasmid curing

After confirmation of gene insertion, the pEcgRNA plasmid was cured as previously described.[11,12] In brief, cells are inoculated in an overnight culture in LB containing kanamycin and 100 mM rhamnose at 37 °C with shaking. The cultures were plated onto LB-kan plates and incubated overnight. Selected colonies were then added to 50 µL LB-kan and streaked onto LB-kan + spec plates. After overnight incubation, plates with no growth observed on the LB-kan + spec plates are considered cured of the pEcgRNA plasmid.

### 2.6 Reverse transcriptase-polymerase chain reaction expression analyses

The Qiagen Rneasy Mini Kit™ was utilized to isolate RNA from each strain. Overnight cultures were prepared of the strains and the following day 200 µL of each culture is added to new media and grown to 1 x $10^7$ cells and centrifuged at 5,000 x g for 5 minutes at 4 °C. The RNA was then isolated according following the manufacturer's protocol. cDNA synthesis was performed using SuperScript™ IV Reverse Transcriptase kit with 50 µM random hexamers following the recommended protocol. Finally, a PCR reaction with Phusion® High Fidelity DNA Polymerase is performed on the reverse transcriptase-polymerase chain reaction (RT-PCR) samples using primers specific to the *Y. pestis* genes (Table 2). Amplified DNA was visualized on a 1 % agarose SYBR™ Safe stained gel is run of the PCR samples at 120 V for 30 minutes.

### 2.7 Matrix-assisted laser desorption/ionization time-of-flight mass spectrometry

Preparation of lipid A extracts for matrix-assisted laser desorption/ionization time-of-flight (MALDI-TOF) analyses were prepared as previously described.[13] In brief, overnight cultures were prepared in 5 mL LB-Miller broth with their respective selective antibiotic at 37 °C and shaking overnight. Next 1 mL of overnight culture is taken from each sample and resuspended in 400 µL of 100 mM sodium acetate pH 4.0. After resuspension the samples were incubated at 100 °C for 30 minutes, while being vortexed every 10 minutes. After cooling on ice, the samples were centrifuged at 8,000 x g for 5 minutes. The supernatant was removed, and the cell pellets were washed with 95 % ethanol and 100 µL of 12:6:1 chloroform/methanol/water was added, and the samples were centrifuged at 5,000 x g for 5 minutes. The supernatant spotted on stainless steel plates previously spotted with 10 mg/mL norharmane in

12:6:1 chloroform/methanol/water. Mass spectra were collected under negative ion mode on the smartfleX MALDI-TOF MS System (Bruker).

## 3. RESULTS

### 3.1 Genetic insertions of *Y. pestis* lipid A biosynthesis genes into *E. coli* genome

Previously, a series of genetic deletions and mutations to generate 'endotoxin free' strains of *E. coli* in various backgrounds, including *E. coli* BL21(DE3) were utilized.[8] These strains retained the minimal lipid A unit required for survival, lipid $IV_a$, and were created as ideal strains for the expression and purification of proteins which typically bind endotoxin (Figure 1A).[8] Here we chose this strain, known as ClearColi™, as a scaffold in which we can attempt to recreate the wild type *Y. pestis* lipid A in an *E. coli* genetic background. Utilizing several previously described reports which have detailed the structure and genetic biosynthesis pathways associated with outer membrane biosynthesis in *Y. pestis*, we selected three genes to insert into the ClearColi™ genome.[5,9,10,14] Specifically, the genes *lpxM* and *lpxP* encoding late acyl-transferase enzymes, that catalyze the addition of myristate and palmitoleate respectively to the lipid chain (Figure 1B). In addition, we determined that 3-deoxy-d-manno-oct-2-ulosonic (kdo) carbohydrate biosynthesis would need to be restored through the addition of *kdsD* which is a D-arabinose 5-phosphate isomerase.

Having identified *Y. pestis* genes of interested to insert in the ClearColi™ genome, we utilized a two-plasmid CRISPR-Cas9 genome editing system designed for *E. coli* to make the insertions.[11] First, the ClearColi™ genome was sequenced at the homolog loci for *lpxM*, *lpxP*, and *ksdD* to identify flanking PAM site that would be the insertion site for *Y. pestis* genes following Cas9 cleavage and repair (Figure 2A). We were unable to acquire data that aligned with prior reports of the *E. coli kdsD* deletion in the ClearColi™ background which prevented identifying a PAM to target as an insertion site. The *E. coli* genome contains two homologous D-arabinose 5-phosphate isomerases, KdsD and GutQ, both of which catalyze kdo biosynthesis.[8,15,16] While *Y. pestis* only contains the homolog to KdsD, we chose to target the *gutQ* genomic loci as our *kdsD* insertion site so kdo biosynthesis restored. Once the PAM was identified for each target, the repair template, which includes the *Y. pestis* gene of interest flanked by ~500 bp of ClearColi™ genome on either side, was acquired as synthetic DNA and amplified by PCR (Figure 2B). Next the Cas9 vector, the guide RNA targeting vector, and the repair template DNA were transformed into the ClearColi™ strain and resultant transformants were screened for successful gene insertion. As indicated by the black arrows in Figure 2B, inserted *Y. pestis* genes were confirmed by PCR utilizing one primer within the *Y. pestis* gene and the other outside of the repair DNA template (Figure 2C). Positive clones were confirmed by DNA sequencing. In succession, we generated ClearColi:*lpxM*, ClearColi:*lpxM:lpxP*, and finally ClearColi:*lpxM:lpxP:kdsD* strain derivatives.

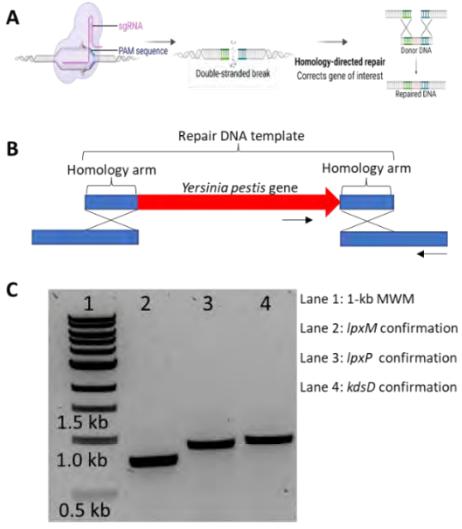


**Figure 2. Insertion of *Y. pestis* genes into the ClearColi™ genome with CRISPR-Cas9 recombineering. A) Schematic representing CRISPR-Cas9 site directed double stranded DNA cleavage and homology guided repair. B) Design of repair templates utilized for genome editing. The *Y. pestis* genes of interest (red) were designed to have regions of homology to**

**the ClearColi™ genome (blue). Primers for confirming the insertion are designated by the black arrows. C) 1% SYBR™ Safe stained agarose gel includes amplified DNA from a colony PCR screen. Lane 1 includes the NEB Quick-Load® 1 kb DNA Ladder. Lane 2 is the amplified reaction from the internal *Y. pestis* lpxM primer and primer outside of the *E. coli* ClearColi™ homology arm region with an expected size of 861 bp. Lane 3 is the similarly explained primer set for the specific *Y. pestis* lpxP insertion with an expected size of 1,019 bp. Lane 4 is the conformation of the specific *Y. pestis* kdsD insertion with an expected size of 967 bp.**

### 3.2 *Y. pestis* lipid A biosynthesis genes are expressed in the engineered *E. coli* ClearColi™ strain

Having successfully confirmed the insertion of the three *Y. pestis* lipid A biosynthesis genes into the background ClearColi™ genome, we next set to confirm that the genes were being expressed as we would expect. Through the genetic manipulations, only the coding regions of the *Y. pestis* genes were inserted into the ClearColi™ genome meaning that the transcription of the genes is under the control of the native *E. coli* promotors. Total RNA was isolated from early logarithmic phase growth for wild type ClearColi™ and ClearColi:lpxM:lpxP:kdsD and cDNA synthesis was performed. The expression of *lpxM*, *lpxP*, and *kdsD* was confirmed using primers specific to the *Y. pestis* gene with the cDNA as a template and analyzed by gel electrophoresis. As expected, we observed expression for each of the *Y. pestis* genes in the edited strain with no expression in the wild type ClearColi™ (Figure 3). Together, this data demonstrates that not only have the *Y. pestis* genes been inserted into the ClearColi™ genome, but they are transcribed under the control of the native *E. coli* promotors.

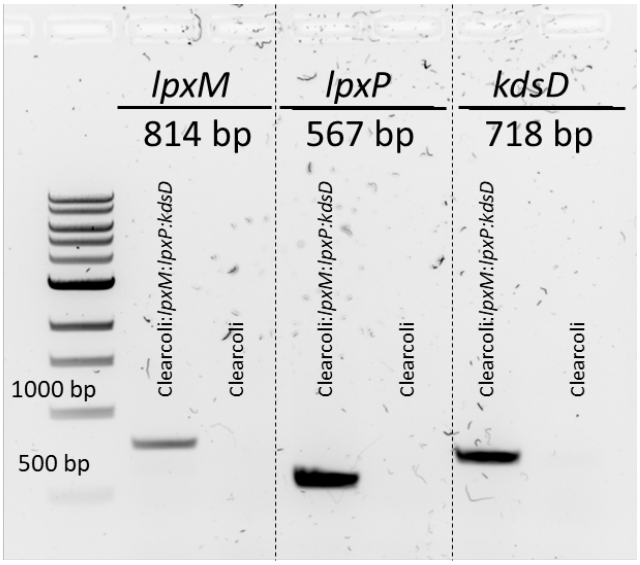


**Figure 3. RT-PCR expression analyses of *Y. pestis* genes inserted in the ClearColi™ genome. Total RNA was isolated from mid-exponential cultures to screen for *Y. pestis* gene expression. The reverse transcribed cDNA was used as templates for the PCR reactions. The products were analyzed on a 1 % SYBR™ Safe stained agarose gel. cDNA from the wild type ClearColi™ strain was used as a negative control for expression analyses.**

### 3.3 *Y. pestis* lipid A biosynthesis genes are unable to restore hexa-acylated lipid A in engineered *E. coli*

Having confirmed that each of the genes were being expressed as expected, we set out to determine if the functions of LpxM, LpxP, and KdsD in lipid A biosynthesis in the ClearColi™ background with *Y. pestis* genes were restored. The lipids from wild type ClearColi™, ClearColi:lpxM, ClearColi:lpxM:lpxP, and ClearColi:lpxM:lpxP:kdsD, were prepared utilizing a previously described method for analyses by matrix-assisted laser desorption ionization – time of flight (MALDI-TOF) mass spectrometry.[13] In wild type ClearColi™, we observed a major peak at 1404 m/z corresponding to the presence of just lipid $IV_a$ as reported previously (Figure 4A).[8] Next, we examined the lipid structures of ClearColi:lpxM and ClearColi:lpxM:lpxP to determine if the late acyl transferase genes were functional in this background. In either background, we only observed the 1404 m/z corresponding to the lipid $IV_a$ rather than the expected mass of 1852 m/z which would indicate the enzymes function as expected (Figures 4C). This result is not surprising as previous reports have suggested that lipid $IV_a$ is not the substrate for LpxM or LpxP and that the genes act downstream of kdo incorporation, requiring $(kdo)_2$-lipid $IV_a$ as a substrate.[8,17] Finally, we characterized the lipids from ClearColi:lpxM:lpxP:kdsD by MALDI-TOF to determine if hexaacylated lipid A biosynthesis was

restored. Again, in this case, only the 1404 m/z corresponding to lipid $IV_a$ with no high molecular weight moieties identified (Figure 4D). This result indicates that simply adding the genes encoding LpxM, LpxP, and KdsD is not sufficient to rescue lipid A biosynthesis in the *E. coli* ClearColi™ background.

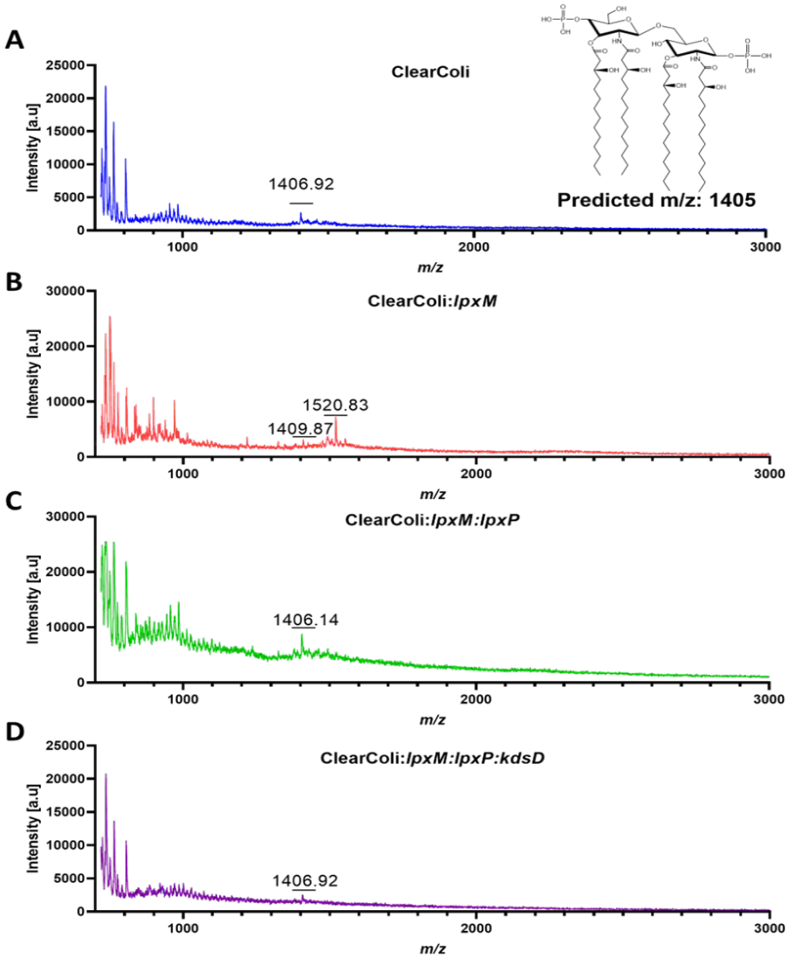


**Figure 4. MALDI-TOF characterization of lipid A structures isolated from engineered ClearColi™ strains. Lipids were isolated from A) WT ClearColi™ inset represents the expected lipid $IV_a$ structure and predicted mass, B) ClearColi:lpxM, C) ClearColi:lpxM:lpxP, and D) ClearColi:lpxM:lpxP:kdsD.**

### 3.4 *Y. pestis* lipid A modifying genes are functional in engineered ClearColi™ strain

Despite being unsuccessful in our attempts in recapitulating hexaacylated lipid A biosynthesis in ClearColi™ with *Y. pestis* genes, we next set out to characterize lipid A modifying genes important to *Y. pestis* biology, *arnT* and *eptA*. The lipid A modifying enzyme ArnT catalyzes the addition of aminoaribinose to the phosphate groups of lipid A and in *Y. pestis* has been shown to be involved in antimicrobial resistance and the function seems to be growth temperature dependent. Similarly, EptA catalyzes the addition of phosphoethanolamine to the same 1' and 4' phosphate groups on the lipid A structure which again contributes to resistance to antimicrobials in *Y. pestis* (Figure 5A). In order to determine if the *Y. pestis eptA* and *arnT* homologs are functional in our engineered ClearColi™ strain, each gene was cloned into an inducible expression vector and transformed into ClearColi:lpxM:lpxP:kdsD. Again, we confirmed that the genes were being expressed by RT-PCR and as expected we were able to observe expression utilizing *Y. pestis* specific primers and cDNA as a template for PCR (Figure 5B). Having confirmed expression of both *arnT* and *eptA*, we again utilized MALDI-TOF mass spectrometry to examine if the enzymes are functioning and decorating lipid $IV_a$ as we would expect. When ArnT was expressed in ClearColi:lpxM:lpxP:kdsD, we observed the expected peak at 1405 m/z corresponding the lipid $IV_a$ as well as an additional peak at 1538 m/z which is what we would expect for the addition of a single aminoarabinose modification (Figure 5B). This result indicates that the *Y. pestis* ArnT is in fact

functional in the ClearColi:lpxM:lpxP:kdsD background. Similarly, when examining the function of EptA in ClearColi:lpxM:lpxP:kdsD + pD451_YpEptA we observed a mass at 1529 m/z corresponding to a single phosphoethanolamine addition to the lipid $IV_a$ structure (Figure 5B). Taken together, using heterologous expression vectors, we successfully rescued the function of both lipid A modifying enzymes ArnT and EptA in the ClearColi:lpxM:lpxL:kdsD background.

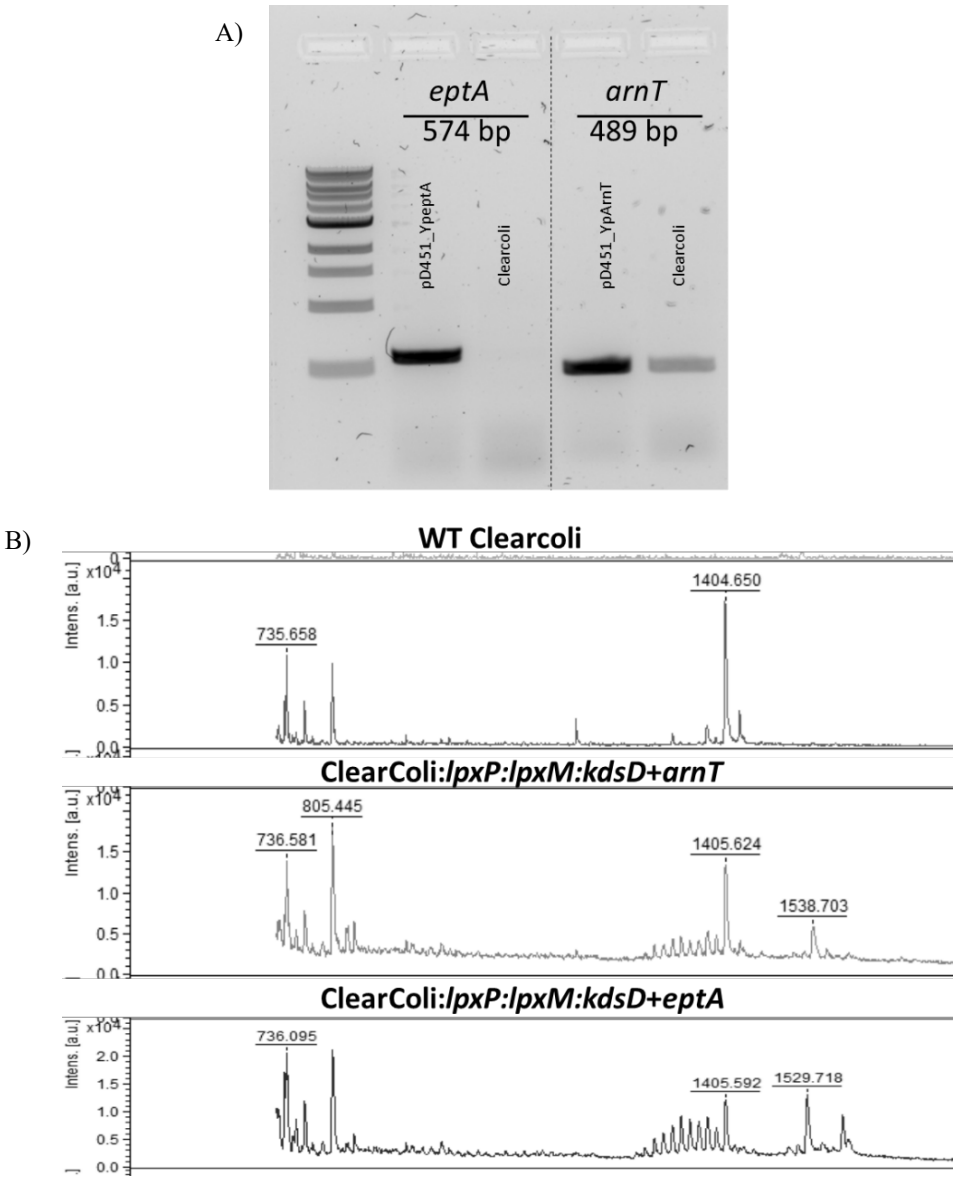


**Figure 5. Characterization of lipid A modifying enzymes ArnT and EptA. Top. RT-PCR expression analyses of *Y. pestis* genes inserted in the ClearColi™ genome. Total RNA was isolated from mid-exponential cultures to screen for *Y. pestis* gene expression. The reverse transcribed cDNA was used as templates for the PCR reactions. A) The products were analyzed on a 1 % SYBR™ Safe stained agarose gel. cDNA from the WT ClearColi™ strain was used as a negative control for expression analyses. Lipids were isolated from part A and further characterizd. B) WT ClearColi™ inset represents the expected lipid $IV_a$ structure and predicted mass ClearColi™, ClearColi:lpxM:lpxP:kdsD+arnT and ClearColi:lpxM:lpxP:kdsD+eptA.**

## 4. DISCUSSION

In this report, we set out to recapitulate *Y. pestis* lipid A biosynthesis in a previously engineered of strain of *E. coli* which expresses the tetra-acylated lipid $IV_a$ outer membrane structure. We hypothesized that if we inserted three critical genes; *kdsD*, *lpxM*, and *lpxP* from *Y. pestis*, into *E. coli* ClearColi™, the engineered strain would express a hexa-acylated lipid A, as is observed in *Y. pestis* at lower temperatures. Despite successfully inserting the genes into the homologous loci in *E. coli* ClearColi™ and confirming expression, we were unable to restore the hexa-acylated lipid A in the engineered strain as determined by MALDI-TOF analyses.

There are several potential explanations as to why hexa-acylated lipid a was not achieved in the engineered *E. coli*. As expected, we did not observe the acylation from insertion of *lpxM* and *lpxP* in the absence of kdo biosynthesis as lipid $IV_a$ is not a substrate for these enzymes.[8] However, once the *Y. pestis kdsD* was inserted in the ClearColi™ genome, we expected kdo biosynthesis to be restored and LpxM and LpxP to be functional but this result was not observed. It is possible that *kdsD* insertion by itself does not restore kdo biosynthesis.

In addition to the potential non-functional kdo biosynthesis, a second explanation for the inability to restore hexa-acylated lipid A is through a point mutation in the lipid A transport protein MsbA. Previous studies have demonstrated that, for deficient kdo biosynthesis to be a non-lethal mutation, suppressor mutations in *msbA* or *yhjD* are required under fast growing conditions.[17] In fact, the ClearColi™ strain does have a G to A mutation in *msbA* at position 52 which enables this strain to be viable with lipid $IV_a$ as its outer membrane.[8] Furthermore, in the absence of these suppressor mutations, *E. coli* strains exhibiting just lipid $IV_a$ or $(kdo)_2$-lipid A have only been achieved under slow growing medium conditions at lower temperatures but were not evaluated in this study.[17] Future efforts are targeted at exploring repairing the *msbA* mutation in the ClearColi™ strain or via overexpression of WT *msbA* in the engineered strain to determine if hexa-acylated lipid A can be restored.

The goal of this work was to utilize CRISPR-Cas9 genome engineering to recreate the *Y. pestis* outer membrane in an *E. coli* scaffold strain. Bacterial outer membranes are highly immunostimulatory and can be harnessed for vaccine development; additionally, the outer membranes of Gram-negative bacteria are primary targets for detection and typing of pathogens. Recent studies have demonstrated that engineered outer membrane vesicles, derived from pathogens can be used as safe alternatives for vaccine developments.[18] While we were unable to fully restore the *Y. pestis* outer membrane, this work enables sets the stage for the development of novel detection assays and medical countermeasures.

## ACKNOWLDEGEMENTS

We would like to thank Kelley Betts for assistance in generating graphics and the Combat Capabilities Development Command Chemical Biological Center In-house Laboratory Independent Research Program for thoughtful discussion and programmatic support. Funding was provided by the U.S. Army via the In-house Laboratory Independent Research Program (PE 0601101A Project 91A) at the Combat Capabilities Development Command Chemical Biological Center.

## REFERENCES

[1] Raetz, C.R.; Whitfield, C. Lipopolysaccharide endotoxins. *Annu Rev Biochem.* **2002**, *71*, pp 635–700.

[2] Knirel, Y.A.; Valvano, M.A. *Bacterial lipopolysaccharides: structure, chemical synthesis, biogenesis and interaction with host cells*; Springer Science & Business Media, **2011**.

[3] Gronow, S.; Brade, H. Lipopolysaccharide biosynthesis: which steps do bacteria need to survive? *J. Endotoxin Res.* **2001**, *7* (1), pp 3–23.

[4] Prior, J.L.; Hitchen, P.G.; Williamson, D.E.; Reason, A.J.; Morris, H.R.; Dell, A.; Wren, B.W.; Titball, R.W. Characterization of the lipopolysaccharide of Yersinia pestis. *Microb. Pathog.* **2001**, *30* (2), pp 49–57.

[5] Kawahara, K.; Tsukano, H.; Watanabe, H.; Lindner, B.; Matsuura, M. Modification of the Structure and Activity of Lipid A in *Yersinia pestis* Lipopolysaccharide by Growth Temperature. *Infect. Immun.* **2002**, *70* (8), pp 4092–4098.

[6] Knirel, Y.A.; Lindner, B.; Vinogradov, E.V.; Kocharova, N.A.; Senchenkova, S.N.; Shaikhutdinova, R.Z.; Dentovskaya, S.V.; Fursova, N.K.; Bakhteeva, I.V.; Titareva, G.M.; Balakhonov, S.V.; Holst, O.; Gremyakova, T.A.; Pier, G.B.; Anisimov, A.P. Temperature-Dependent Variations and Intraspecies Diversity of the Structure of the Lipopolysaccharide of *Yersinia pestis*. *Biochemistry.* **2005**, *44* (5), pp 1731– 1743.

[7] Han, Y.; Zhou, D.; Pang, X.; Song, Y.; Zhang, L.; Bao, J.; Tong, Z.; Wang, J.; Guo, Z.; Zhai, J.; Du, Z.; Wang, X.; Zhang, X.; Wang, J.; Huang, P.; Yang, R. Microarray analysis of temperature-induced transcriptome of Yersinia pestis. *Microbiol. Immunol.* **2004**, *48* (11), pp 791–805.

[8] Mamat, U.; Wilke, K.; Bramhill, D.; Schromm, A.B.; Lindner, B.; Kohl, T.A.; Corchero, J.L.; Villaverde, A.; Schaffer, L.; Head, S.R.; Souvignier, C.; Meredith, T.C.; Woodard, R.W. Detoxifying *Escherichia coli* for endotoxin-free production of recombinant proteins. *Microb. Cell Fact.* **2015**, *14* (1), pp 1–15.

[9] Rebeil, R.; Ernst, R.K.; Jarrett, C.O.; Adams, K.N.; Miller, S.I.; Hinnebusch, B.J. Characterization of Late Acyltransferase Genes of *Yersinia pestis* and Their Role in Temperature-Dependent Lipid A Variation. *J. Bacteriol.* **2006**, *188* (4), pp 1381–1388.

[10] Chandler, C.E.; Harberts, E.M.; Pelletier, M.R.; Thaipisuttikul, I.; Jones, J.W.; Hajjar, A.M.; Sahl, J.W.; Goodlett, D.R.; Pride, A.C.; Rasko, D.A. Trent, M.S.; Bishop, R.E.; Ernst, R.K. Early evolutionary loss of the lipid A modifying enzyme PagP resulting in innate immune evasion in *Yersinia pestis*. *Proc. Natl. Acad. Sci. U. S. A.* **2020**, *117* (37), pp 22984–22991.

[11] Li, Q.; Sun, B.; Chen, J.; Zhang, Y.; Jiang, Y.; Yang, S. A modified pCas/pTargetF system for CRISPR-Cas9-assisted genome editing in Escherichia coli. *Acta Biochim. Biophys. Sin.* **2021**, *53* (5), pp 620– 627.

[12] Jiang, Y.; Chen, B.; Duan, C.; Sun, B.; Yang, J.; Yang, S. Multigene editing in the Escherichia coli genome via the CRISPR-Cas9 system. *Appl. Environ. Microbiol.* **2015**, *81* (7), pp 2506–2514.

[13] Liang, T.; Leung, L.M.; Opene, B.; Fondrie, W.E.; Lee, Y.I.; Chandler, C.E.; Yoon, S.H.; Doi, Y.; Ernst, R.K.; Goodlett, D.R. Rapid Microbial Identification and Antibiotic Resistance Detection by Mass Spectrometric Analysis of Membrane Lipids. *Anal Chem.* **2019**, *91* (2), pp 1286–1294.

[14] Knirel, Y. A.; Anisimov, A. Lipopolysaccharide of Yersinia pestis, the Cause of Plague: Structure, Genetics, Biological Properties. *Acta Naturae.* **2012**, *4* (3) pp 46–58.

[15] Meredith, T.C.; Woodard, R.W. Escherichia coli YrbH is a D-arabinose 5-phosphate isomerase. *J. Biol. Chem.* **2003**, *278* (35), pp 32771–32777.

[16] Meredith, T.C.; Woodard, R.W. Identification of GutQ from Escherichia coli as a D-arabinose 5-phosphate isomerase. *J. Bacteriol.* **2005**, *187* (20), pp 6936–6942.

[17] Klein, G.; Lindner, B.; Brabetz, W.; Brade, H.; Raina, S. Escherichia coli K-12 Suppressor-free Mutants Lacking Early Glycosyltransferases and Late Acyltransferases: minimal lipopolysaccharide structure and induction of envelope stress response. *J. Biol. Chem.* **2009**, *284* (23), pp 15369–15389.

[18] Cheng, K.; Zhao, R.; Li, Y.; Qi, Y.; Wang, Y.; Zhang, Y.; Qin, H.; Qin, Y.; Chen, L.; Li, C.; Liang, J.; Li, Y.; Xu, J.; Han, X.; Anderson, G.J.; Shi, J.; Ren, L.; Zhao, X.; Nie, G. Bioengineered bacteria-derived outer membrane vesicles as a versatile antigen display platform for tumor vaccination via Plug-and-Display technology. *Nat. Commun*. **2021**, *12* (1), pp 1–16.

# Fundamental exploration into advanced plasmonic ceramic nitrides as multispectral obscurants

Danielle L. Kuhn[a]*, Zachary B.S. Zander[a], Lena Vlahakis[b], Joshua Smith[b]
[a]U.S. Army Combat Capabilities Development Command Chemical Biological Center, Research & Operation Directorate, 8198 Blackhawk Rd, Aberdeen Proving Ground, MD 21010
[b]Luna Labs USA, LLC, 706 Forest St. #A, Charlottesville, VA, 22903

## ABSTRACT

Obscurant materials play a crucial role in protecting the U.S. warfighter. They are materials which will absorb, scatter, or emit radiation in the visible, infrared, and millimeter wavelengths to interrupt the line of sight and infrared sensors between an objective and observer. However, current fielded visible/infrared obscuration technologies (i.e., broadband obscurants, such as brass and graphite) are limited in obscuring modern devices due to low obscuring performance, incompatibilities with explosive dissemination, and poor de-agglomeration of the materials upon dissemination in atmospheric conditions. By utilizing a facile hydrothermal synthetic strategy, we will prepare doped-titanium nitride nanofibers. We hypothesize that the fabrication of both plasmonic ceramic nanofibers and their doped forms by hydrothermal synthesis will result in enhanced optical and electrical properties designed for the broadband attenuation necessary for the next generation of high-performing obscurants. By fundamentally investigating the synthesis of advanced plasmonic ceramic nanofibers, this work is expected to provide new obscuring materials and synthetic strategies to address the Army's need for broadband obscuration, and further the basic underlying phenomena relating metal-nitride ceramic doping, conductivity, and photonic absorption/scattering.

**Keywords:** Obscuration, plasmonic materials, broadband attenuation, synthetic chemistry

## 1. INTRODUCTION

Obscurants are materials that absorb, scatter, or emit radiation in the visible, infrared (IR), and millimeter wavelength range to interrupt the line of sight between an objective and observer. These materials play a crucial role in protecting the U.S. warfighter by decreasing the electromagnetic (EM) energy available for the functioning of sensors, seekers, trackers, optical enhancement devices, and the human eye. However, current visible/IR obscuration technologies (i.e., broadband obscurants, such as brass and graphite) are limited in obscuring modern devices due to low obscuring performance, incompatibilities with explosive dissemination, and poor de-agglomeration of the materials upon dissemination in atmospheric conditions.

From water distillation to cancer treatment, plasmonic nanoparticles (NPs) have found a variety of applications in the energy, defense, and medical sectors.[1–3] Plasmonic materials possess unique characteristics stemming from resonant oscillations of free electrons as a response to EM waves.[1] By controlling the size, shape, conductivity, dopants, and environment, the extinction efficiency and resonance position is readily tuned.[2,3] This strong and tunable interaction with EM waves has attracted immense attention over the last few decades. While Au and Ag are the most well-known plasmonic materials and have had the most interest due to their superior performance in the visible region, these materials are less than ideal of broadband obscuration. Besides the great expense associated with manufacturing, these noble metals are limited to the visible and near-IR region of the EM spectrum, possess low melting points, and are easily compressed.[4] In contrast, transition metal nitrides are known to exhibit plasmon resonances at longer wavelengths. Along with their unique plasmonic properties, metal nitrides are known for their refractory properties, meaning chemically stable at temperatures above 2000 °C, as well as high conductivity. The low cost, high stability, and high optical extinction of transition metal nitride NPs may be the ideal solution to solve the current problems existing in broadband obscurant systems. Until now, the shape-controlled synthesis of metal nitrides has been expensive, hazardous, and non-scalable.[1,5] For instance, previous work used low temperature solid-state metathesis of titanium (III) chloride and sodium azide without the use of a solvent.[6] This approach utilized chemicals which were highly corrosive and explosive, making it less than ideal to use as a method for scaled-up production. Thus, there is a critical need for facile and safe synthetic strategies to metal nitride NPs.

Recently, plasmonic nitrides such as titanium nitride (TiN) and zirconia nitride have received significant interest due to their low cost, scalability, and high durability. However, the synthetic methodologies to precisely control the size, shape, and composition of nitride NPs are significantly limited when compared to methods used to produce precious metal plasmonic NPs. Leveraging a facile hydrothermal method, a versatile method to functionalize and/or dope TiN NPs with different metals was developed. This new synthetic methodology unlocks new opportunities in designing TiN NPs with unique optoelectronic properties.

As alluded to above, the diversity of applications of plasmonic NPs arises from the ability to readily tune the localized surface plasmon resonances (LSPRs) of NPs.[4,7] LSPRs occur in plasmonic materials (i.e., those that exhibit negative real permittivity) that have one or more dimensions smaller than the wavelength of incident light.[4,7] A surface plasmon resonance is produced when a material's electron density couples with incident EM radiation to create a coherent, collective oscillation of the conduction electrons.[4,7] By confining a resonance to dimensions smaller than the wavelength of light, the electron density oscillates locally around the NP, and, thus, the plasmon's behavior is defined by the structural features of the NP.[4,7] This localization means that the extinction (scattering + absorbance) spectra and electric field (EF) enhancements of plasmonic NPs can be modified for specific applications by changing their size, shape, composition, and environment.[4,7] The wavelength (λ) dependent extinction spectrum of a spherical metal NP can be calculated by Equation 1, in which size (α, radius), shape (χ, which equals 2 for a sphere), composition ($\varepsilon_i$ and $\varepsilon_r$, the imaginary and real components of the metal dielectric function), and environment ($\varepsilon_{out}$, dielectric of surrounding media) all contribute to the scattering and absorption behavior.[4,7]

$$E(\lambda) = \frac{24\pi^2 N\alpha^3 \varepsilon out^{3/2}}{\lambda \ln(10)} \left| \frac{\varepsilon i(\lambda)}{(\varepsilon i(\lambda)+\chi\varepsilon out)^2+\varepsilon i(\lambda)^2} \right| \quad (1)$$

This work focused on developing a strategy to functionalize or dope the TiN NPs. Recall, functionalization is a broad term for adding metal to the TiN NPs. Doping refers to substitution of metal atoms into the crystal lattice.

## 2. EXPERIMENTAL

### 2.1 Supercritical $CO_2$ drying

The material suspension is dried by purging with supercritical $CO_2$ ($scCO_2$) in a high-pressure vessel. The $CO_2$ pressure in the vessel during the drying operation is 3000 psig and the temperature is gradually increased from ~ 65 °C to ~ 83 °C while purging with $CO_2$. Huff-and-puff steps, in which the vessel pressure is decreased and then increased back to 3000 psig to achieve more rigorous drying, are also a part of the drying cycle (Figure 1). The cycle times may be changed depending on the amount of paste being dried.

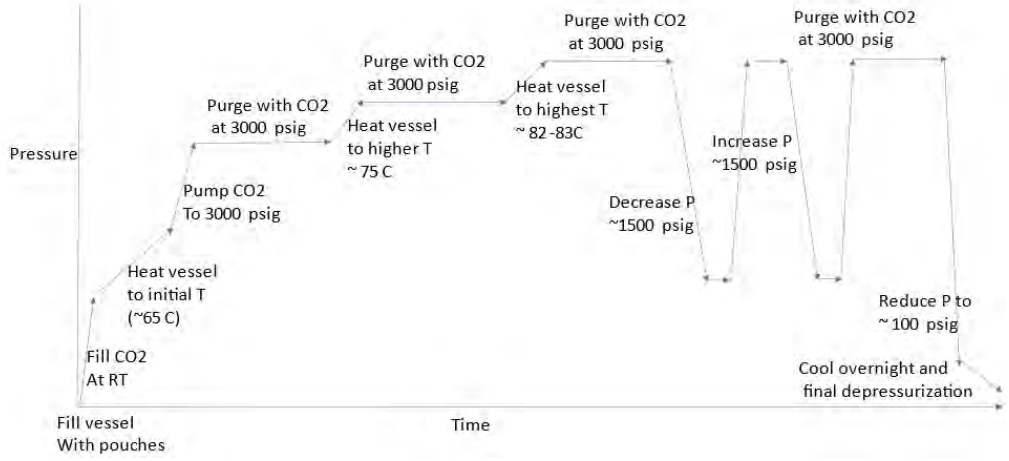


**Figure 1. Supercritical $CO_2$ drying cycle.**

### 2.2 Oxynitride synthesis

The synthetic method for producing oxynitride, as reported in literature involves sonicating gallium metal with ethylene diamine to form a gallium ethylene diamine complex, which is then heated in a hydrothermal reactor followed by a thermal anneal to produce gallium oxynitride (GaON).[8]

Following the literature methods, gallium metal was sonicated with ethylene diamine at 50 °C, which is above gallium metal's melting point. Initially, this method did not result in the black dispersion which was expected to indicate the formation of the gallium ethylene diamine complex. Next, the temperature was increased to 70 °C. However, it was found that the bath sonicator was not able to maintain the temperature required. As an alternative, a ceramic dish was used to heat a water bath to 70–75 °C and a probe sonicator was used to sonicate the gallium and ethylene diamine. Ultimately, a reaction was observed when the solution was manually agitated by shaking or stirring, while using the water bath to maintain the high temperature. When color change was observed after stirring and manual agitation, the solution was allowed to stir for 30 minutes. Afterward, no silver gallium metal was observed within the dispersion, suggesting successful complexing. Water was added and the solution was transferred to a hydrothermal reactor to heat to 200 °C for 24 hours. The material was washed by centrifugation, oven dried, and annealed for 5 hours at 500 °C.

### 2.3 Mass extinction coefficient chamber measurements

The aerosol test chamber is a 6-meter by 7-meter, 190 cubic meter volume capable of spraying dried powders, liquids, and explosive/pyrotechnic dissemination. At minimum, 6–10 grams of material are required per trial. It is recommended to perform three trials per materials to establish an average. The chamber is set up with a variety of analysis equipment to include, laser lock-in amplifier, flow meter data acquisition box, circulation fan, temperature and humidity detectors, Fourier-transform infrared (FTIR) spectroscopy detectors to cover mid-IR and near-IR as well as ultraviolet/visible. House air is used to disseminate until transmittance falls below 80 %. The mass in grams of disseminated material is recorded. Two filter samples are collected using Whatman 47 mm GF/F glass microfiber filters. Data is processed using MatLab to determine mass extinction coefficient (MEC) and yield factor which is the effectiveness of dissemination of the aerosol. Equations can be seen in Equations 2 and 3.

$$T = e^{-a*C*L} \Rightarrow a = \frac{-\ln(T)}{Concentration \cdot Pathlength} \tag{2}$$

$$YF = \frac{mass\ of\ airborne\ material}{initial\ mass\ of\ material} \tag{3}$$

## 3. RESULTS AND DISCUSSION

### 3.1 Additive studies

Since varying ratios of water to isopropanol did not yield notable difference in spectral properties from pure water as a solvent, additives with OH groups may direct the growth of TiN into rods and wires. Therefore, additives with OH groups and different steric environments were selected to determine the influence of additives on morphology and spectral properties, and down select the additives that resulted in the best spectral properties.

Additives with OH groups were investigated to determine if rod-like growth was directed via acidic OH groups. A variety of additives were compared, including those with C–OH groups like polyethylene glycol (PEG), which led to the best optically performing nanorods in previous work, and carboxylic groups, which can complex and bind to metal atoms to, in this case, Ti atoms.[8,9] Carboxylic groups may bind to the Ti atoms and direct rod-like growth which could then be compared to additives like PEG, which contain C–OH groups, to determine the ideal additive to promote TiN rod growth.

During this study, varying acidic additives with OH groups were investigated in both water and isopropanol (IPA) with a 1:1 molar ratio to TiN to determine if acidic additives would increase the optical performance of TiN powders. The resulting materials were characterized by measurements of absorbance, transmission, average particle size, and image visibility to examine obscuration performance and NP morphology.

The additives investigated in this study were acetic acid, benzoic acid, glucose, L-ascorbic acid, citric acid, and PEG (Figure 2). PEG was investigated in water only, due to the potential pressures in IPA exceeding the reactor limits. The characterization results of the TiN additive studies in IPA and water are shown in Figure 3 and Figure 4 respectively, including MECs, transmittance spectra measurements, average particle size determined via dynamic light scattering (DLS), and Michaelson contrast values (MCVs).

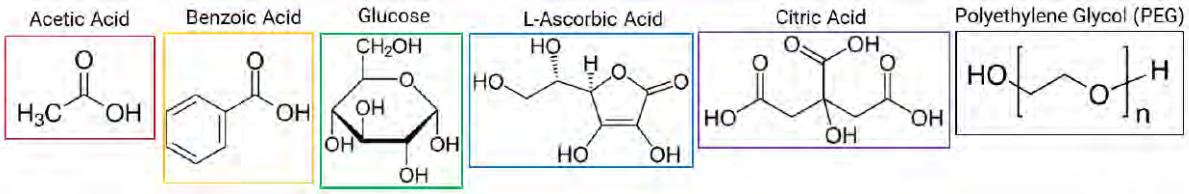


**Figure 2. Molecular diagrams of additives used for TiN hydrothermal experiments in IPA and water.**

The MEC plots calculated from UV-Vis absorption measurements (Figures 3A, 3E) show that for both water and IPA solvents, the glucose and L-ascorbic acid additives flatten the spectra in the near-IR region compared to standard TiN. Both glucose and L-ascorbic acid are reducing agents, which could be reducing the TiN and flattening the spectra in the near-IR region. Both additives also do not contain carboxylic functional groups, only C–OH groups. The remaining additives are comparable in spectral shape, with higher MECs. Acetic acid, benzoic acid, and citric acid have carboxylic functional groups, implying carboxylic functional groups in additives may help to produce better spectrally performing particles than additives with C–OH groups only.

The FTIR transmittance plot in Figure 3B shows the materials synthesized in IPA result in similar spectral shapes and transmittance. The additives in water (Figure 3F) result in slightly more variation in FTIR spectral shape, with glucose and L-ascorbic acid having flatter line shapes than the other additives in IPA as well as the additives in water. Average particle measurements via DLS show that the additives vary with average particle size in water (Figure 3D). PEG produces the largest average size, while citric acid produces the smallest average size. However, in IPA (Figure 3H), benzoic acid produces NPs that are significantly larger than the other additives in IPA, similar to the size range of PEG in water. Other than benzoic acid, the average particle sizes in IPA are very similar. The much larger average particle sizes with benzoic acid and PEG may be a result of aggregated particles.

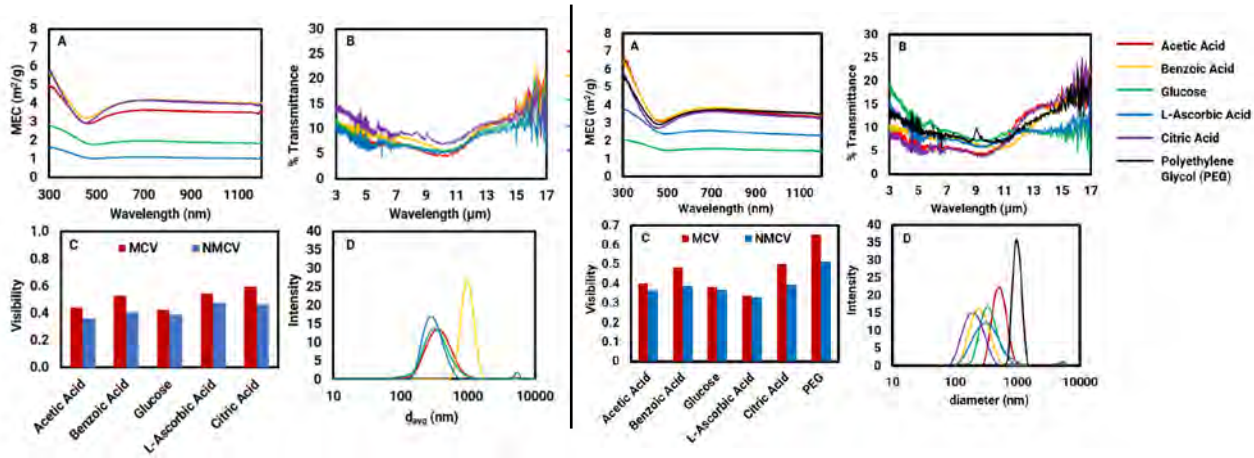


**Figure 3. (A) UV-Vis MECs, (B) FTIR Transmittance, (C) MCVs, and (D) average particle sizes recorded for TiN (left) and TiN NPs synthesized in water with various acid additives (right).**

MCVs were calculated for both IPA and water studies (Figures 3C, 3G). The products produced by the additives followed the same trends between water and IPA, except for L-ascorbic acid. TiN synthesized with L-ascorbic acid in IPA produced a significantly higher MCV than TiN synthesized in water. Overall, TiN synthesized with acetic acid, citric acid, and benzoic acid produced the best MECs in both water and IPA, followed by PEG in water. Synthesizing TiN with these additives in IPA results in a slight increase in MEC in the near-IR region, while synthesizing in water gives a slight increase in the visible region, so both water and IPA as solvents are recommended, with water being a less expensive alternative to IPA.

### 3.2 Solvent studies

Previous work showed that TiN nanowires formed in the presence of KOH and NaOH base, and nanorods formed in the presence of PEG. This work indicated the presence of OH groups could increase the optical performance of TiN NP powders. Therefore, a study was devised to determine the influence of the reaction solvent during the hydrothermal synthesis of TiN, where it was hypothesized that a reaction solvent with a higher concentration of OH groups would increase the optical properties of the TiN. Utilizing isopropanol as the solvent would drastically increase the amount of OH groups available to direct nanorod growth compared to water. A set of experiments was performed to explore

the ratios of water and IPA in the absence of other hydroxide species during the solvothermal synthesis of TiN NPs. A set of reactions was conducted using water and IPA in different ratios. The resulting materials were characterized by measures of transmission, absorbance, and particle size (Figure 4).

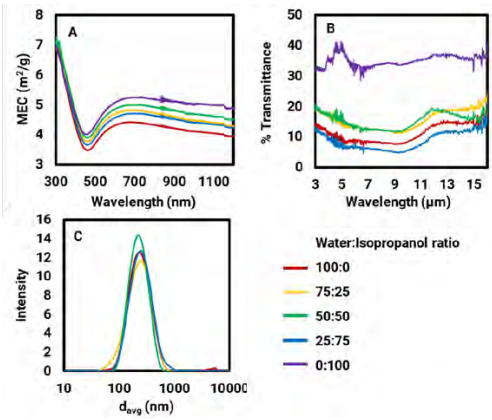


**Figure 4. (A) UV-Vis MECs, (B) FTIR transmittance plots, and (C) particle size distributions recorded for hydrothermal TiN NPs synthesized with various water:IPA ratios.**

Qualitative analysis of the UV-Vis and FTIR spectra in Figure 4A, B show that there are no significant differences in their properties while varying the amount of isopropanol in the reaction. The range in average particle sizes is very tight (200–215nm), and the differences in MECs are within the error of the measurement. The powder that was synthesized with 100 % isopropanol and no water did demonstrate a higher IR transmittance than the other ratios, indicating that a solution containing isopropanol as a solvent may not be a desired route. Overall, the amount of alcohol in the reaction compared to water does not appear to significantly affect the spectral properties of the TiN powders. Given this, water and IPA were both included for further experimentation.

### 3.3 Scaleup for aerosol testing

Over the course of the varied TiN synthesis experiments, three synthesis conditions were each chosen to be replicated at the 20-gram scale. The three scaled-up materials include TiN synthesized in IPA, TiN synthesized in a solution of citric acid in water, and TiN synthesized in a solution of PEG in water. The samples were all characterized by measurements of absorbance, transmission, average particle size, and image visibility. The characterization results of the down selected TiN (Figure 5).

The IPA, citric acid, and PEG TiN samples were similar UV-Vis MECs (Figure 5A). The IPA sample showed the lowest MCVs (Figure 5C), indicating the highest visual obscuration performance. The IPA samples also showed the greatest deviation in FTIR spectra (Figure 5B). The IPA and citric acid samples had similar particle sizes, while the PEG samples showed a slightly higher average particle size but a much narrower size distribution. After washing, samples remained dispersed in isopropanol and set aside for $scCO_2$ drying. Supercritical drying directly from solution aims to minimize particle aggregation for improved obscurant performance in the aerosol.

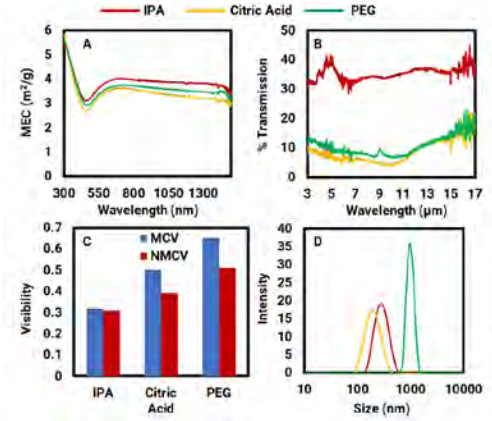


**Figure 5. (A) UV-Vis MECs, (B) FTIR Transmittance, (C) MCVs, and (D) average particle sizes recorded for TiN NPs synthesized under various hydrothermal or solvothermal conditions.**

### 3.4 Supercritical $CO_2$ drying

The suspension of material is contained in a sealed semi-permeable pouch and placed in the high-pressure drying vessel (500 mL). The semi-permeable pouch allows the solvent and $CO_2$ to permeate its walls while retaining the material. The pore openings in the pouch material are small; the pouch contains particles larger than 0.3 microns. The $CO_2$ purge fluid dissolves the solvent from the suspension and leaves the drying vessel. The drying continued until the solvent is removed from the suspension. After drying, the environment present in the drying vessel is $scCO_2$ and the TiN nanorods with only trace amount of the initial solvent. The pressure reduction of the vessel at the end of drying is done in a manner so that $CO_2$ transitions from supercritical state to gas phase without going through the liquid phase, allowing particles to come to atmospheric conditions under zero surface tension thereby eliminating particle agglomeration.

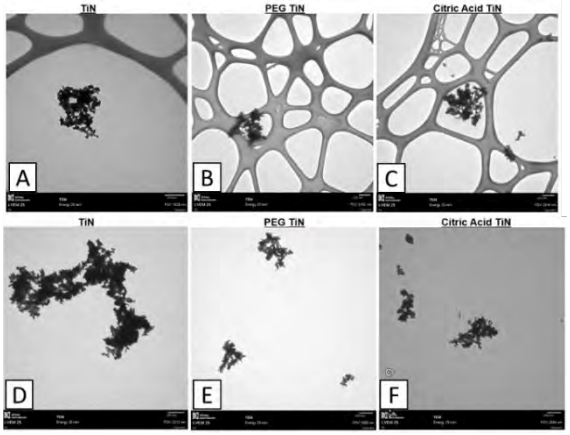


**Figure 6. Transmission electron microscopy imaging prior to $scCO_2$ drying of A) TiN, B) PEG TiN, C) Citric acid TiN compared to samples post $scCO_2$ drying of D) TiN, E) PEG TiN, F) Citric acid TiN.**

The solvent leaving the high-pressure vessel can be collected in the low-pressure glass collector downstream of the fine metering valve. The flow rate of the $CO_2$ is controlled so that the flow through the drying vessel is laminar with minimal by-pass flow. The solvent leaving the high pressure can be collected and weighed periodically. The drying is continued by purging with $CO_2$ until all the solvent has been removed. Upon removal of the dried product, some was set aside for characterization while the remainder was disseminated in the aerosol chamber for mass extinction coefficient analysis. Those results are annotated in the next section. The various TiN samples (TiN, PEG TiN, and citric acid TiN) were imaged using transmission electron microscopy prior to undergoing $scCO_2$ drying (Figure 6A–C) and immediately after (Figure 6D–F) for comparison. There is significant agglomeration of the rods, but what was more surprising was the presence of nanometer-size particles decorating the surface in all samples (Figure 6).

The assumption based on previous success with $scCO_2$ that after undergoing the drying process would result in a decrease of the capillary action holding the particles together. Therefore, the resulting product would be well dispersed rods. This however was not the case post $scCO_2$ drying. Not only is there significant nanometer particle decoration along the surface but there was no separation of the rods, as if they are fused together.

To better understand the crystalline structure and composition of the samples, X-ray diffraction was performed (Figure 7). While rods are present it was difficult to make a conclusion based on the number of particles decorating the surface and causing even more agglomeration, making it difficult to prove or refute the hypothesis that the additive of PEG or citric acid to the hydrothermal process would result in more OH groups present to facilitate rod growth.

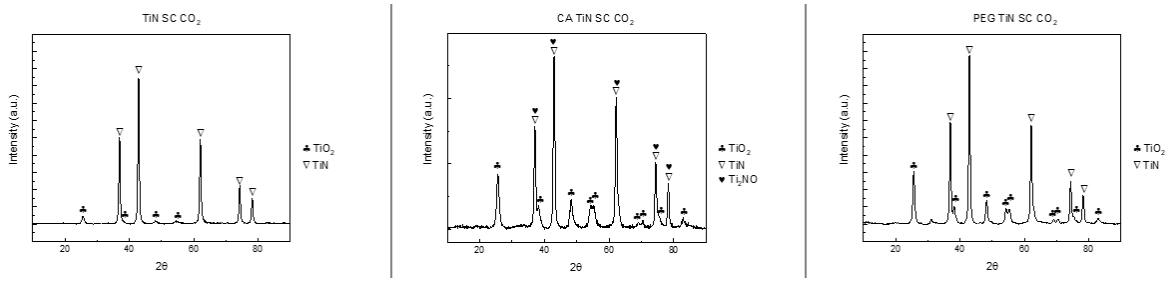


**Figure 7. X-ray diffraction patterns of supercritically dried TiN (left), citric acid TiN (center), and PEG TiN (right).**

Based on the diffraction patterns of TiN, PEG TiN, and citric acid TiN, it was determined that the introduction of additive promoted the formation of other species: specifically, titanium dioxide and titanium oxynitrides. The presence of more OH groups present in the hydrothermal synthesis resulted in more dominating species in the TiN sample. The results and conclusions drawn from of the transmission electron microscopy and X-ray diffraction analysis became more supported by the mass extinction coefficient measurement made in the aerosol chamber.

### 3.5 Mass extinction coefficient chamber measurements

The aerosol test chamber is a 6-meter by 7-meter, 190 cubic meter volume capable of spraying dried powders, liquids, and explosive/pyrotechnic dissemination. The samples that were supercritically dried in section 3.4 (TiN, PEG TiN, citric acid TiN) were disseminated into the aerosol test chamber for analysis of MEC. With the objective to attenuate bispectrally (visible thru far-IR) with a performance metric, MEC of $\geq 7 m^2/g$. Beer Lambert's Law states for a given material sample path length and concentration of the sample are directly proportional to the absorbance of the light. Yield is also denoted below as the amount of material that is aerosolized in the cloud (Figure 8).

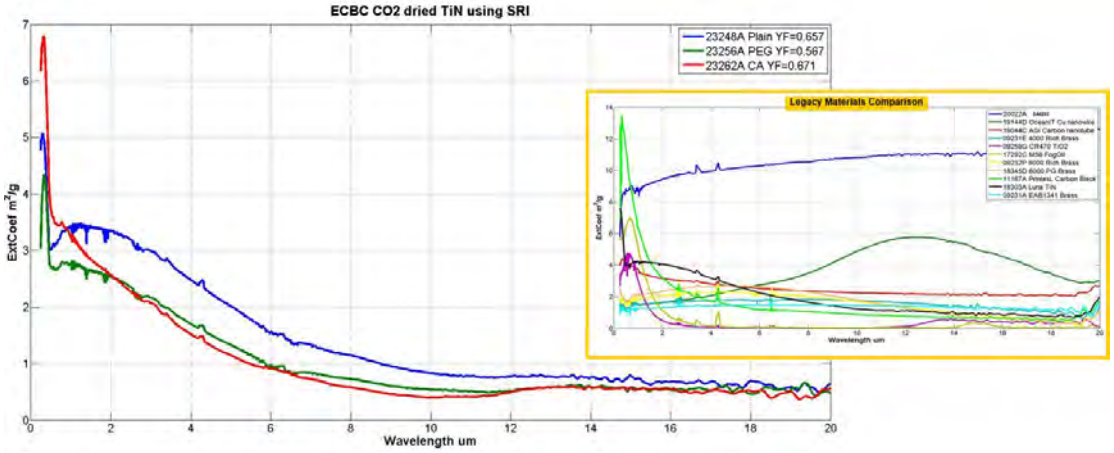


**Figure 8. Aerosolized mass extinction coefficients of TiN (blue), PEG TiN (green), and citric acid TiN (red). Inset (yellow) is comparison to legacy obscurant materials and their corresponding MEC measurements.**

The resulting MEC measurements were in opposition to what was initially hypothesized. Although the addition of the additive during synthesis improved the growth of nanorods in the visible spectrum, it impaired the overall performance in the IR region of the spectrum, aligning with what was seen in the transmission electron microscopy images. The decorated surface of the rod in spherical particles justifies the higher performance in the visible. Spherical particles are based off Mie theory and therefore, the smaller the particle the better visible attenuation.

When the supercritically dried TiN samples are compared to the legacy and other experimental materials (yellow inset in Figure 8) there is a distinct lack of performance. There are other better candidates including already field bispectral obscurant materials. Based on this result and conclusions there is a need for a major shift in program direction.

### 3.6 Oxynitride synthesis

Oxynitride synthesis began by investigating methods for hydrothermal synthesis of aluminum oxynitride, zirconium oxynitride, and gallium oxynitride (GaON) in the literature. Methods found generally included the synthesis of a metal oxide powder followed by a high-temperature nitridation to form the oxynitride.[10-13] First, the synthesis gallium oxynitride using a hydrothermal method combined with a low temperature anneal was performed.[14] This lower temperature method is preferable compared to the high temperature requirement of nitridation, which is less easily achievable in a tube furnace. It was anticipated that successful gallium oxynitride synthesis could also provide new opportunities to synthesize other oxynitrides using this lower temperature hydrothermal method. The synthetic method as reported in literature involves sonicating gallium metal with ethylene diamine to form a gallium ethylene diamine complex, which is then heated in a hydrothermal reactor followed by a thermal anneal to produce GaON.[14]

Following the literature methods, gallium metal was sonicated with ethylene diamine at 50 °C, which is above gallium metal's melting point. Initially, this method did not result in the black dispersion which was expected to indicate the formation of the gallium ethylene diamine complex so the temperature was increased to 70 °C. However, it was found that the bath sonicator was not able to maintain the temperature required. As an alternative, a ceramic dish was used

to heat a water bath to 70–75 °C and a probe sonicator was used to sonicate the gallium and ethylene diamine. Ultimately, a reaction was observed when the solution was manually agitated by shaking or stirring while using the water bath to maintain the high temperature. Figure 9A shows the heated sonication bath setup, and Figure 9B shows the solution turning from clear to darker grey after adding a stir bar to the solution.

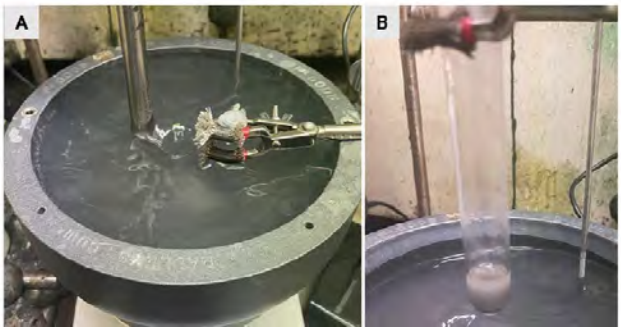


**Figure 9. (A) Sonication setup with a probe in a water bath. Ethylene diamine and gallium metal are sonicated in the glass vial until a black complex formed. (B) The complex went from clear to dark grey color after heating and stirring.**

After stirring and manual agitation, a color change occurred, and the solution was stirred for half an hour further. At this point, no silver gallium metal was observed within the dark grey dispersion, suggesting successful complexing. Water was added and was transferred to a hydrothermal reactor to heat at 200 °C for 24 hours. The material was then washed by centrifugation, oven dried, and then annealed for 5 hours at 500 °C. The dry powder from this experiment was characterized by measurements of absorbance, transmission, and average particle size to examine obscuration performance both before and after the final anneal. The UV-Vis MECs, FTIR transmittance, and DLS particle size measurements for the as-synthesized GaON material, as well as the same material after the 5-hour anneal (Figure 10).

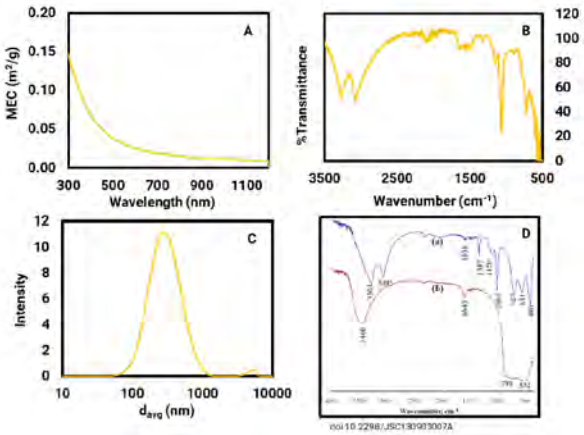


**Figure 10. (A) UV-Vis MECs, (B) FTIR transmittance, and (C) particle size distributions recorded for AlON attempted by a hydrothermally synthesis method. (D) Reference spectrum for AlOOH (blue) and aluminum oxide ($Al_2O_3$, red).[17]**

The difference between the pre- and post-annealed GaON material is minimal (Figure 11A, 11B). The most significant difference comes in the average particle sizes, where the material shows a slightly smaller average particle size, as well as a narrower distribution in sizes after annealing. It is important to note that the GaON samples did not disperse well in either water or isopropanol solution for characterization. It is likely that many particles settled out of solution before the data could be recorded. Therefore, the UV-Vis MECs and DLS results made in solution are likely not fully representative of the material. This also contributed to the low MECs overall noted for these materials, as the concentration of the actual solution at the time of data collection was much lower than the concentration used to make the MEC calculations. Similarly, these solution effects prevented the successful characterization of solution MCVs. For MECs and MCVs, more accurate measurements would have to be made in the aerosol phase to circumvent the solution dispersion effects. In these initial studies, the mass of material generated was not sufficient to conduct aerosol testing. However, this would be the recommendation for any potential future studies of this material.

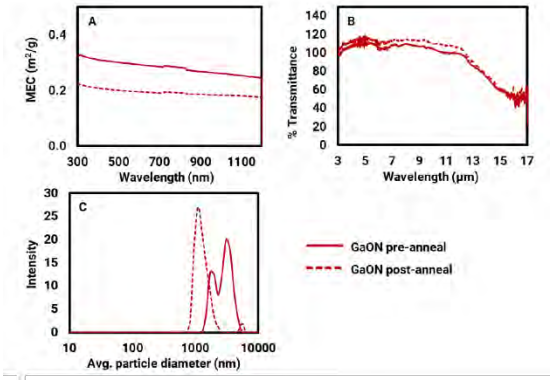


**Figure 11. (A) UV-Vis MECs, (B) FTIR transmittance, and (C) particle size distributions recorded for hydrothermally synthesized GaON both before and after annealing.**

Additional recommendations for further experimentation will be to determine the optimal combination of heat, sonication, and stirring to form the gallium ethylene diamine complex, as well as adjusting the temperature and time parameters of the hydrothermal reaction to potentially tune the particle size and morphology. Further experimentation was carried out to determine if this method could be used to synthesize aluminum oxynitride (AlON) at similarly low temperatures using the hydrothermal process. This would provide a significant advantage over the current literature methods which require much higher temperatures and nitrogen gas.[10,11,15,16]

Following the complexing of gallium with ethylene diamine, aluminum metal was added to ethylene diamine and stirred in a water bath at 75 °C. After two hours with no reaction, the sonication was added for a further two hours. No reaction occurred between the aluminum metal and ethylene diamine, suggesting that the low melting point of gallium contributed to the formation of the complex in the previous method. To remedy the solubility issue, aluminum chloride was chosen for further investigation due to its solubility in organic solvents. Aluminum chloride was stirred and sonicated with ethylene diamine at 75 °C, but no reaction occurred. Because aluminum chloride is soluble in ethanol, a solution of aluminum chloride in ethanol was stirred and then ethylene diamine was added. The resulting slurry was stirred for a further two hours before being transferred to the hydrothermal reactor and a small amount of water was added before being heated at 200 °C for 24 hours. The product was then washed via centrifugation in water and isopropanol then and oven dried. The dry powders from these experiments were characterized by measurements of absorbance, transmission, and average particle size to examine obscuration performance (Figure 11).

The synthesis to make AlON did not result in the desired FTIR spectrum. The spectrum in Figure 11B instead corresponds with boehmite aluminum oxide hydroxide (γ-AlOOH). Peaks at 3290 nm, 3070 nm, 1150 nm, 1070 nm, and 728 cm-1 are indicative of γ-AlOOH and are only slightly shifted from those seen in Figure 11D.[17] Since the pre-annealed powder was not AlON, the annealing process was not performed. Overall, this material showed similar solvent dispersion issues to the GaON, and the MEC for the γ-AlOOH was low with a wide size dispersion by DLS. Ultimately, this material is not recommended for obscuration applications, and more advanced characterization was not completed for these samples. However, γ-AlOOH can be used as a fire retardant, and in composite materials and ceramics.[18] Overall, the low temperature hydrothermal synthesis was not successful in creating AlON. Due to the inability to adapt the GaON synthesis to AlON, an adaptation to zirconium oxynitride was not performed. Future studies will explore alternative synthesis routes, likely requiring higher temperatures as illustrated in the literature.

## 4. CONCLUSIONS

Based on the results discussed above, there is a need for a major shift in program direction. In the case of including additives which containing higher amount of OH group to promote rod growth during the synthetic process resulted in no change in rod growth and a high concentrated decoration of the surface in spherical NPs. The $scCO_2$ drying process has been used on other high-performing obscurant candidates with great success (five-fold increase in performance), $scCO_2$ drying yielded no change in the imaging that would correlate with better dispersion or performance in all samples. When evaluating a potential candidate material, oxynitride synthesis was unsuccessful and the correct geometry could not be fabricated, and therefore it never made it to the scale up procedure and MEC testing. Moving forward, it is important to maintain focus on relevant Army missions and materials for obscuration.

Therefore, we will adjust according to meet those need while still focusing on completing the objective set forth in this program.

## REFERENCES


[1] Smith, J.D.; Woessner, Z.J.; Skrabalak, S.E. Branched Plasmonic Nanoparticles with High Symmetry. *J. Phys. Chem. C.* **2019**, *123* (30), pp 18113–18123.

[2] Willets, K.A.; Van Duyne, R.P. Localized Surface Plasmon Resonance Spectroscopy and Sensing. *Annu. Rev. Phys. Chem.* **2007**, *58*, pp 267–297.

[3] Guler, U.; Naik, G.V.; Boltasseva, A.; Shalaev, V.M.; Kildishev, A.V. Performance analysis of nitride alternative plasmonic materials for localized surface plasmon applications. *Appl. Phys. B.* **2012**, *107* (2), pp 285–291.

[4] Rasaki, S.A.; Zhang, B.; Anbalgam, K.; Thomas, T.; Yang, M. Synthesis and application of nano-structured metal nitrides and carbides: A review. *Prog. Solid State Chem.* **2018**, *50*, pp 1–15.

[5] Joshi, U.A.; Chung, S.H.; Lee, J.S. Low-temperature, solvent-free solid-state synthesis of single-crystalline titanium nitride nanorods with different aspect ratios. *J. Solid-State Chem.* **2005**, *178* (3), pp 755–760.

[6] Shin, H.; Kim, H.-i.; Chung, D.Y.; Yoo, J.M.; Weon, S.; Choi, W.; Sung, Y.-E. Scaffold-Like Titanium Nitride Nanotubes with a Highly Conductive Porous Architecture as a Nanoparticle Catalyst Support for Oxygen Reduction. *ACS Catal.* **2016**, *6* (6), pp 3914–3920.

[7] Hayashi, H.; Hakuta, Y. Hydrothermal Synthesis of Metal Oxide Nanoparticles in Supercritical Water. *Materials.* **2010**, *3 (7)*, pp 3794–3817.

[8] Kefalas, E.T.; Panagiotidis, P.; Raptopoulou, C.P.; Terzis, A.; Mavromoustakos, T.; Salifoglou, A. Mononuclear Titanium (IV)-Citrate Complexes from Aqueous Solutions: pH-Specific Synthesis and Structural and Spectroscopic Studies in Relevance to Aqueous Titanium(IV)-Citrate Speciation. *Inorg. Chem.* **2005**, *44* (8), pp 2596–2605.

[9] Qu, Q.; Geng, H.; Peng, R.; Cui, Q.; Gu, X.; Li, F.; Wang, M. Chemically Binding Carboxylic Acids onto $TiO_2$ Nanoparticles with Adjustable Coverage by Solvothermal Strategy. *Langmuir.* **2010**, *26* (12), pp 9539–9546.

[10] Naderi-beni, B.; Alizadeh, A. Preparation of Single Phase AlON Powders Aided by the Nitridation of Sol-Gel-Derived Nanoparticles. *Ceram. Int.* **2019**, *45* (6), pp 7537–7543.

[11] Su, M.; Zhou, Y.; Wang, K.; Yang, Z.; Cao, Y.; Hong, M. Highly Transparent AlON Sintered from Powder Synthesized by Direct Nitridation. *J. Eur. Ceram. Soc.* **2015**, *35* (4), pp 1173–1178.

[12] Zhao, S.; Song, J.; Xu, R.; Nie, L.; Ma, J.; Deng, C.; Cheng, X.; Zhao, X.; Hao, S.; Li, J. Fabrication of Zirconium Nitride Nanopowder with a High Specific Surface Area by Introducing Fructose as a Double-Function Additive. *Ceram. Int.* **2021**, *47* (16), pp 23267–23274.

[13] Zhao, S.; Ma, J.; Xu, R.; Lin, X.; Cheng, X.; Hao, S.; Zhao, X.; Deng, C.; Liu, B. Synthesis and Characterization of Zirconium Nitride Nanopowders by Internal Gelation and Carbothermic Nitridation. *Sci. Rep.* **2019**, *9* (1), p 19199.

[14] Oberländer, A.; Kinski, I.; Zhu, W.; Pezzotti, G.; Michaelis, A. Structure and Optical Properties of Cubic Gallium Oxynitride Synthesized by Solvothermal Route. *J. Solid State Chem.* **2013**, *200*, pp 221–226.

[15] Wang, S.; Qi, J.; Xie, X.; Wang, Y.; Huang, Z.; Feng, Z.; Qiao, H.; Wei, N.; Huang, W.; Lu, T. Transmittance Enhancement of AlON Transparent Ceramic by Aqueous Gel-Casting with Phosphoric Acid-Treated Powder. *J. Eur. Ceram. Soc.* **2016**, *36* (16), pp 4197–4203.

[16] Galakhov, A. B.; Zelenskii, V. A.; Vinogradov, L. V.; Antipov, V. I.; Alymov, M. I. Synthesis of Aluminum Oxynitride from Starter Organic Compounds. *Refract. Ind. Ceram.* **2012**, *53* (4), pp 269–271.

[17] Abdollahifar, M.; Zamani, R.; Beiygie, E.; Nekouei, H. Synthesis of Micro-Mesopores Flowerlike γ-Al2O3 Nano-Architectures. *J. Serb. Chem. Soc.* **2014**, *79* (8), pp 1007–1017.

[18] Dar, F.A.; Sofi, A.H.; Shah, M.A. Boehmite (AlOOH) Nanostrips and Their Growth Mechanism. *Int. Nano Lett.* **2015**, *5* (2), pp 67–70.

# Cryptographically protected bioproduction strains

David C. Garcia[a,b], Bryan Gerber[c], Casey B. Bernhards[a]*
[a]U.S. Army Combat Capabilities Development Command Chemical Biological Center, Research & Operations Directorate, 8198 Blackhawk Rd, Aberdeen Proving Ground, MD 21010
[b]National Research Council, 500 5th St NW, Washington, DC 20001
[c]California Institute of Technology, 1200 E California Blvd, Pasadena, CA 91125

## ABSTRACT

Protecting intellectual property relevant to national interests is an ongoing challenge requiring forethought and redundant levels of security. As biological production continues to expand in relevance to the development of mission critical accelerants, chemical precursors, and fuels, our ability to safeguard these systems from espionage and theft will need to expand in kind. Biological production inherently relies on microbial bioproduction strains that can be stolen and regrown with easily duplicated methodologies and expertise, such that introducing safeguards to prevent the acquisition and culturing of these strains will be essential to maintaining control over crucial intellectual property. To this end, we propose the development of bioproduction organisms with lock and key growth phenotypes that can only be activated using non-canonical (i.e., unnatural) amino acids and orthogonal tRNA synthetase/tRNA pairs, which serve as the keys and locks, respectively.

**Keywords:** biomanufacturing, bioproduction, biocontainment, genetic code expansion, noncanonical amino acids, directed evolution

## 1. INTRODUCTION

As the role of biological production strains continues to expand for domestic manufacturing, so too will their importance to supply chains crucial to national security needs. The ability to produce fuels, chemicals, and even building materials presents a novel opportunity to establish a biomanufacturing ecosystem with billions of dollars in economic impact.[1] However, while our ability to engineer new and bioproduction organisms has only continued to advance, our ability to protect those strains from espionage, misuse, and theft has severely lagged. This goal of this work is to begin addressing those challenges by taking advantage of the tools of synthetic biology to place barriers between strains of critical importance to the Department of Defense missions and those that would misuse them.

Recoded strains are organisms engineered to be completely missing one of the triplet DNA sequences, known as codons, which code for the 20 canonical amino acids found across life.[2] Strains with the TAG stop codon completely removed from the genome, for instance, have effectively been used for various applications including preventing viral infections, integrating non-canonical amino acids (ncAAs) into proteins, and creating effective auxotrophies in *Escherichia coli*.[3-5] Auxotrophies specifically occur when the deleted codon in a recoded genome is placed back into an essential gene along with a tRNA synthetase/tRNA pair that adds a ncAA at that codon's new position. However, an alternative strategy can be followed wherein stop codons are strategically added without recoding. While this may cause deleterious effects to cell growth, it substantially eases the burden of genetic engineering while allowing for the creation of the lock and key auxotrophy. In both cases, growth of the strain is prevented when the specific ncAAs are not provided exogenously, as the cell cannot make ncAAs. *Vibrio natriegens* (*V. nat*) is a promising bacterial strain to expand these efforts due to its prominence as the fastest replicating lab strain, its relevance for industrial applications, and our ability to engineer large sections of its genome simultaneously.[6,7] *V. nat* functions both as a potentially critical biological tool and as a fertile ground from which to characterize the physiology of an organism with important implications as a biosecurity platform.

In this study, the mechanisms for creating *V. nat* strains capable of being secured with auxotrophic growth will be explored to understand the biological principles of bioproduction chassis with security in mind. This work will use a *V. nat* strain as a base to produce and elucidate the phenotypes of subsequent mutants with ncAA auxotrophies (Figure 1). These mutated strains will then be used to explore methodologies to more easily produce tRNA synthetase/tRNA pairs for specific ncAAs that can be used as models for strains that can only be grown in the presence

of their respective ncAA.[8,9] Our aim is to demonstrate that we can understand how to engineer organisms relevant to bioproduction efforts with bespoke security measures for both benchtop and pilot scale bioproduction studies. We anticipate this work will be foundational in the field of biosecurity and advance both our understanding of the fundamental principles dictating cellular growth in *V. nat* as well as the mechanisms by which we can modify *V. nat* towards productive functions.

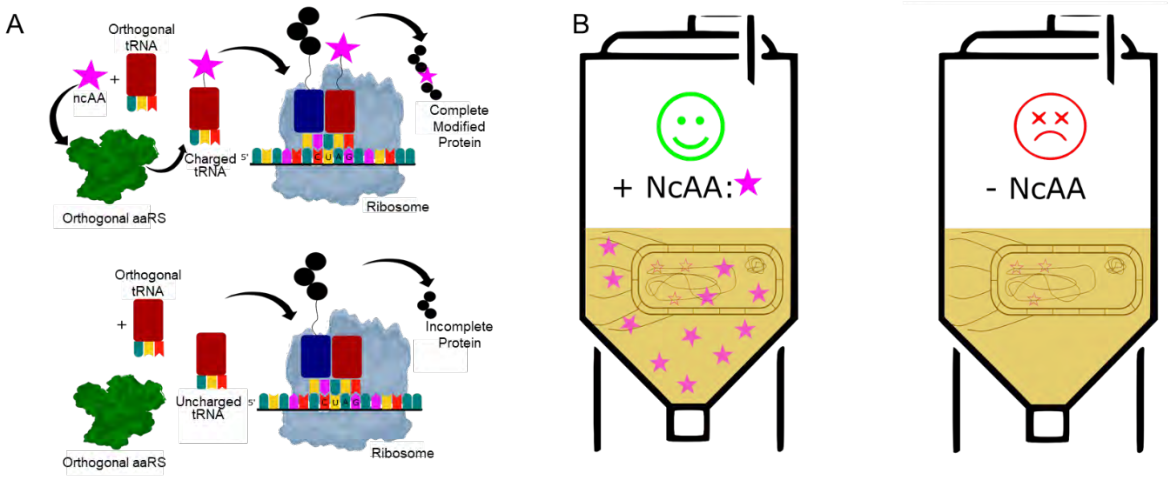


**Figure 1. Overview of proposed strategy for securing bioproduction strains. (A) NcAAs (pink stars) (keys), are charged using tRNA synthetase (aaRS)/tRNA pairs (locks) and used as protein building blocks when the codon added by the researcher is present. (B) In the absence of the ncAA, an auxotrophy prevents proper cell growth as the codon added into the genome cannot add an amino acid and complete the protein. Stolen strains would fail to grow in the absence of the proper key, their ncAA.**

## 2. METHODOLOGIES

### 2.1 Genome engineering

#### *2.1.1 Strain growth*

*V. nat* (ATCC 14048) was grown at 37 °C in Luria-Bertani (LB)v2 or LB3 media for liquid cultures and plates. LBv2 is LB-Miller medium supplemented with v2 salts (LB-Miller: 10 g/L tryptone, 5 g/L yeast extract, and 10 g/L NaCl; v2 salts: 204 mM NaCl, 4.2 mM KCl, and 23.14 mM $MgCl_2$). LB3 was made using LB-Miller supplemented with 2 % NaCl. Antibiotic stocks were used at the following final concentrations: carbenicillin: 25 µg/mL, kanamycin: 200 µg/mL, chloramphenicol: 2 µg/mL for plates and 4 µg/mL for liquid cultures. For long-term storage as glycerol stocks at -80 °C, cells were first washed in fresh LB before the addition of glycerol (~15–20 % w/v final).

#### *2.1.2 Assembly of NT-CRISPR plasmids and recombination selection*

Natural transformation (NT)-CRISPR is a genome engineering method combining natural transformation and CRISPR-Cas9 counterselection for direct mutations, deletions, or additions to the genome of *V. nat*.[10] *V. nat* can naturally incorporate extracellular DNA into its genome by homologous recombination, termed Multiplex Genome Editing by Natural Transformation (MuGENT).[7] The recombination process is facilitated by the transformation of transfer DNA (tDNA) into the cells via chemical signal. *V. nat* genomic DNA was used to PCR amplify tDNA with necessary TAG stop codons directly incorporated into the primers. Genomic DNA was isolated using the Wizard® Genomic DNA Purification Kit (Promega). Gibson assembly was used to anneal tDNA fragments containing TAG stop codons into a carrier plasmid, pST_140_LVL2 cam. *E. coli* cells were transformed with tDNA plasmids using a heat shock method, plated on LB agar medium containing chloramphenicol (25 µg/mL), and incubated at 37 °C overnight. PCR using the 5′ and 3′ ends of the left and right homology arms, respectively, was used to amplify the tDNA from the carrier plasmid. CRISPR--Cas9 expression was performed using guide RNAs (gRNAs) directly assembled into plasmid NT4_Addgene 179335 using Golden Gate assembly. CRISPR-Cas9 counterselection mediated MuGENT was performed as previously described.[10] Briefly, precultures of *V. nat* were grown overnight at

30 °C in LBv2 medium supplemented with 4 µg/mL chloramphenicol and 100 µM isopropyl-β-D-1-thiogalactopyranoside (IPTG) to induce production of Tfox. Natural transformation was started by adding 3.5 µL of the precultures (OD600 of ~9–11) to 350 µL Instant Ocean® Sea Salt with 100 µM IPTG. A total of 10 ng of tDNA with homologous flanking DNA was then added, briefly vortexed, and incubated statically at 30 °C for 5 h. CRISPR-Cas9 induction was started by addition of 1 mL of LBv2 medium containing 200 ng/mL anhydrotetracycline (ATc) to the MuGENT cultures. Following a 30 °C incubation for 1 h with shaking at 250 rpm, 100 µL of the cells were plated on LBv2 agar plates with 2 µg/mL chloramphenicol and 200 ng/mL Atc.

#### *2.1.3 Multiplex Automated Genome Engineering*

Multiplex Automated Genome Engineering (MAGE) was used to introduce TAG stop codons at sites located in essential genes related to growth and cell cycle control.[11] MAGE DNA oligos were designed to add a TAG at key amino acids. The ncAA was incorporated using an orthogonal, constitutively expressed tRNA and tRNA synthetase pair. Using the pORTMAGE-ec system (Addgene 138474), 12 cycles of MAGE were carried out on *E. coli* grown in 10 mM Nα-(tert-Butoxycarbonyl)-L-lysine (BOC-lysine) for the pilot experiment described in Section 3.2.1. The cells were transformed using 64 oligos targeting 35 proteins. The pORTMAGE-ec plasmid protocol used in this study followed previously outlined methods.[11] Briefly, cells were grown to an OD600 of 0.3–0.5, induced for recombination using 1 mM m-toluic acid, washed three times with water by centrifuging at 12,000 x g for 30 s, and electroporated with 200 µM final oligo mix in a volume of 100 µL. This process was repeated 12 times. The final culture was plated on agar plates with BOC-lysine, and single colonies were grown with and without BOC-lysine in LB medium at 37 °C to search for auxotrophs. Cells were designated as auxotrophs if they had a growth defect in the absence of BOC-lysine and recovered growth in its presence.

### 2.2 Computational methods

#### *2.2.1 Protein modeling*

Protein homology models were created using the Protein Homology/analogy Recognition Engine V 2.0 (Phyre2) by providing the target amino acid sequence from UniProt for *E. coli* for the protein of interest.[12] The Phyre Investigator was used to analyze model quality, mutation sites, and functional sites. The mutational sensitivity function was used to choose target amino acids with high mutation sensitivity to replace with ncAAs.

#### *2.2.2 Analysis of gene essentiality*

Gene essentiality data was analyzed from a pooled genome-wide CRISPR) interference (CRISPRi) screen as previously reported.[6] Putative essentiality to the cell's function was chosen based on an agreement for the gene being essential to function for both *V. nat* and *E. coli* (K-12). Gene essentiality data to cross reference for *E. coli* was acquired from a previous study using transposon analysis.[13]

## 3. RESULTS

### 3.1 Identification of proteins for ncAA incorporation

Initial efforts in understanding ideal points for incorporation of the ncAAs involved finding a method of choosing proteins where the incorporation of the ncAA would have a disruptive effect on cell survivability. To achieve this goal, we looked for data that would directly correlate abundance of a protein with essentiality of its presence for growth. Unfortunately, no proteomic data for *V. nat* could be found but a CRISPRi analysis that disrupted *V. nat* function by directly targeting all of the putative genes in *V. nat* was available (Table 1).[6] Though not a direct measure of protein abundance, the total transcripts per million (TPM) serves as a proxy for the abundance of a protein. This allowed for the protein abundances to be ranked and the gene essentiality compared to an *E. coli* transposon analysis.[6,13] Ideally, we would be able to pick a mixture of highly and lowly expressed proteins to select targets with two potential effects expected. The first being that disrupting proteins with high abundance would allow for readthrough effects of the TAG stop codon to not be disruptive to the auxotrophy, as many protein copies would be required for the growth phenotype to recover.[14] The second would be that picking a low abundance protein would allow for efficient incorporation of the ncAA by the ribosome to leave no copies of the protein to recover growth.

**Table 1. Representative data of CRISPRi analysis cross-referenced for specific proteins against essentiality in *E. coli*.**

| Protein encoding genes (PEG) | *V. nat* transcripts per million | Protein name | Essential in *E. coli* |
|---|---|---|---|
| FIG\|691.12.PEG.1662 | 20.28 | Lipoprotein releasing system ATP-binding protein LolD | TRUE |
| FIG\|691.12.PEG.1663 | 25.23 | Lipoprotein releasing system transmembrane protein LolC | TRUE |
| FIG\|691.12.PEG.419 | 27.07 | tRNA(Ile)-lysidine synthetase (EC 6.3.4.19) tilS | TRUE |
| FIG\|691.12.PEG.1661 | 27.74 | Lipoprotein releasing system transmembrane protein (LolE) | TRUE |
| FIG\|691.12.PEG.103 | 29.53 | FIG000906: Predicted Permease (LptG) | TRUE |
| FIG\|691.12.PEG.2100 | 30.11 | Proposed peptidoglycan lipid II flippase MurJ | TRUE |
| FIG\|691.12.PEG.1849 | 32.04 | DNA ligase (EC 6.5.1.2) (LigA) | TRUE |
| FIG\|691.12.PEG.1975 | 35.56 | Chaperone protein DnaJ | FALSE |
| FIG\|691.12.PEG.2415 | 13880.47 | LSU ribosomal protein L28p | TRUE |
| FIG\|691.12.PEG.2304 | 16546.93 | LSU ribosomal protein L36p | TRUE |
| FIG\|691.12.PEG.2320 | 17353.83 | LSU ribosomal protein L22p (L17e) | TRUE |
| FIG\|691.12.PEG.2326 | 26182.77 | SSU ribosomal protein S10p (S20e) (RpsJ) | TRUE |

## 3.2 Identification of protein sites for TAG modifications

### *3.2.1 Disruption of protein pool using MAGE for target selection*

Following the identification of proteins with disruptive effects based on essentiality, the focus was then to find ideal regions where disruptions could be made in the protein amino acid sequence to render the protein ineffective through the amino acid auxotrophy. From an initial screen of 35 different proteins using MAGE as the method of incorporating TAG stop codons, we found specific proteins that were more likely to both have the TAG stop codon and have a deleterious effect on growth as a result of the absence of the ncAA BOC-lysine. From a set of 17 isolates with a growth defect phenotype based on the absence of BOC-lysine, the presence of single-nucleotide polymorphisms (SNPs) was used as the determining factor for the presence of the TAG stop codon (Figure 2). From this data, we decided to select the targets *dnaT, dnaN, murJ, murE, ftsE,* and *mukF* for downstream analysis as TAG modifications to those genes were commonly found and would provide a variety of cellular mechanisms to disrupt with the auxotrophy.

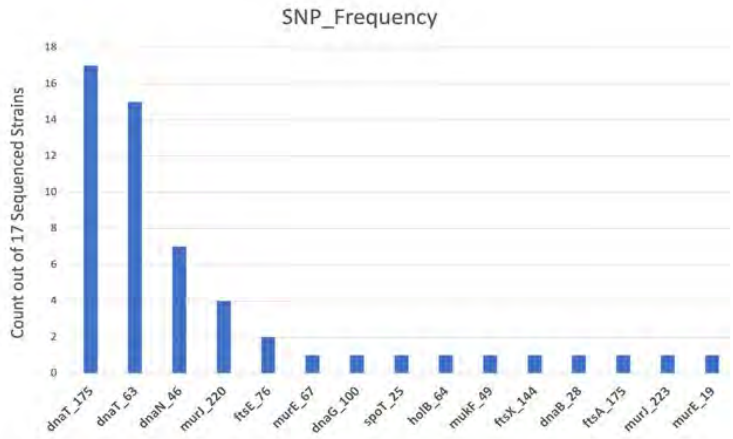


**Figure 2. Population of 17 strains found to produce growth defects when not grown on BOC-lysine. Bars indicate how often a particular SNP appeared in the 17 strains sequenced.**

### *3.2.2 Selection of disruptive positions in proteins*

Importantly, while it may seem that disrupting the protein at the start site would be the most effective method of creating the auxotrophic effect, the mutational analysis showed minor disruption from the amino acids may occur while being read by the ribosome. This would cause a protein with a missing amino acid to still potentially function, as a natural amount of readthrough still occurs because of the ribosome simply skipping the TAG stop codon and creating a protein with a missing, but non-disrupting, amino acid. However, if an amino acid important to structure or function were to be selected, then it is far more likely that any readthrough by the ribosome would impede the function of the protein and maintain the auxotrophic phenotype (Figure 3). Keeping this heuristic in mind, amino acid positions with high mutational sensitivity in the proteins were selected and MAGE oligos specific for disrupting those positions were created (Table 2).

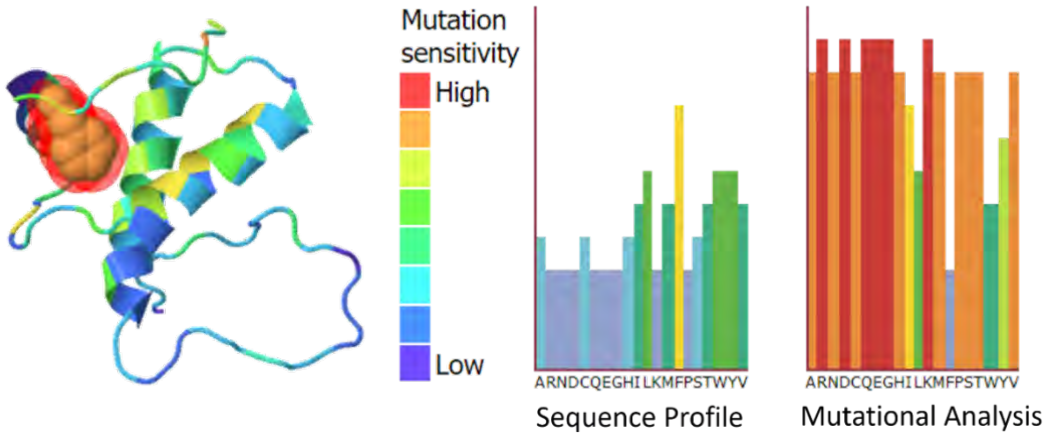


**Figure 3. Representative data from a mutational analysis of a protein, DnaT, targeted for protein disruption using a TAG stop codon. The protein structure for DnaT is represented as a ribbon model with the red highlighted balls indicating the amino acid phenylalanine at position 101 (Phe101). The sequence profile indicates residue preferences in the protein at Phe101. Similarly, the mutational analysis shows the likelihood that a replacement of Phe101 with particular amino acids will disrupt protein function, with red being a high likelihood and blue indicating wild-type function.**

The process of producing a list of relevant modifications to make in *E. coli* provides a proxy by which to test modifications that will ultimately be made in *V. nat*. This is necessary as NT-CRISPR does not lend itself well to multiplexed recombineering. This incentivizes the use of MAGE for selecting potential targets as it allows for a large number of regions to be tested without the need to remake and test NT-CRISPR gRNA and tDNA plasmids. Oligos to perform these disruptions were created and will be used to ultimately select the ideal auxotrophies for *V. nat* based on which are most often found in the sequencing data and provide the strictest lock and key (Table 2).

**Table 2. MAGE oligos designed to disrupt selected proteins at key amino acid positions with high mutational sensitivity. Each oligo is phosphorothioated (*) on the 5′ bases for increased inter-nucleotide resistance to nuclease degradation.[15]**

| Gene Name | Amino Acid Position | MAGE Oligo Sequence (5′ to 3′) |
|---|---|---|
| *dnaT* | Met91 | G*A*ACCGCAAGCCGCTCCCGTTGCTGTACCCATGGGGAAATTCGCCtagTATCCGGACT GGCAACCCGATGCCGATTTTATCCGCCTGGCG |
| *dnaT* | Phe101 | A*T*GGGGAAATTCGCCATGTATCCGGACTGGCAACCCGATGCCGATtagATCCGCCTGG CGGCGCTATGGGGCGTGGCGCTAAGAGAGCCG |
| *dnaN* | Leu273 | T*T*TTCGCTGACATAAAGACGTACGCCGCGGAATTTCTCGTTAGActaAATCGCCGCGC GAGCAAACGCCTGCTTGAGCAGATCGCAGCCA |
| *dnaN* | Leu263 | A*A*TTTCTCGTTAGAGAGAATCGCCGCGCGAGCAAACGCCTGCTTctaCAGATCGCAGC CAGCTTCCAGATGTTTGTCCGGGTTCTTCGGC |
| *murJ* | Phe157 | A*A*TCATGCTGATGTTAAGCAGTGTTGGAGCAAACGCCGGAATCGActAGCGGTTCCA CGTATTCAGAATCGCTCCCACCAGCGACGCCAG |
| *murJ* | Phe64 | A*C*TTGTTACGCCGTATCTTTGCCGAAGGGGCATTTTCCCAGGCAtagGTACCGATTCTG GCGGAATATAAAAGTAAGCAGGGTGAAGACG |
| *murE* | Arg193 | G*C*TTAAGTTGGTAAAGACCGACGCCGCAAATTTCAATGCCGCCACctaGTGCTGTACC AGCCCGTGGGAGGAAACTTCCATTGCGCAAAA |

| Gene Name | Amino Acid Position | MAGE Oligo Sequence (5′ to 3′) |
|---|---|---|
| *murE* | Thr143 | T*A*TTTTCTGTCGGGATCACTTTCCCCAGCAGGCCGTTACCAACGGTGCCCATTACCG CGCTGATTTCGCCAAGCAGTTGGCTCCACTGCG |
| *ftsE* | Pro164 | C*A*GACGTAAAATGCCTTCCGACAGCGCGTCGTCCAGGTTACCAGTctaTTCGTCCGCC AGCAGTACCGCGGGCTTGTTCACCACCGCGCG |
| *ftsE* | Leu18 | A*G*AAACGCCATCTCACCCGGCTGCATATGGAACGTAACGCCCTGCAGCGCCTGTCTC CCACCGAGATAAGCCTTGCTGACATGTTCAAAG |
| *mukF* | Leu193 | A*A*GCAACAATTCACAGCTGGAAATCGCCGCCCGCCAGTCTTTGTTctaCAACTGGGCG ATATCGTCCTTCACCTGCTGCTGCTGTTCGTC |
| *mukF* | Ile189 | C*A*GCTGGAAATCGCCGCCCGCCAGTCTTTGTTCAGCAACTGGGCctaATCGTCCTTCA CCTGCTGCTGCTGTTCGTCCATCAGACGTTGC |

### 3.3 Production of DNA for *V. nat* genome engineering

#### *3.3.1 Assembly of tDNA*

With much of the computational work performed, we attempted to make use of the NT-CRISPR system, first by attempting to delete the *dns* gene in *V. nat*. This gene encodes the Dns nuclease which reduces the integrity of plasmid DNA and increases the timeframe for subsequent transformation of DNA. We decided to produce a tDNA cassette to perform a clean deletion of the gene and subsequently induce Cas9 expression to select for cells with the disruption. Multiple disruption schemes were designed depending on whether the goal would be deleting a gene or adding a TAG stop codon (Figure 4, Top). Our first test using the clean deletion scheme showed that the plasmid could be successfully made and was PCR-verified by taking resultant colonies and checking for a plasmid with both the left and right 3,000 bp homology arms that would allow for the recombination event in *V. nat* (Figure 4, Bottom).

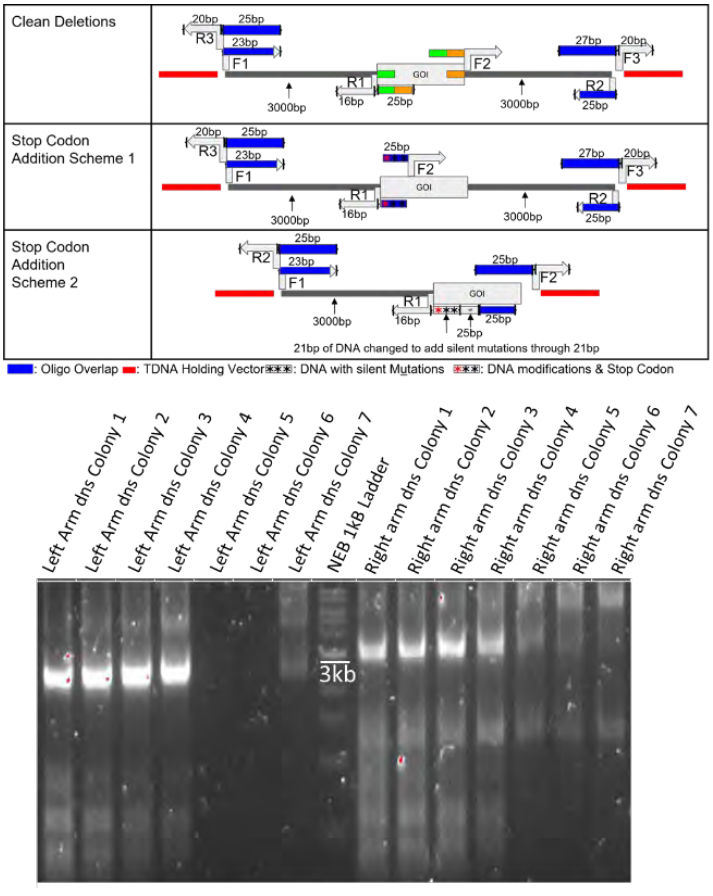


**Figure 4. Strategy to design and verify the production of tDNA plasmids. Top: Schemes designed for creating tDNAs for genetic modifications of the V. nat genome. F1–3, forward primers; R1–3, reverse primers; gene of interest (GOI). Bottom: PCR verification that both homology arms are in the tDNA plasmid being used for deletion of the *dns* gene.**

### *3.3.2 Assembly of gRNA plasmid for* dns *gene deletion*

As a selection mechanism, we also attempted to create a plasmid carrying a gRNA that would cleave the *dns* gene and allow for selection of cells with the desired deletion. To ensure that the plasmid was being made correctly, we sequenced the plasmid and found the gRNA to be in the correct orientation (Figure 5). Following induction of Cas9 with the *dns* gRNA, and transformation with the tDNA described above, we found no colonies survived following plating. This indicated that while our Cas9-mediated killing of the incorrect mutants was successful, we likely were not getting a recombination event.

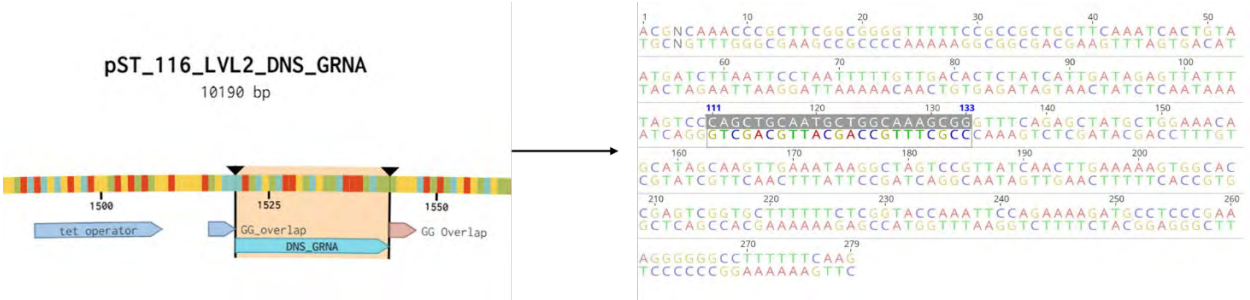


**Figure 5. Construction and verification strategy for gRNA plasmids. Left: Plasmid map of the expected plasmid following Golden Gate assembly of the plasmid backbone and gRNA. Right: Representative sequencing results from gRNA plasmids. Highlighted region indicates the presence of the gRNA in the plasmid at the desired position.**

## 4. CONCLUSIONS

This report describes the progress towards producing cryptographically protected strains through the introduction of ncAA auxotrophies in the bioproduction strain *Vibrio natriegens*. We identified key proteins for the potential disruption of growth functions that would illicit a strong auxotrophic effect. We further performed a modeling effort to find key amino acids within these proteins for strict auxotrophies. We also demonstrated our ability to produce the necessary genetic constructs to produce the auxotrophic strains. Together, these pieces will enable our ability to further test the genetic elements and ultimately produce and test cryptographic protection as a tool for securing biological productions strains relevant to national security and key supply chains.

## ACKNOWLEDGMENTS

We thank Dr. Tanya Tschirhart from the U.S. Naval Research Laboratory for providing strains and valuable technical discussions, and Charles Sanfiorenzo from the California Institute of Technology for providing expertise on bioinformatic methods. We also thank Dr. B Thuronyi from Williams College and Dr. Matthew Lux from the U.S. Army Combat Capabilities Development Command Chemical Biological Center for helpful discussions in support of this work. Funding was provided by the U.S. Army via the In-house Laboratory Independent Research Program (PE 0601101A Project 91A) at the Combat Capabilities Development Command Chemical Biological Center.

## REFERENCES

[1] Hodgson, A.; Maxon, M.E.; Alper, J. The U.S. Bioeconomy: Charting a Course for a Resilient and Competitive Future. *Industrial Biotechnology*. **2022**, *18* (3), pp 115–136.

[2] Lajoie, M.J.; Rovner, A.J.; Goodman, D.B.; Aerni, H.-R.; Haimovich, A.D.; Kuznetsov, G.; Mercer, J.A.; Wang, H.H.; Carr, P.A.; Mosberg, J.A.; Rohland, N.; Schultz, P.G.; Jacobson, J.M.; Rinehart, J.; Church, G.M.; Isaacs, F.J. Genomically Recoded Organisms Expand Biological Functions. *Science.* **2013**, *342* (6156), pp 357–360.

[3] Oza, J.P.; Aerni, H.R.; Pirman, N.L.; Barber, K.W.; ter Haar, C.M.; Rogulina, S.; Amrofell, M.B.; Isaacs, F.J.; Rinehart, J.; Jewett, M.C. Robust production of recombinant phosphoproteins using cell-free protein synthesis. *Nat. Commun*. **2015**, *6*, p 8168.

[4] Rovner, A.J.; Haimovich, A.D.; Katz, S.R.; Li, Z.; Grome, M.W.; Gassaway, B.M.; Amiram, M.; Patel, J.R.; Gallagher, R.R.; Rinehart, J.; Isaacs, F.J. Recoded organisms engineered to depend on synthetic amino acids. *Nature*. **2015**, *518* (7537), pp 89–93.
[5] Nyerges, A.; Vinke, S.; Flynn, R.; Owen, S.V.; Rand, E.A.; Budnik, B.; Keen, E.; Narasimhan, K.; Marchand, J.A.; Baas-Thomas, M.; Liu, M.; Chen, K.; Chiappino-Pepe, A.; Hu, F.; Baym, M.; Church, G.M. A swapped genetic code prevents viral infections and gene transfer. *Nature*. **2023**, *615* (7953), pp 720–727.
[6] Lee, H.H.; Ostrov, N.; Wong, B.G.; Gold, M.A.; Khalil, A.S.; Church, G.M. Functional genomics of the rapidly replicating bacterium *Vibrio natriegens* by CRISPRi. *Nat. Microbiol.* **2019**, *4* (7), pp 1105–1113.
[7] Dalia, T.N.; Hayes, C.A.; Stolyar, S.; Marx, C.J.; McKinlay, J.B.; Dalia, A.B. Multiplex Genome Editing by Natural Transformation (MuGENT) for Synthetic Biology in *Vibrio natriegens*. *ACS Synth. Biol*. **2017**, *6* (9), pp 1650–1655.
[8] Zhang, M.S.; Brunner, S.F.; Huguenin-Dezot, N.; Liang, A.D.; Schmied, W.H.; Rogerson, D.T.; Chin, J.W. Biosynthesis and genetic encoding of phosphothreonine through parallel selection and deep sequencing. *Nat. Methods.* **2017**, *14* (7), pp 729–736.
[9] Bryson, D.I.; Fan, C.; Guo, L.-T.; Miller, C.; Söll, D.; Liu, D.R. Continuous directed evolution of aminoacyl-tRNA synthetases. *Nat. Chem. Biol*. **2017**, *13* (12), pp 1253–1260.
[10] Stukenberg, D.; Hoff, J.; Faber, A.; Becker, A. NT-CRISPR, combining natural transformation and CRISPR-Cas9 counterselection for markerless and scarless genome editing in Vibrio natriegens. *Commun. Biol*. **2022**, *5* (1), p 265.
[11] Wannier, T.M.; Nyerges, A.; Kuchwara, H.M.; Czikkely, M.; Balogh, D.; Filsinger, G.T.; Borders, N.C.; Gregg, C.J.; Lajoie, M.J.; Rios, X.; Pál, C.; Church, G.M. Improved bacterial recombineering by parallelized protein discovery. *Proc. Natl. Acad. Sci. U.S.A.* **2020**, *117* (24), pp 13689–13698.
[12] Kelley, L.A.; Mezulis, S.; Yates, C.M.; Wass, M.N.; Sternberg, M.J.E. The Phyre2 web portal for protein modeling, prediction and analysis. *Nat. Protoc.* **2015**, *10* (6), pp 845–858.
[13] Goodall, E.C.A.; Robinson, A.; Johnston, I.G.; Jabbari, S.; Turner, K.A.; Cunningham, A.F.; Lund, P.A.; Cole, J.A.; Henderson, I.R. The essential genome of *Escherichia coli* K-12. *mBio.* **2018**, *9* (1).
[14] Dunn, J.G.; Foo, C.K.; Belletier, N.G.; Gavis, E.R.; Weissman, J.S. Ribosome profiling reveals pervasive and regulated stop codon readthrough in *Drosophila melanogaster*. *eLife.* **2013**, *2*, p e01179.
[15] Wang, H.H.; Isaacs, F.J.; Carr, P.A.; Sun, Z.Z.; Xu, G.; Forest, C.R.; Church, G.M. Programming cells by multiplex genome engineering and accelerated evolution. *Nature.* **2009**, *460* (7257), pp 894–898.

# Sporulated phage: towards the goal of "ready and waiting" phage decontamination

Courtney E. Love*, Anna M. Crumbley
U.S. Army, Combat Capabilities Development Command Chemical Biological Center, Research & Operations Directorate, 8198 Blackhawk Rd, Aberdeen Proving Ground, MD 21010

## ABSTRACT

Bacteriophage are viruses that infect and kill bacteria that have the capacity to serve as a non-corrosive decontamination or detection tool. Antibiotic resistance has opened the door for phage to be leveraged as a treatment for drug resistant bacterial infections or hospital infection mitigation of difficult to treat bacteria. Polyvalent phage, capable of targeting multiple bacterial strains, may have additional advantages for action against bacteria linked at the species, genus, or family level. Here, we seek to utilize computational and experimental techniques to identify phage that target multiple bacterial species and modify them for enhanced field applications including incorporating a colorimetric tag to improve visibility of a contaminated area. Additionally, we plan to enclose tagged bacteriophage inside natures armor: bacterial spores. Co-germinating bacteria and phage has been shown to protect the phage genomic material against common degradation risks such as heat, UV radiation, and pH fluctuations. Here, we report the groundwork development of computational and experimental methods that will inform phage-spore cocktail design for decontamination, as well as ways to utilize phage as a detection technique for alternate applications.

**Keywords:** *Bacillus anthracis*, bacteriophage, polyvalent, Basic Local Alignment Search Tool, surrogate, biosafety, biothreat

## 1. INTRODUCTION

Using phage as a decontamination tool could enable targeted biothreat elimination without materiel degradation. With the global rise of antibiotic resistance, bacteriophage are being increasingly explored as an alternative weapon in the antimicrobial arsenal, both for direct phage therapy and as targeted decontamination in hospitals.[1-3] One phage, Bacillus gamma (γ), is used by the Centers for Disease Control and Prevention as a confirmational diagnostic tool to distinguish between closely-related *Bacillus* species and pathogenic *B. anthracis*, although false positives have been reported.[4] Phage have also been developed at commercial scales and approved by the Food and Drug Administration as food safety control tools to address risks by *Listeria*, *Shigella*, and others in frozen foods.[5,6]

Classical experimental methods for phage isolation screening typically involve challenging solid and liquid environmental samples against laboratory strains in hope of a match.[7] Screening results are heavily influenced by the collection of available strains, the source of the environmental sample, collection-related events, and laboratory factors such as temperature, phage to bacteria inoculation ratios, and mutations to the laboratory strains over time. Finding phage active against biothreat strains adds a layer of complexity as high-risk strains are not available for screening in most laboratories. Thus, lower-risk surrogate strains are often utilized for phage isolation, e.g. *B. anthracis* str. Sterne as an alternative to *B. anthracis* str. Ames. This reduces risk, however, the differences between the strains may result in a phage active against a surrogate strain that does not interact with the biothreat strain.

Advances in DNA sequencing and computational biology methodologies speed up the search for phage.[7-9] Access to increasingly cost-effective sequencing technologies and advances in bioinformatics analysis tools and machine learning algorithms provide additional approaches for a phage investigator to use when investigating the potential to expect phage-microbe interactions, with multiple implementations accessible using command-line and web-based tools.[8] Alignment-based methods utilize shared virus-host sequences left by evolutionarily-distant previous phage infections as evidence of the potential for reinfection by similar phage, while alignment-free methods typically utilize codon-usage bias to identify phage with high likelihood of adapting to survival in a certain host microbes.[8] Machine learning methods use a variety of data inputs, often including both sequence alignment and codon bias data in their black-box approach.[7] Regardless of computational approach, experimental validation screens continue to remain the

field standard, with computational approaches requiring both initial experimental isolation and laboratory-based DNA sequencing.

Both experimental and computational screens can have bias during phage-host matching, often defining the strain used to isolate the phage as the "host," followed by testing the isolated phage against other strains.[8] Historically, phage were thought to only target one specific microbe, often at the species or strain level;[9] however, identification of polyvalent phage, defined as phage infecting multiple hosts at the genus level or higher, was reported as early as 1944.[10] Polyvalent phage are thought to target more broadly-available receptors on microbes, with a greater chance of experimental isolation and better likelihood of taking action against multiple microbes of interest – a powerful benefit when looking for biothreat targets using attenuated and surrogate microbes.

In addition to influence by laboratory and computational bias, phage stability during storage also plays a critical role in host screening and development of phage as a decontamination tool. Unstable phage are typically discarded and not subject to further study, even if their performance is otherwise promising.[11] As unprotected DNA particles, phage can be sensitive to UV light, temperature, and solution pH.[12] Regardless of storage method, phage viability and performance can vary over time.[13] Recent research also indicates that phage can be encapsulated for storage. Engineered encapsulation techniques, including the use of polymers, nanoparticles, liposomes, and calcium alginate have been reported to increase stability of phage.[11] Phage can also be encapsulated by sporulating microbes, where phage genomes are stored with the microbial genome during the spore formation process.[14] When a spore germinates, phage replicate, and, in the case of lysogenic phage, eventually break the host microbe's newly grown cell and are released into the environment. Spores represent a promising encapsulation method for phage stability as bacterial spores are stable against environmental extremes including pH, temperature, and UV radiation.[15]

## 2. MATERIALS AND METHODS

### 2.1 Computational methods

#### *2.1.1 Sequence access*

DNA sequences of microbial strains were obtained from the National Center for Biotechnology Information (NCBI) at the National Institute for Health on multiple dates.[18] DNA sequences of bacteriophage were obtained from the NCBI Virus database using the Virus and Host search functions to narrow the query and downloaded as either raw nucleotide FASTA or annotated GenBank files where available.[18]

#### *2.1.2 Pangenomic analysis (GView Server)*

In pangenomic analysis, query sequences are compared against a reference sequence. If a gene is not present in the reference sequence, it is added to the sum-total "pangenomic sequence." All sequences are compared to the "pangenomic sequence" and regions of similarity in more than one sequence are considered positive hits and recorded.

Pangenomic analysis conducted using the Pangenomic Analysis Type on GView Server as directed by the developer.[18] Basic Local Alignment Search Tool (BLAST) parameters included File Feature query set to [sequence], and the recommended other parameter settings: expected cutoff value of [1e-10], genetic code [Bacterial and Plant Plastid], alignment length cutoff removing matches shorter than [100] base pairs (bps), and a percent identity cutoff of [80%]. Filtering of low complexity sequences was turned [off]. Output graphics place the Seed Genome on the ring immediately outside of the compiled pangenomic sequence, with genomes in order of decreasing similarity.

#### *2.1.3 Alignment-based screening approach*

The NCBI BLAST was used to align bacteriophage sequences with bacterial DNA to investigate potential polyvalency.[19] Sequence accession numbers were identified from NCBI Virus Name search or from literature publications and used for DNA-to-DNA blast searches (blastn). Search Sets were used as recommended by the developer, specifically the [Standard Database (nr etc.)] with the [Nucleotide collection (nr/nt)]. Organisms were specified as noted in literature publications for method development or in Table 1. All other parameters under "Choose Search Set" were left as recommended by the developer. Program selection was set to [Highly similar sequences (megablast)] for initial searches. If no results were returned, the search parameter was broadened to [Somewhat similar

sequences (blastn)]. Under algorithm parameters, the max target sequences value was increased to [500] (from 100) to increase the likelihood of observing results outside of immediate strain and species hits.

BLAST results were filtered using the Filter Results – Organism with Exclude turned [ON] as necessary based on returned results. In some cases, multiple entries for closely related sub-strains and clinical isolates overwhelmed the target range, requiring intentional exclusion of known phage microbe host(s) from the search by repeating the search with Organisms: Exclude turned [ON]. E-value represents the number of alignment hits that would be expected to be present by chance.[20] E-values closer to [0.0] indicate a smaller chance of a random hit; suggesting a unique result.

Table 1 details the strains, phage, and their NCBI Accession numbers screened for this work.

**Table 1. Strains and phage evaluated computationally in this work.**

| **Bacteriophage** | | | | | |
|---|---|---|---|---|---|
| **Known host microbe** | **Screened phage** | **NCBI accession no.** | **Known host microbe** | **Screened phage** | **NCBI accession no.** |
| *Escherichia coli* | KFS-EC3 | MZ065353 | *Bacillus sp.* | Bacteriophage PT1028 | AY954948 |
| *Salmonella sp.* | Salmonella phage S144 | MT663719 | *Bacillus sp.* | Bacillus phage Sole | NC_074560 |
| *Shigella sp.* | Shigella phage 2019SD1 | NC_049820 | *Bacillus sp.* | Bacillus phage AP50 | NC_011523 |
| *Escherichia coli* | Escherichia phage LPEK22 | OK283619 | *Yersinia* | Yersinia phage PYps3T | NC_079177 |
| *Staphylococcus sp.* | Staphylococcus phage K | NC_005880 | *Bacillus sp.* | Bacillus phage 0105phi7-2 | NC_073091 |
| *Bacillus sp.* | Bcp1 | NC_024137 | *Bacillus sp.* | Bacillus phage vB_BsuS_PJN02 | NC_071050 |
| *Bacillus sp.* | SP01 | FJ230960.1 | *B. megaterium* | Bacillus phage vB_BmeM-Goe8 | NC_048797 |
| *Bacillus sp.* | B. subtilis F | - | *B. megaterium* | Bacillus phage vB_BmeM-Goe8 | MN043729 |
| *Bacillus sp.* | Bacillus SPP1 | NC_004166 | *Bacillus sp.* | *Bacillus* phage gamma (γ) | NC_007458 |
| *Bacillus sp.* | B. subtilis S-a | - | *Bacillus sp.* | B. pumilus PBP1 | - |
| *Bacillus sp.* | B. subtilis SP10 | - | *Bacillus sp.* | B. subtilis PMB12 | - |
| **Bacterial strains** | | | | | |
| **Species** | **Strain** | **NCBI Accession No.** | **Species** | **Strain** | **NCBI Accession No.** |
| *B. cereus* | 03BB102 | 572264 | *B. subtilis* | subsp. subtilis strain 168 | 224308 |
| *B. cereus* | D17 | 1454382 | *B. thuringiensis* | serovar Kurstaki (btk) | 714359 |
| *B. cereus* | 4342 | 1396 | *B. anthracis* | Sterne | 260799 |
| *B. cereus* | E33L (Zebra killer) | 288681 | *B. anthracis* | Δ Sterne | 1392 |
| *B.thuringiensis* | Al Hakam | 412694 | *B. anthracis* | Ames | 198094 |
| *B. pumilus* | - | 1408 | | | |

## 2.2 Bacterial strains and bacteriophages

Bacterial strains and bacteriophages were obtained from American Type Culture Collection (ATCC), Biodefense and Emerging Infections Research Resources Repository (BEI Resources), or from in-house strain collections. Strains, phage, and recommended media are detailed in Table 2. Incubation temperatures are 37 °C unless otherwise noted.

**Table 2. Strains and phage evaluated experimentally in this**

| **Bacterial** | | | | |
|---|---|---|---|---|
| **Species** | **Strain** | **Label** | **Source** | **Media** |
| *Bacillus cereus* | 03BB102 | BACI234 | In-house/UCC | TSA/TSB |
| *Bacillus cereus* | D17 | BACI262 | In-house/UCC | TSA/TSB |
| *Bacillus cereus* | 4342 | BACI263 | In-house/UCC | TSA/TSB |
| *Bacillus cereus* | E33L (Zebra killer) | BACI267 | In-house/UCC | TSA/TSB |
| *Bacillus thuringiensis* | Al Hakam | BACI229 | In-house/UCC | TSA/TSB |
| *Bacillus pumilus* | - | BEI NRS605 | BEI | TSA/TSB (30 °C) |
| *Bacillus subtilis* | subsp. Subtilis (Ehrenberg) | ATCC 27370 | ATCC | Enriched Nutrient Agar/Broth |
| *Bacillus anthracis* | Sterne | BACI012 | In-house/UCC | TSA/TSB |
| *Bacillus subtilis* | NRS 231 | BACI033 | In-house/UCC | TSA/TSB |
| *Bacillus anthracis* | Delta Sterne | BACI056 | In-house/UCC | TSA/TSB |
| *Bacillus thuringiensis* | Kurstaki | BACI204 | In-house/UCC | TSA/TSB |

| Bacteriophage | | | | |
|---|---|---|---|---|
| **Phage** | **Label** | **Known Host** | **Source** | **Media** |
| *B. subtilis* SP01 | Phage 27370-B1 | *B. subtilis* subsp. Subtilis (Ehrenberg) | ATCC | Enriched Nutrient Agar/Broth, Top agar 0.5% |
| *B. subtilis* F | Phage 27505-B1 | - | ATCC | Not indicated |
| *B. subtilis* S-a | Phage 15741-B1 | - | ATCC | Nutrient Agar/Broth, Top agar 0.5% |
| *B. subtilis* SP10 | Phage 23059-B1 | - | ATCC | Nutrient Agar/Broth, Top agar 0.5% |
| *B. pumilus* PBP1 | Phage HM615 | *B. pumilus* | BEI | LB Lennox+10mM $MgSO_4$ Agar/ Broth, Top agar 0.7% (30°C) . |
| *B. subtilis* PMB12 | Phage HM616 | *B subtilis* subsp. Subtilis (Ehrenberg) | BEI | LB Lennox+10mM $MgSO_4$ Agar/ Broth, Top agar 0.7% (30°C) |

## 2.3 Experimental screening

### *2.3.1 Agar-based*

Double agar overlays were performed as generally practiced: a thin agar plate of appropriate media (1.5 % agar w:v) was pre-warmed to the desired temperature. Molten soft agar (0.6 % agar w:v) was maintained at 53 °C until use. Log phase culture and phage solution were added to the molten soft agar, inverted once, poured over the plate, and swirled to cover the whole surface (100 µL culture, 100 µL phage solution, 4 mL soft agar). Once the top layer solidified, the plates were transferred to the incubator for the desired incubation time. Spot assays were performed as generally practiced: log phase culture was added to molten soft agar, inverted once, poured over the plate, and swirled to cover the whole surface (100 µL culture, 4 mL soft agar). Once the top layer solidified, 5–10 µL spots of phage solution was added to the plate and allowed to adsorb, then incubated once dry.

### *2.3.2 Liquid-based*

Phage expansions were performed in 50 mL conical tubes at 2–10mL volumes. An overnight culture of the host strain was diluted 1:4 in fresh media with an addition of 100 µL phage solution and incubated with shaking. After adequate growth time, solutions were centrifuged at 3000 x g, 4 °C, for 20 minutes, and the supernatant was filtered through a 0.2 µm Polyethersulfone filter and retained. Plate-reader assays were performed using a clear 96-well plate with a lid. Each well is filled with 100 µL sterile media or phage dilution. 2.5 or 5 % v:v culture is added to each desired well. The plate is incubated for ~24 hours in a BioTek Synergy H4 Hybrid Multiplate reader with the settings: Absorbance 600 nm, temperature 37 °C with continuous shaking, read every 10 minutes for 24 hours.

## 2.4 Spore formation

Following a published procedure,[21] *Bacillus subtilis* vegetative culture was pelleted and resuspended in sporulation media as described by Karava, et al. and incubated at 37 °C for 96 hours. The pellet was washed two times with sterile 1 X PBS and resuspended at a final volume of 50 mL. Heat shock test of spores was performed by heating aliquots of the spore resuspensions at 65 °C for 30 minutes.

## 2.5 Phage sequencing

DNA extractions of phage solutions were completed as previously described.[21] In short, phage solution was treated with DNase I and RNase A for 90 min at 37 °C without shaking; the enzymes were quenched using 0.5 M EDTA. Next, phage capsids were digested using Proteinase K incubated at 56 °C for 90 min. This solution proceeded through the Qiagen DNeasy blood and tissue kit protocol for animal blood or cells, starting at the step for adding AL buffer. DNA was double eluted at the last step. The bacteriophage library was prepared using Illumina's Nextera XT kit and the indexes were incorporated during 15 cycles of amplification. The quality of the library was determined by Qubit and Bioanalyzer analysis. The library was diluted to 13.3 pM and sequenced on a MiSeq using Illumina's MiSeq v2 Reagent Kit. The paired end run consisted of a total of 318 cycles. Illumina MiSeq reads were mapped to the reference genome (NC_011421.1) using Bowtie (v1.3.1). SAMtools (v1.15.1) was used to generate the consensus sequence and coverage statistics.

# 3. RESULTS AND DISCUSSION

## 3.1 Identification of polyvalent phage using computational analysis tools

### *3.1.1 Pangenomic analysis of relevant strains of interest*

Pangenomic comparison of *Bacillus* strains of relevance to this work was used to quantify and visualize the genetic variation between pathogenic biothreat, attenuated, and surrogate microbes. Using *B. anthracis* str. Ames as the reference strain, a pangenomic comparison of *Bacillus* strains of interest was conducted using GViewer.[18] Accompanying quantitative analysis indicated a maximum of 16.04 % sequence change between biothreat *B. anthracis* str. Ames and *B. subtilis* str. Subtilis (Ehrenberg). Relatively little differentiation is observed between genes in pathogenic *B. anthracis* str. Ames (inner, purple) and closely related attenuated and surrogate strains, except for *B. pumilus* (outer, orange) and *B. subtilis* str. Subtilis (Ehrenberg) (outer, red) (Figure 2A). Switching the seed strain to *B. subtilis* str. Subtilis (Ehrenberg) and repeating the analysis, the differences within the strain set can be seen more clearly, including the lack of several genes in *B. subtilis* (Ehrenberg) and *B. pumilus* native to *B. cereus* D17 and other more closely related microbes (Figure 2B). For the alignment-based screening theory, identification of phage active against *B. anthracis* str. Sterne, *B. anthracis* str. ΔSterne, or *B. cereus* D17 suggests high likelihood for activity against biothreat *B. anthracis.* Conversely, phage active against *B. subtilis* str. Subtilis (Ehrenberg) are less likely to be active against biothreat *B. anthracis.*

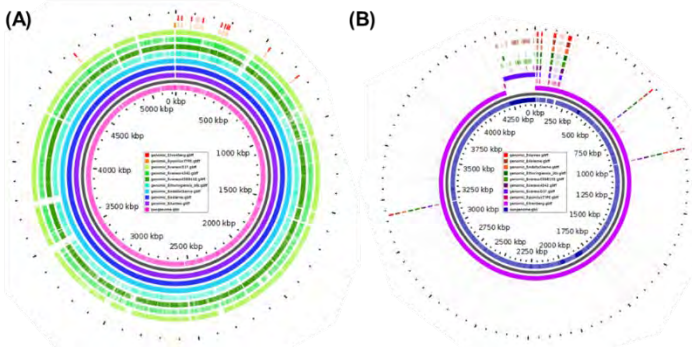


**Figure 2. Pangenomic comparison of *Bacillus* strains of interest (coding regions shown) using GViewer.[8] (A) If genes are present in one or more of the query strains, the CDS is colored. *B. anthracis* str. Ames is the seed genome for analysis. (B) *B. subtilis* str. Subtilis (Ehrenberg) is the seed genome for analysis.**

### *3.1.2 Alignment-based method development*

Because of the limited sequence information available for the few reports of experimentally observed *Bacillus* polyvalency in the published literature, the BLAST search method described in the Methods section was retroactively applied to reports of phage polyvalency in other hosts for development and refinement. Data published for phage KFS-EC3 (Accession No. MZ065353), experimentally investigated 57 strains spanning 12 genera, reporting polyvalency against 7 of the strains, including 4 *E. coli* O157:H7, 3 *Salmonella,* and 1 *Shigella* strain.[5]

In this work, the Basic Local Alignment Search Tool (BLAST) was used on KFS-EC3 against the subset of the experimentally tested microbes for which sequence information was available in the NCBI sequence database. This subset included *B. cereus* ATCC 14579 (taxid:226900), *E. coli* O157:H7 (taxid:83334), *S. dublin* (taxid:98360), *S. sonnei* (taxid:624), *S. aureus* subsp. aureus Rosenbach 1884 (taxid:46170), and *V. vulnificus* (taxid:672). The BLAST results identified 247 positive hits within NCBI records, all of which could be assigned to one of four genera. The most hits, ~150, were assigned to *E. coli* O157:H7 at a e-value of 1e-10, followed by 60 hits for *S. sonnei* with an e-value of 1e-19, then *S. enterica* subsp. enterica serovar Dublin at 20 hits of e-value 1e-8, and finally less than 10 hits for *V. vulnificus* at an e-value of 1e-7.

Comparison of the results of the computational predictions with the literature-reported experimental results suggested that a [1e-10] E-value threshold may be a good threshold for identifying polyvalent phage using BLAST confidence. At an E-value cutoff of [1e-10], 100 % of the phages were accurately predicted with no phage overpredicted, while at an E-value cutoff of [1e-08], 100 % of the phage were accurately predicted but 50 % were also overpredicted. Given the high workload associated with experimentally testing bacteriophage viability, the decision was made to retain the more conservative [1e-10] threshold. At a fundamental level, demonstrating alignment of the KFS-EC3 phage sequence with microbial sequences indicated BLASTing phage sequences could potentially result in alignment hits if

alignments exist, and that phage sequence alignment with microbes other than the "host" microbe used to isolate the phage could indicate the potential for polyvalency.

### *3.1.3 Alignment based method validation and refinement*

After setting the putative polyvalency BLAST cutoff criteria, the polyvalency detection method was evaluated by screening additional phage reported in the literature to be polyvalent. A total of six literature reports of experimentally validated polyvalent phage were identified, four of which contained host strain sequences available in the NCBI database.[24] Method validation BLAST searches were conducted using exact or type to challenge this method.

Computational prediction of alignment-based screening method with an E-value cutoff of [1e-10] correctly identified that the isolated phage would be polyvalent 71 % of the time, but overpredicted 14 % of the time. Broadening the E-value threshold to [1e-8] increased polyvalency prediction to 86 %, but also increased the rate of false positives to 29 %. Adding average percent sequence identity (% ID) cutoff of 80 % at the species level as a second predictive factor resulted in a 100 % prediction of phage polyvalency with 0 % overprediction.

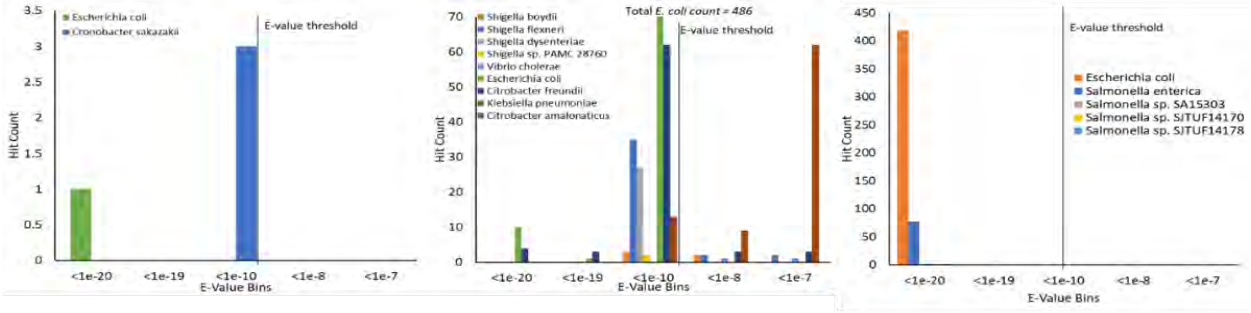


*Salmonella spp.* phage S144 *Shigella* phage *2019SD1* *Escherichia* phage LPEK22

**Figure 4. BLAST alignment hits for method validation study. E-value threshold noted at [1e-10]. Left, *Salmonella* ssp, phage S144; middle, *Shigella* phage 2019SD1; right *Escherichia* phage LPEK22.**

### *3.1.4 Method application for Bacillus phage polyvalency exploration*

The method described was applied to identify phage as being polyvalent for targeting multiple *Bacillus* species. E-value threshold and %ID values for a phage sample investigated for polyvalency are reported in Table 6. Phages were chosen for evaluation because they were reported in the literature as active against one or more *Bacillus* species or as polyvalent. Only one phage screened, Bacteriophage PT1028, returned a single BLAST hit with low likelihood of activity against *B. cereus*. All other phage returned at least two BLAST hits. If a hit was returned against a strain of interest, that result was highlighted. Otherwise, results were reported at the genus level.

**Table 3. Polyvalency screen results – *Bacillus.***

| Phage | Species | E value | Avg % Identity | Phage | Species | E value | Avg % Identity |
|---|---|---|---|---|---|---|---|
| *Bacillus* phage Bcp1 | *B. anthracis* Sterne | <1e-10 | 70 % | *Bacillus* phage gamma (γ) | *B. anthracis* | <1e-10 | 98 % |
| | *B. cereus* 03BB102 | <1e-10 | 70 % | | *B. cereus* | <1e-10 | 86 % |
| | *B. cereus* D17 | <1e-10 | 70 % | | *B. cereus* ATCC 4342 | <1e-10 | 90 % |
| | *B. cereus* E33L | <1e-10 | 47 % | | *B. cereus* D17 | <1e-10 | 95 % |
| | *B. pumilus* | <1e-10 | 70 % | *Bacillus* phage SP01 | *B. anthracis* Sterne | <1e-10 | 77 % |
| | *B. subtilis* subsp. *Subtilis* 168 | <1e-8 | 75 % | | *B. cereus* 03BB102 | <1e-10 | 76 % |
| | *B. thuringiensis* str. Al Hakam | <1e-10 | 70 % | | *B. cereus* D17 | <1e-10 | 77 % |
| *Bacillus* phage Wip1 | *B. mycoides* | <1e-10 | 88 % | | *B. pumilus* | <1e-10 | 75 % |
| | *B. thuringiensis* | <1e-10 | 80 % | | *B. subtilis subsp. Subtilis* 168 | <1e-7 | 78 % |
| | *B. thuringiensis* kurstaki | <1e-10 | 81 % | | *B. thuringiensis* Al Hakam | <1e-10 | 76 % |
| Bacterioph-age PT1028 | *B. cereus* | <1e-7 | 70 % | *Bacillus* phage SPP1 | *B. cereus* | <1e-8 <1e-10 | 68 % |
| *Escherichia* phage KFS-EC3 | *B. anthracis* | <1e-10 | 83 % | | *B. anthracis* | <1e-8 | 67 % |
| | *B. cereus* | <1e-7 | 81 % | | *B. pumilus* | <1e-10 | 69 % |
| | *B. pumilus* | <1e-8 | 82 % | | *B. cereus* D17 | <1e-8 | 66 % |
| | *B. subtilis subsp. Subtilis* 168 | <1e-7 | 82 % | | N/A | N/A | N/A |

Assessing the possibility of polyvalency among the phage surveyed, it was observed that few of the alignment percent identities were greater than 70 % average identity, even among strains reported to be susceptible to the phage. Conversely, in a few cases microbes known to be resistant to a particular phage were still identified. Literature reports for *Bacillus* phage, where available, suggest very few isolated phage are reactive against only one species, including the Centers for Disease Control and Prevention *B. anthracis* diagnostic phage gamma (γ), which was recently reported to also show activity against some *B. cereus* and *B. thuringiensis* strains after a five-day delay.[4] One of the six phage commercially available to Combat Capabilities Development Command Chemical Biological Center, *Bacillus* phage SP01, had a sequence available in NCBI and reported percent identities of ~75 %, indicating a relatively high likelihood of polyvalency.

## 3.2 Identification of polyvalent phage by laboratory experiments

### *3.2.1 Recovery of commercial phage samples*

Purchased bacteria were isolation streaked onto agar and a single colony was inoculated into liquid media as recommended on the product insert sheet. Purchased phage were thawed or resuspended as indicated on the product insert sheet and spotted onto the host strain. Phages 27370-B1 and HM615 revealed culture clearing in a spot assay using this method (Figure 5A). The remaining phage were expanded in their host bacteria for three hours, filtered, and spotted on bacteria. HM616 revealed plaques using this method (Figure 5B). These phages were stored using the glycerol stock method as described in Section 2.3.2.

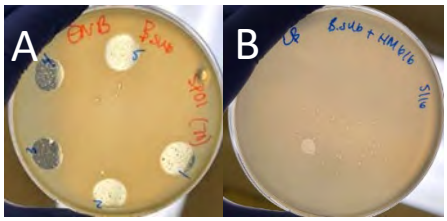


**Figure 5. Plate photos from commercially sourced phage recovery, from initial spot method (A) and after expansion in liquid culture (B). Hazy portions of the plate are the bacterial lawn; the clear circles are bacteria lysed by phage.**

### *3.2.2 Agar-based cross-screening*

Phage cross-reactivity was first probed using spot assays on six different *Bacillus* strains. Overnight cultures of the strains were added to a top agar overlay. Filtered phage solution (5 µL) was added to each plate so every phage was spotted onto every strain. These plates were incubated at either 37 °C or 30 °C overnight. Positive results as a table and photos are below in Table 4 and Figure 6. Negative results were observed using phages 27505-B1, 15741-B1, and 23059-B1; and strains BACI234, BACI263, BACI267, BACI229, BACI012, BACI056, and BACI204.

**Table 4. Results of agar-based cross-screening.**

| Label | Species | Strain | 27370-B1 *B. subtilis* SP01 | HM615 *B. pumilus* PBP1 | HM616 *B. subtilis* PMB12 |
|---|---|---|---|---|---|
| **BACI262** | *B. cereus* | D17 | **Pos.** | **Pos.** | **Pos.** |
| **BEI NRS605** | *B. pumilus* | N/A | Neg. | **Pos. (ctl)** | Neg. |
| **ATCC 27370** | *B. subtilis* | subsp. Subtilis Ehrenberg | **Pos. (ctl)** | Neg. | **Pos. (ctl)** |
| **BACI033** | *B. subtilis* | NRS 231 | **Pos.** | Neg. | **Pos.** |

**Figure 6. Selection of plate photos of cross-reactivity spot assays.**

### 3.2.3 *Liquid-culture cross-screening*

Additional cross-reactivity was explored using liquid cultures. Phage expansions were performed using the previously used method for four hours and filtered. Each phage in Table 2 was incubated in seven different strains and plated on both the original and incubated host. This variation allows the phage to infect the new host and expand over time, which may not occur on solid media. Table 5 summarizes the positive results from both cross-reactivity tests, highlighting the new interactions that were observed with the additional liquid incubation step. A selection of plates from this experiment set is shown in Figure 7. Negative results with phages 27505-B1, 15741-B1, and 23059-B1, and strains BACI012, BACI056, and BACI204 are not included in this table despite being tested experimentally.

**Table 5. Cross-screening results (Table 7) with additional data from liquid results (indicated by a * before the result).**

| Label | Species | Strain | 27370-B1 *B. subtilis* SP01 | HM615 *B. pumilus* PBP1 | HM616 *B. subtilis* PMB12 |
|---|---|---|---|---|---|
| **BACI234** | *B. cereus* | 03BB102 | ***POS.** | ***POS.** | ***POS.** |
| **BACI262** | *B. cereus* | D17 | **POS.** | **POS.** | **POS.** |
| **BACI263** | *B. cereus* | 4342 | ***POS.** | Neg. | Neg. |
| **BACI267** | *B. cereus* | E33L (Zebra killer) | ***POS.** | Neg. | Neg. |
| **BACI229** | *B. thuringiensis* | Al Hakam | ***POS.** | Neg. | Neg. |
| **BEI NRS605** | *B. pumilus* | N/A | ***POS.** | **POS. (ctl)** | ***POS.** |
| **ATCC 27370** | *B. subtilis* | subsp. subtilis (Ehrenberg) | **POS. (ctl)** | Neg. | **POS. (ctl)** |
| **BACI033** | *B. subtilis* | NRS 231 | **POS.** | Neg. | **POS.** |

**Figure 7. Spot assays from liquid culture cross screening. The center of the plate indicates the strain of bacteria on the plate (i.e., "sol: B. sub" is *B. subtilis*) and the numbers on the rim indicate the liquid culture the phage was incubated.**

### 3.2.4 *Growth curves*

To observe the earlier time points of these interactions and explore different multiplicities of infection for the phages and strains, a plate reader assay was performed with phages HM615, HM616, and 27370-B1, both neat and diluted 1:10, inoculated into *Bacillus* strains *B. subtilis*, *B. pumilus*, BACI234, BACI262, and BACI229, at 2.5 and 5 % v:v in the well. The concentration of plaque forming units (PFU/mL) was also evaluated on the inoculation day. An interaction was identified as a variation from the growth of the positive control well (bacteria + media at the correct % v:v, no phage). Phages 27370-B1 and HM616, both native to *B. subtilis*, showed interactions with two additional species of *Bacillus*: *pumilus* and *cereus*. HM615, native to *B. pumilus*, indicated an interaction with a *B. cereus* strain tested. Thus, both HM616 and 27370-B1 are expressing polyvalent behavior and are candidates to move forward in our development pipeline. Figure 8 reveals a curve where the max OD600 of biomass is reduced from the control; the strain BACI234 grows to OD600 ~0.8 and then decreases again, where phage overtook the growth of the bacteria and started killing off the culture. These cultures do "bounce back" later in the experiment but is noted for optimizing the time necessary for the highest phage concentration and the addition of phage into the spore germination cycle.

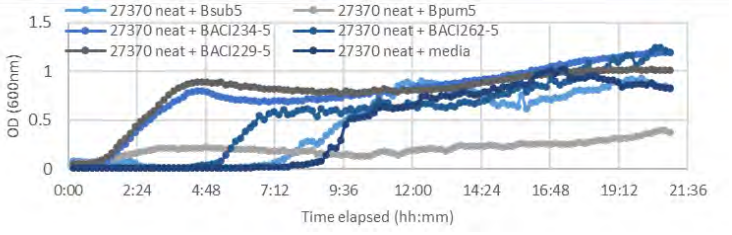


**Figure 8. Growth curve data of phage 27370-B1 undiluted interacting with all bacteria at 5 % v:v.**

### 3.3 DNA extraction and quality assessment for sequencing

Phage 27370-B1 was chosen to proceed through the pipeline because a reference strain is available for sequencing. The phage was expanded to a 100 mL volume, centrifuged, and the supernatant was filtered. This filtrate was then concentrated using a MilliporeSigma Amicon® Ultra-15 Centrifugal Filter Unit tube, increasing the concentration from 1.0E+10 PFU/mL to 3.0E+11 PFU/mL in the retentate volume. DNA was extracted from this retentate and resulted in 31.5 ng/µL of high-quality DNA, with one band present in each sample between 15000–48500 bp. Illumina sequencing and alignment to the reference genome, performed in the BioDefense Branch at DEVCOM CBC, revealed mapping of the sample to 99.96 % of the reference at a mean depth of 1840 x. The mismatched base pairs were in repetitive or homopolymer regions, which are not needed for DNA engineering.

### 3.4 Sporulation of *B. subtilis*

To ensure that phage 27370-B1 and the *B. subtilis* host was appropriate for the spore encapsulation of the phage, a preliminary sporulation study was completed. Both unheated and heated samples were titered to determine a difference in CFU/mL. Theoretically, the vegetative material would be inactivated by heat and spores would survive, observed by a decrease in CFU/mL. A sample of the titration plates for the final resuspension is shown in Figure 10, with a greater number of colonies present before heat treatment (NH) than after (65 °C). In all three suspensions, the colony count decreased after heat treatment: where 26 % of the 200 mL culture formed colonies following heat treatment, 36 % of the 100 mL resuspension, and finally 23 % of the final 50 mL resuspension. This preliminary study suggests that spores were present, increasing confidence that this strain is appropriate for use in Objective 3. Spores will be further characterized prior to phage encapsulation experiments.

**Figure 10. Dilution plates for titration of spore solutions both before (NH) and after (65 °C) heat treatment.**

## 4. CONCLUSIONS

Here we describe efforts to develop and challenge a computational method for predicting the infectivity of a bacteriophage. We have preliminarily defined BLAST screening parameters that validate experimental data produced and reported by other labs and reported in the literature and utilized this technique to select bacteriophage samples to purchase and experimentally screen in our labs. Three of the six bacteriophage samples purchased revealed polyvalent behavior through plate-based and liquid-based screening techniques, and one phage has been selected to proceed through the synthetic biology and sporulation objectives in this program. Additionally, we have developed a brief method for obtaining high-quality genomic DNA from bacteriophage samples for sequencing and engineering.

## ACKNOWLEDGMENTS

Funding was provided by the U.S. Army via the In-house Laboratory Independent Research Program (PE 0601101A Project 91A) at the Combat Capabilities Development Command Chemical Biological Center. Thank you to United States Military Academy West Point Department of Chemistry & Life Science leadership for project support and continued collaboration. Thank you to Kelley Betts for continual graphic and poster design and report editing.

## REFERENCES


[1] Crown, K. Bacteriophage Host-Range Expansion to Include Two Strains of Clostridium Sporogenes. Ph.D. Dissertation, University of New Mexico, Albuquerque, NM, **2014**. https://digitalrepository.unm.edu/biol_etds/20.

[2] Reuter, M.; Kruger, D.H. Approaches to optimize therapeutic bacteriophage and bacteriophage-derived products to combat bacterial infections. *Virus Genes*. **2020**, *56* (2), pp 136–149.

[3] Knoll, B.M.; Mylonakis, E. Antibacterial bioagents based on principles of bacteriophage biology: an overview. *Clin. Infect. Dis*. **2014**, *58* (4) pp 528–534.

[4] Kolton, C.B.; Podnecky, N.L.; Shadomy, S.V.; Gee, J.E.; Hoffmaster, A.R. Bacillus anthracis gamma phage lysis among soil bacteria: An update on test specificity. *BMC Res. Notes*. **2017**, *10* (1), pp 4–9.

[5] Kim, S.-H.; Adeyemi, D.E.; Park, M.-K. Characterization of a New and Efficient Polyvalent Phage Infecting *E. coli* O157:H7, *Salmonella* spp., and *Shigella sonnei*. *Microorganisms*. **2021**, *9* (10), p 2105.

[6] Kim, M.H.; Kragl, F.J.; Anderson, B.G. *The 1000 L Scale-up Production And Purification Of Bacteriophages Against Escherichia Coli O157: H7*; ECBC-TR-1441; U.S. Army Edgewood Chemical Biological Center: Aberdeen Proving Ground, MD, **2017**; UNCLASSIFIED Report.

[7] Versoza, C.J.; Pfeifer, S.P. Computational Prediction of Bacteriophage Host Ranges. *Microorganisms*. **2022**, *10* (1), p 149.

[8] 10 Andrade-Martínez, J.S.; Camelo Valera, L.C.; Chica Cárdenas, L.A.; Forero-Junco, L.; López-Leal, G.; Moreno-Gallego, J.L.; Rangel-Pineros, G.; Reyes, A. Computational Tools for the Analysis of Uncultivated Phage Genomes. *Microbiol. Mol. Biol. Rev*. **2022**, *86* (2).

[9] Boeckaerts, D.; Stock, M.; Criel, B.; Gerstmans, H.; De Baets, B.; Briers, Y. Predicting bacteriophage hosts based on sequences of annotated receptor-binding proteins. *Sci. Rep*. **2021**, *11*, pp 1–14.

[10] Fouts, D.E.; Rasko, D.A.; Cer, R.Z.; Jiang, L.; Fedorova, N.B.; Shvartsbeyn, A.; Vamathevan, J.J.; Tallon, L.; Althoff, R.; Arbogast, T.S.; Fadrosh, D.W.; Read, T.D.; Gill, S.R. Sequencing *Bacillus anthracis* Typing Phages Gamma and Cherry Reveals a Common Ancestry. *J. Bacteriol*. **2006**, *188* (9), pp 3402–3408.

[11] Yu, P. Polyvalent Bacteriophages: Isolation, Modification, and Applications in Environmental Systems. Ph. D. Dissertation, Rice University, Houston, TX, **2017**. https://scholarship.rice.edu/handle/1911/105568.

[12] Alonzo, L.F.; Jain, P.; Hinkley, T.; Clute-Reinig, N.; Garing, S.; Spencer, E.; Dinh, V.T.T.; Bell, D.; Nugen, S.; Nichols, K.P., Le Ny, A.-L.M. Rapid, sensitive, and low-cost detection of *Escherichia coli* bacteria in contaminated water samples using a phage-based assay. *Sci. Rep*. **2022**, *12*, pp 1–11.

[13] Schade, A.L.; Caroline, L. The Preparation Of A Polyvalent Dysentery Bacteriophage in a Dry and Stable Form. *J. Bacteriol*. **1944**, *46* (5) pp 243– 251.

[14] Gabiatti, N.; Yu, P.; Mathieu, J.; Lu, G.W.; Wang, X.; Zhang, H.; Soares, H.M.; Alvarez, P.J.J. Bacterial Endospores as Phage Genome Carriers and Protective Shells. *Appl. Environ. Microbiol*. **2018**, *84* (18), pp 1– 12.

[15] Riesenman, P.J.; Nicholson, W.L. Role of the Spore Coat Layers in *Bacillus subtilis* Spore Resistance to Hydrogen Peroxide, Artificial UV-C, UV-B, and Solar UV Radiation. *Appl. Environ. Microbiol*. **2000**, *66* (2), pp 620–626.

[16] *National Center for Biotechnology Information (NCBI)*. https://www.ncbi.nlm.nih.gov/ (accessed 22 November 2023).

[17] *NCBI Virus*. https://www.ncbi.nlm.nih.gov/labs/virus/vssi/#/ (accessed 23 September 2023)

[18] Stothard, P.; Grant, J.R.; Van Domselaar, G. Visualizing and comparing circular genomes using the CGView family of tools. *Briefings Bioinf*. **2019**, *20* (4), pp 1576–1582.

[19] Salmond, G.P.C.; Fineran, P.C. A century of the phage: Past, present and future. *Nat. Rev. Microbiol*. **2015**, *13* (12), pp 777–786.

[20] *E-value and Bit-score*. (www.metagenomics.wiki, https://www.metagenomics.wiki/tools/blast/evalue (accessed 23 September 2023)).

[21] Karava, M.; Bracharz, F.; Kabisch, J. Quantification and isolation of *Bacillus subtilis* spores using cell sorting and automated gating. *PLoS ONE*. **2019**, *14* (7), e0219892.

# Designing membrane-bound proteins as sensors for use in cell-free protein systems

Nathan D. McDonald[a], Ethan N. Walters[b], Frank J. Kragl III[a], Katherine A. Rhea[a]*
[a]U.S. Army Combat Capabilities Development Command Chemical Biological Center, Research & Operations Directorate, 8198 Blackhawk Rd, Aberdeen Proving Ground, MD 21010
[b]Oak Ridge Institute for Science and Education, 1299 Bethel Valley Rd, Oak Ridge, TN 37830

## ABSTRACT

Cell-free expression (CFE) systems are a standard mechanism for transcription and translation without whole cell manipulation. Tunable synthetic structures comprised of artificial membranes within a CFE system could improve control over biosensors. The initial approach for a membrane-based sensor in CFE may involve bacterial two-component system, signal transduction pathways that enable bacteria to sense and respond to stimuli. QseBC is a well-characterized, two component systems that is activated by the quorum sensing autoinducers epinephrine and norepinephrine that could be incorporated into a biosensor. Here, the QseBC biosensor was integrated into a CFE system by measuring fluorescent output in the presence of epinephrine using a plasmid encoding superfold green fluorescent protein controlled by the qseBC promoter. The functionality of the sensor using recombinant QseB and QseC in a CFE system supplemented with lipids and mechanical disruption was also evaluated. Epinephrine led to superfold green fluorescent production using both a sonicating water bath and an aggressively shaking plate reader but was increased with constant disruption. When evaluating the sensor using CFE plasmids that produce QseB and QseC, a similar signal was generated with spiked recombinant proteins. Overall, this work suggests CFE systems are a viable platform for membrane-based sensors, but further optimization is required to develop fieldable biosensors.

**Keywords:** Cell-free expression, bacterial two component system

## 1. INTRODUCTION

The advences and commercialization of cell-free expression (CFE) systems have enabled major advancements in the field of synthetic biology. Cell-free lysates are not a novel concept and have been widely used in basic research since the 1960's when translation machinery was first extracted from cells. Since then, lysates have been a standard mechanism for studying transcription and translation without the hindrance of whole organisms or membrane structures. Mass-produced and ready to use kits like myTXTL and PureXpress have provided high throughput and standardized mechanisms for research and assay development. *Escherichia coli* based CFE systems have been used in a variety of applications including prototyping, biosensors, viral synthesis, large scale bio manufacturing, production of synthetic substrates, and integration into the Design-Build-Test-Learn (DBTL) workflow. Despite the widespread use of these systems across a multitude of research applications, a major gap still exists in membrane-based biosensors. The CFE systems offer a unique platform to introduce complex, synthetically derived custom membranes comprised of targeted membrane sensor proteins that are traditionally difficult to study in whole-cell organisms.[1,2]

Thus far, CFE researchers have largely avoided the use of membranes within CFE reactions as one of the main purposes of using these systems is to remove the physical barriers that membranes create. Introducing phospholipids/membrane structures back into these systems may seem counterintuitive, however, controlled introduction of specific membranes and associated proteins in a "tunable" fashion in what has been deemed transcription/translation synthetic cells could improve the ability to study and control membrane-based sensor systems. The only published example of this work included the introduction of external lipids containing membrane channels to a cell-free synthesis reaction. The system included the necessary building blocks of transcription and translation produced externally and green fluorescent protein (GFP) that was produced internally. The experiment determined that membranes and membrane proteins can function in a typical cell-free reaction, and the artificial membranes or synthetic cells can be adjusted to contain varying amounts of membrane proteins that effect the internal production of

protein.[3] This system, although not as complex as a membrane-based sensor, appropriately lays the foundation for larger more elaborate membrane associations.

The initial approach for a membrane-based sensor should involve a well-characterized and thoroughly understood system. The bacterial two-component system (TCSs), a signal transduction pathway that enable a bacterium to sense and respond to stimuli both inside and outside of the cell, is a logical system to exploit for the creation of a membrane-based sensor. These TCSs are widely used in synthetic biology and have been engineered to induce an immune response, release drugs into a system, activate enzymes or the biological stress response, and trigger artificial biochemical pathways to improve genetically engineered systems. These pathways can be manipulated and modified into custom biosensors that can detect any manner of biological or chemical stimuli. These systems enable researchers to increase detection capabilities and generate a better understanding of complex biological systems.

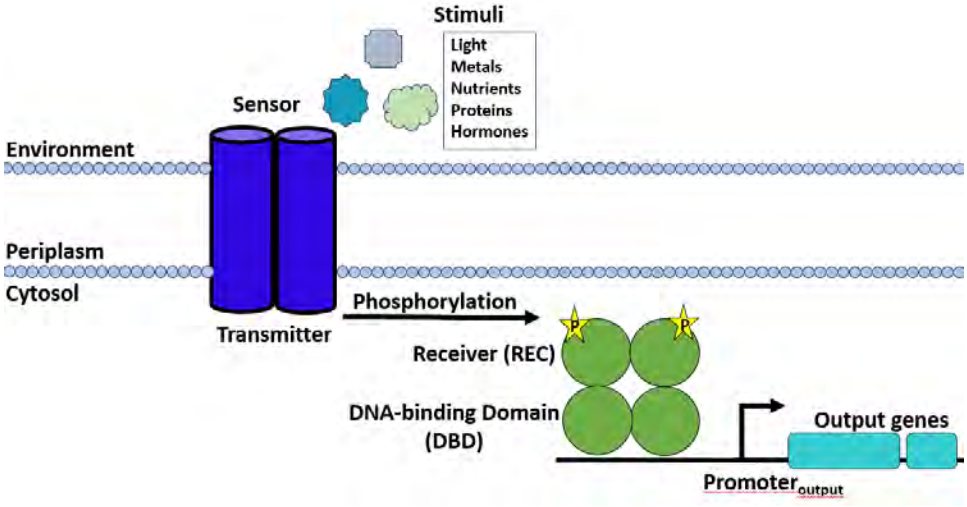


**Figure 1. Representative schematic of a bacterial TCS.**

The prototypical TCS consists of an RNA molecule or protein that binds to a ligand and responds to a stimuli by altering gene expression. Most TCS sensors consist of sensor histidine kinase (SHK), a response regulator (RR), and an output promotor (Figure 1). The SHK consists of a transmembrane portion with an N-terminal sensor domain and a C-terminal transmitter domain. A trigger ligand binds to the sensor domain, typically located outside of the cell, and initiates a conformational change within the SHK that relays to the transmitter domain that kinase activity needs to increase. The transmitter domain, now in the activated state, modifies the RR, via phosphorylation, at its N-terminal receiver (REC) domain. This initiates a conformation change within the RR that communicates to the C-terminal DNA binding-domain (DBD) that transcription should begin. When a triggering ligand is no longer present, the SHK transmitter domain will also dephosphorylate the RR, which effectively halts transcription and closes the response loop.[4]

A specific, well-characterized and relevant TCS that has the potential to make the transition into cell-free protein systems (CFPS) is QseBC, a quorum sensing and virulence regulator found in *Enterobacteria* and *Pasteurella.* QseC is the SHK located on the cytoplasmic membrane with the sensor domain located within the periplasmic space and the transmitter domain resting inside of the cytoplasm. QseB is the RR that is modified by the QseC, it consists of a REC domain and a helix-turn-helix (HTH) DBD. In *Escherichia coli*, the model system of choice, the QseC responds to autoinducer-3 and epinephrine/norepinephrine (Figure 2) QseC functions as an adrenergic receptor and binding of epinephrine/norepinephrine can be inhibited by adrenergic antagonists, which offers another built in mechanism of control within the system. The QseBC TCS activates transcription of the qseBC promotor as well as the flhDC promotor of the flagella regulon. The qseBC promotor controls the expression of ygiW, a protein which enables increased resistance to stressors through modification of the lipopolysaccharides (LPS) while the *flhDC* promotor controls the expression of proteins that increase motility thus enhancing virulence and survival capabilities.[5-8]

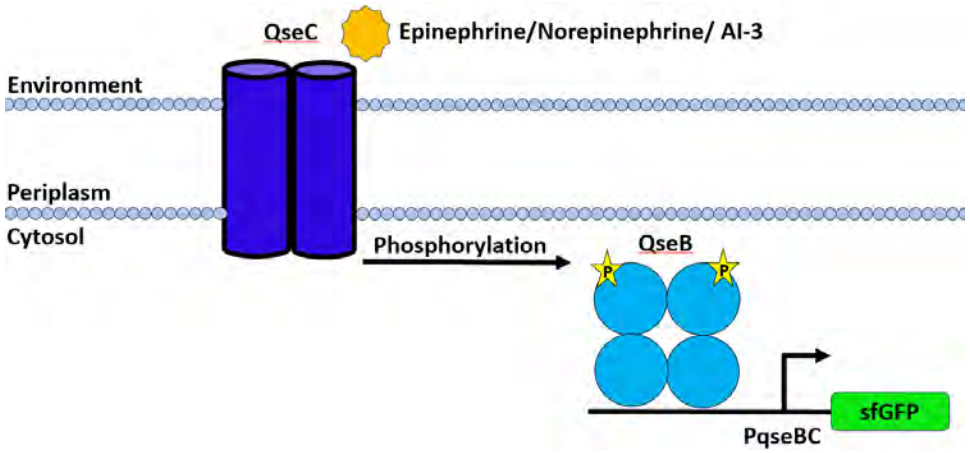


**Figure 2. The QseBC TCS is activated by the epinephrine/norepinephrine/AI-3 and turns on flhDC and qseBC promotors.**

Together, the CFE systems and bacterial TCS have the potential to make a novel sensing mechanism. The further development and exploration of membrane-based systems within a CFPS has the potential to enhance our understanding of CFE and TCSs as well as push the boundaries within the field of synthetic biology. *E. coli* proves to be the best model to use for both CFE and TCSs as it is the most well characterized and historically the most productive and functional of the published CFE systems. This should translate to the highest probability of success when attempting to implement an *E. coli* based TCS into an *E. coli* based CFE. Here, a bacterial TCS (QseBC) can be incorporated into artificial membranes and can be used as a membrane-based sensor in an *E. coli* CFE to sense epinephrine. This work highlights the ability of CFE systems to produce membrane-based biosensors entirely within the CFE system and suggests that future work using alternative TCS based biosensors of relevance could serve as alternative approaches to enhance detection and potential medical countermeasures in a safe and efficient manner.

## 2. MATERIALS AND METHODS

### 2.1 Extract preparation

In general, cell free lysates were produced following the work previously described.[9] When necessary, the protocol was modified to accommodate the scale of the preparation: Note: Day 1–3 must be performed in sequential order, but Day 4 may begin up to two weeks after Day 3 ends.

Day 1: Four fresh 2XYTP agar plates were inoculated from a glycerol stock of DeltaLacZ KO *E. coli* and incubated at 37 °C for 16–18 hours.

Day 2: Using a sterile large loop, material from two starter plates was scraped and transferred into 750 mL of 2XYTP broth in a 2.8 L Erlenmeyer flask. This was repeated for the additional two starter plates, for a total of 1.5 L of inoculated media. The cultures were inoculated 16 hours before the start of the final culture and incubated at 37 °C with a shaking speed of 200 rotations per minute (rpm). For 100 L fermentation, the media was prepared in the Industrial Fermentation (IF) 150L (New Brunswick Scientific) fermenter by adding 3.1 kg of 2XYT media powder, 700 g of potassium phosphate dibasic (Sigma Cat, P3786), 300 g of potassium phosphate monobasic (Sigma, P5655) and 5 mL of antifoam 204 (Sigma, A8311) to 100 L of deionized (DI) water. The media was aerated overnight with a rotor speed of 100 rpm, airflow of 20 standard liters per minute (slpm) and set to 37 °C.

Day 3: The overnight cultures were combined and OD600 measured using a spectrophotometer (Genesys 20, Fisher Scientific) and the inoculation amount calculated. The 100 L culture is seeded at a starting density of approximately 0.05 optical density 600 nm using a 2 L pre-sterilized transfer bottle to inject the media with the appropriate amount of overnight culture based on starting optical density. The fermenter settings were adjusted to 300 rpm, 50 standard liter per minute air flow and the dissolved oxygen (DO) meter was calibrated to 100 %. The OD600 was measured every hour until 0.6–1.0 at which point the culture was induced with 100 mL of 1M isopropyl B-D-1-thiogalatopyranoside (IPTG) (GoldBio, I2481C) for a final concentration of 1 mM. The fermentation continued and when DO levels fell below 50 % the rotation speed was increased to 500 rpm (usually occured around OD600 2–2.5).

Upon reaching OD600 3.5, the culture was cooled to 4 °C, and the centrifugation process initiated. The material was centrifuged using a pre-chilled (4 °C) powerfuge pilot, 1.1 L bowl, system (CARR Biosystems) in ~8 hours. When the entire 100 L culture was processed the centrifuge is deconstructed and the bowl scraped of all pelleted bacteria. The pellet was flattened into Ziploc™ bags, ~300 g per bag, and placed at -80 °C.

Day 4: Pellet material was removed from the freezer and thawed on ice. The material was resuspended using 1 mL of S30B buffer per gram of cell mass. The material was passed through a microfluidizer at 15,000 psi, and the lysate was collected in its entirety. The resulting lysate material was clarified by centrifugation at 12,000 x g for 10 minutes. Runoff reactions were performed on the clarified lysate material by heating to 37 °C, with shaking at 200 rpm in a standard shaking incubator (New Brunswick). After heating, the material was clarified further by centrifugation at 12,000 x g for 10 minutes and the resultant supernatant was placed in 250 mL dialysis flasks (Fisher, 87762) inside of 5-gallon buckets (Home Depot) filled with S30B buffer, two flasks per bucket, and allowed to dialyze overnight (~24 hours).

Day 5: After the material has sufficiently dialyzed it is further clarified by centrifugation at 12,000 x g for 10 minutes and the resulting supernatant is aliquoted and flash frozen using liquid nitrogen.

### 2.2 Cell-free reactions

All regents were prepared as previously described[10] and combined into a single Energy Buffer mix, aliquoted, and flash frozen for use. Cell free reactions were made with 100 µL 1-palmitoyl-2-oleoyl-sn-glycero-3-phosphocholine (POPC) (1 mg total) lipids dissolved in chloroform were placed in a 5 mL glass test tube and nitrogen gas was used to evaporate excess chloroform. The lipids were kept on an ice rack until mixed with the cell free extract and energy buffer. Each reaction consisted of 55 µL of extract, 54 µL of energy buffer, 1 µL of 10 mg/mL epinephrine (Sigma, E4375) in water and various amounts of DNA and recombinant protein as noted for each experiment. All volumes were normalized, and water was used to compensate in the negative controls. Each reaction was sonicated in a water bath (Cole Parmer, Unit #) at 37 °C for 30 minutes–24 hours. After sonication, reactions were pipetted into a 96 well U bottom plate for reading on a Biotek H1 plate reader at F:488, 525 nm from the bottom.

### 2.3 Strains and plasmids

*E. coli* strain Gold Bl21 DE3 (Agilent, 200131) was used for all recombinant protein expression and NEB® 10-beta *E. coli* (New England Biolabs, C3019) was used for all DNA expression of cell-free plasmids. Recombinant proteins QseC and QseB were cloned into the pCold1 vector (Takara, 3361). All cell-free constructs were cloned in the pJL1 vector that was cut from pJL1-sfGFP (Addgene, 102634) or pY71 vector cut from pY71-LacZ.

### 2.4 Protein incorporation into vesicles

After the proteins were cleaved, two different approaches were used to incorporate the membrane protein QseC into the POPC vesicles: a lipid extruder (Avanti Polar Lipids, 610000) or a sonicating water bath (Cole-Parmer, UX-08895-59). The lipid and QseC protein solution containing 1 mg/mL of protein and 1 mg of POPC lipids in phosphate-buffered saline was passed through the extruder 11 times and an identical protein solution was heated in a 37 °C sonicating water bath for 30 minutes with constant sonication.

### 2.5 Recombinant protein production and purification

For production of QseC and QseB, the glycerol stocks containing the constructs were streaked out on 2XYT agar containing ampicillin and allowed to incubate overnight at 37 °C. The next day a single colony was selected and added to 5 mLs of 2XYT broth with ampicillin and incubated overnight at 37 °C with shaking at 200 rpm. The following morning, 16–18 hours post inoculation, the culture was scaled by adding the 5 mL culture to 60 mL of 2XYT containing ampicillin at 100 µg/mL. This midi scale was allowed to incubate at 37 °C with shaking for 8 hours. Following the incubation, the 60 mL culture was used to seed the final maxi culture by adding 15 mLs of midi culture to four 2.8 L Erlenmeyer flasks with 750 mL of overnight express instant terrific broth media (Sigma, 71491) for a total of 3 L of maxi culture. These cultures were incubated at 37 °C for 24 hours with shaking. The cultures were then spun at 5000 x g for 10 minutes, the supernatant was removed, and pellets were weighed and frozen as previously described.

For purification of QseC and QseB, pellets were removed from the freezer and allowed to thaw on ice for several hours. His-tag wash buffer (25 mM sodium phosphate, 150 mM NaCl, and 20 mM Imidazole) was used to resuspend the pellet at a ratio of 5 mL for every 1 gram of material. The suspension was processed through a microfluidizer at 15,000 psi and then clarified for 3 hours at 40,000 x g. The supernatant was removed and passed through a 0.22-micron filter in preparation for the AKTAxpress. The sample was run over a 1 mL HisTrap FF crude histidine-tagged protein purification column (Cytiva, 11000458), washed with 10 column volumes, and eluted using fixed volume gradient elution settings into His-tag elution buffer (25 mM sodium phosphate, 150 mM NaCl, and 500 mM imidazole). The eluted protein fractions were quantified using the Agilent 2100 Bioanlazyer and the Nanodrop One and imaged on an SDS-PAGE protein gel. Similar fractions were combined, and the vector was cleaved using purified thrombin at a concentration of 1 mg/mL. The tag was removed by incubation with nickel affinity resin and the eluant was collected and further characterized as previously noted.

## 3. RESULTS

### 3.1 Recombinant QseBC within a CFE system

To successfully build a CFE circuit capable of detecting external stimuli via a membrane bound receptor, we first demonstrated that the proteins can be expressed, and that the membrane protein will incorporate into the synthetic membrane vesicles. The membrane protein QseC and REC protein QseB were purified recombinantly (Figure 3) and analyzed on the Agilent 2100 Bioanalyzer to assess protein purity and concentration.

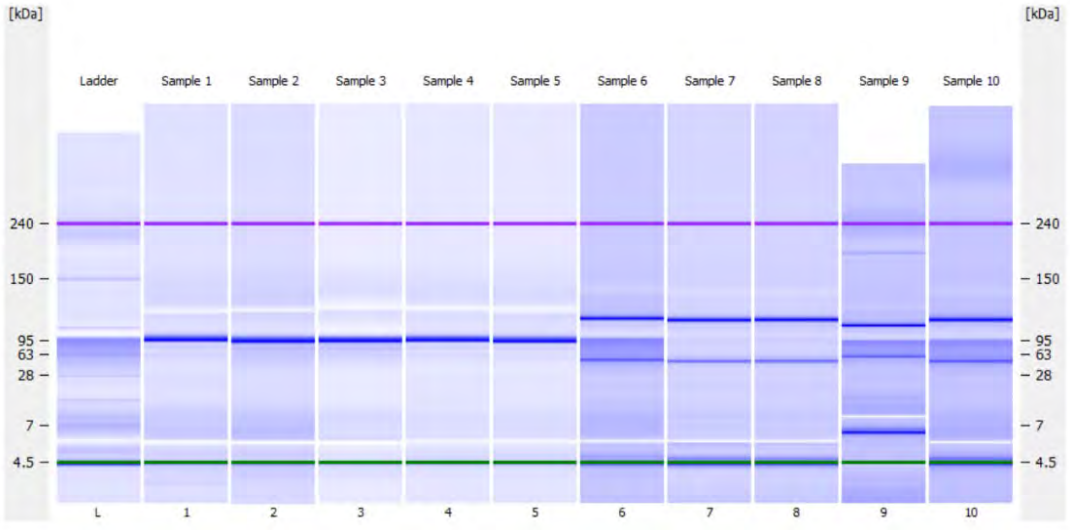


**Figure 3. Agilent Bioanalyzer digital gel of QseB and QseC recombinant proteins. Lanes 1–5 are purified QseB (bands at 80 kDa) with a ~80 % purity, and lanes 6–10 are purified QseC (bands at 100 kDa) with a percent purity ~60 %.**

Following this analysis, we cleaved the pCold1 tag from the purified protein due to its large size and potential to interfere with conformational binding and activity and confirmed this with an SDS-PAGE protein gel. After the proteins were cleaved, a comparison of cleaved to uncleaved protein, using both methods of protein incorporation into membranes, as described in the methods is shown in Figure 4. Uncleaved proteins do not generate any response over the blank, but the cleaved proteins using both methods of protein incorporation into the vesicles have more than twice the fluorescent response of the negative control that did not contain any proteins of the TCS. Epinephrine at a fixed concentration of 1 mg/mL and the reporter pqseBC-sfGFP fixed at 5 nM were present in all reactions to show there was not any background production.

The endpoint data at 16 hours (Figure 4: Panel A) shows the sonication bath method of incorporation is slightly more productive than the extruder (impinged) method. The uncleaved proteins using both methods show no significant difference from that of the blank reaction containing no proteins. The time course data (Figure 4B) shows the reactions begin production of sfGFP at about the same timepoint for both incorporation methods and maintain a similar rate of production throughout the course of the experiment. The increased error across replicates towards the end of the

experiment suggests a need to use large reaction volumes due to the combination of normal evaporation and the elevated reaction temperature of 37 °C.

Together these data show that the sonication method of integration maybe the best method of QseC incorporation for the CFE reactions and detection of epinephrine. This coupled with the fact that this method is also cheaper and faster than the extruder due to filter costs suggests that it should be adopted as the preferred method moving forward.

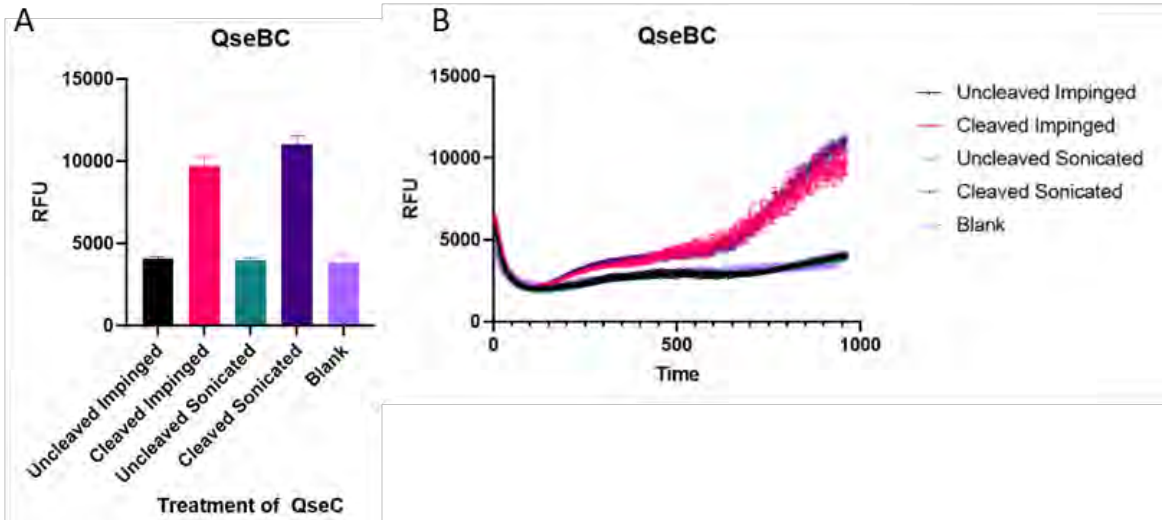


**Figure 4. A) Comparison of endpoint data of different protein incorporation into membrane vesicles as well as cleaved versus uncleaved proteins according to relative fluorescent units (RFU). B) Comparison of time course data of both protein incorporation methods and the cleaved versus uncleaved data.**

### 3.2 QseBC TCS made directly in a CFE system

To assess the ability to use this system entirely in cell free without the need for purifying recombinant proteins and spiking them in the reactions, we first determined that QseB and recombinant QseC sonicated with vesicles would detect epinephrine. The same conditions outlined above for integrating QseC into the POPC vesicles was followed before being added to the cell free reaction along with the DNA for py71-QseB, pqseBC-sfGFP and epinephrine. This data (not shown) worked similar to the previous experiments with both recombinant proteins of the TCS. After confirmation that producing QseB in the CFE system by adding plasmid DNA produced a functional sensor, the DNA for QseC, QseB, pqseBC-sfGFP, lysate, energy buffer and epinephrine was added to POPC lipids and sonicated the solution overnight in a 37 °C water bath for 24 hours. A recombinant system was used as previously described as a positive control or a blank with no TCS was used as a negative control. The sonication was applied through the entirety of the cell free reaction to ensure that QseC could be incorporated into disrupted vesicles as it was being translated. One of the cell free plasmids, pJL1-QseBC, did not lead to significant production of sfGFP relative to the negative control but the other plasmid pair, pY71-QseBC, was comparable to the recombinant system (Figure 5). Although this method generated a higher RFU response and thus theoretically more production of sfGFP, the experimental method is not practical. The entirely CFE based QseBC cascade on a plate reader without any sonication or external interference was then run. Both cell free plasmid pairs, recombinant QseBC as a positive control, and a blank reaction on an aggressively shaking plate reader was run overnight and showed a significant amount of sfGFP production over the negative control (Figure 6). This data shows the system will function without overnight sonication and may serve as a more practical approach. Both plasmid pairs worked better than the spiked recombinant proteins, but all systems produced a signal higher than the negative reaction.

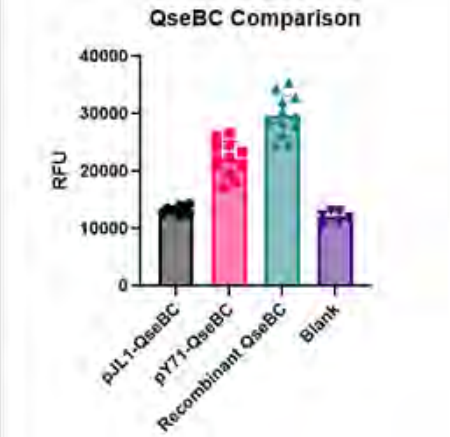


**Figure 5. Initial test of the entirely CFE QseBC system using a sonicating water bath overnight.**

## 4. DISCUSSION

Bacterial TCSs have been broadly studied and have been found to sense a variety of different stimuli ranging from temperature, light, heavy metals, antimicrobials, and many other small molecules and metabolites. Furthermore, previous work has shown that TCS can be evolved *in vitro* to alter the ligand binding specificity opening the door for the development of novel proteins capable of sensing molecules of Department of Defense interest.[11] We plan to take the application and workflow developed for QseBC and apply the same techniques to an alternative TCS to determine if it is broadly applicable across TCSs in CFE. Cell-free systems designed at sensing external stimuli offer several advantages over whole cell biosensors or alternative sensing systems. One of the primary utilities of cell-free systems is that they can be freeze-dried for storage with all necessary components for function. In the field, these freeze-dried sensors can be rehydrated with the sample of interest and the cell-free reaction will run as expected. The ultimate goal of this work is to progress to the point of a field deployable relevant biosensor that generates a response within 20 minutes at ambient temperatures. Further research is required to optimize the sensor itself, determine appropriate reagents for stability in a ruggedized system, and transition this sensor to a format that is readily visual to the naked eye.

The immediate next steps to achieve this goal are to improve the performance of the QseBC sensor by incorporating QseC protein both recombinant and CFE produced into more diverse artificial membranes composed of POPC, 1-palmitoyl-2-oleoyl-sn-glycero-3-phospho-L-serine (POPS) and cholesterol to ensure the best possible conditions for proper folding and activity. We plan to test stabilizing devices for the QseC protein called nanodiscs that have been shown to assist membrane proteins in CFE systems[12]. If these methods prove successful, the likelihood of implementing this workflow effectively for another bacterial TCS becomes more probable.

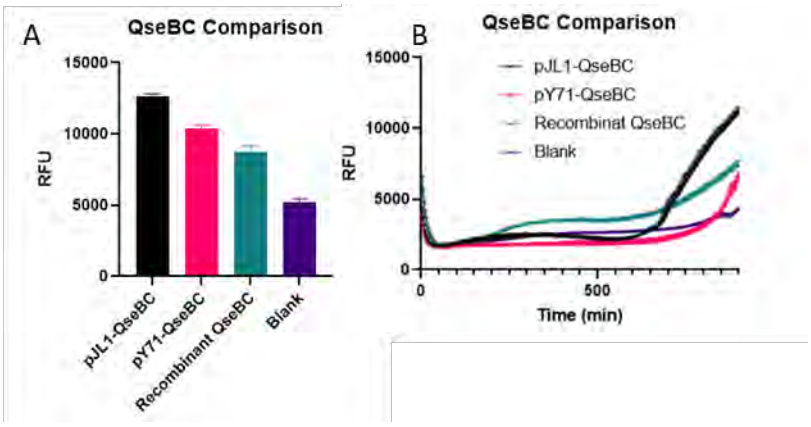


**Figure 6. A) Endpoint data of QseBC generated entirely in a CFE system using only shaking in a plate reader. B) Time course data of QseBC generated entirely in CFE system from panel A.**

## ACKNOWLEDGMENTS

We would like to thank Dr. Daniel Phillips for assistance in all things related to the lipid and liposome work. Funding was provided by the U.S. Army via the In-house Laboratory Independent Research Program (PE 0601101A Project 91A) at the Combat Capabilities Development Command Chemical Biological Center.

## REFERENCES

[1] Garenne, D.; Haines, M.C.; Romantseva, E.F.; Freemont, P.; Strychalski, E.A.; Noireaux, V. Cell-free gene expression. *Nat. Rev. Methods Primers.* **2021**, *1* (49), pp 1–18.

[2] Cole S.D.; Miklos, A.E.; Chiao, A.C.; Sun, Z.Z.; Lux, M.W. Methodologies for preparation of prokaryotic extracts for cell-free expression systems. *Synth. Syst. Biotechnol*. **2020**, *5* (4), pp 252–267.

[3] Garenne, D.; Thompson, S.; Brisson, A.; Khakimzhan, A.; Noireaux, V. The all-E. coliTXTL toolbox 3.0: new capabilities of a cell-free synthetic biology platform. *Synth. Biol*. **2021**, *6* (1), p ysab017.

[4] Lazar, J.T.; Tabor, J.J. Bacterial two-component systems as sensors for synthetic biology applications. *Curr. Opin. Syst. Biol.* **2021**, 28, p 100398.

[5] Weigel, W.A.; Demuth, D.R. QseBC, a two-component bacterial adrenergic receptor and global regulator of virulence in Enterobacteriaceae and Pasteurellaceae. *Mol. Oral Microbiol*. **2016**, *31* (5), pp 379–397.

[6] Moreira, C.G.; Sperandio, V. The Epinephrine/Norepinephrine/Autoinducer-3 Interkingdom Signaling System in Escherichia coli O157:H7. *Adv. Exp. Med. Biol*. **2016**, *874*, pp 247–261.

[7] Clarke, M.B.; Sperandio, V. Transcriptional autoregulation by quorum sensing Escherichia coli regulators B and C (QseBC) in enterohaemorrhagic E. coli (EHEC). *Mol. Microbiol*. **2005**, *58* (2), pp 441–455.

[8] Sperandio, V.; Torres, A.G.; Kaper, J.B. Quorum sensing Escherichia coli regulators B and C (QseBC): a novel two-component regulatory system involved in the regulation of flagella and motility by quorum sensing in E. coli. *Mol. Microbiol*. **2002**, *43* (3), pp 809–821.

[9] Levine, M.Z.; Gregorio, N.E.; Jewett, M.C.; Watts, K.R.; Oza, J.P. Escherichia coli-Based Cell-Free Protein Synthesis: Protocols for a robust, flexible, and accessible platform technology. *J. Visualized Exp.* **2019**, *144*, p 58882.

[10] Silverman, A.D.; Kelley-Loughnane, N.; Lucks, J.B.; Jewett, M.C. Deconstructing Cell-Free Extract Preparation for *in Vitro* Activation of Transcriptional Genetic Circuitry. *ACS Synth. Biol*. **2019**, *8* (2), pp 403–414.

[11] Kohanski, M.; Collins, J.J. Rewiring bacteria, two components at a time. *Cell*. **2008**, *133* (6), pp 947–948.

[12] Roos, C.; Kai, L.; Haberstock, S.; Proverbio, D.; Ghoshdastider, U.; Ma, Y.; Filipek, S.; Wang, X.; Dötsch, V.; Bernhard, F. High-level cell-free production of membrane proteins with nanodiscs. *Methods Mol. Biol.* **2014**, *1118*, pp 109–130.

# CBAMMS
## PROJECTS

# Non-expanding reactive compacts using intermetallic and thermite reactions

Amee L. Polk[a]*, Steven W. Dean[b], Michael R. Flickinger[c], Erica R. Valdes[a], Kyle Fisher[c], Timothy P. Weihs[c]
[a]U.S. Army Combat Capabilities Development Command Chemical Biological Center, Research & Operations Directorate, 8198 Blackhawk Rd, Aberdeen Proving Ground, MD 21010
[b]U.S. Army Combat Capabilities Development Command Army Research Laboratory, Army Research Directorate, 459 Mulberry Point Dr, Aberdeen Proving Ground, MD 21005
[c]Department of Materials Science and Engineering, Johns Hopkins University, 3400 North Charles St, Baltimore, MD 21218

## ABSTRACT

We investigate no/low gas generating thermites composed of ball-milled Al:Zr fuel and $TiO_2$ (anatase). Sample composition was controlled by varying the Al:Zr atomic ratio. Milling conditions (single- and dual-stage milling) varied sample microstructures. Resulting powders were studied for ignition temperatures, heat release, and product phases. Single stage milled samples had better intermixing of Al, Zr, and $TiO_2$ and differential thermal analysis under Ar identified lower Al melt temperatures and Zr oxides formed. Differential thermal analysis also indicated higher Zr contained an intermediate $Al_3Zr$ cubic phase, while Al-rich samples had the stable, tetragonal $Al_3Zr$ phase. All thermites containing Zr showed a decreased ignition temperature compared to Al:$TiO_2$. All compacted thermites burned near the adiabatic reaction temperature. In compaction studies, reaction front propagation speed and temperature were measured. Single- and dual-stage milled Al-rich samples reacted with an exfoliating appearance. Dual-stage milled Al:Zr did not expand, had the slowest average burn rate at 1.6 mm/s, and a two-stage reaction front. This unique dual reaction front is thought to occur when Al and Zr form $Al_3Zr$ then $Al_3Zr$ oxidation. All samples reacted well below the melting temperature of Al and Zr, promoting the condensed phase reaction.

**Keywords:** thermite, intermetallic, milling, compaction

## 1. INTRODUCTION

Thermites are a class of materials that undergo an oxidation-reduction reaction between a metal fuel and an oxide, resulting in a more stable oxide produced from the starting metal. The most common thermite, aluminum and iron oxide, has been used for centuries in welding, such as in railroads.[1,2] Recent developments have led to the use of thermites in applications like breaching, chemical/biological agent defeat, decoy materials, and enhanced energetics.[3-6] Some applications, such as heat sources in sealed vessels, require high energy output and tunable reaction velocities with little or no gas generation or product expansion.

An ideal oxide would generate little gas while reacting in the condensed phase. $TiO_2$ offers little toxicity, low cost, and condensed phase products. In addition, the Al + $TiO_2$ reaction has one of the lowest recorded adiabatic reaction temperatures at 1,479 °C,[7] well below the boiling point of Al at 2,470 °C.[7] Using modeling software (Cheetah exp6i v9.0), the adiabatic reaction temperature of Zr + $TiO_2$ was measured at 1,463.76 °C, again well below the boiling point of Al. This choice allows us to reduce Al vapor during the thermite reaction, unlike the adiabatic reaction temperature of Al + $Fe_2O_3$ at 2,861.85 °C.[7] For the metal fuel, we added Zr which oxidizes rapidly in the condensed phase to Al by fabricating composite Al-Zr powders. These powders have low ignition thresholds even at the microscale due to the intermetallic reaction between Al and Zr.[8-11] Thus, reactivity is enhanced while avoiding the hazards associated with nanoscale Al and Zr powders.[9,12,13] The lower ignition temperature of the composite powders will reduce the risk that the thermite reactions quench during self-propagation. However, with both Al and Zr oxidizing in the condensed phase at much lower temperatures than Al + $Fe_2O_3$, the ability to avoid quenching needs to be demonstrated.

Here we employ arrested reactive ball-milling[14] as the mechanical properties, reactive properties, and microstructures of the resulting particles can be tuned with milling procedures.[10,14,15] We prepare Al/Zr/$TiO_2$ powders using two different Al-Zr ratios—3Al:Zr and Al:Zr. In doing so, we leverage earlier studies of the Al-Zr intermetallic system to

drive our process parameters,[9-11,16] and explore how best to combine Al, Zr, and $TiO_2$ powders using both single-stage (1S) and dual-stage (2S) milling. The reaction properties and products of powders and compacts are examined for both 3Al:Zr and Al:Zr chemistries combined in stoichiometric ratios with $TiO_2$. Lastly, they are compared with two traditional thermite samples that are fabricated by combining Al powders with $TiO_2$ or $Fe_2O_3$.

## 2. MATERIALS PREPARATION AND CHARACTERIZATION

### 2.1 Material synthesis

Both single-stage milled and dual-stage milled thermites were made using commercial Al (Alfa Aesar, 99.5 % pure, -325 mesh, APS 7–15 μm), Zr (Atlantic Equipment Engineers, 99.5 % pure, -20 to +60 mesh), $Fe_2O_3$ (Alfa Aesar, 98 % pure, -325 mesh), and $TiO_2$ (Aldrich, >99% pure, -325 mesh, anatase) powders. The Al and $TiO_2$ powders were selected based on similar particle sizes, while the larger Zr starting particle size was chosen for safe handling due to its pyrophoric nature. $Fe_2O_3$ was chosen as the baseline oxide due to its commonplace use in commercial applications. All materials were processed in a planetary ball mill (Retsch, PM400) at 350 RPM for one hour. In single-stage milled compositions, the Al, Zr, and $TiO_2$ were loaded under Ar into custom made hardened steel vials with a total internal volume of 186 mL. Powders were loaded with 40 mL of hexanes (Fisher Chemical, 98.5 % pure) as a process control agent and 9.525 mm 440 stainless steel milling balls at a ball to powder ratio of 3. The milling cycle consisted of four, 15 min active milling sessions separated by 30 min rest cycles. The sample vials were air cooled during the milling process. These 1S stoichiometric formulations consisted of three atomic compositions: 57at%Al 43at%$TiO_2$ (Al:$TiO_2$), 41at%Al 14at%Zr 45at%$TiO_2$ ((3Al:Zr):$TiO_2$), and 27at%Al 27at%Zr 47at% $TiO_2$ ((Al:Zr):$TiO_2$). For samples prepared via 2S milling, the Al and Zr fuels were pre-milled together in air following methods detailed elsewhere.[12] These pre-milled fuels were then milled in a second stage with the $TiO_2$ under Ar following the same procedure as the single-stage milled thermite formulations. The formulations consisted of two compositions: 41at%Al 14at%Zr 45at%$TiO_2$ ((3Al:Zr):$TiO_2$), and 28at%Al 28at%Zr 47at% $TiO_2$ ((Al:Zr):$TiO_2$).

To prepare compacts from the powders, a uniaxial load press (Denison) was used with a force indicator (Dillon, FI-127) and load cell (Dillon, SGMC 5,000 lb). Compacts were consolidated in a custom Elizabeth Carbide 7.37 mm diameter ram/die set. Thermite powders were loaded into the die with a weight of 1.0 ± 0.05 g and were compressed with 4448 N and a 10 sec dwell, resulting in a normal stress of approximately 104.5 MPa. This resulted in compacts with lengths from 8.2 mm to 11.4 mm (aspect ratios of 1.1 to 1.5), depending on the material's density. To prepare a compact of the traditional thermite Al:$Fe_2O_3$ sample for comparison, Al and $Fe_2O_3$ powders were mixed and compressed with the atomic composition 39at%Al 61at%$Fe_2O_3$ (Al:$Fe_2O_3$).

### 2.2 Material characterization

All milled samples were dry sieved using a motorized shaker (Dual Manufacturing Co. Inc., D-4326) at 2,000 vpm in a 3-inch, 75 μm brass sieve for a minimum of 30 min to eliminate any larger particles and reduce agglomeration. As confirmed by particle size analysis, very little material was captured by the 75 μm sieve. Particle size distributions for milled powders were obtained using a particle size analyzer (Horiba, LA-950 V2). The powders were dispersed in isopropanol, ultrasonicated to break agglomerates, and then sized using low angle laser scattering. Each sample was run six times to obtain an average particle size distribution.

The morphologies of the loose particles were characterized in a field emission scanning electron microscope (JEOL, JSM-7900F) using secondary electrons (SE). We determined composition using energy dispersive spectroscopy (EDS, Oxford Aztec with X-Max 80 mm detector). Cross sectioned images were captured by mounting the sieved powders in epoxy and polishing using a Struers Tegramin-20 with SiC polishing paper in sequentially finer grits. High resolution backscattered electron (BSE) images were collected using the field emission scanning electron microscope. These images allowed for comparison of the refinement of Zr in the Al matrix of the composite particles, as well as intermixing with the $TiO_2$ with the Al and Zr.

Crystalline phases of the thermites were determined using x-ray diffraction (XRD, Malvern PANlytical Empyrean Series 3 Diffractometer with PIXcel 1D detector at a tension of 45 kV and current of 40 mA with Cu-Kα radiation). Samples were mounted on a low background Si disc and scanned from 5° to 90° 2θ with a step size of 0.01° and 0.5 sec per step. Each sample was run 10 times, and a simple sum average was performed on the resulting 10 scans. The resulting XRD patterns were analyzed using HighScore Plus4 software.

### *2.2.1 Heat of reaction characterization*

The heat of reaction produced by the intermetallic and oxidation reactions were characterized using differential thermal analysis (DTA). The DTA (TA Instruments, Discovery SDT650) was loaded with 10 mg samples heated twice from 50–1,000 °C at a rate of 40 °C/min under high purity Ar flowing at 100 mL/min. The first heating assumes the reactions are irreversible and was used for determination of the heat output, while the second gave the baseline heat capacity of the reacted sample and crucible; this second scan was subtracted from the first to give final net heat flow. Samples were heated in Ar and rapidly quenched at 600 °C, 800 °C, and 1,000 °C to identify phases formed during heating. These temperatures were selected to capture the phases at the end of each exotherm seen on the DTA scans and were analyzed using XRD.

### *2.2.2 Loose powder ignition temperature*

The ignition temperatures of the sieved powders were measured as a function of heating rate in room air. A custom designed system was built for the heated nichrome wire ignition tests, described elsewhere.[9,10,11] Dilute suspensions of the powders were painted onto a 10-cm length of 28-gauge pre-tensioned nichrome wire. The wire was heated using three 12 V absorbent glass mat car batteries connected in series for 36 V direct current. The system was triggered by a 500 ms pulse generated through a LabView program. Temperature of the wire was recorded using a pyrometer (Luna Sense two-color, low-temperature infrared) calibrated between 200 °C and 1,000 °C. The ignition was captured using a high-speed camera (Photron Limited Fastcam SA-Z) recording at 20,000 fps. The videos were analyzed using a custom MATLAB program to determine the moment of first light to within one frame (0.5 ms) accuracy. This time resolution corresponds to ~15 °C at a typical heating rate of 30,000 °C/s. The sample ignition temperature was determined by correlating the temperature of the wire to the moment of first light.

### *2.2.3 Thermite compact laser ignition*

Thermite compacts were top-ignited using a high rep-rate pulsed Nd:YAG laser (Coherent, Avia NX-65, 65 W, 532 nm, 150 kHz, 40 ns/pulse). A mechanical shutter was used to block the low-energy idler pulses continuously emitted by the laser, while allowing high-energy pulse trains to pass when triggered. Samples were ignited with a high-energy pulse train 500 ms in total length (approximately 75,000 pulses). No optics were used to focus the 3.5 mm beam onto the sample. Four-color pyrometry and filtered high-speed video were used to study reaction propagation as shown in Figure 1.

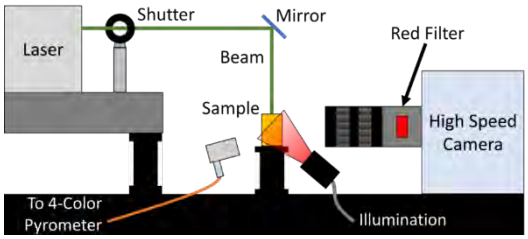


**Figure 1. Experimental configuration for compact ignition studies.**

### *2.2.4 Four-color pyrometry*

Analysis of four-color pyrometry data proceeded with methods used by Weismiller et al. and others.[17-21] The intensity response of the pyrometer was calibrated using a stabilized tungsten lamp with a known spectral intensity distribution (Thorlabs, SLS201L). For each time step of spectral data, the temperature was determined from the slope of a plot of:

$$\frac{C2}{\lambda} \; vs \; -\ln I * \lambda 5 \tag{1}$$

where C2 is the second radiation constant (C2 = 1.4388 X 10-2 m*K), λ is the wavelength of light, and I is the calibrated light intensity measured at that wavelength. Python scripts were written to execute these calculations.

The four-color pyrometer includes a bandpass filter centered at 770 nm, a band which includes a strong K atomic emission line. The selection of this filter for the four-color pyrometer was inadvertent and based on considerations related to available optics more than on atomic emission features. Comparison between temperatures determined with four pyrometer colors and only three (dropping the 770 nm channel) result in almost identical values. This is likely

due to K atomic emission being a relatively minor contributor to total emitted light compared to the thermal emission from the sample at the same wavelength.

## 3. RESULTS AND DISCUSSION

### 3.1 Particle morphology and microstructure

The particle size distributions display a uniform, unimodal size distribution for the Al:$TiO_2$ composition which we attribute to the similar particle sizes of the starting materials. The powders with bimetallic Al-Zr fuels, though, show bimodal particle size distributions, likely due to fracturing of the $TiO_2$. As seen in the loose powder scanning electron microscopy (SEM) images (Figure 2), nanosized particles are visible, while the EDS images indicate these particles are comprised of $TiO_2$. This bimodal distribution is more notable in the higher Zr at% compositions, with (Al:Zr):$TiO_2$_1S being the most pronounced. Anatase $TiO_2$ has a higher Mohs hardness than the brittle Zr and ductile Al, making it prone to fracturing. Additionally, as has been seen in previous work,[11] finer particles were observed in the higher Zr at% composition, with no cold welding of Al seen for any formulation.

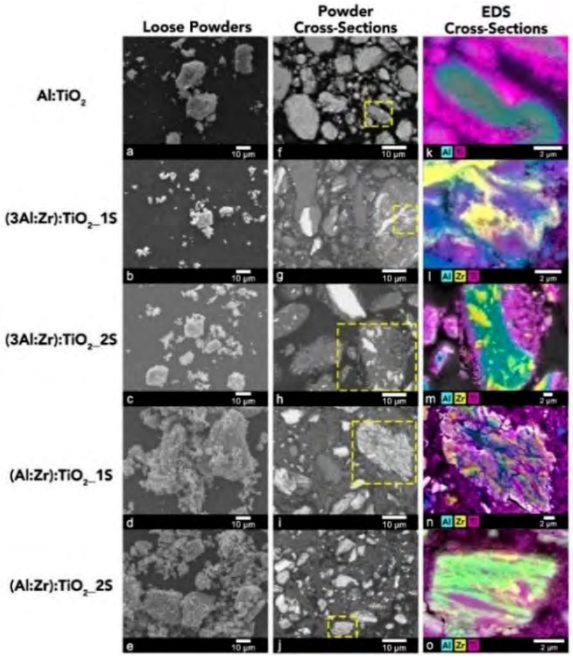


**Figure 2. Representative SEM images of loose, milled powders captured with SE for compositions at 500 x magnification on the left, BSE images of cross sections at 2,000 x magnification in the center, and on the right, and EDS images of cross sections at 7,000 x on the right. The yellow dashed lines indicate location of EDS image.**

SEM and EDS images representative of the sieved powders are shown in Figure 2, with SE images of loose particles on the left (500 X magnification), BSE images of cross sections in the center (2,000 X magnification), and EDS images of cross sections on the right (7,000 X magnification). All powders have similar morphologies, with rough, jagged surfaces and approximately equiaxed shapes. As seen in the loose powder images (left column) as well as the cross-sectional BSE images (center column), a range of particle sizes was produced with (Al:Zr):$TiO_2$_2S having the smallest particles. The BSE cross sections also allow for visualization of the Zr inclusions in the Al matrix; they appear bright white due to their higher atomic number. However, the $TiO_2$ and Al phases cannot be distinguished due to their similar z-contrast. EDS was performed on the cross-sectioned particles as well to differentiate the Al and $TiO_2$ phases. The (Al:Zr):$TiO_2$_1S and (3Al:Zr):$TiO_2$_1S samples show more intermixing of Ti (oxygen was omitted for clarity, but overlays with Ti) within the particles as well as unmixed regions of Al and Zr. These single-stage milled particles do not have the distinct Zr inclusions within an Al matrix as seen previously for single stage milling of just Al and Zr.[11] The dual-stage milled samples show less incorporation of the $TiO_2$ into the particles, but they do display an Al matrix with Zr inclusions. We see larger Zr inclusions or particles in both the (3Al:Zr):$TiO_2$ thermites, likely due to the higher volume fraction of Al cushioning the Zr and preventing its fracture. In both the (Al:Zr):$TiO_2$ thermite

samples the Zr inclusions/particles are smaller and there is better intermixing of all three components compared to the (3Al:Zr):$TiO_2$ samples, with (Al:Zr):$TiO_2$_1S appearing more homogeneous than (Al:Zr):$TiO_2$_2S.

XRD scans for the sieved thermites show an increase in the Al peak intensities with increasing Al content. In each scan, we identified the initial starting materials and small ZrC peaks that are present for all samples containing both Al and Zr, as shown previously when milling Al-Zr.[11] The Al peaks for the (Al:Zr):$TiO_2$_2S sample show a broadening and slight shift to lower 2θ values, consistent with the formation of an Al-Zr solid solution or variations in elastic strains due to local dislocation density fluctuations.

### 3.2 Differential thermal analysis

DTA scans of sieved thermites are displayed in Figure 3. The Al:$TiO_2$ thermite shows minimal activity until Al melts at 660 °C, followed by two large exothermic peaks attributed to the oxidation of Al by reduction of $TiO_2$. For most powders containing Zr, a broad exotherm begins around 200 °C and continues until Al melts at 660 °C. We attribute this exotherm to the intermixing of Al-Zr and the formation of the $Al_3Zr$ intermetallic compound, as seen in earlier studies.[11,12,22] The (3Al:Zr):$TiO_2$_2S and (Al:Zr):$TiO_2$_2S samples exhibit a second small peak around 550 °C, attributed to $Al_2Zr$ formation and the polymorphic transformation of $Al_3Zr$.[10] After the endotherm for Al melting, all thermite compositions have two or three broad exotherms due to the reduction-oxidation reactions of Al/$TiO_2$ and Zr/$TiO_2$. The exotherms and endotherm in the (Al:Zr):$TiO_2$_2S and (3Al:Zr):$TiO_2$_2S thermites are shifted to lower temperatures compared to the single stage compositions, and the Al endotherm is smaller. Table 1 gives the melting temperature and peak onset for the Al melt endotherm determined from the DTA scans. The lower Al melting temperature in the double stage milled samples is attributed to the intermixing of Zr into Al during milling.

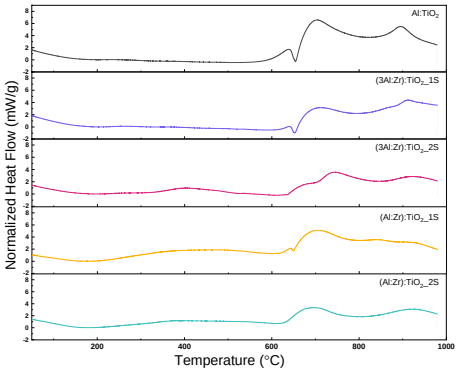


**Figure 3. DTA traces of sieved powders, < 75 µm, heated in Ar. Variations in heat flow below 100 °C are artifacts of the DTA furnace, and the shaded regions represent one standard deviation.**

**Table 1. Al melting temperature and endotherm onset calculated from the DTA scans.**

| Target Composition/Sample ID | Melt T (°C) | Onset T (°C) |
|---|---|---|
| Al (pure) | 660.3[22] | - |
| Al:$TiO_2$ | 654.7 ± 0.1 | 642.8 ± 0.5 |
| (3Al:Zr):$TiO_2$_1S | 652.7 ± 0.1 | 643.2 ± 0.2 |
| (3Al:Zr):$TiO_2$_2S | 635.5 ± 0.3 | 606.5 ± 1.5 |
| (Al:Zr):$TiO_2$_1S | 649.9 ± 0.5 | 643.8 ± 0.5 |
| (Al:Zr):$TiO_2$_2S | 628.0 ± 1.6 | 593.1 ± 5.8 |

XRD analysis of phases that appear after heating to 600 °C in the DTA are given in Table 2. All thermite samples display peaks for the initial constituents, with the samples containing Zr also showing peaks for the $Al_3Zr$ intermetallic. Of note, the crystal structure of $Al_3Zr$ in both of the (Al:Zr):$TiO_2$ thermites is cubic, while in both (3Al:Zr):$TiO_2$ thermites it is the equilibrium tetragonal phases. However, after DTA heating to 800 °C in Ar and then cooling, the cubic $Al_3Zr$ is no longer seen, only the tetragonal phase appears in samples containing Zr, except the (Al:Zr):$TiO_2$_2S sample that has more Zr-rich Al-Zr phases. Lastly, the single stage milled samples show oxidation of Zr, with the (Al:Zr):$TiO_2$_1S sample displaying a reduced fraction of titania. Several oxidation states of Ti and Zr are seen, as well as $Al_2O_3$, and multiple Al-Ti and Al-Zr intermetallics (excluding $Al_3Zr$).

**Table 2. Phases determined by XRD analysis of thermites heated at 40 °C/min in Ar to 600 °C and cooled.**

| Sample ID | Al | Zr | $TiO_2$ | TiO | $Al_3Zr$ Cubic | $Al_3Zr$ Tetra | $ZrO_2$ | ZrC | $Zr_3O$ |
|---|---|---|---|---|---|---|---|---|---|
| Al:$TiO_2$ | X | | X | | | | | | |
| (3Al:Zr):$TiO_2$_1S | X | X | X | | | X | | X | X |
| (3Al:Zr):$TiO_2$_2S | X | X | X | | | X | | X | |
| (Al:Zr):$TiO_2$_1S | X | X | X | X | X | | X | X | |
| (Al:Zr):$TiO_2$_2S | X | X | X | | X | | | X | |

### 3.3 Wire ignition

Hot-filament ignition tests were conducted at atmospheric pressure in air. Table 3 lists averages of the heating rates and ignition temperatures for a minimum of seven trials per thermite sample. All ignition temperatures are below the ignition temperature of pure Al, which is dependent on the particle size varying from the melting point of pure Al (660 °C) for nanosized particles to the melting point of the native oxide (2,050 °C) for micron sized particles.[22,23] In addition, all samples containing Zr ignite in air at temperatures that are approximately 100 °C lower than the Al:$TiO_2$ sample.

**Table 3. Average ignition temperatures and heating rates for experiments conducted in air.**

| Sample ID | Heating rate (°C/s) in Air | Ignition temp. (°C) in Air |
|---|---|---|
| Al:$TiO_2$ | 30,936 ± 1,285 | 600 ± 36 |
| (3Al:Zr):$TiO_2$_1S | 29,672 ± 2,519 | 467 ± 39 |
| (3Al:Zr):$TiO_2$_2S | 29,777 ± 3,957 | 511 ± 40 |
| (Al:Zr):$TiO_2$_1S | 31,392 ± 1,722 | 451 ± 12 |
| (Al:Zr):$TiO_2$_2S | 29,799 ±1,254 | 474 ± 14 |

Higher Al at% thermites result in higher ignition temperatures in air, as has been seen in recent work involving Al-Zr only composite powders.[10,11] Additionally, the double stage samples exhibit higher ignition temperatures than their single stage counterparts, suggesting the refinement of the Zr phase may be limiting oxidation of Zr. Additionally, particle size will impact the ignition temperature, with smaller particles having a greater ratio of surface oxide to volume, resulting in a higher ignition temperature. We see this trend between the single stage and double stage samples, as the double stage samples for both (3Al:Zr):$TiO_2$ and (Al:Zr):$TiO_2$ are smaller than their single stage counterparts. In all configurations the thermites burn primarily on the wire.

### 3.4 Properties of self-propagating reactions in compacts

Densities were determined for the compacts. The theoretical maximum density (TMD) was calculated for comparison and values are reported in Table 4. The percent TMD increases slightly as the at% of Al rises, owing to the ductile nature of Al. However, all pellets were well below 100 % TMD, characteristic of uniaxial compaction.

**Table 4. Densities of the sieved and compacted pellets with calculated TMD.**

| Target Composition/Sample ID | TMD ($g/cm^3$) | Compact ($g/cm^3$) | Compact % of TMD |
|---|---|---|---|
| Al:$TiO_2$ | 2.95 | 2.57 ± 0.05 | 79.6 |
| (3Al:Zr):$TiO_2$_1S | 3.93 | 2.53 ± 0.03 | 67.1 |
| (3Al:Zr):$TiO_2$_2S | 3.93 | 2.49 ± 0.04 | 66.0 |
| (Al:Zr):$TiO_2$_1S | 4.76 | 2.70 ± 0.02 | 63.1 |
| (Al:Zr):$TiO_2$_2S | 4.76 | 2.81 ± 0.01 | 65.7 |
| Al:$Fe_2O_3$ | 4.32 | 2.57 ± 0.05 | 72.1 |

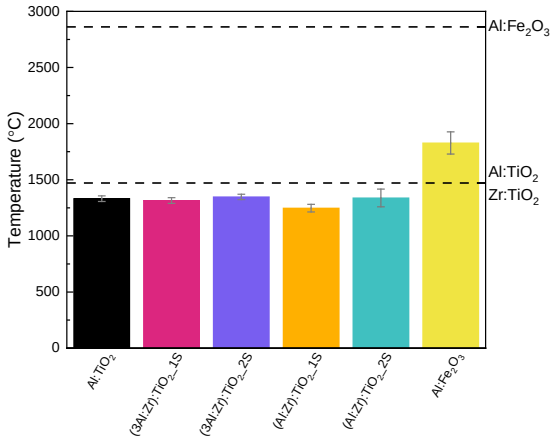


**Figure 4. Average burn temperature of each pellet measured by four-color pyrometry. Each value is the average obtained from multiple tests. Adiabatic reaction temperatures are added as dashed lines.**

The average measured temperatures for reactions in the thermite compacts are plotted in Figure 4. The average compact temperatures during the reactions were obtained using the four-color pyrometer and by averaging over the entire burn duration for three separate samples. The pyrometer field of view does not include the top of the compact ignited by the laser, and thus the signal from the laser is not included. The measured values show that the reactions containing $TiO_2$ burn at relatively similar temperatures, close to but below the adiabatic temperatures for the stoichiometric reactions: 1,479 °C for Al + $TiO_2$,[7] and 1,463.76 °C for Zr + $TiO_2$.[26] The difference is attributed mainly to the fact that the experimental values are averages over the entire recorded reaction duration. In sharp contrast, the thermite reactions containing $Fe_2O_3$ burn at much higher temperatures but well below Al + $Fe_2O_3$ adiabatic reaction temperature of 2,861.85 °C,[7] suggesting incomplete reaction prior to the advection of material from the reacting interface as seen in Figure 5.

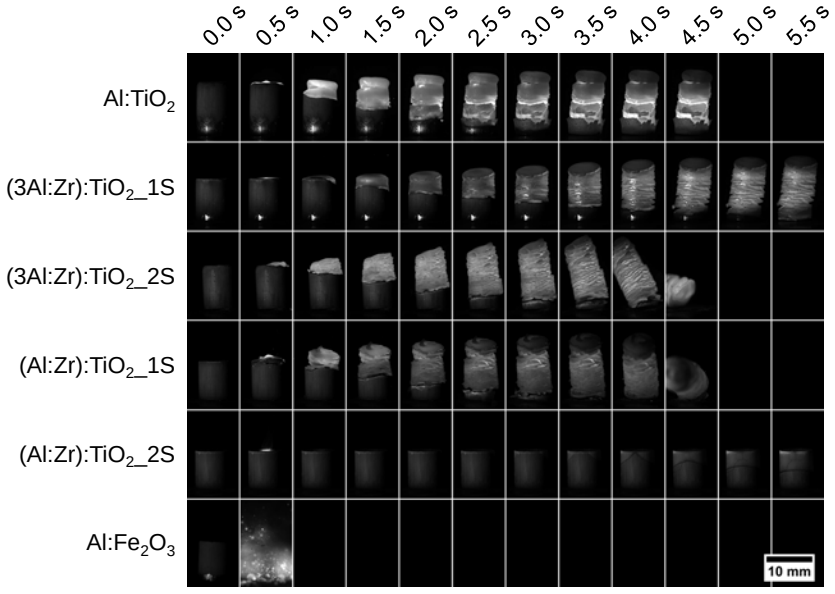


**Figure 5. Montage of images constructed from every 500th image in the high-speed video. Al:$Fe_2O_3$ burned significantly faster than the $TiO_2$ based thermites, and thus has only two frames before the reaction reached completion.**

The average burn rates were determined by analyzing high-speed video recordings of the reaction propagation. Montages of the high-speed videos are shown in Figure 5 with every 500th frame of the video included. ImageJ[24] was used to convert the recorded videos into pseudo-streak images following the method previously described.[25] An example of a pseudo-streak image generated from the reaction of an Al:$TiO_2$ sample is shown in Figure 6. There is a 100 ms delay before high power laser pulses are triggered. The laser impinges on the target for 500 ms, which can be seen as a bright horizontal line on the left of the image; this is the top of the sample. The reaction then propagates down the sample in

a relatively steady manner for several hundred ms, before transitioning to a slower propagation regime characterized by forward propagation followed by sample pullback. Average burn rates were determined for each sample by fitting best-fit lines to the propagation front and determining slopes. All streak data collected was averaged to determine the burn rate for each thermite composition. This data is presented in Table 5. The Al:$Fe_2O_3$ thermite reaction is dramatically faster than any of the $TiO_2$ based thermites, with the thermites containing Zr all burning slower than Al:$TiO_2$. The (Al:Zr):$TiO_2$_2S thermite has the slowest burn rate, and also displays almost no expansion during burning, as evidenced by Figure 6 and Table 5.

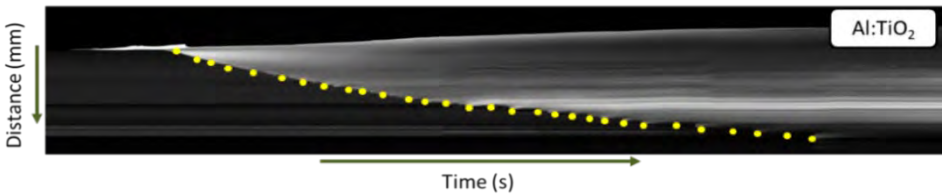


**Figure 6. Example pseudo-streak image used to determine sample burn rate.**

**Table 5. Average burn rates and expansion ratios determined from streak images.**

| Sample ID | Average Burn Rate (mm/sec) | Expansion Ratio (mm/mm) |
|---|---|---|
| Al:$TiO_2$ | 3.6 ± 0.6 | 1.3 ± 0.05 |
| (3Al:Zr):$TiO_2$_1S | 2.3 ± 0.2 | 1.3 ± 0.02 |
| (3Al:Zr):$TiO_2$_2S | 2.8 ± 0.4 | 1.8 ± 0.21 |
| (Al:Zr):$TiO_2$_1S | 3.4 ± 0.3 | 1.6 ± 0.07 |
| (Al:Zr):$TiO_2$_2S | 1.6 ± 0.1 | 1.0 ± 0.03 |
| Al:$Fe_2O_3$ | 83.3 ± 45.8 | N/A |

Each of the samples were evaluated for expansion during its reaction. All compacts (except (Al:Zr):$TiO_2$_2S) expand with a "flaking" appearance, most pronounced in the (3Al:Zr):$TiO_2$_2S sample. In the (Al:Zr):$TiO_2$_2S samples there is no "flaking"; however, some cracking of the compacts is observed which does not cause an expansion. ImageJ was used to determine an overall length of the compact prior to ignition, and then a length was determined at the end of the video after reaction completion. The resulting expansion ratios are listed in Table 5. These measurements were done in triplicate for every compact except Al:$Fe_2O_3$ which could not be evaluated due to its intense production of gaseous products causing destruction of the compact. The (Al:Zr):$TiO_2$_2S thermite shows almost no expansion while the (3Al:Zr):$TiO_2$_2S sample has the highest and the Al:$TiO_2$ sample falls in between.

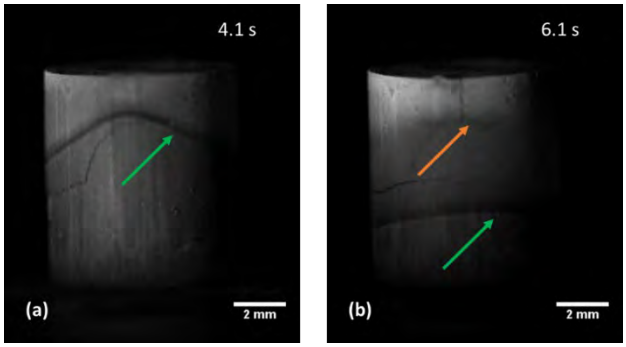


**Figure 7. (Al:Zr):$TiO_2$_2S compact demonstrating two reaction fronts: (a) shows the preceding reaction front indicated by the green arrow, and (b) shows the luminous front seen in all reacting $TiO_2$ thermites indicated by the orange arrow.**

### 3.5 Two-stage reaction

As evidenced by the videos captured for the compacts after ignition, a luminous front can be seen propagating within each compact as it reacts. In the (Al:Zr):$TiO_2$_2S thermite, however, an additional reaction front can be seen preceding the luminous reaction front, as shown in Figure 7. Considering this two-stage reaction, we explored how reaction velocity can change with time during propagation. Using the streak image, the position of the dark front and luminous front were determined and plotted versus time for a compact of (Al:Zr):$TiO_2$_2S. The slopes were determined for the

dark and luminous fronts individually, and show a drastic difference in reaction rates, with the dark front at 0.74 mm/s and the luminous at 2.09 mm/s.

The $TiO_2$ allows for a reduction in the thermite burning temperature, well below that of Al vaporization. This confines the reaction to condense phases and thus minimizes expansion substantially. However, even though Al vaporization is avoided, the reactions do not quench. We hypothesize that the Al-Zr intermetallic reaction is assisting in the reduction of vaporous products by reducing the available Al to oxidize. We see the formation of the Al-Zr intermetallic species at lower temperatures than the Al oxidation products. With Al bound in the Al-Zr intermetallic, excess Zr will oxidize in the condensed phase, again limiting expansion. These compacts were not fully dense, some of the expansion in the Al-Zr-$TiO_2$ thermites could be due to vapor existing in the voids within the compact, as well as oxidation of excess Al producing a small amount of vaporous products. As the reaction propagates and heats it is also possible for vapor trapped in these voids of the compacts to expand and cause "flaking". To describe the burn rate modification, we believe the addition of Zr is effectively slowing the kinetics of the reaction. These reactions are well below the melting temperature of Zr (1,855 °C), bolstering its reaction in the condensed phase. Thermal conductivities are lower for condensed phase reactions, additionally slowing the reaction rate. The $Al_3Zr$ intermetallic is likely also contributing to the reduced reaction rate, as its melting temperature (1,580 °C) is near the reaction temperature of the thermites, and thus its melting will impact the overall kinetics. We believe this sustained reaction at low temperatures is enhanced by leveraging the Al-Zr intermetallic reaction to reduce the ignition temperature of the thermites.

The unexpected two-stage reaction seen in the (Al:Zr):$TiO_2$_2S has been attributed to two factors: a lack of molten Al due to early formation of $Al_3Zr$, and the requirement of $Al_3Zr$ to oxidize to initiate the luminous reaction. As has been shown in previous works,[8] the products generated from Al and Zr is dependent on the rate at which the reaction proceeds, and thus with the formation of the $Al_3Zr$ intermetallic, we effectively slow the oxidation rates of Al and Zr. In the case of the (Al:Zr):$TiO_2$_2S thermite, the double stage milling is promoting the intermetallic reaction by reducing the diffusion limits between Al and Zr.

## 4. CONCLUSIONS

We eliminated gas production and compact expansion by first using an oxide that generates less heat ($TiO_2$) and also lowered the reaction temperature below the boiling point of Al, thereby confining the reaction to condensed phases. Second, to prevent quenching at the lower reaction temperatures the reactivity of the thermite system was enhanced by adding a metal (Zr) to Al that produces heat on mixing with Al and oxidizes well in the condensed phase.

Results of the powder characterizations show that the Al-Zr-$TiO_2$ powders have smaller mean particle sizes, lower ignition temperatures, an exothermic heat release prior to Al melt compared to the simple Al:$TiO_2$ powders. The Zr containing samples also produce the $Al_3Zr$ intermetallic after heating to 600 °C. Comparing the two milling protocols, the single stage milling yielded better intermixing of the starting constituents while the formulations milled in two stages a less heterogeneous mixing particle morphology, with particles exhibiting Zr inclusions in an Al matrix, surrounded by $TiO_2$ particles. All samples containing Zr had ignition temperatures below that of Al:$TiO_2$.

High speed videos show that the (Al:Zr):$TiO_2$_2S sample displayed unique attributes with a slow, two-stage reaction and almost no product expansion or gas production. This desirable behavior was attributed to the intermetallic reactions between Al and Zr being favored over the oxidation/reduction reactions. In all other thermite formulations, we see an expansion of the compact during reaction and only a luminous reaction front. However, in the (Al:Zr):$TiO_2$_2S thermite we observe two reaction fronts. We note only the (Al:Zr):$TiO_2$_2S thermite has a decreased and broadened peak for Al melt heat of reaction. In this formulation, the Al is bound in the $Al_3Zr$ intermetallic, and thus is unavailable to oxidize resulting in the thermite reaction progressing via the oxidation of $Al_3Zr$. This oxidation of $Al_3Zr$ is required to initiate the luminous reaction, allowing for the visualization of the two different reaction fronts.

## ACKNOWLEDGMENTS

Authors wish to thank Kevin McNesby and Nino Bonavito for their technical oversight. Funding was provided by the U.S. Army via the Chemical Biological Advanced Materials and Manufacturing Science Program (PE 0601102A Project VR9) at the Combat Capabilities Development Command Chemical Biological Center.

## REFERENCES


[1] Goldschmidt, H.; Weil, O. Method of manufacturing metals. US 895,628, **1905**.
[2] Deppeler, J.H. Rail joint welding of main line track by thermit process. *J. Weld*. **1929**, p 58.
[3] Monk, I.; Schoenitz, M.; Dreizin, E.L. The effect of heating rate on combustion of fully dense nanocomposite thermite particles. *Combust. Sci. Technol*. **2018**, *190* (2), pp 203–221.
[4] Glavier, L.; Taton, G.; Ducéré, J.-M.; Baijot, V.; Pinon, S.; Calais, T.; Estève, A.; Rouhani, M.D.; Rossi, C. Nanoenergetics as pressure generator for nontoxic impact primers: Comparison of Al/$Bi_2O_3$, Al/CuO, Al/$MoO_3$ nanothermites and Al/PTFE. *Combust. Flam.* **2015**, *162* (5), pp 1813–1820.
[5] McCollum, J.; Pantoya, M.L.; Iacono, S.T. Catalyzing aluminum particle reactivity with a fluorine oligomer surface coating for energy generating applications. *J. Fluorine Chem.* **2015**, *180*, pp 265–271.
[6] Wu, T.; Zachariah, M.R. Silver ferrite: a superior oxidizer for thermite-driven biocidal nanoenergetic materials. *RSC Adv.* **2019**, *9*, pp 1831–1840.
[7] Fischer, S.H.; Grubelich, M.C. Theoretical energy release of thermites, intermetallics, and combustable metals. *24th Inter. Pyrotech. Sem.*, **1998**, Monterey, CA.
[8] Arlington, S.Q.; Neuhauser, T.; Short, M.; Woll, K.; LaVan, D.A.; Fritz, G.M.; Weihs, T.P. Leveraging high heating rates to attain desirable reaction products in Al/Zr/C nanocomposites. *Mater. Des.* **2023**, *225*, p 111514.
[9] Lakshman, S.V.; Gibbins, J.D.; Weihs, T.P. Evaluating the effect of microstructural refinement on the ignition of Al-Mg-Zr ball-milled powders. *Powder Technol*. **2021**, *379*, pp 447–456.
[10] Wainwright, E.R.; Weihs, T.P. Microstructure and ignition mechanisms of reactive aluminum-zirconium ball milled composite metal powders as a function of particle size. *J. Mater. Sci*. **2020**, *55*, pp 14243–14263.
[11] Polk, A.L.; Chintersingh, K.A.; Flickinger, M.R.; Valdes, E.R.; Gardner, W.L.; Weihs, T.P. Effect of composition and process control agents on the microstructure and ignition properties of ball-milled Al-Zr powders. *Powder Technol.* **2023**, *427*, p 118729.
[12] Hastings, D.; Schoenitz, M.; Dreizin, E.L. Highly reactive spheroidal milled aluminum. *Mater.* **2021**, *15*, p 100959.
[13] Lustman, B.; Kerze, F. *The Metallurgy of Zirconium;* McGraw-Hill Book Company, **1955**.
[14] Dreizin, E.L.; Schoentiz, M. Mechanochemically prepared reactive and energetic materials: a review. *J. Mater. Sci.* **2017**, *52*, pp 11789–11809.
[15] Suryanarayana, C. Mechanical alloying and milling. *Prog. Mater. Sci.* **2001**, *46* (1–2), pp 1–184.
[16] Dreizin, E.L.; Schoenitz, M. Reactive and Metastable Nanomaterials Prepared by Mechanical Milling. In *Metal Nanopowders: Production, Characterization, and Energetic Applications.* 1st ed.; Gromov, A.; Teipel, U., Eds.; Wiley-VCH, 2014; pp 227–278.
[17] Weismiller, M.R.; Lee, J.G.; Yetter, R.A. Temperature measurements of Al containing nano-thermite reactions using multi-wavelength pyrometry. *Proc. Combust. Inst*. **2011**, *33* (2), pp 1933–1940.
[18] Ng, D.; Fralick, G. Use of a multiwavelength pyrometer in several elevated temperature aerospace applications. *Rev. Sci. Instrum.* **2001**, *72* (2), pp 1522–1530.
[19] Bazyn, T.; Krier, H.; Glumac, N. Evidence for the transition from the diffusion-limit in aluminum particle combustion. *Proc. Combust. Inst.* **2007**, *31* (2), pp 2021–2028.
[20] Moore, D.S.; Son, S.F.; Asay, B.W. Time-Resolved Spectral Emission of Deflagrating Nano-Al and Nano-$MoO_3$ Metastable Interstitial Composites. *Propel., Explos., Pyrotech.* **2004**, *29* (2), pp 106–111.
[21] Goroshin, S.; Mamen, J.; Higgins, A.; Bazyn, T.; Glumac, N.; Krier, H. Emission spectroscopy of flame fronts in aluminum suspensions. *Proc. Combust. Inst*. **2007**, *31* (2), pp 2011–2019.
[22] Yetter, R.A.; Risha, G. A.; Son, S.F. Metal particle combustion and nanotechnology. *Proc. Combust. Inst.* **2009**, *32* (2), pp 1819–1838.
[23] Dreizin, E.L. Metal-based reactive nanomaterials. *Prog. Energy Combust. Sci.* **2009**, *35* (2), pp 141–167.
[24] Schneider, C.A.; Rasband, W.S.; Eliceiri, K.W. NIH Image to ImageJ: 25 years of image analysis. *Nat. Methods*. **2012**, *9* (7), pp 671–675.
[25] Parker, G.R.; Asay, B.W.; Dickson, P. M. Note: A technique to capture and compose streak images of explosive events with unpredictable timing. *Rev. Sci. Instrum.* **2010**, *81* (1), p 016109.
[26] Fried, L.E. *Cheetah 1.0 users manual*; UCRL-MA-117541;. Lawrence Livermore National Lab: Livermore, CA, **1994**.

# Functionalization of polymer fibers and particles via incorporation of cell-free protein synthesis

Jennifer A. Lee[a,b]*, Susan K. Kozawa[a,c], John R. Biondo[a,d], Kristian M. Van de Voorde[a], Anne Y. Walker[a], Ava B. Darling[a], Tahiyah Brinkley[a], Barbara Hayes[a], Matthew W. Lux[a], Marilyn S. Lee[a]*

[a]U.S. Army Combat Capabilities Development Command Chemical Biological Center, Research & Operations Directorate, 8198 Blackhawk Rd, Aberdeen Proving Ground, MD 21010

[b]Defense Threat Reduction Agency, 2800 Bush River Rd, Gunpowder MD 21010

[c]Oak Ridge Institute for Science and Education, 1299 Bethel Valley Rd, Oak Ridge, TN 37830

[d]Excet Inc., 6225 Brandon Ave, Suite 360, Springfield, VA 22150

## ABSTRACT

Envisioned smart materials integrate sensing and computation functions to signal the presence of a hazard, decontaminate, or change physical properties in response to stimuli. Equipment with smart materials could expand functionality while reducing size, weight, and power requirements. Cell-free protein synthesis (CFPS) technology presents a novel way to deliver synthetic biology functions with DNA-programmable control to polymeric form factors as CFPS reagents are stable to polymer casting conditions. In addition, polymers can impact the function of CFPS reactions by providing a protective matrix and controlling exposure to water that affects activation and shelf stability. Polymer fibers created by spinning techniques create high performance materials while particles can protect delicate cargo for delivery capabilities or incorporation into other materials. In this work, we incorporate CFPS reactions into the fabrication of polymer fibers and particles to understand how morphology of the polymer bio-composite affects CFPS shelf-life and function. Solution blow spinning is used to prepare CFPS-encapsulating fibers with several types of polymers and synthesis of fluorescent or colorimetric reporter proteins is demonstrated in fibers. The fiber spinning process is optimized and validated for CFPS activity with reduced loading of costly bio-reagent cargo and several methods for preparing CFPS-polymer particles are tested.

**Keywords:** cell-free protein synthesis, polymers, fibers, particles

## 1. INTRODUCTION

High performance polymers are a critical class of materials integrated into essential gear for the warfighter, including protective barriers in clothing, filters, masks, wipes, and coatings that defend from harmful chemical and biological agents. These materials are often formed from spun fibers to achieve both strong and resilient physical properties, high surface area to trap contaminants, and controlled porosity for breathability or fluid flow. Innovation in the field of smart materials has achieved much to craft polymers with dynamic properties like mechanical response to light, pH, redox or small molecules, self-cleavage or self-repair, or catalytic composites that degrade contaminants.[1–3] Despite their versatility, the field has yet to design "smart materials" that possess both useful mechanical characteristics and dynamic functions that could enable equipment to alert and protect the warfighter against threats.

Recently, researchers have begun to harness synthetic biology and embed DNA-programmable microorganisms within materials.[4,5] Microbes can produce biomolecules that perform all types of functions, including agent sensing with visual outputs, chemical catalysis to break down threats, or production of structural materials. However, the stability of live organisms can prevent the incorporation of microbes into polymers, which can require organic solvents, heat, or radical polymerization. Previous work demonstrated cell-free systems offer a solution to this problem.[6,7] Cell-free protein synthesis (CFPS) reactions utilize crude microbial lysates to enact DNA-programmed functions outside of a living cell.[8] Compared to live cells and purified proteins, CFPS systems are unusually stable where CFPS activity is maintained after freeze-drying and exposure to certain polymer casting conditions.[6,9] When CFPS-polymer composites are exposed to water, freeze dried CFPS reagents are re-activated *in situ* to produce sensor gene circuits and functional antimicrobial proteins.[6] Thus far, CFPS-polymer composites have only been demonstrated in a film format using

poly lactic-co-glycolic acid and polycaprolactone (PCL) polymers. From this work, solvent screens uncovered solvent compatibility limitations that reduce the range of compatible polymers. Further, the geometry of the cast, distribution of CFPS components, and chemical identity and crystallinity of the polymer can all influence gene expression and water infiltration within the CFPS-polymer unit.[7] It is important to investigate these effects to approach a design with optimal mechanical and bio-activation characteristics.

Addressing this challenge, this work develops methods to cast CFPS-polymers into fiber and particle morphologies, with the aim of studying the effects of cast geometry on CFPS activity. We hypothesize that fiber and particle geometries can be tuned to control reactivation dynamics. In this study we used solution blow spinning (SBS), a straightforward, scalable, and economical method in which high speed air jets pull polymer solutions into nonwoven, fiber mats.[10] Because SBS only requires a polymer solution with a volatile solvent, fewer variables will interfere with the function of the CFPS system in comparison to other spinning techniques.

Polymer particles may act as a protective carrier to allow processing with solvents, UV, or other conditions that are incompatible with CFPS activity if applied directly. Particles with encapsulated CFPS have been generated using lipid vesicles.[11-13] Similar vesicles might be formed using synthetic polymers instead of lipids.[12,14] CFPS vesicle preparations have not yet been shown to tolerate lyophilization or encapsulation within a larger polymer matrix – so a deeper understanding is necessary to determine if vesicle-type particles are applicable to smart materials. SBS parameters can also be tailored to induce spraying into droplets for CFPS-polymer particles.

Here, multiple methods to produce fibers with CFPS activity via SBS and efforts to characterize different CFPS-polymer formulations for morphology, composition, and activity are described. Results show CFPS loaded in polymer films and fibers can be reduced while still observing protein synthesis activity localized to pockets within the larger polymer phase. Particle generation is approached via both polymer vesicles and solution spraying methods.

## 2. RESULTS AND DISCUSSION

### 2.1 Polymer selection

Polymers were chosen for this study based on three factors: solvent compatibility with CFPS, amenability of the polymer solution to SBS, and having a range of polymer properties. Previous studies screened solvents for compatibility with CFPS activity and revealed that some solvents allow CFPS to perform well (acetonitrile, ethyl acetate, dichloromethane, acetone, chloroform, and THF) while others decrease or completely inactivate protein synthesis (DMF, methanol, ethanol, dimethyl sulfoxide). Further, while water could be used as a solvent, lyophilized CFPS reactions are activated by water rehydration, thus polymer processing would need to be done at low temperatures (~4°C) and within time limits of ~1 hour to limit the progression of the CFPS reaction. With these conditions in mind we chose polymers with which we had previous experience (PCL), with a range of physical properties (polyethylene oxide (PEO) and poly(vinylidene fluoride-co-hexafluoropropylene) (PVDF-co-HFP)), that could be spun in CFPS compatible solvents (acetone and $CHCl_3$). These polymer properties are depicted below (Table 1).

**Table 1. Selection of polymers for testing SBS fibers encapsulating CFPS.**

| Polymer | Melting Pt (°C) | $T_g$ (°C) | Crystallinity (%) | Properties | Applications |
|---|---|---|---|---|---|
| **PVDF-HFP** | 140–145* | -62[15] | 28[16] | Semi-crystalline, thermoplastic, hydrophobic, chemical resistant, flexible | Turf fields, membranes, batteries, chromatography columns |
| **PCL** | 55–64[17] | -60[17] | 40–60[18] | Biodegradable, biocompatible, semi-crystalline | Tissue engineering, medical, drug delivery |
| **PEO** | 61–66* | -50[19] | 60–80[20] | Hydrophilic, linear, biocompatible, water soluble | Medical, drug delivery, thickeners, lubrication aids |

**According to manufacturer*

### 2.2 Reduced CFPS loading in polymer films and fibers

One of the primary drawbacks of applying CFPS reactions in materials is the cost of reagents. In typical lab studies, reactions are prepared on a microliter scale, yet fiber spinning experiments require CFPS preparations on the milliliter

scale or more. To offset some of this cost, we tested the effect of reducing CFPS loading in polymer films on activity. Loading tests were performed in PCL films (12 wt% in acetone). The ratio of CFPS to polymer solution was varied between 1:3 to 1:40 in a series of films cast with CFPS expressing the mRuby fluorescent protein (representative dilutions between 1:3 to 1:20 shown in Figure 1). Using microscopy, mRuby fluorescence was detected in all dilution ratios as discrete pockets of activity that become sparser as CFPS reagents are diluted in the polymer. Interestingly, films with higher loading of CFPS cargo also show increased clouding, as observed by the films' dark appearance by differential interference contrast (DIC) microscopy. This could be a result of increased amounts of CFPS providing more pathways for water to infiltrate, causing rapid hydrolysis in the PCL. Reduced CFPS loading was also tested in PCL fibers (not shown), and a 1:5 ratio was adopted for many of the follow-on experiments described here.

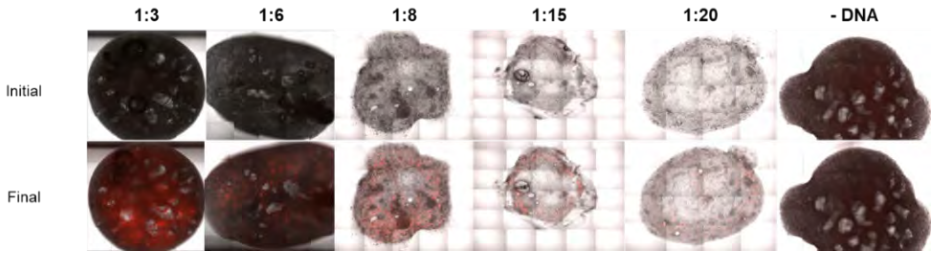


**Figure 1. Reduced CFPS loading in PCL films.**

### 2.3 Process development and characterization of SBS fibers

There were several challenges transitioning CFPS-polymer composites from poly lactic-co-glycolic acid films to fibers made from other polymers (Figure 2). First, the CFPS reaction preparations were scaled from microliter quantities to several milliliter quantities per batch. Second, a glass tissue homogenizer was used to grind lyophilized components in the presence of solvent to achieve a suspension with particle sizes small enough to flow through the needle (18 gauge) fitted to the SBS instrument. Lastly, fiber samples were collected by spinning directly onto a substrate appropriate for characterization. For example, fibers were spun onto glass coverslips for fluorescence microscopy and onto an N95 mask for application demonstrations. For microscopy imaging, the polymers tended to drift when CFPS was activated with water, thus polymer samples had to be immobilized using either an overlay of 1% agarose hydrogel or by placing a washer weight and coverslip atop the fiber mat.

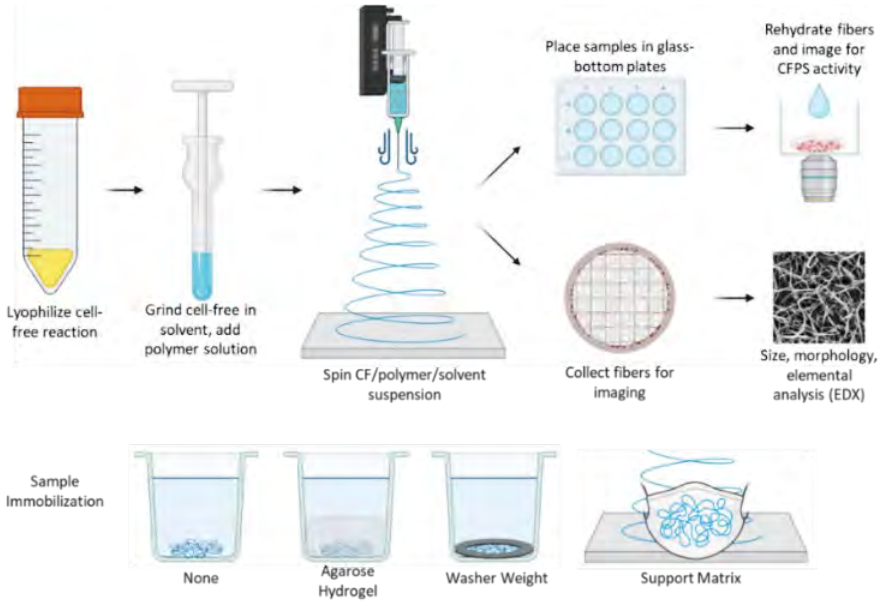


**Figure 2. Diagram of CFPS-polymer spinning and characterization process.**

The diameter and elemental composition of spun CFPS-polymer fibers were measured via SEM, energy dispersive X-ray spectroscopy (EDX), and DIC microscopy (Figure 3). Average fiber diameters were all less than 10 µm, with PCL having greater variability than PEO or PVDF-HFP. Some beading was observed across polymer types due to the

inclusion of larger CFPS particles. EDX elemental analysis shows elevated nitrogen and potassium levels in fibers with encapsulated CFPS compared to fibers composed of pure polymer.

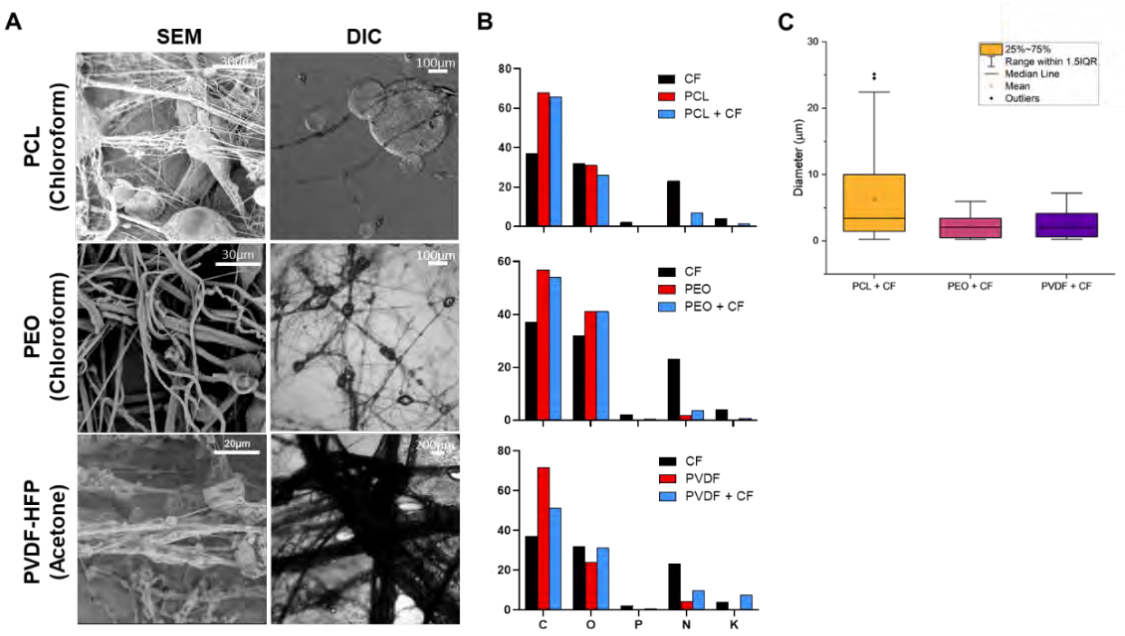


**Figure 3. Fiber morphology and composition. (A) SEM (left) and DIC microscopy (right) of fibers spun with 5 wt% polymer and encapsulated CFPS. (B) EDX elemental analysis showing weight concentrations of each element with symbol on the x-axis. (C) Fiber diameter measurements for each polymer.**

The protein synthesis activity of the fibers is determined by the DNA added. Thus far, we have tested constitutive production of colorimetric reporter enzyme β-gal (Figure 4) and fluorescent protein mRuby (Figure 5), both of which were encoded within a DNA plasmid with a T7 promoter. β-gal converts the yellow dye chlorophenol red-b-D-galactopyranoside (CPRG) to a purple color. For β-gal expression, PCL fibers with embedded CFPS powder were tested both on an N95 mask as a support and alone. After rehydrating the fibers with water containing CPRG, the first signs of color change were observed after 30 minutes. Color change continued to darken the solution over several hours. The supernatant was removed from the PCL fibers to show color change in the supernatant solution, as well as slight color change of the fibers (Figure 4D). Endpoint conversion of CPRG in supernatant samples is quantified by plate reader absorbance measurements (Figure 4C, E).

The red fluorescent protein mRuby was also produced by CFPS embedded in PCL and PVDF-HFP fibers (Figure 5A–C). Mean grey value for fluorescence intensity is quantified for two different regions of interest for the PVDF-HFP fiber experiment (Figure 5D). Further work is required to quantify and compare fluorescence intensity to background values found in fibers that don't contain DNA. Background fluorescence and light scattering can problematically change over time in microscopy measurements of the fiber mats, indicating the colorimetric reporter may be better suited for quantifying protein synthesis without confounding factors.

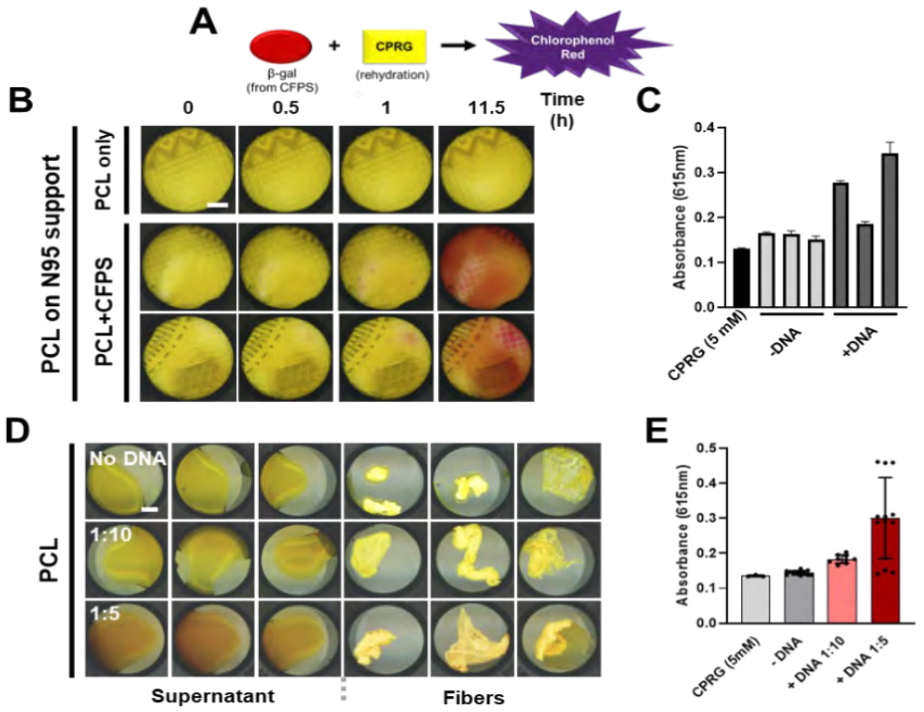


**Figure 2. CFPS of colorimetric reporter in fibers. (A) CFPS production of β-gal enzyme in PCL fibers converts yellow CPRG dye to a purple color. (B) Color change is observed from PCL fibers spun onto an N95 mask support material (C) Absorbance is quantified for samples run during experiment (B). (D) PCL fibers alone with CFPS loading varied from 1:5 to 1:10, and a negative control with No DNA and 1:5 loading. (E) Absorbance is quantified for samples shown in (D). All scale bars shown indicate 5 mm.**

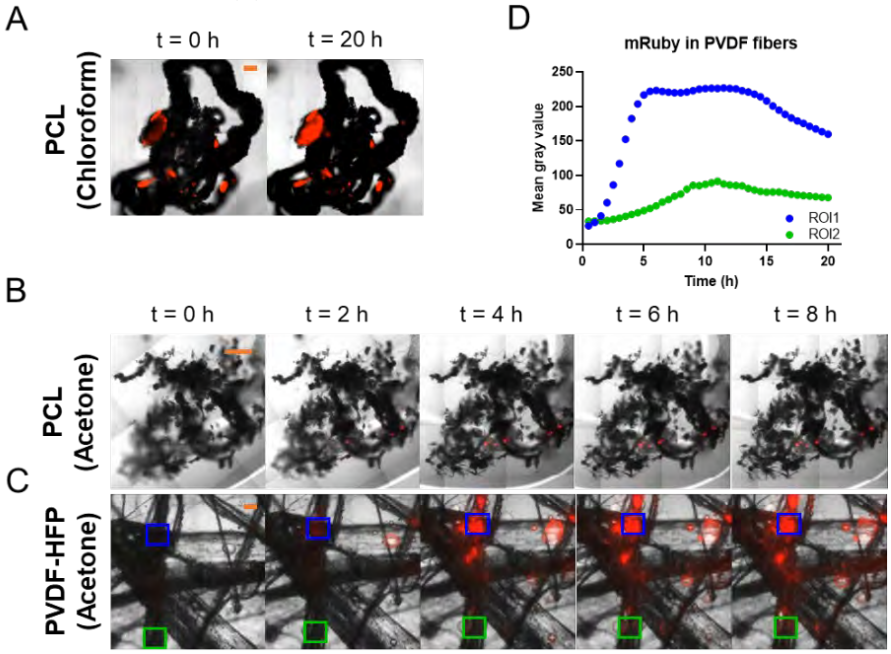


**Figure 3. Fluorescent protein production in fibers. Merged DIC and mRuby microscopy images over time for several CFPS-polymer formulations. (A) PCL cast from 6 wt% PCL in chloroform with 1:5 CFPS loading, scale bar is 500 µm. (B) PCL cast from 5 wt% PCL in acetone with 1:5 CFPS loading, scale bar is 500 µm. (C) PVDF-HFP from 5 wt% solution in acetone with 1:5 CFPS loading. Scale bars represent 200 µm. (D) Quantification of mean gray value (fluorescence intensity) over time in the regions of interest (ROI) 1 and 2 boxed in blue and green in (C).**

### 2.4 Solution spray CFPS-polymer particles

CFPS-polymer particles were fabricated by adapting similar concepts to SBS (Figure 6). PCL in acetone (5 wt %) with a 1:3 CFPS dilution was used. Sprayed particles collected on foil created flat disc shaped particles as the solvent did not have enough time to evaporate prior to collection. Sprayed particles were then collected in polyalphaolefin (PAO) to preserve their 3D shape. Further optimization is needed as the morphology of the particles are nonuniform and include defects indicating uneven solvent evaporation.

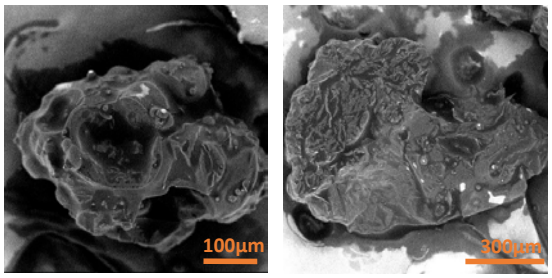


**Figure 4. Solution blow sprayed CFPS-polymer particles. SEM images of particles depict the uneven surface indicating poor solution evaporation and/or impact of particle in PAO causing defects.**

### 2.5 CFPS encapsulation in diblock copolymer vesicles

Aqueous CFPS can also be encapsulated into vesicles. Vesicles can be formed by emulsion methods and are delimited by surfactant-type molecules with both polar and non-polar groups to interact with aqueous and oil liquid phases. In biology, vesicles are made from lipids like the cellular membrane, however, synthetic vesicles (polymersomes) can be made with amphiphilic block copolymers which can be designed with stronger stability than typical lipid vesicles. Polymer vesicles have previously been used before encapsulate CFPS[12] and were used to encapsulate CFPS in similar vesicles and assess the ability to incorporate the vesicles within a polymer matrix. Diblock copolymers with a PEO hydrophilic block and a poly(butadiene) (PBD) hydrophobic block were used and the effect of increasing chain lengths was evaluated. Emulsion vesicle preparations made from these polymers were called E1 ($PEO_9$-b-$PBD_{12}$), E2 ($PEO_{16}$-b-$PBD_{20}$), and E3 ($PEO_{34}$-b-$PBD_{40}$). Because the time scales and temperatures necessary to cast polymers were too harsh for aqueous CFPS reactions, a lyophilized vesicle formulation was used.

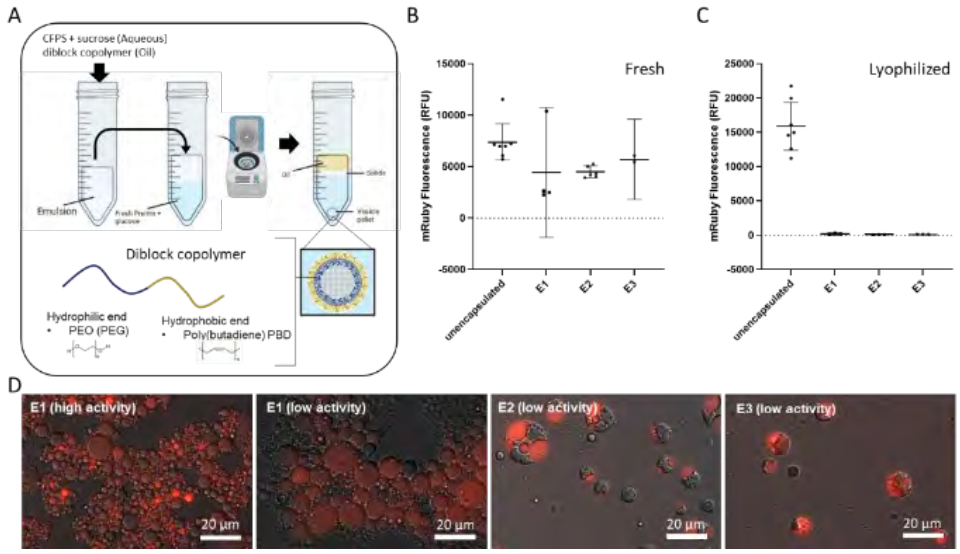


**Figure 5. CFPS encapsulation in diblock copolymer vesicles. (A) Diagram of vesicle encapsulation process with PEO-PBD diblock copolymer. (B) Plate reader quantification of mRuby fluorescence produced from freshly prepared unencapsulated or vesicle encapsulated CFPS. E1, E2, and E3 are vesicle preparations derived from three batches of diblock copolymer with increasing chain lengths. (C) Plate reader quantification of mRuby fluorescence produced from samples that have been lyophilized and rehydrated. (D) Fluorescence microscopy depicting vesicle morphology and localized mRuby produced via CFPS in diblock copolymer vesicle preparations E1-3 (same samples quantified in (B)).**

Aqueous CFPS reaction solution containing added sucrose was prepared and block copolymers were each dissolved in mineral oil (Figure 6A). The oil solution was layered over the CFPS and vortexed to form an emulsion then layered over an outer aqueous phase and centrifuged to collect vesicles in a pellet. mRuby fluorescent protein expression was used to assess the activity of encapsulated CFPS in freshly prepared vesicles and after lyophilizing the vesicles and rehydrating with water (Figure 6B and 6C). Vesicle samples produced mRuby fluorescence, but the signal developed slower in encapsulated samples. However, the 20 h endpoints indicate only slightly decreased productivity for vesicle samples compared to free reactions. Unfortunately, while the free reaction retains robust mRuby productivity after lyophilization, all vesicle samples were inactive. This indicates the vesicles are not stable and disruption of the membrane during freezing and drying could destabilize proteins and deactivate the CFPS components.

Fluorescence microscopy of freshly prepared vesicles was used to examine mRuby localization and vesicle morphology (Figure 6D). Because no size selection or extrusion was used during the process, vesicles of many sizes were observed, some of which were agglomerated or not well-formed. mRuby fluorescence signal can be observed localized to vesicle structures. However, there is some concern that CFPS may be producing mRuby outside of the vesicles, with mRuby adsorbing to the vesicles. Further control experiments are required to confirm true encapsulation of active CFPS and tests with lyo-protectant additives are needed to seek stabilization of vesicles during lyophilization.

## 3. METHODOLOGY

### 3.1 Reagent and DNA sources

Unless otherwise noted, reagents were purchased from Millipore Sigma, St. Louis, MO. A PY71sfGFP plasmid (Genbank MT346027) template was utilized for T7-polymerase driven expression of sfGFP via CFPS.[21] The mRuby sequence was inserted in place of sfGFP on the same plasmid backbone (PY71mRuby) for production of red fluorescence. Likewise, a PY71 plasmid was used for constitutive expression of β-gal (aka LacZ) with a β-gal insert.[22] Plasmid DNA was purified from transformed *E. coli* using a Promega PureYield plasmid midiprep kit, followed by ethanol precipitation, or by a Qiagen gigaprep kit without additional purification.

### 3.2 Preparation of CFPS reaction mixtures and lyophilization

*E. coli* lysates were prepared from a ΔlacZα derivative of Rosetta 2 (DE3) *E. coli* (Novagen) grown in a 100 L culture scaled up from a flask culture method described previously.[23] Cultures were grown in 2xYPTG media starting from agar plates, transferred to a 1.5 L starter culture, then to a 150 L fermenter (New Brunswick Scientific). Cultures were seeded in the fermenter at an $OD_{600}$ of 0.05 and incubated at 37 °C, 300 rpm, with 50 standard liter per minute air flow. The production of T7 RNA polymerase was induced by addition of 1 mM isopropyl ß-D-1-thiogalactopyranoside when the culture in the fermenter reached $OD_{600}$ 0.6–1.0. When dissolved oxygen levels reached 50 %, the impeller speed was increased to 500 rpm. Once the $OD_{600}$ reached 3.5, cells are cooled to 4 °C, pelleted by bowl centrifuge over 8 h (powerfuge pilot, 1.1 L bowl, CARR Biosystems), and frozen at -80 °C. Pellet material was later thawed and resuspended in buffer S30B at 1 mL per gram wet cell weight as described previously.[9] Lysis was performed by homogenization in one pass using a Microfluidizer (Microfluidics M-110P) at 15,000 psi. Lysate is clarified by centrifugation at 12,000 x g for 10 min, followed by 37 °C runoff reaction with shaking, and a second clarification step. Dialysis was then performed in 250 mL dialysis flasks in 5 gal buckets of S30B buffer. A third clarification step was performed, with the supernatant product aliquoted and flash frozen by liquid nitrogen before storage at -80 °C.

CFPS reactions contained 30% v/v lysate and additional reagents following the PANOx-sp recipe as described in detail previously.[9] mRuby or β-gal plasmid DNA is added at a concentration of 10 ng/uL while an equivalent volume of water is added for no DNA controls. After mixing, CFPS reactions were either used in vesicle encapsulation preparations as described below or lyophilized for polymer film, spinning, and solvent spray particle formation experiments. For films, reactions were lyophilized in 10–20 µL volumes in 1.5 mL snap cap tubes. For spinning fibers and spraying particles, reactions were typically dried in batches of 1–5 mL in glass vials, 15 or 50 mL falcon tubes, or in a 30 mL polypropylene luer lock syringe. Reaction solutions are flash frozen in liquid nitrogen, then dried using a shelf-type lyophilizer (SP Scientific, VirTis Wizard 2.0) with a primary overnight drying step at shelf temperature-20 °C. A secondary drying step of at least 2 hours with shelf temperature at 15 °C was then conducted. In larger samples, drying progress can be monitored by temperature probe as the sample temperature equilibrates at or above the shelf set point when each drying phase is complete. After removal from the lyophilizer, CFPS powders were stored for minimal time in a desiccator at room temperature, if necessary, prior to treatment or rehydration.

### 3.3 Solution blow spinning

Solution blow spinning was completed using a system acquired from the Nonwovens Institute (NC State University, Raleigh, NC). Lyophilized CFPS powders were added to solvent at ratios indicated for each experiment and ground into a fine suspension using a Tenbroeck tissue homogenizer. The CFPS/solvent suspension was then used to dilute a solution of polymer/solvent to the desired final polymer concentration. Polymers used in this report include poly(vinylidene fluoride-co-hexafluoropropylene) (Mw 455,000, 427179-100G, Aldrich), polycaprolactone (Mn ~80,000, 440744-500G, Aldrich), and polyethylene oxide (Mv 100,000, 181986-250G, Aldrich). The CFPS/polymer solution was transferred to a 5 mL syringe (14-823-16D, BD 301027, Fisher Scientific) and placed on a syringe pump (New era pump systems, Farmingdale, NY) at a flow rate of 0.3 ml/min. Compressed air (40–45 psi) was used to pull CFPS/polymer solutions through a blunt end, 2 inch 18-gauge needle (CU Innovations, Champaign, IL) suspended 250 mm above a perpendicular platform to form fibers. A surrounding cylinder or box confined the spun area to prevent any fibers from escaping the collection base. Fibers were captured on substrates specified for each experiment (foil, glass, or N95 mask) and either taken immediately for analysis or stored in a desiccator for shelf-life studies.

### 3.4 Polymer film casting

Polymer films were prepared as described in previous work.[6] The selected polymer is dissolved in an organic solvent as described for individual experiments. The polymer solution is added to the dried CFPS material and ground with a pestle. The CFPS:polymer ratio notation used in the text is the volume ratio of CFPS solution prior to drying compared to the volume of polymer solution added. The suspension (10 µL) is dropped into coverslip-bottom well plates. Polymer films form as solvent evaporates. Films were activated when 200 µL of nuclease free water was added to each well and slides were imaged by microscope as described below.

### 3.5 Solution spray CFPS-polymer particles

Solution spray CFPS-polymer particles were fabricated using a Master Airbrush, model G233, with air compressor attached. The CFPS-polymer solution was prepared as described in section 3.3. The solution was then poured into the fluid cup of the airbrush and sprayed at a downward angle towards a collection vessel. Particles were collected on foil or particles were sprayed into a solution of poly alpha olefin (PAO) (DCS 121120, Air Techniques International, Owings Mills, MD). Particles collected in PAO were filtered (Whatman 42, 1442-125) and washed with ethanol.

### 3.6 Diblock copolymer vesicle preparation

Diblock copolymers were purchased from Polymer Source, Inc. (Dorval, Canada): $PEO_9$-b-$PBD_{12}$ (P43810-BdEO), $PEO_{16}$-b-$PBD_{20}$ (P41721A-BdEO), and $PEO_{34}$-b-$PBD_{40}$ (P10951-BdEO). Each polymer is dissolved at 25 mM in 200 µL chloroform in a 1.5 mL snap-cap tube. The tube is rolled to coat the sides with polymer. Compressed air was used in the hood to accelerate solvent evaporation, followed by application of vacuum for 4 h. Mineral oil (200 µL) was added to the dry polymers and incubated at 80 °C for 30 minutes, vortexed for 10 seconds, and cooled on ice. CFPS reaction solution with 10 ng/µL mRuby plasmid DNA is prepared on ice as described above, except sucrose is also added to a final concentration of 200 mM. An outer solution is prepared that contains all buffer components included in the CFPS reaction excluding lysate and DNA and contains added glucose at a final concentration of 200 mM. A total of 45 µL of inner CFPS solution was layered over 200 µL mineral oil solution, vortexed for 30 seconds, and kept on ice for 5 min. The emulsion was layered over 100 µL outer solution and incubated on ice for 5 min. The tube is centrifuged at 16k relative centrifugal force at 4 °C for 20 min. The vesicle pellet is transferred to a new tube and mixed with equal volume fresh outer solution and distributed into plates with 5 µL per well. The samples are monitored over 24 h in a plate reader for mRuby fluorescence before 2 µL endpoint samples from each well were placed between a glass microscope slide and a 1.5H glass coverslip for fluorescence microscopy imaging.

### 3.7 Fluorescence and colorimetric imaging and measurement

A Zeiss Axio Observer Z1 inverted microscope with an incubation cabinet, automated stage, and auto focusing was used to image fluorescent protein production in particles, films, and fibers. Images were captured with a Plan-Apochromat 10x/0.45 M27 objective or a Plan-Apochromat 63x/1.40 oil DIC M27 objective and an Axiocam 506 camera while samples were incubated at 37 °C. The light source was Colibri 7 with a 475 nm LED used for green fluorescence (sfGFP and background lysate signal) and a 567 nm LED for mRuby. Tiled time course images of each

sample were taken using DIC, sfGFP (ex: 480 nm, em: 505 nm, 9 % intensity), and mRuby (ex: 577, em: 603, 100 % intensity) channels. Fluorescent CFPS activity over time was analyzed using FIJI software.[24]

Images of CPRG color change were capture with an incubator scanner setup. Samples were rehydrated with 500 µL of 5 mM CPRG and incubated at 37 ℃ for 12 h. Images were taken every 30 minutes using an Epson Perfection V600 scanner placed inside of the incubator, with automated imaging controlled via custom software.[25]

A plate reader was used to measure the overall fluorescence of samples producing fluorescent proteins and also used to measure the absorbance of CPRG color change in samples producing β-gal. Samples are sealed in microplates with a polypropylene mat or adhesive plate seal and measured in a BioTek Synergy H1 or Neo2 microplate reader. Endpoint measurements were single timepoints without incubation and time course data is captured with incubation at 37 °C. Formation of mRuby fluorescence was monitored with ex/em: 558/605 nm with the extended gain setting. Endpoint absorbance measurements for CPRG color change were taken at 615 nm.

### 3.8 SEM/EDX

A Phenom ProX SEM/EDX instrument is used to image samples mounted on aluminum pedestals with double-sided carbon tape. The sample mounted pedestals were then sputter coated with gold using a sputter coater (108 Manual Sputter Coater, Ted Pella, Inc.) prior to imaging. Fiber diameter was quantified from the SEM images using the macro general image fiber tool (GIFT)[26] in the software FIJI.

## 4. CONCLUSIONS

Three types of polymer fibers were spun and tested according to their ability to permit CFPS activation. CFPS activity was successfully recovered in PCL and PVDF-HFP fibers produced via SBS. Improvements to the spinning and characterization process and validation of samples with reduced CFPS loading enable further experimentation. This work also featured progress toward the production of CFPS-polymer particles, though more experiments are needed to confirm protein synthesis activity in this format and begin testing incorporation of the particles into other polymer matrices. Other future work will include developing core-shell CFPS fibers with a coaxial SBS nozzle, continuing to improve fiber characterization, and assessing the different polymer formats for changes in shelf life and activity dynamics. Continued development will enable the application of CFPS and synthetic biology in smart materials.

## ACKNOWLEDGMENTS

Funding was provided by the U.S. Army via the Chemical Biological Advanced Materials and Manufacturing Science Program (PE 0601102A Project VR9) at the Combat Capabilities Development Command Chemical Biological Center. Special thanks to Katherine Rhea with assistance from the Biotechnology branch for supplying *E. coli* lysate and CFPS reagents.

## REFERENCES

[1] Png, Z.M.; Wang, C.-G.; Yeo, J.C.C.; Lee, J.J.C.; Surat'man, N.E.; Tan, Y.L.; Liu, H.; Wang, P.; Tan, B.H.; Xu, J.W.; Loh, X.J.; Zhu, Q. Stimuli-responsive structure–property switchable polymer materials. *Mol. Syst. Des. Eng.* **2023**, *8* (9), pp 1097–1129.

[2] Wang, S.; Urban, M.W. Self-healing polymers. *Nat. Rev. Mater.* **2020**, *5* (8), pp 562–583.

[3] Peterson, G.W.; Lee, D.T.; Barton, H.F.; Epps, T.H.; Parsons, G.N. Fibre-based composites from the integration of metal–organic frameworks and polymers. *Nat. Rev. Mater.* **2021**, *6* (7), pp 605–621.

[4] Tang, T.-C.; An, B.; Huang, Y.; Vasikaran, S.; Wang, Y.; Jiang, X.; Lu, T.K.; Zhong, C. Materials design by synthetic biology. *Nat. Rev. Mater.* **2020**, *6* (4), pp 332–350.

[5] Liu, A.P.; Appel, E.A.; Ashby, P.D.; Baker, B.M.; Franco, E.; Gu, L.; Haynes, K.; Joshi, N.S.; Kloxin, M.; Kouwer, P.H.J.; Mittal, J.; Morsut, L.; Noireaux, V.; Parekh, S.; Schulman, R.; Tang, S.K.Y.; Valentine, M.T.; Vega, S.L.; Weber, W.; Stephanopoulos, N.; Chaudhuri, O. The living interface between synthetic biology and biomaterial design. *Nat. Mater.* **2022**, *21* (4), pp 390–397.

[6] Lee, M.S.; Lee, J.A.; Biondo, J.R.; Lux, J.E.; Raig, R.M.; Berger, P.N.; Bernhards, C.B.; Kuhn, D.L.; Gupta, M.K.; Lux, M.W. Cell-free protein expression in polymer materials. *BioRxiv.* **2023**.
[7] Lee, M.S.; Lus, J.A.; Biondo, J.R.; Lux, J.; Kuhn, D.L.; Browe, M.A.; Gupta, M.K.; Lux, M.W. Extending Bio-Functionality in Materials via Controlled Polymer Erosion. *FY22 Proceedings of the U.S. Army Combat Capabilities Development Command Chemical Biological Center In-House Laboratory Independent Research and Chemical Biological Advanced Materials and Manufacturing Science Programs.* **2022**.
[8] Silverman, A.D.; Karim, A.S.; Jewett, M.C. Cell-free gene expression: an expanded repertoire of applications. *Nat. Rev. Genet.* **2020**, *21* (3), pp 151–170.
[9] Lee, M.S.; Raig, R.M.; Gupta, M.K.; Lux, M.W. Lyophilized Cell-Free Systems Display Tolerance to Organic Solvent Exposure. *ACS Synth. Biol.* **2020**, *9* (8), pp 1951–1957.
[10] Dadol, G.C.; Kilic, A.; Tijing, L.D.; Lim, K.J.A.; Cabatingan, L.K.; Tan, N.P.B.; Stojanovska, E.; Polat, Y. Solution blow spinning (SBS) and SBS-spun nanofibers: Materials, methods, and applications. *Mater. Today Commun.* **2020**, *25*, p 101656.
[11] Sharma, B.; Moghimianavval, H.; Hwang, S.W.; Liu, A.P. Synthetic Cell as a Platform for Understanding Membrane-Membrane Interactions. *Membranes (Basel).* **2021**, *11* (12), p 912.
[12] Boyd, M.A.; Thavarajah, W.; Lucks, J.B.; Kamat, N.P. Robust and tunable performance of a cell-free biosensor encapsulated in lipid vesicles. *Sci. Adv.* **2023**, *9* (1), p eadd6605.
[13] Gonzales, D.T.; Yandrapalli, N.; Robinson, T.; Zechner, C.; Tang, T.D. Cell-Free Gene Expression Dynamics in Synthetic Cell Populations. *ACS Synth. Biol.* **2022**, *11* (1), pp 205–215.
[14] Steinkuhler, J.; Jacobs, M.L.; Boyd, M.A.; Villasenor, C.G.; Loverde, S.M.; Kamat, N.P. PEO-b-PBD Diblock Copolymers Induce Packing Defects in Lipid/Hybrid Membranes and Improve Insertion Rates of Natively Folded Peptides. *Biomacromolecules.* **2022**, *23* (11), pp 4756–4765.
[15] Mouraliraman, D.; Shaji, N.; Praveen, S.; Nanthagopal, M.; Ho, C.W.; Varun Karthik, M.; Kim, T.; Lee, C.W. Thermally Stable PVDF-HFP-Based Gel Polymer Electrolytes for High-Performance Lithium-Ion Batteries. *Nanomaterials (Basel).* **2022**, *12* (7), p 1056.
[16] Wang, X.; Xiao, C.; Liu, H.; Huang, Q.; Hao, J.; Fu, H. Poly(vinylidene Fluoride-Hexafluoropropylene) Porous Membrane with Controllable Structure and Applications in Efficient Oil/Water Separation. *Materials (Basel).* **2018**, *11* (3), p 443.
[17] Piyasin, P.; Yensano, R.; Pinitsoontorn, S. Size-Controllable Melt-Electrospun Polycaprolactone (PCL) Fibers with a Sodium Chloride Additive. *Polymers (Basel).* **2019**, *11* (11), p 1768.
[18] Blazquez-Blazquez, E.; Perez, E.; Lorenzo, V.; Cerrada, M.L. Crystalline Characteristics and Their influence in the Mechanical Performance in Poly(epsilon-Caprolactone) / High Density Polyethylene Blends. *Polymers (Basel).* **2019**, *11* (11), p 1874.
[19] Polaskova, M.; Peer, P.; Cermak, R.; Ponizil, P. Effect of Thermal Treatment on Crystallinity of Poly(ethylene oxide) Electrospun Fibers. *Polymers (Basel).* **2019**, *11* (9), p 1384.
[20] St-Onge, V.; Cui, M.; Rochon, S.; Daigle, J.-C.; Claverie, J.P. Reducing crystallinity in solid polymer electrolytes for lithium-metal batteries via statistical copolymerization. *Commun. Mater.* **2021**, *2* (1), p 83.
[21] Bundy, B.C.; Swartz, J.R. Site-specific incorporation of p-propargyloxyphenylalanine in a cell-free environment for direct protein-protein click conjugation. *Bioconjug. Chem.* **2010**, *21* (2), pp 255–263.
[22] Blum, S.M.; Lee, M.S.; Mgboji, G.E.; Funk, V.L.; Beabout, K.; Harbaugh, S.V.; Roth, P.A.; Liem, A.T.; Miklos, A.E.; Emanuel, P.A.; Walper, S.A.; Chavez, J.L.; Lux, M.W. Impact of Porous Matrices and Concentration by Lyophilization on Cell-Free Expression. *ACS Synth. Biol.* **2021**, *10* (5), pp 1116–1131.
[23] Kwon, Y.C.; Jewett, M.C. High-throughput preparation methods of crude extract for robust cell-free protein synthesis. *Sci. Rep.* **2015**, *5*, p 8663.
[24] Schindelin, J.; Arganda-Carreras, I.; Frise, E.; Kaynig, V.; Longair, M.; Pietzsch, T.; Preibisch, S.; Rueden, C.; Saalfeld, S.; Schmid, B.; Tinevez, J.Y.; White, D.J.; Hartenstein, V.; Eliceiri, K.; Tomancak, P.; Cardona, A. Fiji: an open-source platform for biological-image analysis. *Nat. Methods.* **2012**, *9* (7), pp 676–682.
[25] Davidson, C.E.; Dixon, M.M.; Williams, B.R.; Kilper, G.K.; Lim, S.H.; Martino, R.A.; Rhodes, P.; Hulet, M.S.; Miles, R.W.; Samuels, A.C.; Emanuel, P.A.; Miklos, A.E. Detection of Chemical Warfare Agents by Colorimetric Sensor Arrays. *ACS Sens.* **2020**, *5* (4), pp 1102–1109.
[26] Götz, A.; Senz, V.; Schmidt, W.; Huling, J.; Grabow, N.; Illner, S. General image fiber tool: A concept for automated evaluation of fiber diameters in SEM images. *Measurement.* **2021**, *177*, p 109265.

# Janus metal organic framework micromotors for the efficient removal of chemical agents

Matthew D. Collins[a], Eric R. Languirand[a]*, Angus Unruh[b], Errie Gibson Parilla[b], Cecilia Phung[a], Nathanael Smith[b], Ayusman Sen[b]
[a]U.S. Army Combat Capabilities Development Command Chemical Biological Center, Research & Operations Directorate, 8198 Blackhawk Rd, Aberdeen Proving Ground, MD, 21010
[b]Department of Chemistry, Pennsylvania State University, 77 Pollock Rd, State College, PA, 16802

## ABSTRACT

Chemically powered micromotors are an active matter system that have been developed with potential DoD applications in chemical warfare agent decontamination. Specifically, active micromotors can increase the rate of chemical warfare agent decontamination through their movement compared to non-active decontamination particles limited by passive diffusion. In this work, we have functionalized Janus micromotors with UiO66 metal organic frameworks that have been previously shown to be effective at decontaminating chemical warfare agents because of their high porosity/surface area. In this report, we present our progress of characterizing the motion of bubble propelled Ag@UiO-66@$SiO_2$ and electrophoretic Pt@UiO-66@$SiO_2$ micromotors. Additionally, we show our results of the ability of the bubble propelled Ag@UiO-66@$SiO_2$ to decontaminate methyl paraoxon simulant with ultraviolet-visible analysis. The report continues with preliminary plasmon resonance results of the metal organic frameworks micromotors. Future work will explore further optimization of the metal organic framework micromotors, chemical warfare agent decontamination, and the ability of the metal organic framework-micromotors to detect chemical warfare agent decontamination using surface enhanced Raman spectroscopy. In this project, we seek to determine an optimal micromotor design for rapid and efficient chemical warfare agent decontamination.

**Keywords:** micromotors, active matter, Janus particles, metal organic frameworks, chemical warfare agent, decontamination

## 1. INTRODUCTION

The goal of this project is to create an active matter system for the rapid and efficient removal of hazardous chemical warfare agents (CWA). Most currently available systems for CWA neutralization are passive in that the decontamination particles must reach the CWA molecules by simple Brownian diffusion. In theory, the process can be sped up if the decontamination particles can move autonomously and actively "seek out" the CWA molecules. Creating mobile decontamination agents might be particularly beneficial in accelerating the rate of decontamination against CWA molecules embedded within surface micro cracks that are traditionally hard to reach for mitigation.

This potentially greater decontamination rate can be accomplished through an "active" system that can self-propel by harvesting energy locally. One type of active system is chemically powered micromotors, which have been developed over the last decade with potential applications in self-assembly, chemical sensing, and targeted drug delivery.[1–4] Additionally, these micromotors are beginning to be explored for possible DoD-related applications, such as CWA detection or decontamination.[5–7] Typically, these motors are asymmetric particles that catalyze a chemical reaction and convert the released chemical energy into directed mechanical motion.[3] The classic example is platinum/gold microrods that achieve motion by a generated proton gradient when adding hydrogen peroxide as fuel.[3,8] There are other types of catalytic motors that use other propulsion mechanisms such as metal/polymer Janus particles, metal/oxide photocatalytic motors, and enzyme-powered motors. Additionally, micromotors with metal-organic frameworks (MOFs) have started to be explored for water purification/nuclear waste removal.[9–12] Previously, MOFs on their own have shown great potential for rapid CWA decontamination due to their highly porous surface.[13,14] These prior works imply that combining these two research efforts into MOF-based micromotors can potentially be used for

the rapid and efficient decontamination of a broad spectrum of chemical agents, which has not been explored until now.

Specifically, the objective of this work is to synthesize a micromotor for organophosphate-based CWA decontamination by applying metal onto one hemisphere of the UiO-66@$SiO_2$ particles. The resulting Janus MOF micromotors have two faces: one side with Ag (or Pt) to achieve motion by catalytically decomposing hydrogen peroxide fuel and the other side with UiO-66 MOF with active sites to decontaminate CWA. We hypothesize that the Janus MOF micromotors will decontaminate CWA at a faster rate compared to non-active UiO-66 MOFs without any mechanical stirring. This report summarizes the current progress of our results, which is comprised of three main components: 1) MOF micromotor speed dependance on the movement mechanism, 2) MOF micromotor methyl paraoxon (DMNP) simulant decontamination with ultraviolet-visible light (UV-Vis), and 3) preliminary MOF micromotor surface-enhanced Raman spectroscopy (SERS) sensing results.

## 2. METHODOLOGY

### 2.1 Chemicals and materials

The base substrate particles used to synthesize the Ag@UiO-66@$SiO_2$ bubble micromotors were spherical 40–75 µm amine-functionalized silica beads (Millipore Sigma, 79297). For Ag@UiO-66@$SiO_2$ or Pt@UiO-66@$SiO_2$ electrophoretic micromotors, the base particles used were amine-functionalized silica beads that were 1 µm (Polysciences, 24757-1) or 5 µm (Polysciences, 24758-1). Next, the chemicals needed to synthesize UiO-66 MOFs onto the $SiO_2$ base substrate particles include N,N-Dimethyl formamide (DMF, Omnisolv, DX1726-6), glacial acetic acid (Fisher, A38-500), terephthalic acid (Thermo Scientific, 180722500), zirconium (IV) chloride (Millipore Sigma, 8089130250), and ethanol (Millipore Sigma, 459844). The metal sources that used to coat the UiO-66@$SiO_2$ substrate particles were either 1–3 mm silver shots (Millipore Sigma, 327050) or platinum metal targets (Ted Pella, 91114) to yield Ag@UiO-66@$SiO_2$ or Pt@UiO-66@$SiO_2$ micromotors. Other chemicals used include: methanol (Sigma Aldrich, 322415), deionized (DI) water (Neu-Ion), 30% hydrogen peroxide (Sigma Aldrich, H1009), sodium dodecyl sulfate (SDS) (Fisher Scientific, BP1311-1), Sodium Cholate (Sigma Aldrich, 229101), 4-ethyl morpholine (Millipore Sigma, 04500), commercial pH 10 fisher chemical brand buffer (fisher scientific, SB116-500), and methyl paraoxon (also known as DMNP, Millipore Sigma, 46192). All chemicals were used as received.

### 2.2 UiO-66@$SiO_2$ particle synthesis

The UiO-66@$SiO_2$ particles were synthesized according to a previous procedure.[15] Briefly, zirconium (IV) chloride (0.343 mmol, 0.80 g), amine-functionalized silica spheres (0.100 g), and 20 mL N,N-Dimethylformamide (DMF) were added to a 50 mL round bottom flask. The zirconium (IV) chloride was dissolved and stirred at room temperature for 3 hours. Terephthalic acid (0.343 mmol, 0.057 g), 10 mL DMF, and 1 mL 0.1 M acetic acid were added and stirred for 30 minutes. The resulting mixture was stirred while heated at 120 °C for 24 hours in a sand bath on top of a hot plate with a digital probe to track the temperature overtime. After cooling, the mixture was transferred to a 50 mL plastic Falcon tube using 5 mL DMF to rinse out the original round bottom flask. Next, the 50 mL plastic Falcon tube was centrifuged at 3000 rpm for 15 minutes. The supernatant was decanted and 7.5 mL DMF as well as 7.5 mL ethanol were added. The resulting mixture was initially vortexed, sonicated for 5 minutes, centrifuged, and the supernatant was decanted again. A total of 10 mL of ethanol was added and the previous step of vortexing, sonicating, centrifuging, and decanting the supernatant was repeated. After the final supernatant was decanted, 5 mL of ethanol was added to transfer the final product to a glass storage container.

### 2.3 Ag@UiO-66@$SiO_2$ (or Pt@UiO-66@$SiO_2$) micromotor synthesis

A schematic showing the synthetic steps to make either Ag@UiO-66@$SiO_2$ or Pt@UiO-66@micromotors can be seen in Figure 1. A shell of UiO-66 MOFs was synthesized on amino-functionalized $SiO_2$ microbeads to form UiO-66@$SiO_2$ particles according to Section 2.2 (Figure 1A). These UiO-66@$SiO_2$ particles were then suspended in methanol as a fast-evaporating solvent and drop casted on clean glass microscope slides to form an approximately monolayer of UiO-66@$SiO_2$ particles on the glass microscope slide when dried. Afterwards, as shown in the bottom portion of Figure 1, about 20 nm of Ag or Pt was deposited onto the UiO-66@$SiO_2$ particles with a Denton Explorer thermal evaporator or Cressington 208 HR sputter coater (80 mA current) for Pt. Microscope brushes were used to

suspend the micromotors into DI water. The micromotor sample was centrifuged and washed twice to result in the micromotor sample used in the following experiments.

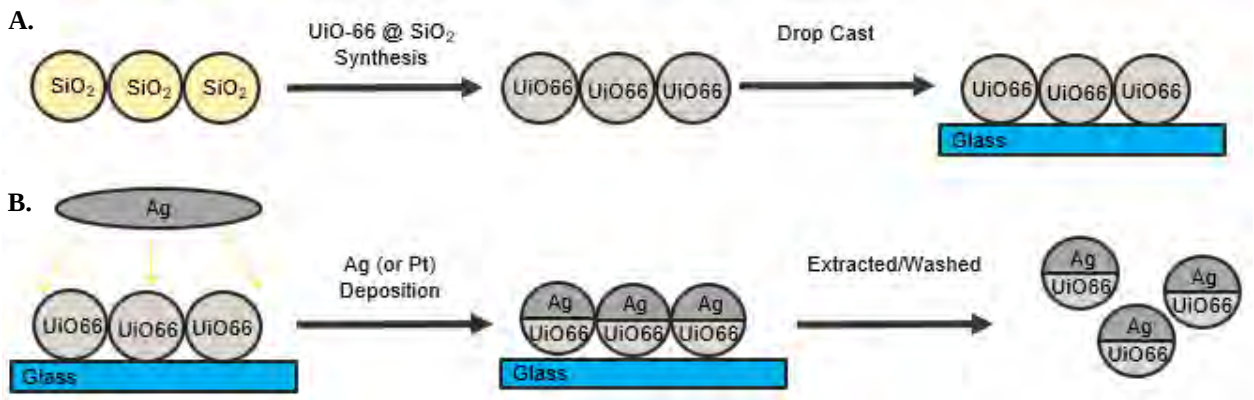


**Figure 1. Schematic showing the synthesis steps to make Ag@UiO-66@$SiO_2$ or Pt@UiO-66@$SiO_2$ micromotors. A) Step one is to synthesize UiO-66@$SiO_2$ particles. B) Step 2 is to coat the UiO-66@$SiO_2$ particles with silver (or platinum) metal to result in Ag@UiO-66@$SiO_2$ (or Pt@UiO-66@$SiO_2$) micromotors.**

### 2.4 Micromotor motion characterization

The motion of the micromotors was characterized in aqueous solution with a Keyence optical microscope. The micromotor sample of interest, hydrogen peroxide fuel, and any surfactant (only for bubble-propelled motors) were pipetted into a 1.5 mL Eppendorf tube. The solutions were mixed by vortex and/or sonication and 20 µL were placed on a clean glass microscope slide. Videos of the micromotors' motion were recorded at 15 fps. Self-electrophoretic motors were recorded with 1000 X at the solution/glass interface to prevent any observed fluid flows. The bubble-propelled motors were recorded at the air/solution interface for optimized viewing with 200 X magnification. All videos were tracked with Image J FIJI to record the position of each particle's center of mass between frames. The tracked data of the micromotors was used to calculate the trajectory of each particle as well as the average speed of each micromotor sample of interest.

### 2.5 MOF Micromotor UV-Vis simulant decontamination experiments

The decontamination of the simulant DMNP (methyl paraoxon) with the MOF micromotors under UV-Vis (Varian Cary 50 Conc UV-Visible Spectrophotometer) was conducted according to a modified procedure adapted from previous literature.[16,17] There were two methods used to evaluate simulant decontamination with the MOF micromotors: 1) spectral scan over a range of wavelengths, and 2) real-time kinetics at a set wavelength. For the first method of spectral scan over a range of wavelengths, a reaction vessel containing the experimental solutions of interest was prepared by adding 500 µL Ag@UiO-66@$SiO_2$ micromotors, 500 µL 26.5 % $H_2O_2$, 100 µL 10 % SDS surfactant, and 4 µL DMNP (0.025 mmol) with DI water as the solvent. At each measurement time point, 10 µL of this reaction mixture was placed in 5 mL of a buffer (pH 9.5 4-ethylmorpholine or pH 10 commercial Fisher Chemical brand buffer) and measured at 3 minutes after contact under UV-Vis with a standard 1 cm path length quartz cuvette under the wavelength range of 250–500 nm. For the second method of real time kinetics at a set wavelength, 1400 µL Ag@UiO-66@$SiO_2$ micromotors, 1500 µL 26.5 % $H_2O_2$, 100 µL pH10 commercial Fisher buffer, 300 µL 10 % SDS, and 12 uL 0.8 % DMNP were added to a standard 1 cm path length quartz cuvette. The reaction was monitored under UV-VIS in real time at the 400 nm wavelength every 3 seconds. Note that in both methods, the decontamination of the simulant DMNP is evaluated through the formation of the hydrolysis product 4-nitrophenol at the wavelength 400 nm.

## 3. RESULTS & DISCUSSION

### 3.1 MOF micromotor speed dependance on the movement mechanism

Depending on the size of the micromotor particle, different movement mechanisms are exhibited that lead to variation in the observed speeds. While all these micromotors are coated with a metal that catalytically decomposes hydrogen peroxide fuel to achieve motion, any micromotor particles that are less than 10 µm in size generally show an

electrophoretic movement mechanism while micromotor particles that are greater than 10 µm in size generally show a bubble propelled mechanism. The micromotor particle size was varied by using base substrate particles of different sizes in the initial micromotor synthesis process. In Figure 2, we compared the average speed of smaller 1 µm electrophoretic MOF micromotors to larger 40–75 µm bubble-propelled MOF micromotors when we varied the hydrogen peroxide fuel concentration. The speeds of bubble-propelled micromotors were recorded and observed to be approximately two orders of magnitude larger on average compared to the electrophoretic micromotors (Figure 2). While the electrophoretic micromotors are slower, their speeds are still significantly greater than Brownian diffusion. The faster speeds of the bubble propelled micromotors implies that they are better for CWA decontamination applications as the faster movement speed would lead to more interactions with any CWA present and therefore quicker decontamination. Also, note that the electrophoretic micromotors are coated with platinum while the bubble-propelled micromotors are coated with silver, which were dependent on what metal worked well for that size regime. The difference in metal does not affect the observed movement mechanism, which is dependent on micromotor particle size as previously discussed.

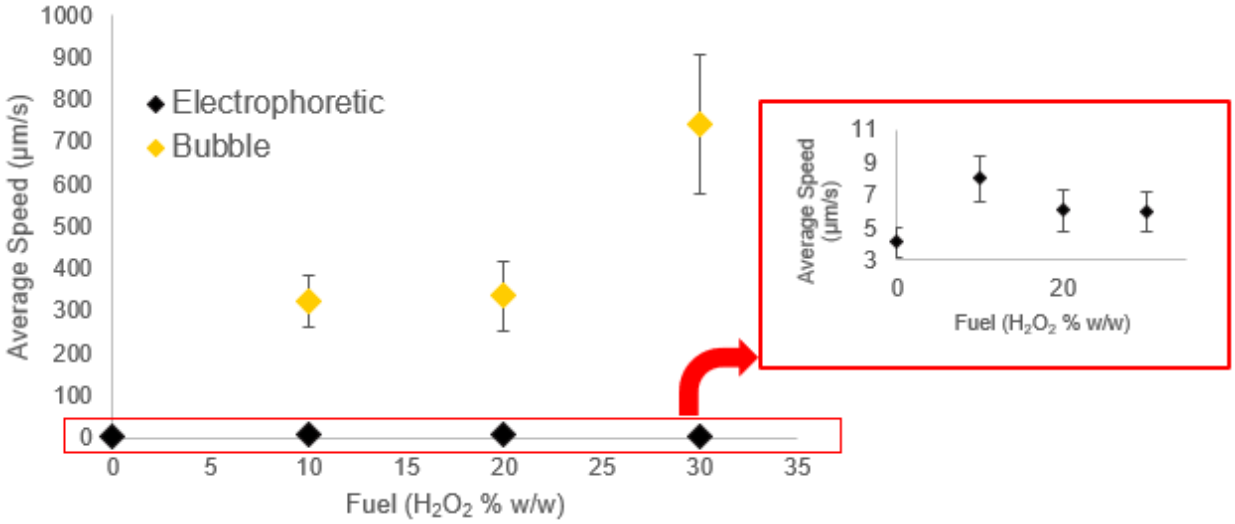


**Figure 2. Comparison of average speed vs hydrogen peroxide fuel concentration for electrophoretic and bubble propelled MOF micromotors. The inset displays the zoomed in speeds of the electrophoretic micromotors. In general, the bubble propelled micromotors display ~two orders of magnitude larger in average speed compared to the electrophoretic micromotors.**

### 3.2 MOF micromotor DMNP simulant decontamination with UV-Vis

We evaluated the ability of the bubble propelled Ag@UiO-66@$SiO_2$ micromotors to decontaminate DMNP simulant with multiple UV-Vis methods. The first method, spectral scan over a range of wavelengths, involved setting up a reaction mixture containing the micromotors, 12 % hydrogen peroxide fuel, 1 % SDS surfactant, 0.025 mmol DMNP, and DI water as the solvent. At each measurement time point, a 10 µL aliquot of the reaction mixture was mixed with 5 mL of base buffer to convert the p-NP hydrolysis product into a form that can be seen at 400 nm under UV-Vis absorbance. The p-NP hydrolysis product is shown to initially increase at a linear rate that can be approximated by 0-order kinetics with a line of best fit (Figure 3). After approximately 15 minutes, the observed p-NP hydrolysis product remains constant indicating a steady state has been reached. While the hydrolysis of DMNP can be viewed with this method, one disadvantage is that the base buffer and presumably the hydrogen peroxide fuel exhibit a side reaction that also cause DMNP hydrolysis, which makes properly standardizing this experimental method difficult to compare between different experiments.

To mitigate standardization of the experimental method, we ran these experiments with a second method of real-time kinetics at a set wavelength. In this other method, we ran the reaction with base buffer in a quartz cuvette so that the hydrolysis reaction could be monitored in real-time to view the formation of p-NP at 400 nm directly. The control-labeled DI water (orange; contains DI water, SDS, base buffer, DMNP) showed an initial hydrolysis rate of 0.0013 µM/min while the control labeled $H_2O_2$ (blue; contains, $H_2O_2$, DI water, SDS, base buffer, DMNP) showed an initial hydrolysis rate of 0.1234 µM/min (Figure 4). The experiment labeled motors + $H_2O_2$ (grey; contains micromotors, $H_2O_2$, SDS, base buffer, DMNP) showed an increased hydrolysis rate of 0.3694 µM/min, indicating a

faster decontamination rate with the micromotors present (Figure 4). Note that the motors + $H_2O_2$ line (grey) starts above the control experiments. The different starting location of the motors + $H_2O_2$ line is due to UV-Vis experiment monitoring having been started 25 minutes into the start of the decontamination reaction and the experiment contains higher DMNP concentration compared to the controls. This was necessary for the motors + $H_2O_2$ experiment to view the p-NP hydrolysis product peak over the bubbling caused by the micromotors movement reaction.

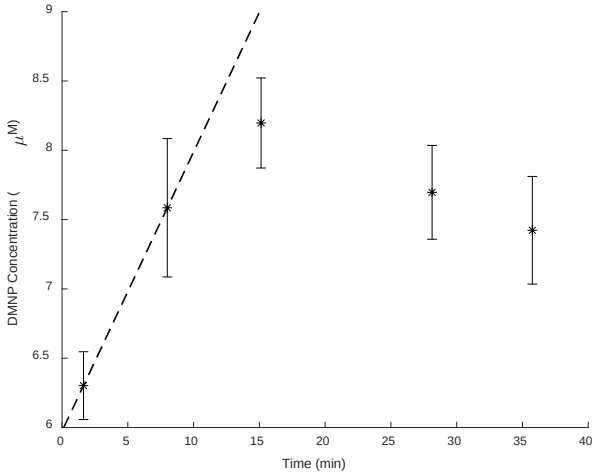


**Figure 3. The decontamination of DMNP with micromotors, 12 % hydrogen peroxide fuel, and 1 % SDS surfactant according to the first decontamination method: spectral scan over a range of wavelengths where a 10 µL aliquot of the reaction mixture is added to 5 mL of buffer before the UV-Vis measurement at each time point. This plot shows the formation of the p-NP hydrolysis product at 400 nm over time.**

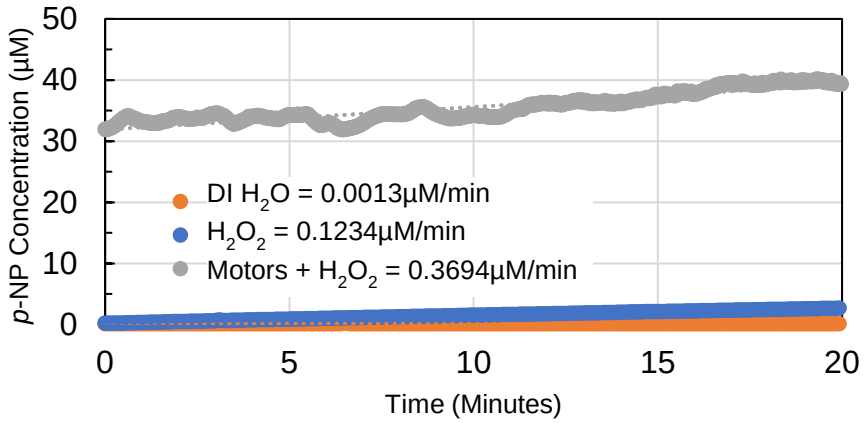


**Figure 4. The comparison of the decontamination rates of DMNP with motors + $H_2O_2$ (grey), $H_2O_2$ (blue), and DI $H_2O$ (orange) through real-time kinetics at a set wavelength the reaction mixture with buffer. The experimental control (labeled DI $H_2O$ in orange containing DI water, SDS, base buffer, and DMNP) showed an initial hydrolysis rate of 0.0013 µM/min while the control (labeled $H_2O_2$ and shown in blue, containing $H_2O_2$, DI water, SDS, base buffer, and DMNP) showed an initial hydrolysis rate of 0.1234 µM/min. The data labeled motors + $H_2O_2$ (shown in grey containing micromotors, $H_2O_2$, SDS, base buffer, and DMNP) showed an increased hydrolysis rate of 0.3694 µM/min, indicating a faster decontamination rate with the micromotors present.**

### 3.3 Preliminary MOF micromotor SERS sensing results

Because the bubble propelled Ag@UiO-66@$SiO_2$ contains a nanoscale roughened metallic surface caused by the Ag coated MOF, preliminary experiments were conducted to evaluate the MOF micromotors for potential SERS sensing. The Ag@UiO-66@$SiO_2$ (blue) exhibits a sharp plasmon resonance peak at 388 nm due to the nanoscale rough silver surface of the MOF micromotor particles (Figure 5). This plasmon resonance peak implies that these MOF micromotor particles may be able to simultaneously sense CWA (and its decontamination product) while performing decontamination.

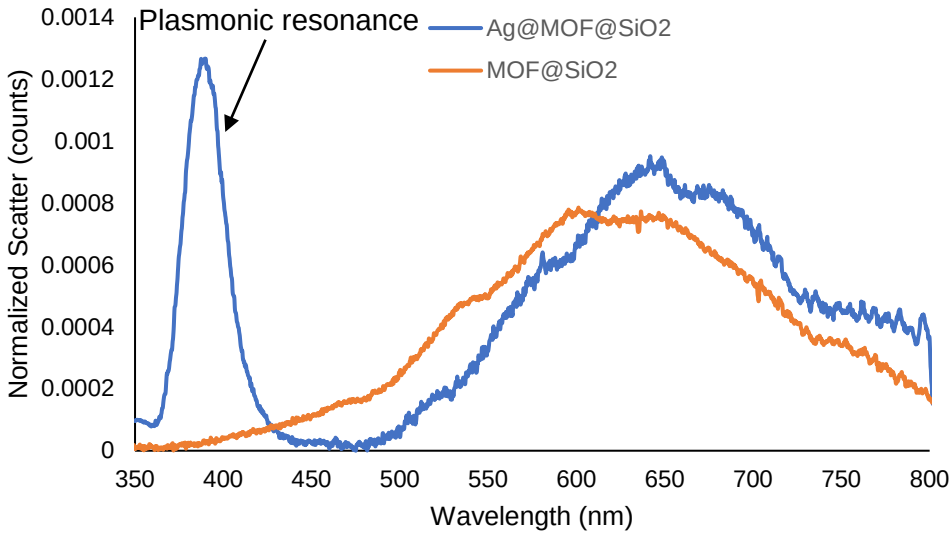


**Figure 5. Evaluation of the Ag@UiO-66@$SiO_2$ (blue) and UiO-66@$SiO_2$ (orange) plasmon resonance peaks. The Ag@UiO-66@$SiO_2$ (blue) exhibits a sharp plasmonic resonance peak at 388 nm, which indicates the potential of using the MOF micromotors for simultaneous sensing and decontaminating applications.**

## 4. CONCLUSIONS

The goal of this project is to show that MOF micromotors can decontaminate CWA/CWA simulant at a faster rate compared to non-aactive MOF particles. In this report, we have demonstrated that bubble propelled MOF micromotors move at a faster rate compared to electrophoretic MOF micromotors in agreement with previous literature of other micromotors.[18] Additionally, we have shown that bubble-propelled MOF micromotors seem to increase the decontamination rate of DMNP simulant, but additional work is needed to fully confirm this hypothesis as the data obtained up to this point is not yet definitive. Furthermore, silver MOF micromotor particles exhibit a sharp plasmon resonance peak, which indicates future work can be done to explore these MOF micromotors for potential applications in simultaneous sensing and decontamination.

More work should be done to repeat the controls with the same DMNP concentration and UV-Vis monitoring at the same time points as the motors + $H_2O_2$ experiment for a better direct comparison. Additional work can be done to minimize the observed bubbling to view the motors + $H_2O_2$ experiment from the start of the decontamination reaction and with the same DMNP concentration as the controls for a better direct comparison. Furthermore, we would like to run another experiment containing the micromotors and without $H_2O_2$ fuel to compare how well the MOF particles can decontaminate DMNP without active movement. We would also like to explore the capability of sensing the analyte concentration simultaneously with the motors acting as a plasmon enhancing material.

Other future work will continue to explore how to optimize the MOF and micromotor components of the MOF micromotors so both components can work in unison to achieve movement and well-defined observable decontamination. We also intend to test the decontamination ability of the MOF micromotors with actual CWA when there is more definitive evidence of the MOF micromotor's ability to decontaminate CWA simulant successfully. Finally, the potential to design the chemistry of the micromotor in future iterations to run on the hazardous CWA as its fuel source so that the micromotor can sense, move towards, and mitigate a hazardous threat in theory will be explored in the future. Overall, this work demonstrated a novel concept to improve hands-off decontamination technology that can be used by the soldier in the field.

## ACKNOWLEDGMENTS

We would like to thank Erik Emmons and Ashish Tripathi of Combat Capabilities Development Command Chemical Biological Center for use of their Cressington 208 HR sputter coater in this work. Additionally, we would like to acknowledge Morgan Hall and Eric Bruni for starting to conduct nuclear magnetic resonance spectroscopy decontamination analysis on our MOF micromotors samples as this report was being written. Funding was provided by the U.S. Army via the Chemical Biological Advanced Materials Manufacturing Science Program (PE 0601102A Project VR9) at DEVCOM CBC.

## REFERENCES

[1] Altemose, A.; Harris, A.J.; Sen, A. Autonomous Formation and Annealing of Colloidal Crystals Induced by Light-Powered Oscillations of Active Particles. *ChemSystemsChem.* **2020**, *2* (1), e1900021.

[2] Jurado-Sánchez, B.; Wang, J. Micromotors for environmental applications: a review. *Environ. Sci.: Nano.* **2018**, *5* (7), pp 1530–1544.

[3] Sengupta, S.; Ibele, M.E.; Sen, A. Fantastic Voyage: Designing Self-Powered Nanorobots. *Angew. Chem., Int. Ed.* **2012**, *51* (34), pp 8434–8445.

[4] Wang, W.; Li, S.; Mair, L.; Ahmed, S.; Huang, T.J.; Mallouk, T.E. Acoustic Propulsion of Nanorod Motors Inside Living Cells. *Angew. Chem., Int. Ed.* **2014**, *53* (12), pp 3201–3204.

[5] Li, J.; Singh, V.V.; Sattayasamitsathit, S.; Orozco, J.; Kaufmann, K.; Dong, R.; Gao, W.; Jurado-Sanchez, B.; Fedorak, Y.; Wang, J. Water-Driven Micromotors for Rapid Photocatalytic Degradation of Biological and Chemical Warfare Agents. *ACS Nano.* **2014**, *8* (11), pp 11118–11125.

[6] Singh, V.V.; Martin, A.; Kaufmann, K.; de Oliveira, S.D.S.; Wang, J. Zirconia/Graphene Oxide Hybrid Micromotors for Selective Capture of Nerve Agents. *Chem. Mater.* **2015**, *27* (23), pp 8162–8169.

[7] Singh, V.V.; Wang, J. Nano/micromotors for security/defense applications. A review. *Nanoscale.* **2015**, *7* (46), pp 19377–19389.

[8] Dey, K.K.; Wong, F.; Altemose, A.; Sen, A. Catalytic Motors—Quo Vadimus? *Curr. Opin. Colloid Interface Sci.* **2016**, *21*, pp 4–13.

[9] Li, J.; Yu, X.; Xu, M.; Liu, W.; Sandraz, E.; Lan, H.; Wang, J.; Cohen, S. M. Metal–Organic Frameworks as Micromotors with Tunable Engines and Brakes. *J. Am. Chem. Soc.* **2017**, *139* (2), pp 611–614.

[10] Wang, R.; Guo, W.; Li, X.; Liu, Z.; Liu, H.; Ding, S. Highly efficient MOF-based self-propelled micromotors for water purification. *RSC Adv.* **2017**, *7* (67), pp 42462–42467.

[11] Yang, Y.; Arqué, X.; Patiño, T.; Guillerm, V.; Blersch, P.-R.; Pérez-Carvajal, J.; Imaz, I.; Maspoch, D.; Sánchez, S. Enzyme-Powered Porous Micromotors Built from a Hierarchical Micro- and Mesoporous UiO-Type Metal–Organic Framework. *J. Am. Chem. Soc.* **2020**, *142* (50), pp 20962–20967.

[12] Ying, Y.; Pourrahimi, A.M.; Sofer, Z.; Matějková, S.; Pumera, M. Radioactive Uranium Preconcentration via Self-Propelled Autonomous Microrobots Based on Metal–Organic Frameworks. *ACS Nano.* **2019**, *13* (10), pp 11477–11487.

[13] Islamoglu, T.; Chen, Z.; Wasson, M.C.; Buru, C.T.; Kirlikovali, K.O.; Afrin, U.; Mian, M.R.; Farha, O.K. Metal–Organic Frameworks against Toxic Chemicals. *Chem. Rev.* **2020**, *120* (16), pp 8130–8160.

[14] Liu, Y.; Howarth, A.J.; Vermeulen, N.A.; Moon, S.-Y.; Hupp, J.T.; Farha, O.K. Catalytic degradation of chemical warfare agents and their simulants by metal-organic frameworks. *Coord. Chem. Rev.* **2017**, *346*, pp 101–111.

[15] Zhang, X.; Han, Q.; Ding, M. One-pot synthesis of UiO-66@$SiO_2$ shell–core microspheres as stationary phase for high performance liquid chromatography. *RSC Adv.* **2015**, *5* (2), pp 1043–1050.

[16] Ploskonka, A.M.; DeCoste, J.B. Insight into organophosphate chemical warfare agent simulant hydrolysis in metal-organic frameworks. *J. Hazard. Mater.* **2019**, *375*, pp 191–197.

[17] Orozco, J.; Cheng, G.; Vilela, D.; Sattayasamitsathit, S.; Vazquez-Duhalt, R.; Valdés-Ramírez, G.; Pak, O.S.; Escarpa, A.; Kan, C.; Wang, J. Micromotor-Based High-Yielding Fast Oxidative Detoxification of Chemical Threats. *Angew. Chem., Int. Ed.* **2013**, *52* (50), pp 13276–13279.

[18] Li, H.; Peng, F.; Yan, X.; Mao, C.; Ma, X.; Wilson, D.A.; He, Q.; Tu, Y. Medical micro- and nanomotors in the body. *Acta Pharm. Sin. B.* **2023**, *13* (2), pp 517–541.

This page left intentionally blank

# Determination of the influence of tunable chemical environment in MOF-polymer composites on the absorption of linear nonpolar toxic compounds

Mark J. Varady[a], Craig S. Schenning[b], Chase B. Thompson[b], Adam R. Hinkle[c], Matthew A. Browe[a], Ivan, O. Iordanov[a], Gregory W. Peterson[a], Anne Y. Walker[a], Brent A. Mantooth[a], Thomas P. Pearl[a]*
[a]U.S. Army Combat Capabilities Development Command Chemical Biological Center, Research & Operations Directorate, 8198 Blackhawk Rd, Aberdeen Proving Ground, MD 21010
[b]Leidos, 11951 Freedom Drive, Reston, VA 20190
[c]DCS Corporation, 4696 Millennium Dr, Suite 450, Belcamp, MD 21017

## ABSTRACT

This proof-of-concept study addresses the chemical environment at the interfaces present in metal-organic framework (MOF)-polymer composites and their role in mass transport behavior for permeating molecular contaminants. While the ultimate focus is on determining the role of interfaces in transport behavior for specific types of toxic compounds, a systematic understanding of chemical interactions and polymer chain behavior at MOF-polymer interfaces is crucial. Work presented here focuses on treating process factors, specifically solvent blends, to control dispersal of UiO-66-$NH_2$, a prototypical MOF, in common polymers. The approach invokes the use of self-consistent field theory in conjunction with Hansen solubility parameters to predict conditions that will result in good or bad dispersal of MOF crystals in polystyrene and poly(methyl methacrylate) in solution-cast thin films. Scanning electron microscopy shows improved dispersion of UiO-66-$NH_2$ in both polymers for the predicted solvent blends, demonstrating the utility of the proposed method. Computational modeling is also being used to complement the experimental efforts by an examination of transport properties at the molecular scale in MOF-polymer composites using atomistic simulations. A hybrid forcefield arrangement is under development that integrates the MOF, polymer, and penetrant interactions into the modeling approach.

**Keywords:** metal-organic frameworks, polymer composites, interfaces, chemical permeability

## 1. INTRODUCTION

For protective coatings, barrier materials, and permeable membranes used in protection and hazard mitigation applications, which are often composed of polymers or polymer composites, there is a need to better understand how to control (i.e., to suppress or enhance) mass transport. Previous work has treated the interaction of toxic chemicals and respective simulants with polymeric materials in order to promote development of more efficacious decontamination processes as well as to contribute to the design of coatings materials (e.g., low gloss paints) to enhance chemical resistance.[1] These composite materials involve the dispersal of solids in polymer matrices to impart specific material properties. Consistently, there has been great difficulty in designing materials of this type with increased resistance to specific compounds, such as linear nonpolar chemicals. In parallel efforts, metal-organic frameworks (MOFs) and MOF-polymer composites have been developed and characterized to establish new materials with customizable functionalities and structures, including the ability to specifically address chemical hazards.[2,3] It would be advantageous to utilize these types of structures to develop new types of barrier materials, but advances in control and tuning of chemical permeation for composites depend on understanding the role of interfacial structures that arise from mixing dissimilar materials in chemical transport.

The dispersion of solids or particles and the chemical and physical environments associated with polymer-particle interfaces have been shown to significantly influence the overall chemical transport properties of a composite,[4,5] including specific MOF examples.[6] The underlying structure-property relationships of polymer composites influence transport of incoming analytes, which are informed by the properties of the penetrant chemical and the nature of dispersal of solids in the composite. Nonpolar molecular species are readily soluble in certain polymer matrices and

exhibit entrainment within surface and bulk layer textures. These challenges exist for a broad class of polymer composites where the solids dispersed in host polymer matrices introduce spatially localized variations in the density and voids in the binder system that can facilitate transport. Molecular size, shape, and functionality of the penetrant chemical are major factors that impact transport and solubility in bulk polymers.[7] A systematic study of these interactions is necessary to design and optimize novel polymer composites that can serve as strong barriers to chemical absorption, including protective paint coatings (as much as 50 μm thick) and conformal thin films. The interface of MOF-polymer composites presents a key challenge since defects often form due to the general incompatibility between nanoparticles and polymers.[8,9] Within films, and especially thin films, these defects can dictate permeation through the substrate. Several approaches are available for enhancing the compatibility between MOFs and polymers,[10] thereby reducing interfacial defects, but an understanding of how to process these types of materials with control over interface and defect structures is still lacking.

The overall objective of this project is to address how the physicochemical environment in polymer-based composites facilitates absorption and transport of specific types of penetrants. Figure 1 shows the relevant aspects of the systems under study in a schematic cross-sectional view, including presence of polymer, MOF crystals, resultant MOF-polymer interfaces, and a penetrant permeating the bulk of the film. Polymer chain interactions with the MOF particle periphery, including pore blockage and penetration, produce interfaces in MOF-polymer composites that can determine chemical permeability in thin films (i.e., greater/lesser disruption of bulk polymer mechanical properties at interfaces will result in less/more chemical resistance). To engender a root-level understanding of what characteristics of composite thin films would promote enhanced transport for linear nonpolar molecules, we have investigated variations in the chemical environment at the interfaces between MOF crystals and the polymer that result from processing conditions for solution-cast thin films. The chemical interactions that dictate the transport behavior for specific chemical species will be interrogated with a combination of experimental tools and modeling methods, which should reveal structure-property relationships that will enable the design of superior barrier materials. The objective of the work is not to optimize a single MOF-polymer system but to understand what factors are most influential in driving transport behavior for a specific class of penetrant.

In this portion of the work, we demonstrated the utility in using a computationally efficient mean field theory in combination with solubility parameters to predict the adsorption and depletion of a polymer layer on a solid surface. This allowed a determination of solvent-driven influence on the dispersion of UiO-66-$NH_2$ in select polymers, polystyrene (PS) and poly(methyl methacrylate) (PMMA), when films were cast from a solution of MOF, polymer, and solvent. This level of prediction for the role of solvent in processing conditions has the potential to inform production of other composite materials and provides a means of assessing the role of defect structure in mass transport due to solvent-induced variations in MOF-polymer interfaces.

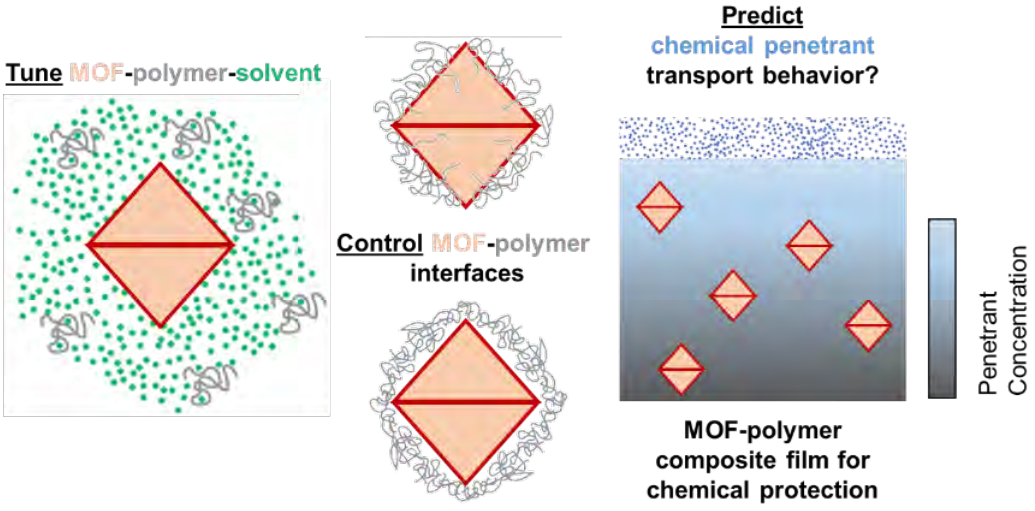


**Figure 1. Illustration of the main components of the project associated with tuning MOF-polymer-solvent combinations to control interface types to permit prediction of chemical permeation properties.**

# 2. MATERIALS AND METHODS

## 2.1 Materials

For this proof-of-concept study, UiO-66-$NH_2$ was prioritized as the principal MOF since it is well-characterized, employed in the relevant application areas,[2,3,11] can be synthesized with controlled crystal shapes and sizes less than 200 nm (which is important for thin films such that crystals do not transverse the film), and is one of the most stable MOFs known.[12] UiO-66-$NH_2$ was provided by NuMat Technologies (Skokie, IL). Two common polymers with high glass transition temperatures ($T_g$), but very different backbone structures, were used for this work. Polystyrene (PS) with an average $M_w$ = 192,000 g/mol and PMMA with an average $M_w$ = 120,000 g/mol were procured from Sigma Aldrich (P/N 430102 and P/N 182230). All solvents used in turbidity measurements and in MOF-polymer film processing were procured from Sigma Aldrich/Supelco (HPLC or ACS reagent grade) and used as received with no further purification.

## 2.2 Experimental

Composite films consisting of approximately 10 wt% UiO-66-$NH_2$ in both PS and PMMA were prepared by solution casting. Because the compositions of the polymer solutions are based on self-consistent field theory (SCFT) calculations and Hansen solubility parameters (HSPs), the details of the composite film preparation are given in the Results and Discussion section. A Phenom GSR desktop scanning electron microscope (SEM) was used to assess the dispersion of UiO-66-$NH_2$ in each polymer. A 1 cm × 1 cm sample of the composite was mounted on an Al stub using double-sided tape, then sputter coated with gold before imaging. Accelerating voltages between 5–15 kV were used with a 10 mm nominal working distance. Differential scanning calorimetry (DSC) was run on a TA Discover Series DSC. Samples were prepared in crimped aluminum pans and subject to a heat-cool-heat cycle from ambient to 150 °C at a heating rate of 10 °C/min. First heating cycles were used to calculate the average $T_g$ of the prepared films to accurately determine the thermal behavior of the polymer samples as-cast.

## 2.3 Computational

Computational methods and tools used for initial work on molecular simulation are described briefly in the Results and Discussion Section.

# 3. RESULTS AND DISCUSSION

## 3.1 Solubility parameters and self-consistent field theory

SCFT calculations were performed with the freely available SFBox code, which provides a numerical implementation of the Scheutjens-Fleer lattice-based SCFT.[13-15] Of particular interest in this work is the concentration of a monodisperse polymer as a function of distance from the solid surface, which has previously been studied for several different systems.[13,16-19] The calculations are specified by the polymer chain length, $N$, bulk polymer volume fraction, $\varphi_b$, polymer-solvent interaction parameter, $\chi$ (equivalent to the Flory-Huggins interaction parameter), and the interaction parameter $\chi_s$, which quantifies the *relative* polymer-solid and solvent-solid interactions ($\chi_s < 0$ indicates the polymer interacts more strongly with the solid than does the solvent and vice versa for $\chi_s > 0$). With a given system specification, the SFBox code outputs $\varphi(z)$, which is a profile of polymer volume fraction, $\varphi$, as a function of distance, $z$, (in lattice units) from the solid surface. An excess adsorbed amount, $\Gamma_{ex}$, defined as the integrated deviation from the bulk polymer solution concentration, was also calculated from the following equation.

$$\Gamma_{ex} = \int_0^\infty [\varphi(z) - \varphi_b] dz. \quad (1)$$

Figure 2 shows examples of $\varphi(z)$ profiles and the corresponding values of $\Gamma_{ex}$. for a specific combination of $\chi$, $N$, and $\varphi_b$. For negative $\chi_s$ values, polymer adsorption occurs, yielding a positive value of $\Gamma_{ex}$. On the other hand, for positive values of $\chi_s$, a depletion layer forms where the polymer concentration near the surface is less than in the bulk solution and $\Gamma_{ex} < 0$.

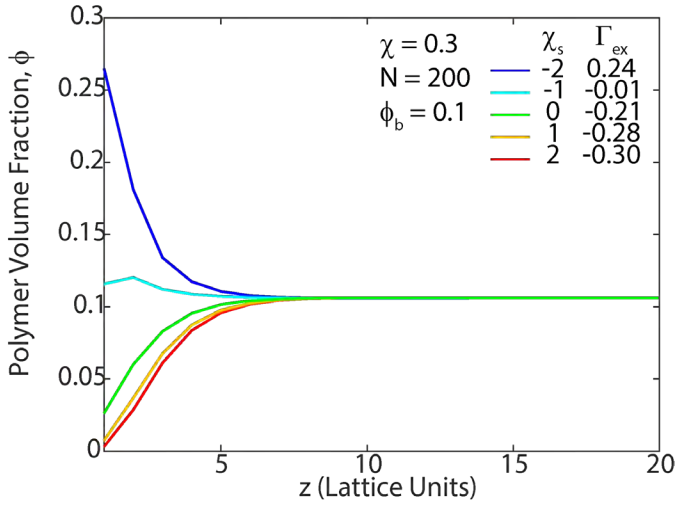


**Figure 2. Polymer volume fraction profiles computed by SFBox for $\chi_s$ between -2 and 2, yielding different values of the excess adsorbed amount, $\Gamma_{ex}$.**

Recent work has used SCFT to study the adsorption/depletion behavior of homopolymers in solution near the critical point of the polymer solution where phase separation begins to occur (i.e., the extremal point of the spinodal curve).[20] This work interestingly showed that the value of $\Gamma_{ex}$ increases dramatically (mathematically, $\Gamma_{ex} \to +\infty$) near the bulk solution critical point when the energy of attraction between the polymer and surface is larger than the energy at which point a transition between depletion and adsorption is observed. Likewise, $\Gamma_{ex} \to -\infty$ when the reverse is true. This amplification of the adsorption or depletion behavior as a function of the physical state of the polymer solution could be utilized to better control the dispersion of solid inclusions and possibly the polymer structure near the solid interface in solution-cast composite materials. Typically, solution processing uses a good solvent to dissolve the polymer, but this can lead to issues with subsequent dispersion of a solid component if it is more favorable for the polymer to be in the solvent than on the surface of the solid component. This situation can lead to depletion attraction between the solid inclusions, causing agglomeration of the particles in addition to poor polymer adhesion at the interface. Rational selection of the polymer + solvent + solid system such that it exists near the bulk solution critical point with $\chi_s < 0$ could be a viable processing method for producing composites with improved properties.

This strategy was applied to control the dispersion of UiO-66-$NH_2$ in PS and PMMA. The bulk critical solution condition for the polymers, including volume fraction ($\varphi_c$) and interaction parameter ($\chi_c$), can be estimated from the number of Kuhn segments (chain length), $N$, for each polymer chain, $\varphi_c \cong N^{-0.5}$ and $\chi_c \cong 0.5 + N^{-0.5}$.[21] From the $M_w$ of the polymers (192,000 g/mol and 120,000 g/mol for PS and PMMA, respectively) and the mass of the Kuhn monomers[21] (720 g/mol and 655 g/mol for PS and PMMA, respectively), the number of Kuhn segments was $N$ = 267 for PS and $N$ = 184 for PMMA. Therefore, an average value of $N$ = 200 was used for all cases in the SCFT model here, which results in $\varphi_c \cong 0.07$ and $\chi_c \cong 0.57$.

To support the computation of $\chi_s$ values, Hansen solubility-style parameters were acquired for 200 nm diameter UiO-66-$NH_2$ crystals based on time-dependent turbidity measurements involving MOF crystals dispersed in a specific set of probe chemicals designed to predict chemical interaction types as previously reported. Based on those turbidity measurements, the position of the solubility sphere for UiO-66-$NH_2$ in Hansen solubility parameter space ($\delta_D$, $\delta_P$, and $\delta_H$) was determined through Hansen Solubility Parameters in Practice (HSPiP) to be $\delta_D$=13.9, $\delta_P$=11.7, $\delta_H$=11.8. The HSP describe the dependence of molecular, polymer, and nanoparticle properties like solubility and diffusion on dispersion ($\delta_D$, van der Waals), polarity ($\delta_P$, related to dipole moment), and hydrogen bonding ($\delta_H$) type chemical interactions.

Using HSPs available in the HSPiP software for PS ($\delta_D$ = 18 $MPa^{0.5}$, $\delta_P$ = 5 $MPa^{0.5}$, and $\delta_H$ = 5 $MPa^{0.5}$) and PMMA (average of top 5 results in the database: $\delta_D$ = 17.3 $MPa^{0.5}$, $\delta_P$ = 8.2 $MPa^{0.5}$, and $\delta_H$ = 7.6 $MPa^{0.5}$), the interaction parameters for each polymer and UiO-66-$NH_2$ dispersed in different solvent blends were computed using the following equation,[22,23]

$$\chi_{ab} = \frac{\bar{V}_r}{RT}[(\delta_D^a - \delta_D^b)^2 + 0.25(\delta_P^a - \delta_P^b)^2 + 0.25(\delta_H^a - \delta_H^b)^2]. \quad (2)$$

The superscripts $a$ and $b$ refer to the components of the mixture (polymer, MOF, or solvent), and $\bar{V}_r$ is a reference molar volume. For interaction parameters in which the solvent is one component, $\bar{V}_r$ is the molar volume of the solvent or the average of the solvent mixture, while for the MOF-polymer interaction parameter, $\bar{V}_r$ is the molar volume of a monomer unit.

For PS, chloroform/hexane mixtures were explored for improved dispersion of UiO-66-$NH_2$ compared to using pure chloroform. For PMMA, acetone/hexane mixtures were used to improve UiO-66-$NH_2$ dispersion while acetonitrile/ethanol (ACN/EtOH) mixtures were used to purposely cause agglomeration of UiO-66-$NH_2$ crystallites. The solubility parameters of the solvent mixtures were computed as a linear combination of the pure component values weighted by volume fraction. Except for the pure chloroform case, the compositions of the solvent mixtures were adjusted such that the value of solvent-polymer interaction parameter computed from the HSPs was $\chi = \chi_c = 0.57$.

The results summarized in Table 1 indicate that depletion of PS and PMMA at the surface of UiO-66-$NH_2$ is expected in pure chloroform and ACN/EtOH, respectively ($\chi_s > 0$) while adsorption of PS and PMMA is anticipated in chloroform/hexane and acetone/hexane, respectively ($\chi_s < 0$). The conditions summarized in Table 1 are also denoted by the dashed black lines in Figure 3, and the values of the excess adsorbed amount, $\Gamma_{ex}$, near the critical concentration align with anticipated adsorption/depletion behavior for each system.

**Table 1. Solubility parameters of solvent mixtures and corresponding interaction parameters for the indicated polymer with UiO-66-$NH_2$ in each solvent mixture.**

| Solvent 1 | Solvent 2 | $\phi_1$ | $\delta_d^{mix}$ (MPa$^{0.5}$) | $\delta_p^{mix}$ (MPa$^{0.5}$) | $\delta_h^{mix}$ (MPa$^{0.5}$) | $\bar{V}^{mix}$ (cm$^3$/mol) | Polymer | $\chi_s$ | $\chi$ |
|---|---|---|---|---|---|---|---|---|---|
| $CHCl_3$ | N/A | 1 | 17.8 | 3.1 | 5.7 | 80.7 | PS | 0.43 | 0.03 |
| $CHCl_3$ | Hexane | 0.29 | 15.7 | 0.9 | 1.7 | 116.7 | PS | -0.91 | 0.57 |
| Acetone | Hexane | 0.43 | 15.2 | 4.5 | 3.0 | 106.6 | PMMA | -0.81 | 0.57 |
| ACN | EtOH | 0.2 | 15.7 | 10.6 | 16.7 | 85.4 | PMMA | 0.43 | 0.57 |

Plots of $\Gamma_{ex}$ as a function of the bulk polymer solution volume fraction, $\varphi_b$, below and above the estimated $\varphi_c$, for values of $\chi_s$ ranging from -2 to 2 are shown in Figure 3a ($\chi = 0$) and Figure 3b ($\chi = \chi_c = 0.57$). The amplification of the adsorption/depletion layer is observed near the critical point, and is qualitatively similar to the results shown by Zhang.[20]

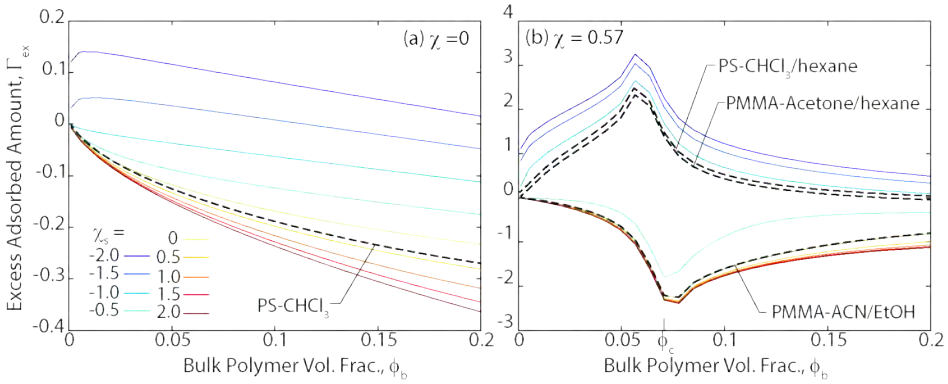


**Figure 3. Calculations of excess adsorbed polymer, $\Gamma_{ex}$, as a function of bulk polymer solution volume fraction for (a) $\chi = 0$ and (b) $\chi = 0.57$ for values of $\chi_s$ from -2 (blue lines) to 2 (red lines). The conditions corresponding to the polymer-solvent-MOF mixtures provided in Table 1 are denoted by the dashed black lines.**

### 3.2 Characterization of MOF dispersal and film properties

It should be emphasized that the SCFT predictions are not expected to be exact. Rather, the results serve as a guide to narrow the parameter space to explore to achieve the desired adsorption/depletion behavior. Several factors limit the quantitative accuracy of the method, including the approximate nature of the Flory-Huggins equation and SCFT formulation on which the calculations are based, and that HSPs are approximate and the values for a given substance can vary based on how they are determined. After preparing the polymer solutions outlined in Table 1 with a polymer volume fraction approximately equal to $\varphi_c = 0.07$, the compositions of the solvent blends were adjusted to be just at the cloud point as assessed by eye. This adjustment was necessary to ensure that the solution was close to the critical point and that viable films were formed upon evaporation of the solvent. The final solution compositions after these adjustments are summarized in Table 2.

**Table 2. Compositions for each polymer solution adjusted from the original values calculated using HSPs and SCFT.**

| Polymer | Solvent 1 | Solvent 2 | Calc. $\phi_1$ | Adjusted $\phi_1$ |
|---|---|---|---|---|
| PS | $CHCl_3$ | N/A | 1 | 1 |
| PS | $CHCl_3$ | Hexane | 0.29 | 0.32 |
| PMMA | Acetone | Hexane | 0.43 | 0.70 |
| PMMA | ACN | EtOH | 0.2 | 0.27 |

After preparing the polymer solutions indicated in Table 2, 10 wt% of UiO-66-$NH_2$ with respect to the polymer was added to each solution and mixed with a Scilogex D160 homogenizer on setting 3 for 10 min. Approximately 3 mL of each MOF-polymer-solvent mixture was deposited in a 3.5 cm diameter Teflon dish and placed in a separate enclosure with a 6 mL solvent reservoir to control the vapor headspace. Ideally, the evaporation rates of each solvent can be equalized such that the solution composition remains constant during the drying/film formation process. To achieve this, the following reservoir compositions were used for each respective solution: (a) pure chloroform, (b) a 75 % vol chloroform/hexane mixture, (c) a 70 % vol acetone/hexane mixture, and (d) a 73 % vol ACN/EtOH mixture. Films were allowed to dry overnight before removing from the enclosure. SEM images of the resulting composite films are shown in Figure 4, and as predicted by SCFT calculations using HSPs to estimate interaction parameters, UiO-66-$NH_2$ forms agglomerates in PS when cast in pure chloroform and in PMMA when cast in the ACN/EtOH mixture. Improved dispersion of UiO-66-$NH_2$ was observed in PS when cast in a chloroform/hexane mixture and in PMMA when cast in an acetone/hexane mixture. Quantitative image analysis was also performed to estimate the size of the UiO-66-$NH_2$ particles/agglomerates in each composite using the Fiji distribution of ImageJ (v. 1.53e). In the PS-based composite cast in pure chloroform, the area-averaged agglomerate size was 1.75 µm, while for the composite cast in the chloroform/hexane mixture the particle size was 0.26 µm, which is the approximate size of individual UiO-66-$NH_2$ crystallites. In the PMMA-based composite cast in the ACN/EtOH mixture the area-averaged particle size was 0.77 µm while for the composite cast in the acetone/hexane mixture the particle size was 0.31 µm.

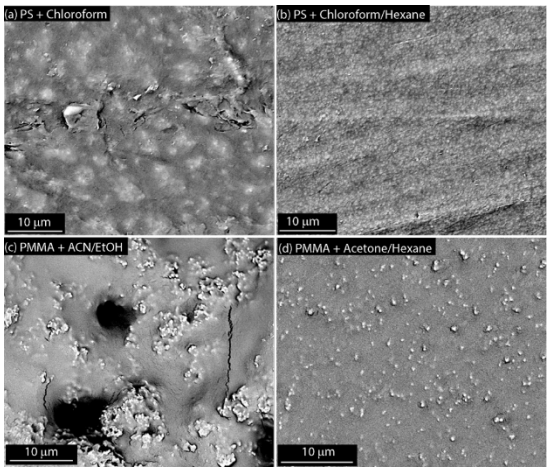


**Figure 4. SEM images of solution cast composite films containing 10 wt% UiO-66-$NH_2$: (a) PS cast in pure chloroform, (b) PS cast in a 32 vol% chloroform/hexane mixture, (c) PMMA cast in a 27 vol% ACN/EtOH mixture, and (d) PMMA cast in a 70 vol% acetone/hexane mixture.**

Glass transition temperature is highly influenced by polymer processing conditions and the effect of polymer-interface interactions as demonstrated in thin films.[24,25] The $T_g$ for both pure polymer controls and composite films determined from DSC are summarized in Table 3. In this study, casting pure PS from chloroform results in high polymer chain entanglement and an appreciable $T_g$ of 92 °C in the first heating cycle. This is depressed in the pure PS film recovered from the poor solvent mixture of chloroform/hexane (73 °C) due to the reduced number of chain entanglements that result from the drying of collapsed chains from the solvent.[26] The PS/UiO-66-$NH_2$ composite film cast from pure chloroform has a depressed $T_g$ relative to its pure polymer control due to the introduction of defects and poor polymer-MOF interfacial interactions. On the other hand, enhanced adsorption of PS on the MOF surface when cast from the chloroform/hexane mixture results in a significant retardation of polymer mobility on the MOF surface, increasing the $T_g$ of the sample relative to the neat polymer film cast from the same solvent mixture.[27] These observations reveal an important tradeoff between increased polymer adsorption but reduced chain entanglements for the composite films cast with the poorer solvent quality for the polymer.

**Table 3. Glass transition temperature of PS films with and without UiO-66-$NH_2$ determined by DSC.**

| Film | $T_g$ (°C) |
|---|---|
| PS cast in $CHCl_3$ | 92.2 |
| PS cast in $CHCl_3$/hexane | 72.6 |
| PS + 10 wt% UiO-66-$NH_2$ cast in $CHCl_3$ | 89.6 |
| PS + 10 wt% UiO-66-$NH_2$ cast in $CHCl_3$/hexane | 77.4 |

### 3.3 Computational modeling of MOF-polymer interfaces

As a parallel effort, computational modeling using atomistic simulations is being used to complement experimental work by an examination of transport properties at the molecular scale in MOF-polymer composites. This follows from past work done on the role of chemical environment on the transport at the interfaces present in silica-polyurethane systems.[28] The aim here is to determine how to theoretically model the interface in a composite with MOF particles where special attention is given to the MOF-polymer interface and surface morphology of the MOF. From this model, the goal is to then calculate diffusivities and study the transport of different chemical species through the porous interface and to probe how and why different properties of the MOF and polymer influence the transport. Recent work has revealed a strong dependence of the composite's structure on the interfacial connectivity,[21] which in turn can greatly affect permeability and selectivity in the presence of diffusive penetrants.[5,29]

The objective herein is to develop a hybrid forcefield arrangement that integrates the MOF, polymer, and penetrant interactions into a single set of interactions. Presently no single, "off-the-shelf" forcefields are available that can treat both Zr-MOF frameworks and other inorganic molecular structures. A universal, robust set of interaction parameters for MOF structures by themselves also does not exist. As shown in Figure 5, there are three regions and sets of interactions: the MOF, the bulk polymer (far from the MOF), and the MOF-polymer interface. In this report the specific coupling of the various components has been achieved such that the MOF-MOF interactions are handled via an MM3 forcefield, the MOF-polymer and MOF-penetrant via Lennard-Jones and Coulomb interactions, and the polymer-polymer and polymer-penetrant via a class II forefield. An MM3 forcefield has been shown to accurately predict material properties of UiO-66 such as its bulk modulus and has previously been used in modeling diffusion of acetone and isopropanol in that MOF.[30,31]

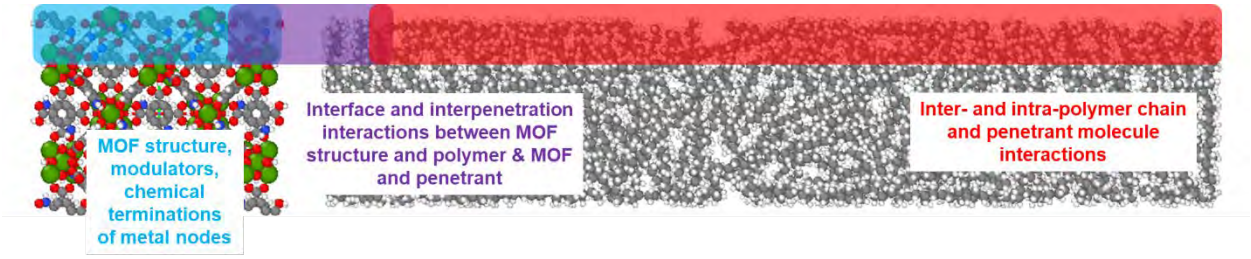


**Figure 5. Identification of interaction types to be accounted for in molecular simulations for MOF-polymer interfaces.**

Figure 6 illustrates the initial introduction of the different components into the simulation cell, i.e., MOF (UiO-66), polymer (PMMA), and a chemical penetrant (hexane). This involves the use of the hybrid forcefield framework to capture interactions coupling the distinct species of the system.

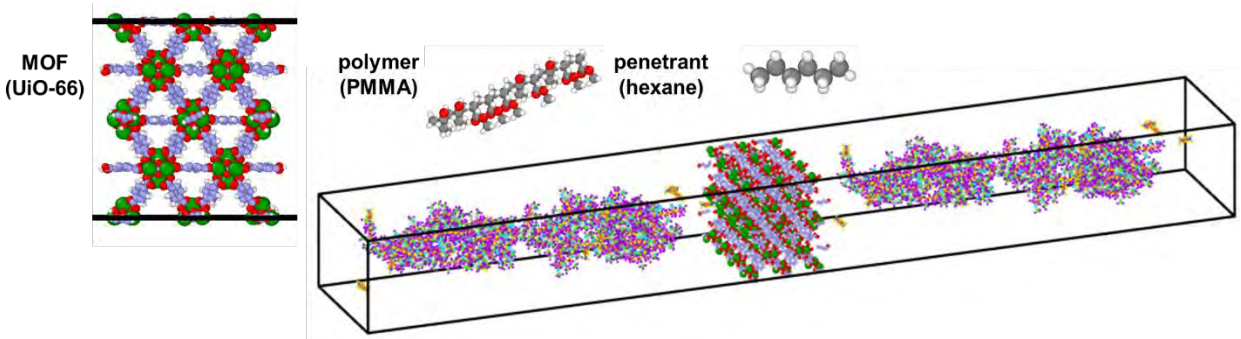

**Figure 6. Example of a simulation box that reflects the integrated forcefield for UiO-66, PMMA, and hexane.**

Modeling will focus on understanding the compatibility of UiO-66-$NH_2$ and select polymers as characterized by the mass density at the interface, polymer rigidity, porosity, and percolation of voids and other defects. Quantitative comparisons of these properties will be made to those of the bulk polymer, and these results will inform subsequent calculations of transport of chemical species.

## 4. CONCLUSIONS AND FUTURE WORK

An approach for generating MOF-polymer composites with variable MOF dispersion in the polymer based on tuned solvent blends was established. These model systems provide control polymer chain interactions with the MOF periphery and result in structures we hypothesize will directly drive mass transport behavior. HSPs of the MOF UiO-66-$NH_2$ were used in conjunction with the Scheutjens-Fleer SCFT formulation to study the adsorption/depletion behavior of polystyrene and poly(methyl methacrylate) on the surface of UiO-66-$NH_2$ crystallites. Using recently published results demonstrating the amplification of adsorption behavior near the solution critical point, solvent blends were identified to control the dispersion of UiO-66-$NH_2$ in both PS and PMMA. SEM imaging of the composite films showed that solution processing in the identified solvent blends resulted in much improved dispersion of the MOF as predicted by the SCFT results. This work shows the potential utility of using HSPs in conjunction with SCFT to identify solvents/blends to control MOF-polymer interactions and the resulting dispersion of MOF crystallites. It would be useful to apply the methods laid out in this work to other MOF-polymer systems of interest and in principle this could also be applied to control the dispersion of any solid inclusions given their corresponding HSPs. Given the limited availability of solubility parameter data for MOFs, it is first necessary to experimentally determine this information and catalogue it for MOFs of interest for such a method to be widely useful.

Additional characterization of the polymer structure and chain dynamics at the MOF interface compared to the bulk would provide a more complete picture of how tuning the three-way MOF-polymer-solvent interactions influences the final state of the composite film. Future work will also focus on chemical permeation measurements using quartz crystal microbalance and Fourier transform infrared-attenuated total reflectance spectroscopy to characterize sorption of a penetrant chemical into different bulk polymers and probe penetrant-polymer interactions.[32-35] This will allow for a determination of the influence of MOF dispersal type on transport behavior as measured and determined for program-specific penetrant chemicals, such as hexane, chlorohexane, dicholorohexane, and 2-chloroethyl ethyl sulfide.

Note, work highlighted herein has now been published as part of a paper that was submitted and accepted for publication after the assembly of this document.[36]

## ACKNOWLEDGMENTS

The authors thank colleagues in Decontamination Sciences, CBR Filtration, and Respiratory Protection Branches at Combat Capabilities Development Command Chemical Biological Center who supported this effort. Funding was provided by the U.S. Army via the Chemical Biological Advanced Materials Manufacturing Science Program (PE 0601102A Project VR9) at DEVCOM CBC.

## REFERENCES

[1] Cooley, K.A.; Pearl, T.P.; Varady, M.J.; Mantooth, B.A.; Willis, M.P. Direct Measurement of Chemical Distributions in Heterogeneous Coatings. *ACS Appl. Mater. Interfaces.* **2014**, *6* (18), pp 16289–16296.

[2] Peterson, G.W.; Browe, M.A.; Durke, E.M.; Epps, T.H. Flexible SIS/HKUST-1 Mixed Matrix Composites as Protective Barriers against Chemical Warfare Agent Simulants. *ACS Appl. Mater. Interfaces.* **2018**, *10* (49), pp 43080–43087.

[3] Peterson, G.W.; Wang, H.; Au, K.; Epps, T.H. Metal-Organic Framework Polymer Composite Enhancement via Acyl-Chloride Modification. *Polym. Int.* **2021**, *70* (6), pp 783–789.

[4] Jancar, J.; Douglas, J.F.; Starr, F.W.; Kumar, S.K.; Cassagnau, P.; Lesser, A.J.; Sternstein, S.S.; Buehler, M.J. Current issues in research on structure-property relationships in polymer nanocomposites. *Polymer*. **2010**, *51* (15), pp 3321–3343.
[5] Keskin, S.; Altinkaya, S.A. Review on Computational Modeling Tools for MOF-Based Mixed Matrix Membranes. *Computation*. **2019**, *7* (36).
[6] DeCoste, J.B.; Denny, M.S.; Peterson, G.W.; Mahle, J.J.; Cohen, S.M. Enhanced aging properties of HKUST-1 in hydrophobic mixed-matrix membranes for ammonia adsorption. *Chem. Sci.* **2016**, *7* (4), pp 2711–2716.
[7] Kwan, K.S.; Subramaniam, C.N.P.; Ward, T.C. Effect of penetrant size and shape on its transport through a thermoset adhesive: I. n-alkanes. *Polymer*. **2003**, *44* (10), pp 3061–3069.
[8] Denny, M.S.; Moreton, J.C.; Benz, L.; Cohen, S.M. Metal-organic frameworks for membrane-based separations. *Nat. Rev. Mater.* **2016**, *1* (12), p 16078.
[9] Semino, R.; Moreton, J.C.; Ramsahye, N.A.; Cohen, S.M.; Maurin, G. Understanding the origins of metal-organic framework/polymer compatibility. *Chem. Sci.* **2018**, *9* (2), pp 315–324.
[10] Kalaj, M.; Bentz, K.C.; Ayala, S.; Palomba, J.M.; Barcus, K.S.; Katayama, Y.; Cohen, S.M. MOF-Polymer Hybrid Materials: From Simple Composites to Tailored Architectures. *Chem. Rev.* **2020**, *120* (16), pp 8267–8302.
[11] Palomba, J.M.; Wirth, D.M.; Kim, J.Y.; Kalaj, M.; Clarke, E.M.; Peterson, G.W.; Pokorski, J.K.; Cohen, S.M. Strong, Ductile MOF-Poly(urethane urea) Composites. *Chem. Mater.* **2021**, *33* (9), pp 3164–3171.
[12] DeCoste, J.B.; Peterson, G.W.; Jasuja, H.; Glover, T.G.; Huang, Y.G.; Walton, K.S. Stability and degradation mechanisms of metal-organic frameworks containing the $Zr_6O_4(OH)_4$ secondary building unit. *J. Mater. Chem. A.* **2013**, *1* (18), pp 5642–5650.
[13] Fleer, G.J.; Cohen Stuart, M.A.; Scheutjens, J.M.H.M.; Cosgrove, T.; Vincent, B. *Polymers at Interfaces*. Springer Science + Business Media: Berlin, Germany, **1998**; p 496.
[14] Scheutjens, J.; Fleer, G.J. Statistical-Theory of the Adsorption of Interacting Chain Molecules. 1. Partition-Function, Segment Density Distribution, and Adsorption-Isotherms. *J. Phys. Chem.* **1979**, *83* (12), pp 1619–1635.
[15] Scheutjens, J.; Fleer, G.J. Statistical-Theory of the Adsorption of Interacting Chain Molecules. 2. Train, Loop, and Tail Size Distribution. *J. Phys. Chem. A.* **1980**, *84* (2), pp 178–190.
[16] Marshall, J.C.; Cosgrove, T.; Leermakers, F.; Obey, T.M.; Dreiss, C.A. Detailed modeling of the volume fraction profile of adsorbed polymer layers using small-angle neutron scattering. *Langmuir*. **2004**, *20* (11), pp 4480–4488.
[17] Postmus, B.R.; Leermakers, F.A.M.; Stuart, M.A.C. Self-consistent field modeling of poly(ethylene oxide) adsorption onto silica: The multiple roles of electrolytes. *Langmuir*. **2008**, *24* (5), pp 1930–1942.
[18] Tuinier, R.; Fleer, G.J. Concentration and solvency effects on the pair interaction between colloidal particles in a solution of nonadsorbing polymer. *Macromolecules*. **2004**, *37* (23), pp 8764–8772.
[19] Vanderlinden, C.C.; Vanlent, B.; Leermakers, F.A.M.; Fleer, G.J. Adsorption of Polymers on Heterogeneous Surfaces. *Macromolecules*. **1994**, *27* (7), pp 1915–1921.
[20] Zhang, P.F. Critical Depletion, Adsorption, and Intersurface Interaction in Polymer Solutions: A Mean-Field Theory Study. *Macromolecules*. **2021**, *54* (8), pp 3790–3799.
[21] Rubinstein, M.; Colby, R.H. *Polymer Physics*. Oxford University Press: **2003**.
[22] Barton, A.F.M. *CRC Handbook of Polymer-Liquid Interaction Parameters and Solubility Parameters*. CRC Press: Boca Raton, FL, **1990**.
[23] Hansen, C.M. *Hansen Solubility Parameters: A User's Handbook, 2nd ed.* CRC Press: Boca Raton, FL, 2007.
[24] Lin, Y.; Tan, Y.Q.; Qiu, B.W.; Shangguan, Y.G.; Harkin-Jones, E.; Zheng, Q. Influence of Annealing on Chain Entanglement and Molecular Dynamics in Weak Dynamic Asymmetry Polymer Blends. *J. Phys. Chem. B.* **2013**, *117* (2), pp 697–705.
[25] Tsui, O.K.C.; Russell, T.P.; Hawker, C.J. Effect of Interfacial Interactions on the Glass Transition of Polymer Thin Films. *Macromolecules*. **2001**, *34* (16), pp 5535–5539.
[26] Li, R.N.; Clough, A.; H., Y.Z.; Tsui, O.K.C. Equilibration of Polymer Films Cast from Solutions with Different Solvent Qualities. *Macromolecules*. **2012**, *45* (2), pp 1085–1089.
[27] Priestly, R.D.; Ellison, C.J.; Broadbelt, L.J.; Torkelson, J.M. Structural relaxation of polymer glasses at surfaces, interfaces and in between. *Science*. **2005**, *309* (5733), pp 456–459.
[28] Hinkle, A.R.; Browe, M.A.; Iordanov, I.O.; Mantooth, B.A.; Pearl, T.P.; Varady, M.J. Effect of Interfacial Regions and Surface Functional Groups on Chemical Transport in Polymer-Particle Composites. *J. Phys. Chem. C.* **2023**, *127*, pp 11231–11239.
[29] Ozcan, A.; Semino, R.; Maurin, G.; Yazaydin, A.O. Modeling of Gas Transport through Polymer/MOF Interfaces: A Microsecond-Scale Concentration Gradient-Driven Molecular Dynamics Study. *Chem. Mater.* **2020**, *32* (3), pp 1288–1296.

[30] Wardzala, J.J.; Ruffley, J.P.; Goodenough, I.; Schmidt, A.M.; Shukla, P.B.; Wei, X.; Bagusetty, A.; De Souza, M.; Das, P.; Thompson, D.J.; Karwacki, C.J.; Wilmers, C.E.; Borguet, C.P.; Rosi, N.L.; Johnson, J.K. Modeling of Diffusion of Acetone in UiO-66. *J. Phys. Chem. C.* **2020**, *124* (52), pp 28469–28478.

[31] Mhatre, C.V.; Wardzala, J.J.; Shukla, P.B.; Agrawal, M.; Johnson, J.K. Calculation of Self, Corrected, and Transport Diffusivities of Isopropyl Alcohol in UiO-66. *Nanomaterials.* **2023**, *13* (11), p 1793.

[32] Boyne, D.A.; Varady, M.J.; Lambeth, R.H.; Eikenberg, J.H.; Bringuier, S.A.; Pearl, T.P.; Mantooth, B.A. Solvent-Assisted Desorption of 2,5-Lutidine from Polyurethane Films. *J. Phys. Chem. B.* **2018**, *122* (7), pp 2155–2164.

[33] Varady, M.J.; Knox, C.K.; Cabalo, J.B.; Bringuier, S.A.; Pearl, T.P.; Lambeth, R.H.; Mantooth, B.A. Molecular dynamics study of competing hydrogen bonding interactions in multicomponent diffusion in polyurethanes. *Polymer.* **2018**, *140*, pp 140–149.

[34] Varady, M.J.; Boyne, D.A.; Pearl, T.P.; Lambeth, R.H.; Mantooth, B.A. Composition-dependent Multicomponent Diffusivity of 2,5-Lutidine with Acetonitrile in Polyurethane. *Polymer.* **2019**, *180*, p 121697.

[35] Bringuier, S.A.; Varady, M.J.; Pearl, T.P.; Mantooth, B.A. Characterization of Composition-Dependent Maxwell-Stefan Diffusivities in Mixtures of Polydimethylsiloxane, Nerve Agent VX, and Methanol. *Ind. Eng. Chem. Res.* **2017**, *56* (13), pp 3713–3725.

[36] Varady, M.J.; Schenning, C.S.; Thompson, C.B.; Mantooth, B.A.; Peterson, G.W.; Pearl, T.P. Solvent Selection Guided by Self-Consistent Field Theory for Improved Dispersion of Metal–Organic Frameworks in Polymers. *ACS Appl. Polym. Mater.* **2024**, *6* (1), pp 888–895.

# Developing design rules for CBRN-relevant additive manufacturing systems by probing network structure and system free volume

Chase B. Thompson[a,b], Susan K. Kozawa[a,c], Anne Y. Walker[a], and Kristian M. Van de Voorde[a]*
[a]U.S. Army Combat Capabilities Development Command Chemical Biological Center, Research & Operations Directorate, 8198 Blackhawk Rd, Aberdeen Proving Ground, MD 21010
[b]Leidos, Inc., 1750 Presidents St, Reston, VA 20190
[c]Oak Ridge Institute for Science and Education, 1299 Bethel Valley Rd, Oak Ridge, TN 37830

## ABSTRACT

Photopolymerization additive manufacturing has gained traction as a platform to produce high performance materials for mulitple applications in areas such as tissue engineering and soft robotics. However, a gap in the current knowledge remains on how minute variations in resin formulation can impact properties of crosslinked 3D printed parts, especially regarding how network heterogeneity develops during the print process. In this study, a series of model resins are printed with precise control over crosslinker functionality and photoinitiator concentration to influence the resulting structure of the crosslinked network. A significant impact on the connectivity and heterogeneity is observed as initiator content is increased, but this relationship is not consistent across crosslinkers with varied functionalities. The shifts in thermomechanical properties are probed by time-temperature superposition studies which highlight that greater heterogeneity results in more fragile—or temperature sensitive—networks. These small changes in the nano- and microscale structuring of the 3D print critically influence its functionality when incorporated into a printable hygromorphic actuating bilayer. Moreover, the reported findings highlight the need for a deep understanding of the polymerization pathways utilized in resin 3D printing as it is the foundation towards precisely predicting thermomechanical and functional properties of 3D printed crosslinked systems.

**Keywords:** additive manufacturing, 3D printing, advanced manufacturing, vat polymerization, digital light processing, polymer networks.

## 1. INTRODUCTION

Additive manufacturing (AM) of soft materials has emerged as a technique capable of rapidly producing complex geometries with a wealth of material chemistries and physical properties.[1,2] Of the 3D printing technologies, vat photopolymerization processes such as digital light processing (DLP) 3D printing offers high spatial resolution, short printing times, material tunability, and robust mechanics. The most familiar and accessible vat polymerization AM method is stereolithography (SLA), popularized by Formlabs and Anycubic. Vat polymerization utilizes liquid polymer resins crosslinked using UV or visible light to produce solid parts. This platform relies on precise projection of light to polymerize photosensitive resin into a desired shape, with spatial resolution determined by the voxel.[3] Layer thickness, cure time, and post-cure conditions dictate specific polymerization pathway of each print layer, with factors such as light penetration and dosage determining how print parameters translate to polymerization kinetics.[3-5] Consequently, the printer and resin formulation dictate the resulting properties of the manufactured part.

Recently, efforts have been conducted to better understand how the printer affects the resulting mechanical properties.[6,7] While the connection of specific printer parameters to the resulting printed part has been established, a lack of understanding on how and to what extent each parameter contributes to the bulk properties still exists. To fill this gap, this project focused study on vat polymerization-based additive manufacturing methods that consider structure-property relationships from tuning different aspects of the printing process. The first aim of this study revolved around the influence of print properties on resultant mechanical properties of a commercially available resin to facilitate future explorations of how those properties are affected by network structure. During this investigation, different mechanical properties were measured for parts manufactured with the same resin but at different printer settings. Those variations in mechanical properties were the result of different microstructures within the printed parts.

To further elucidate information on the microstructure, understanding the resin formulation would be required. As a result, another focus of this project in the previous year was on the development of bespoke resin formulations. Photopolymerization of (meth)acrylate thermosets has been studied to understand how different resin mixtures and polymerization conditions determine the final properties of the crosslinked network.[8,9] The photopolymerization of thermoset acrylates proceeds by initiation, propagation, and termination as described by typical free radical polymerizations; however, the gelation of the network which is caused by the formation of a system-spanning continuous crosslinked structure, substantially influences the polymerization kinetics due to a loss in mobility. Factors such as light dosage and light penetration also contribute to the photopolymerization kinetics and result in polymerization fronts that drive differences in local gelation behavior.[11,12] The onset of gelation in free radical thermosetting (meth)acrylate resins yields distinct differences in the local and global crosslink densities within the network.[8,13] This heterogeneity in chain connectivity results in regions of high crosslink density—termed microgels—separated by long strands with fewer crosslink junctions.[14] Network heterogeneity is influenced by several factors including monomer concentration, reactivity, and crosslinker functionality.[14,15] These structures have a profound impact on the thermal and mechanical properties of the network. Here, a model resin is developed that allows for fine-tuning of print properties by varying photoinitiator concentration and crosslinker functionality. Increasing both the photoinitiator concentration (from 0.2 mol% to 1.0 mol%) and the crosslinker functionality (from $f = 2$ to $f = 4$) allows for control over the connectivity and heterogeneity of the resulting prints and a better opportunity to understand the microstructure of the print. This relationship will provide deeper insight into resulting material properties of our 3D printed parts, extract important information, and enable development of a rational design scheme for relevant AM methods.

## 2. MATERIALS AND METHODOLOGY

### 2.1 Materials

All chemicals were purchased from Millipore Sigma and used as received unless stated otherwise. 2-propanol (IPA) was purchased from Fisher Scientific and used as received.

### 2.2 General methods

#### *2.2.1 Resin formulation*

Calculated amounts of *tert*-butyl acrylate (tBA) and *n*-butyl acrylate (BA) were mixed in an amber jar equipped with magnetic stirring. Afterwards, either 1,6-hexanediol diacrylate (HDDA) or pentaerythritol tetraacrylate (PETA) were added as crosslinkers in calculated amounts to ensure that the resulting resin contained 7:2:1 tBA:BA:crosslinking acrylate functional groups. The formula was adjusted so that there were a constant number of crosslinking functional groups in resins consisting of HDDA (difunctional, 2F) or PETA (tetrafunctional, 4F) crosslinker. After the base resin is thoroughly mixed, phenylbis(2,4,6-trimethylbenzoyl)phosphine oxide (BAPO) was weighed out and added into the mixture in an amount of 0.2, 0.5, or 1.0 mol% of total acrylate content in the resin. Afterwards, the resin was mixed thoroughly. Between formulation and printing, resins were stored in amber jars at 4 °C.

#### *2.2.2 3D printing*

All printing was conducted on an Anycubic Photon M3 printer. Rectangular specimens were prepared for most tests (either 20 mm x 5 mm x 1 mm LWT or 20 mm x 5 mm x 0.5 mm LWT). Layer cure time was set to 12 s. Printed samples were briefly washed with IPA, patted dry with a Kimwipes™ (Kimtech Science), and sandwiched between two glass slides held closed with binder clips for post-curing. UV post curing was conducted in an Anycubic Wash and Cure Plus machine for 20 min such that both sides of the printed specimen were evenly cured.

#### *2.2.3 Kinetic study*

The impact of layer cure time on the conversion of the acrylate network was studied using Attenuated Total Reflectance-Fourier Transform Infrared (ATR-FTIR) spectroscopy. Samples were printed with layer cure times ranging from 4–12 s with a brief IPA wash. The 4 s time interval was omitted from samples containing 0.2 mol% BAPO due to the samples not forming viable prints. Conversion of the printed parts was measured on a Bruker Tensor 27 ATR-FTIR instrument. Background and sample data were collected with 128 scans across the range of 400–4000 $cm^{-1}$ with a spectral resolution of 4 $cm^{-1}$. Baseline corrections were conducted in the OPUS software (Bruker). Conversion was measured by tracking the disappearance of the alkene stretching peaks at 1638 and

1622 $cm^{-1}$ and using the unchanging carbonyl stretch at 1728 $cm^{-1}$ as an internal reference peak. Conversion of the prints before and after post curing was conducted in a similar manner.

#### *2.2.4 Dynamic mechanical analysis*

The thermal characteristics of printed parts were determined using a TA Instruments 850 Dynamic Mechanical Analyzer (DMA) operating in tension mode with film clamps. For measurement of the glass transition temperature and rubbery plateau, samples were subjected to an isochronal temperature ramp. Samples were deformed to a strain of 0.1 % at an oscillation frequency of 1 Hz across a temperature range of -60–150 °C at a ramp rate of 3 °C/min. Each sample run was repeated in triplicate and analysis was performed in the Trios software.

Time-temperature superposition (TTS) master curves were generated in tensile mode at a strain of 0.3 %. Oscillating frequencies between 0.1–10 Hz with 5 points per decade were applied across a temperature range of 0–150 °C at 10 °C intervals. Master curves were made using TRIOS software (TA Instruments) by calculating horizontal shift factors.

#### *2.2.5 Tensile testing*

Tensile testing was performed in a TA Instruments 850 DMA operating in tension mode with film clamps. Testing was conducted at a pre-load force of 0.001 N and a strain rate of 10 % per min up until sample failure. Sample measurements were only considered successful if the film broke in the center during testing. The Young's modulus was calculated from 2.0–3.0 % strain in Origin Pro graphing software. The yield stress was calculated for the 4F sample series by taking the first derivative of the tensile curves and finding the peak of the derivative curve. All measurements were repeated in triplicate with average values and standard deviations reported.

## 3. RESULTS

### 3.1 Sample printing

DLP 3D Printing is a complex process in which photopolymerization is used to print objects in a layer-by-layer fashion; different aspects of the resin chemistry will strongly influence the properties of the printed part. Understanding how the covalent crosslinks develop during the print process is vital for the expanded use of 3D printing as an on-demand manufacturing technique and for developing highly functional and reproducible parts. To study how network connectivity influences print properties, a model resin was first developed for 3D printing. HDDA and pentaerythritol diacrylate (PETA) were chosen as the difunctional and tetrafunctional crosslinker, respectively, to alter crosslink topology of the prints. A monomer mixture of TBA and BA was selected to mix with the selected crosslinker (Figure 1). The mole ratio of 7:2:1 tBA:BA:crosslinker was chosen to offer high quality prints. In all formulations, the total number of crosslinking acrylate groups was kept constant by adjusting the amount of HDDA or PETA by their acrylate functionality of 2 or 4, respectively. This results in the same number of available crosslinking sites in the resin regardless of which reactants were employed.

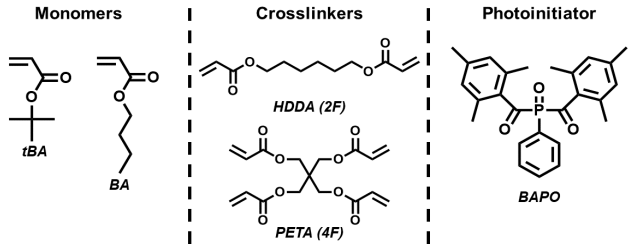


**Figure 1. Components of model resins.**

### 3.2 Resin kinetics

The loading of photoinitiator in the resin formulations was adjusted to alter the polymerization kinetics and, as a result, the network connectivity. As such, by adding more BAPO to the resin, the polymerization kinetics could be altered to influence connectivity of the final network. The concentration of photoinitiator was varied between 0.2, 0.5, and 1 mol% in relation to the total number of reactive acrylates. Sample nomenclature for the printed parts is XF-YI, where X refers to the functionality of the crosslinked (2 or 4) and Y is the mol% of initiator added to the resin formulation. The effects of photoinitiator loading on the print properties were studied first using ATR-FTIR. Samples were printed

in 1” x 1” squares for different layer cure times ranging from 4–12 s. The conversions were then calculated for each resin formulation by tracking the disappearance of the alkene stretching peaks at 1638 $cm^{-1}$ and 1622 $cm^{-1}$.

The carbonyl stretching peak at 1728 $cm^{-1}$ was used as an internal reference. Print conversion of different resin formulations across a range of layer cure times is depicted in Figure 2. The resins with the lowest BAPO loading (4F-0.2I and 2F-0.2I) did not form printed parts at a layer cure time of 4 s, indicating that the conversion had not progressed sufficiently during printing to form a continuous gel network capable of adhering to the build plate. Interestingly, across all resins, there is no distinct differences between the conversion of the samples across different samples time point. All samples show that conversion levels off after 6 s; this indicates that the polymerization has become diffusion limited.[16,17] This approach to understanding the polymerization kinetics is limited due to not being able to sample the reaction at the early stages of the polymerization or directly calculate the gelation point of the polymerization; however, this study still highlights that there is no apparent difference in the printability of these resin formulations based upon the crosslinker functionality or photoinitiator loading. It is shown that at low photoinitiator loadings of 0.2 mol%, it will take more time for gelation to occur in the polymerization and thus achieve a viable print which is in line with previous studies showing that lowering the initiator content in a free radical reaction will increase the gelation time.[8] One interesting observation here is that we do not see a substantial increase in polymerization rate for higher starting initiator concentrations. This has previously been noted to be a direct consequence of the photoinitiators role as a reaction mediator through light absorption as well as being responsible for beginning the polymerization itself.[11] Suggesting an increase in photoinitiator concentration can cause heterogeneous polymerization conditions between the surface and bulk of a resin due to excess light absorption by the photoinitiator nearer to the light source. This is especially relevant in 3D printing, where layer thickness can greatly influence the polymerization kinetics. In our own system, we printed the samples with a layer thickness of 100 µm which could contribute to the frontal polymerization effect and the resulting heterogeneity. For the remainder of the study, a layer cure time of 12 s was chosen to ensure that all resin formulations would be at a similar state of conversion when removed from the build plate. Conversion of the printed parts was also measured before and after post cure; printed objects showed a modest increase in conversion before and after the 20 min post-cure at 405 nm. All the print formulations show a similar acrylate conversion, indicating that differences in their properties can be attributed to differences in network structure and connectivity rather than overall print conversion.

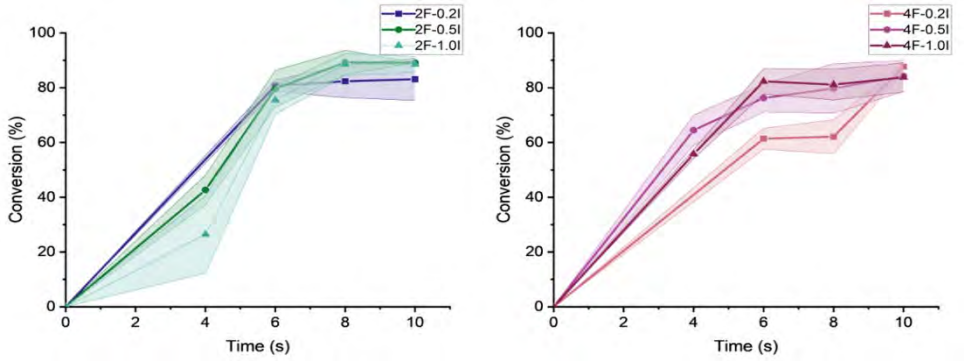


**Figure 2. Conversion plots of printed parts as a function of layer cure time. Extended colors around plots indicate error bards from repeating ATR measurements in triplicate.**

### 3.3 Thermal properties

The prints were subjected to dynamic mechanical analysis (DMA) to establish how small changes in the print formulation influence the thermal properties (Figure 3). The shape of the tanδ curve offers insight into the structure and connectivity of thermoset networks. While the position of the peak can be used to estimate the $T_g$ of a system from the α relaxation, the peak full width half maximum (FWHM) is related to the distribution of chain motions in a system and, therefore, the heterogeneity of the network. A sample with a greater tanδ FWHM is more heterogeneous than a narrower peak as described by the Gaussian distribution of segmental motions during the α relaxation process.[18,19] The tanδ curves for the 2F and 4F print series are shown in Figure 2A and 2B, respectively. In general, the 4F prints have higher $T_g$ values than the corresponding 2F prints by ~15–20 °C (Table 1); this can be attributed to the greater mobility restriction when higher functionality crosslinkers are applied. Interestingly, the 2F series $T_g$ values do not vary much with changing BAPO concentration, while the 4F samples series shows substantial changes with initiator loading. It has been previously noted that heterogeneity in a polymer network increases the average value of

$T_g$.[19] It is also notable that the 4F-0.2I sample has a substantially lower Tg than the 4F-0.5I and 4F-1.0I samples. In fact, the $T_g$ of the 4F-0.2I sample is more closely aligned with the values measured in the 2F sample series. This trend corresponds to the trend in FWHM values measured in the samples (Table 1). The FWHM value of 4F-0.2I was 53.1 ± 3.3 °C, which is closer to the value of the 2F series than the 4F series. This indicates that decreasing the initiator content in the print resin results in a decrease in the network heterogeneity when using a crosslinker with a greater functionality. This change in FWHM is notably absent in the 2F resins, where there is not statistically significant shift in the FWHM with increasing BAPO concentration. This highlights that increasing the crosslinker functionality will create a network that is more sensitive to shifts in polymerization behavior and thus have greater changes in its network connectivity. As noted above, increasing photoinitiator content can enhance the frontal polymerization effect and cause local polymerization rates to differ greatly in a resin, causing differences in the local consumption rate of photoinitiator.11 Since we know from the kinetics that the 2F-0.2I and 4F-0.2I resins take longer to form continuous gels, it can be surmised that the overall polymerization rate is lower, which would favor a more statistical distribution of monomers and crosslinkers rather than the clustered crosslinking in microgel-laden systems such as 4F-0.5I and 4F-1.0I.

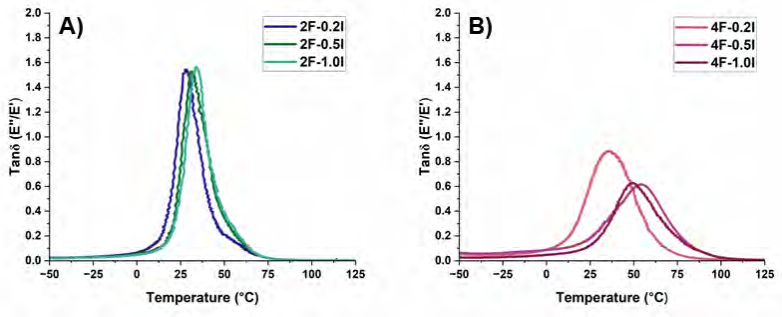


**Figure 3. A. Representative tanδ curves of 2F series samples. B) Representative tanδ curves of 4F series samples. All data collected at an oscillating frequency of 1 Hz and strain of 0.1%.**

**Table 1. DMA data for the 2F and 4F sample sets. Determined from the peak of the tanδ curve.**

| | [a]$T_g$ (°C) | FWHM (°C) | $\nu_e$ x $10^{-3}$ (mol/$m^3$) |
|---|---|---|---|
| **2F-0.2I** | 32.8 ± 4.0 | 43.4 ± 2.2 | 1.76 ± 0.21 |
| **2F-0.5I** | 33.2 ± 2.1 | 46.2 ± 1.4 | 2.06 ± 0.41 |
| **2F-1.0I** | 31.0 ± 2.4 | 48.3 ± 5.5 | 2.24 ± 0.26 |
| **4F-0.2I** | 39.7 ± 2.0 | 53.1 ± 3.3 | 1.91 ± 0.06 |
| **4F-0.5I** | 56.7 ± 0.4 | 64.4 ± 2.0 | 4.10 ± 0.83 |
| **4F-1.0I** | 48.6 ± 1.4 | 65.2 ± 2.8 | 4.02 ± 0.13 |

Effective crosslinking density ($\nu_e$) was determined according to equation 1:

$$\nu_e = \frac{E'}{3RT} \quad (1)$$

Where E' is the plateau storage modulus at temperature T and R is the universal gas constant.[20] In both the 2F and 4F series, there is an increase in the effective crosslink density as the initiator concentration is increased above 0.2; however, the change is much more dramatic in the 4F series where the effective crosslink density doubles between 4F-0.2I and 4F-0.5I. The increase in effective crosslink density—while not being a result of the overall conversion of the network—may be influenced by network defects like dangling chain ends or loops that do not contribute to the overall elasticity of the thermoset network.[15] In systems polymerized with low initiator content (or, equivalently, low UV intensity/irradiance), the short lifetime of propagating radicals can result in dangling chain ends in systems prior to gelation, after which the limited diffusion of radical chain ends allows for a much longer lifetime and continued polymerization. Anastasio *et al.* noted that both low intensity and low initiator concentration resulted in a higher degree of dangling chain ends that resulted in a reduced yield stress and $T_g$ in the studied systems.[21] The greater values

of $\nu_e$ in the 4F series when compared to the 2F series can be explained by the tetrafunctional crosslinker creating more elastically effective junctions than the 2F when fully reacted when bulk conversion is <100 % as previously noted.[22]

### 3.4 Time temperature superposition

To understand the material properties over long timescales, TTS principle was used to superimpose DMA data sets at different temperatures into a master curve that highlights mechanical properties over a wide range of frequencies. Master curves were generated from isothermal frequency sweeps using the horizontal shift factor $a_T$ and a reference temperature ($T_r$) that was closest to the sample's $T_g$ as measured by isochronal temperature ramps (Figure 4A and 4B). The printed samples were confirmed as rheologically simple and valid for TTS experiments using Cole-Cole plots. The Cole-Cole plot of 2F-0.2I is incomplete—and therefore does not display an entire semi-circle—due to the limited low temperature range used when running these samples. When comparing the tanδ for these samples, the trends appear like those noted in the isochronal temperature ramps, as expected. Here, the 4F series shows a much broader temperature transition occurring at lower frequencies, indicating a more constrained crosslink network with greater heterogeneity.

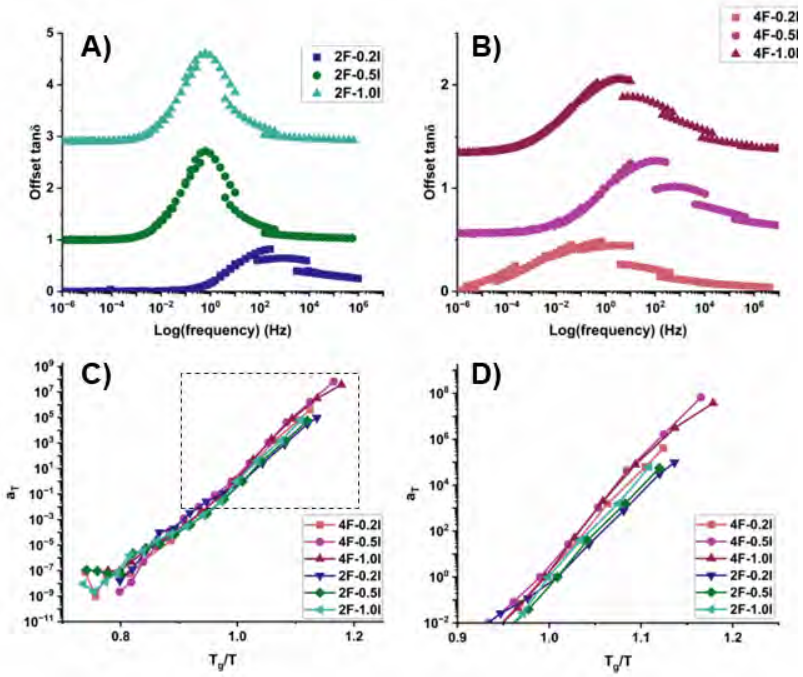


**Figure 4. A) Tan master curve for 2F sample series. B) Tan master curve for 4F sample series. C) Cooperativity plots for printed samples. D) Inset of cooperativity plot highlighting the behavior at low temperatures and near the glass transition as indicated by dashed box in 4 °C.**

In the glass transition region, the horizontal shift factor can be described by the Williams-Landel-Ferry (WLF) equation:

$$a_T = \frac{-C_1(T - T_r)}{C_2 + T - T_r} \quad (2)$$

Where T is the temperature of the acquired frequency sweep data, Tr is the reference temperature, and C1 and C2 are empirical constants adjusted to fit the value of $a_T$.[23] For the printed samples here, WLF fits were generated using data that corresponds to the apparent beginning of the glass transition region—or the onset of the tanδ peak—to 100 ºC above that temperature. For example, for 2F-0.2I, the WLF fit is taken from the shift factor data in a range from 0–100 ºC. Cooperativity plots—also called Angell plots—of $a_T$ vs. Tg/T (Figure 4C and 4D) highlight changes in the slope of the shift factor with changes in resin identity. While on the entire scale the curves appear similar, near the glass transition there are small deviations in slope that can be noted. It has been previously highlighted that an increase in crosslink density results in stronger intermolecular coupling and higher slopes in cooperativity plots.[23] To determine the differences in response of the material to temperature, the fragility index ($m$) was calculated for the samples by calculating the slope of the cooperativity plots at the glass transition temperature. A higher value of $m$ (e.g., 100)

indicates a more fragile material; that is to say, it responds more strongly to changes in temperature while less fragile materials behave oppositely. Figure 5 show the calculated fragility index values for the different printed samples. There is not a substantial shift in fragility between the samples, but there are interesting trends that emerge. The value of *m* increases with increasing photoinitiator, indicating an overall enhancement of the fragility of the sample. Interestingly, this trend indicates that small shifts in the resin formulation impact the response of the network to temperature. In the 2F series, there is a small increase as initiator content is increased, indicating that chains are more fragile in this regime. This could be a result of slightly more elastically effective strands being formed in 2F-0.5I and 2F-1.0I. In all cases, the values for the 4F samples are greater than their 2F counterparts, due to the greater crosslinker functionality tying chains together at a junction. Since there is a greater number of strands per crosslink junction, there is more coupling of the mobility and relaxation of those strands when compared to one another. These experiments highlight how small shifts in resin formulation result in unique network structures, and these changes cannot be tuned independently. The network topology—as controlled here by initiator loading and crosslinker functionality—play an important role in the connectivity of the network, and this is further governed by the functionality of the employed crosslinker.

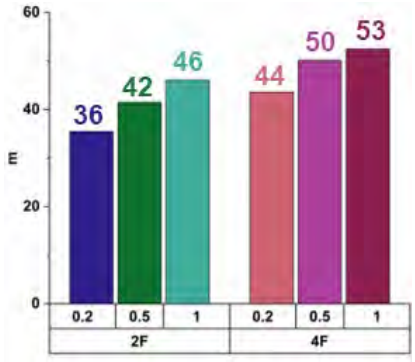


**Figure 5. Fragility index values (*m*) for different printed samples. Calculated values are above respective plots on the chart.**

### 3.5 Tensile properties

The shifts in network connectivity and topology as measured by DMA experiments also result in changes in the bulk mechanical properties of the polymerized networks. Printed samples were subjected to tensile tests to failure, with representative tensile curves displayed in Figure 6. It is immediately apparent that the overall tensile behavior is different between the 2F and 4F samples. All the 2F samples show elastomeric behavior, with a low Young's modulus ($E_y$) and large values of strain-at-break ($\varepsilon_b$). Interestingly, the 2F-0.2I sample shows reduced mechanical properties when compared to the 2F-0.5I and 2F-1.0I samples (Table 2). This mirrors the decreased effective crosslink density measured in DMA experiments in Section 3.2 which is attributed to the increased presence of dangling chain ends due to the early termination of radicals when initiator content is lowered. As initiator content is increased in the 2F series, there is a subsequent increase in the toughness and $\varepsilon_b$. There is no significant change to the $E_y$ in the 2F samples, indicating that the shifts in network connectivity—while substantial in changing deformation at increased strains—do not have a strong effect on properties at low strains. This is because there is little resistance to early deformation since many of the covalent crosslinks don't feel the 'tension' of the deformation yet; deformation in loosely crosslinked elastomers results in reorganization of the network and unraveling of strands prior to engagement of covalent crosslinks and an marked increase in stress response.

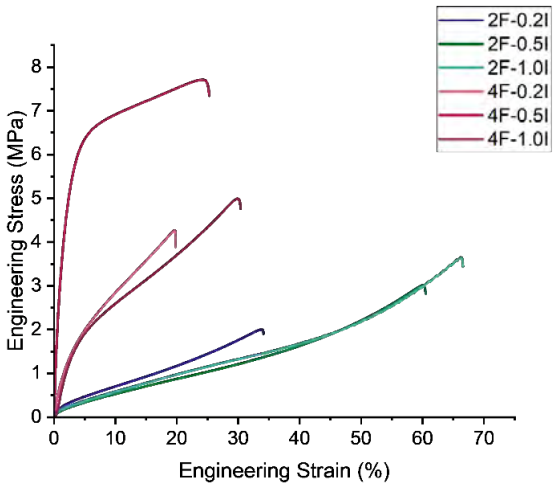


**Figure 6. Representative tensile curves of the printed samples.**

**Table 2. Measured tensile properties from printed samples. Yield stress (σy) was omitted for the 2F sample series due to no discernable value that could be calculated.**

| Sample | $E_Y$ (MPa) | $\varepsilon_b$ (%) | $\sigma_m$ (Mpa) | $\sigma_y$ (Mpa) | Toughness ($MJ/m^3$) |
|---|---|---|---|---|---|
| **2F-0.2I** | 6.30 ± 0.73 | 35.1 ± 1.8 | 2.19 ± 0.32 | - | 0.391 ± 0.07 |
| **2F-0.5I** | 5.16 ± 0.41 | 58.6 ± 3.3 | 2.93 ± 0.44 | - | 0.790 ± 0.12 |
| **2F-1.0I** | 5.51 ± 0.38 | 66.2 ± 0.7 | 3.64 ± 0.17 | - | 1.04 ± 0.06 |
| **4F-0.2I** | 4.74 ± 1.2 | 17.8 ± 2.9 | 4.94 ± 0.49 | 2.84 ± 0.71 | 0.605 ± 0.10 |
| **4F-0.5I** | 8.98 ± 0.12 | 26.6 ± 2.3 | 7.20 ± 0.51 | 6.01 ± 0.37 | 1.76 ± 0.07 |
| **4F-1.0I** | 3.44 ± 0.19 | 30.7 ± 2.6 | 5.11 ± 0.23 | 1.93 ± 0.19 | 1.00 ± 0.09 |

Conversely, the 4F samples show a more plastic deformation, with an apparent yield stress ($\sigma_y$) and higher stress values attained on average when compared to the softer, more deformable 2F materials. This can immediately be related to the limited mobility of the crosslink junctions when the crosslinker functionality is increased from 2 to 4. A more highly constrained network will be unable to reorient itself during deformation, increasing the stress response as noted in the tensile curves. Interestingly, the 4F-0.5I sample shows by far the highest values of $E_y$, σy, and σm of the 4F series, more than doubling the values in some cases. This behavior greatly contrasts the measured values in TTS, where similar values of crosslink density and fragility would indicate the 4F materials to behave in a similar trend to the 2F systems. Instead, the 'push-pull' dynamics of the polymerization here result in optimal mechanics being achieved for 4F-0.5I alone, which can be explained by the starting initiator concentration. At low loadings of BAPO, there is an increased propensity for early radical termination causing dangling chain ends to form, reducing the effective crosslink density and detracting from the mechanical response of the material. On the other hand, increasing the initiator concentration also increases the concentration of microgels that form early in the polymerization as mentioned above. Microgels can contain trapped crosslinks that do not contribute to the bulk mechanics effectively due to clustering of highly crosslinked regimes, resulting in an overall reduction in the $E_y$ and a further limitation to the amount of energy that can be absorbed by the network prior to failure. Furthermore, the high crosslink density of microgels cause surrounding chains to contain relatively few crosslinks, leading to a decrease in the overall mechanical properties. This behavior has been noted in bimodal silicone elastomers designed with and without heterogeneity during crosslinking. As a result of this greater heterogeneity, there is a substantial decrease in the measured tensile properties of 4F-1.0I. The nano- and microstructural changes measured using DMA propagate to the macroscale mechanical properties observed in the printed samples; however, it is important to note that without tensile properties being measured, an incomplete picture of the network topology and its consequences on print

properties would be developed. This study highlights that is not only the degree of crosslinking, but how these crosslinks are distributed relative to one another that dictate bulk behavior.

## 4. CONCLUSION

This study highlights the effects of small changes in resin chemistry on the network connectivity and properties of a series of 3D printed samples. When comparing difunctional and tetrafunctional crosslinkers at identical concentrations, greater network heterogeneityis noted as an increased peak width in the DMA tanδ curve. Interestingly, this heterogeneity is directly impacted by the concentration of photoinitiator even when the overall printed objects have similar conversions after printing and post-processing. In both the case of the difunctional and tetrafunctional crosslinking resin, increasing the initiator concentration increased the effective crosslink density and fragility of the network while also increasing the heterogeneity. This is particularly true in the 4F tetrafunctional prints, where the $T_g$ and tensile properties all reach a maximum in the case of 0.5 mol% BAPO loading. This is surmised to be caused by a balance between rapid network conversion: to minimize early termination and dangling chain end formation, and to minimize the concentration of microgels, which are directly tied to the number of initiation sites. This optimal range of print properties highlights the need to understand polymerization kinetics and chain connectivity in photopolymerized thermosets.

## ACKNOWLEDGMENTS

Funding for this Seedling project was made available through the Department of Defense Funding Laboratory Enhancements Across (X) Four Categories (FLEX 4) in accordance with the Army, Navy, and Air Force efforts funded under the authority in 10 U.S.C. § 4123 through the Fabrication Advanced Materials/Manufacturing Sciences campaign.

## REFERENCES

[1] Boydston, A.J.; Cao, B.; Nelson, A.; Ono, R.J.; Saha, A.; Schwartz, J.J.; Thrasher, C.J. Additive manufacturing with stimuli-responsive materials. *J. Mater. Chem. A.* **2018**, *6*, pp 20621–20645.

[2] Ge, Q.; Jian, B.; Li, H. Shaping soft materials via digital light processing-based 3D printing: A review. *Forces Mech.* **2022**, *6*, p 100074.

[3] Bagheri, A.; Jin, J. Photopolymerization in 3D Printing. *ACS Appl. Polym. Mater.* **2019**, *1*, pp 593–611.

[4] Sahrir, C.D.; Ruslin, M.; Lee, S.-Y.; Lin, W.C. Effect of various post-curing light intensities, times, and energy levels on the color of 3D-printed resin crowns. *J Dent. Sci.* **2023**, *19* (1), pp 357–363.

[5] Schittecatte, L.; Geertsen, V.; Bonamy, D.; Nguyen, T.; Guenoun, P. From resin formulation and process parameters to the final mechanical properties of 3D printed acrylate materials. *MRS Commun.* **2023**, *13,* pp 357–377.

[6] Uzcategui, A.C.; Higgins, C.I.; Hergert, J.E.; Tomaschke, A,E.; Crespo-Cuevas, V.; Ferguson, V.L.; Bryant, S.J.; McLeod, R.R.; Killgore, J.P. Microscale Photopatterning of Through-Thickness Modulus in a Monolithic and Functionally Graded 3D-Printed Part. *Small Sci.* **2021**, *1* (3), p 2000017.

[7] Higgins, C.I.; Brown, T.E.; Killgore, J.P. Digital light processing in a hybrid atomic force microscope: In Situ, nanoscale characterization of the printing process. *Addit. Manuf.* **2021**, *38*, p 101744.

[8] Elliott, J. E.; Bowman, C.N. Kinetics of primary cyclization reactions in cross-linked polymers: An analytical and numerical approach to heterogeneity in network formation. *Macromolecules.* **1999**, *32* (25), pp 8621–8628.

[9] Lovell, L.G.; Berchtold, K.A.; Elliott, J.E.; Lu, H.; Bowman, C.N. Understanding the kinetics and network formation of dimethacrylate dental resins. *Polym. Adv. Technol.* **2001**, *12* (6), pp 335–345.

[10] Wen, M.; Scriven, L.E.; McCormick, A.V. Kinetic gelation modeling: Kinetics of cross-linking polymerization. *Macromolecules.* **2003**, *36* (11), pp 4151–4159.

[11] Terrones, G.; Pearlstein, A.J. Effects of kinetics and optical attenuation on the completeness, uniformity, and dynamics of monomer conversion in free-radical photopolymerizations. *Macromolecules.* **2001**, *34* (26), pp 8894–8906.

[12] Reid, A.; Jackson, J.C.; Windmill, J.F.C. Voxel based method for predictive modelling of solidification and stress in digital light processing based additive manufacture. *Soft Matter*. **2021**, *17* (7), pp 1881–1887.
[13] Jangizehi, A.; Schmid, F.; Besenius, P.; Kremer, K.; Seiffert, S. Defects and defect engineering in Soft Matter. *Soft Matter*. **2020**, *16* (48), pp 10809–10859.
[14] Seiffert, S. Origin of nanostructural inhomogeneity in polymer-network gels. *Polym. Chem.* **2017**, *8* (31), pp 4472–4487.
[15] Lin, T.-S.; Wang, R.; Johnson, J.A.; Olsen, B.D. Topological Structure of Networks Formed from Symmetric Four-Arm Precursors. *Macromolecules*. **2018**, *51* (3), pp 1224–1231.
[16] Anseth, K.S.; Bowman, C.N.; Peppas, N.A. Polymerization kinetics and volume relaxation behavior of photopolymerized multifunctional monomers producing highly crosslinked networks. *J. Polym. Sci., Part A: Polym. Chem.* **1994**, *32* (1), pp 139–147.
[17] Anseth, K.S.; Anderson, K.J.; Bowman, C.N. Radical concentrations, environments, and reactivities during crosslinking polymerizations. *Macromol. Chem. Phys.* **1996**, *197* (3), 833-848.
[18] Young, J.S.; Kannurpatti, A.R.; Bowman, C.N. Effect of comonomer concentration and functionality on photopolymerization rates, mechanical properties and heterogeneity of the polymer. *Macromolecular Chemistry and Physics.* **1998**, *199* (6), pp 1043–1049.
[19] Jones, B.H.; Alam, T.M.; Lee, S.; Celina, M.C.; Allers, J.P.; Park, S.; Chen, L.; Martinez, E.J.; Unangst, J.L. Curing Behavior, Chain Dynamics, and Microstructure of High $T_g$ Thiol-Acrylate Networks with Systematically Varied Network Heterogeneity. *Polymer.* **2020**, *205*, p 122783.
[20] Yu, J.W.; Jung, J.; Choi, Y.-M.; Choi, J.H.; Yu, J.; Lee, J.K.; You, N.-H.; Goh, M. Enhancement of the crosslink density, glass transition temperature, and strength of epoxy resin by using functionalized graphene oxide co-curing agents. *Polym. Chem.* **2016**, *7* (1), pp 36–43.
[21] Anastasio, R.; Peerbooms, W.; Cardinaels, R.; van Breemen, L.C.A. Characterization of Ultraviolet-Cured Methacrylate Networks: From Photopolymerization to Ultimate Mechanical Properties. *Macromolecules.* **2019**, *52* (23), pp 9220–9231.
[22] Elliott, J.E.; Bowman, C.N. Monomer functionality and polymer network formation. *Macromolecules.* **2001**, *34* (13), pp 4642–4649.
[23] Shundo, A.; Aoki, M.; Yamamoto, S.; Tanaka, K. Effect of Cross-Linking Density on Horizontal and Vertical Shift Factors in Linear Viscoelastic Functions of Epoxy Resins. *Macromolecules.* **2021**, *54* (20), pp 9618–9624.

# Beyond behavior: identifying correlates of olfactory responses in military working dogs using physiological monitoring and machine learning

Edgar O. Aviles-Rosa[a], Nathaniel J. Hall[a], Jörg Schultz[b], Brian D. Farr[c], Andrea L. Henderson[c], Erin B. Perry[d], Dakota R. Discepolo[d,j,i], Dana M. Pasquale[e], Eric M. Best [f], Debra L. Zoran[g], Caitlin E. Sharpes[h,j], Michele N. Maughan[h,j], Jenna D. Gadberry[h,j], Aleksandr E. Miklos[j], Patricia E. Buckley[j]*

[a]Texas Tech University, 2500 Broadway West, Lubbock, TX 79409

[b]Tier Wohl Team GbR, Am Muhlschutz 2, 97348 Rödelsee, Germany

[c]Department of Defense Military Working Dog Veterinary Service, Joint Base San Antonio-Lackland, 1219 Knight St, Building 7602, San Antonio, TX 78236

[d]Southern Illinois University, Department of Animal Science, Food and Nutrition, 1263 Lincoln Dr, Carbondale, IL 62901

[e]Valiant Harbor International LLC, 4800 Hampden Ln, Bethesda, MD 20814

[f]University at Albany, College of Emergency Preparedness, Homeland Security and Cybersecurity, 1400 Washington Ave, Albany, NY 12222

[g]Texas A&M University, College of Veterinary Medicine, 400 Bizzell St, College Station, TX 77843

[h]Excet Inc., 6225 Brandon Ave, Suite 360, Springfield, VA 22150

[i]Oak Ridge Institute for Science and Education, 1299 Bethel Valley Rd, Oak Ridge, TN 37830

[j]U.S. Army Combat Capabilities Development Command Chemical Biological Center, Research & Operations Directorate, 8198 Blackhawk Rd, Aberdeen Proving Ground, MD 21010

## ABSTRACT

Detection canines serve critical roles to support the military, homeland security and border protection. Similar to human personnel, dogs are subject to physiological and psychological variables that can influence performance, but the nature and magnitude of these effects are almost entirely unknown. The impact of physical activity on canine olfactory detection thresholds was assessed using a treadmill with automated olfactometry. Dogs showed a substantial decrement in olfactory detection for low odor concentrations under greater physical activity, dropping from an 85 % hit rate to < 50 % hit rate when exercising at 8 Km/h compared to 4 Km/h. Within a session, performance declined with duration, showing near 100 % alert rates at the start of a session and ending near 0 % alert rates after 30 min at 8 Km/h for the lowest concentration odor. Accelerometry and heart rate measurements were used with a Support Vector Machine (SVM) from over 1200 odor present trials to predict whether a trial would end in a hit or a miss. The SVM reached over 90 % overall accuracy and predicted hits at 94 % accuracy and misses at 73 % accuracy, indicating that physical activity monitoring may be a fruitful method to predict potential olfactory detection sensitivity losses due to physical exertion.

**Keywords:** detection canines, machine learning, olfaction, detection threshold, accelerometry

## 1. INTRODUCTION

Working dogs serve critical detection roles for the military, homeland security, border protection, and the biosecurity of food and fiber.[1–3] Within the armed forces, dogs remain the primary tool for in-the-field detection of concealed explosives. Dogs primarily detect these threats through olfaction (i.e., their sense of smell), which enables them to identify trace vapors released from explosive substances.[4]

Still, dogs are not electronic sensors, and like human security personnel, performance is influenced by a myriad of environmental, psychological and biological factors.[5] Indeed, for humans, these factors are well studied. Factors like

attention,[6,7] mental fatigue,[8,9] environmental conditions, sleep deprivation, motivation, to name just a few, have been shown to critically influence performance. In contrast, for detection dogs, only a handful of studies have investigated the impacts of physiological conditions on performance. Factors such as physical fitness and dietary polyunsaturated fat ratios have in some cases led to improved detection capabilities.[10] In contrast, administration of the antibiotic metronidazole may have a negative impact on olfaction.[11] In previous work, we demonstrated that extreme hot and humid environmental conditions can substantially impact dogs' detection limits for a target odor.[12] Similarly, there is some evidence that detection performance for explosives decreases when dogs are under physical exertion.[13]

In addition to these physiological factors, psychological factors can also influence performance. To this end, dogs show decrements in detection when working in environments with very low target densities.[14] Nonetheless, almost no studies have evaluated olfactory performance of a detection dog during physical exercise while directly measuring physiological parameters. Such data would provide unique insights into the relationship between physiology, psychology, and olfaction.

One potential barrier to such research are the few available tools for measuring canine physiology in working animals. More commercial sensors are becoming available for veterinary use, but fewer are available for working dogs. Further, most available sensors are re-purposing of commercial tools for humans, such as the Polar™ heart rate monitor[15] or Actigraph™ accelerometer.[16] There remains a need to identify and evaluate commercial and custom research tools to measure canine physiology.

Additionally, there are minimal tools to standardize assessment of canine detection capabilities. Our team has recently worked to develop such tools for olfactory assessment developing olfactometers designed for canine use.[17] These tools allow the presentation of a standardized and verifiable odor concentration, automatically score the dog's response to the odor presentation, and synchronize performance with physiological data collection.

The aim of this project is to leverage our recently developed olfactory presentation technology (e.g., olfactometers), advances in machine learning, and physiological monitoring advances to assess changes in olfactory detection capabilities when dogs undergo different standardized levels of physical exertion on a treadmill. With this approach, we can elucidate novel relationships between canine physical activity, physiology, and olfactory detection capabilities.

## 2. MATERIALS AND METHODS

### 2.1 General

The study was conducted at the Texas Tech University Canine Olfaction Research and Education Lab. All procedures were approved by the Institutional Animal Care and Use Committee (protocol # 21051-07). Three dogs (3 years of age) were the participants of the study (two neutered males (Charles and Dasty) and one spayed female (Ziggy)). Two dogs (Dasty and Charles) had extensive experience with olfactometers while Ziggy was naive to olfactometers. All three dogs were in good physical condition and owners did not report any history of physical injury or illness. Prior to the study, owners indicated that Dasty and Ziggy did not perform regular extensive cardiovascular physical activity other than going on regular walks with their owner and having some play time (e.g., playing fetch) at the park or their home. Charles had a consistent history of physical activity that included sporadic runs with their owner and multiple weekly sessions of physical conditioning exercises (i.e., Pen Vet Working Dog Fit to Work Program). All testing was conducted at room temperature in a climate-controlled room. Testing was conducted from 0800–1300 depending on owners' availability. Dogs received one or two testing sessions a day (see below for details). After a running session, all dogs receive a high calorie supplement (Nutri-cal, Vetoquinol USA) for replenishing energy, vitamins and minerals as directed by a veterinarian. Dogs had a recovery time of 24 h after a running session.

### 2.2 Apparatus

To test how dogs' olfactory sensitivity was affected by physical activity, we coupled an olfactometer with a treadmill (Figure 1). This allowed the dog's olfactory performance to be tested during walking or trotting. The olfactometer used was similar to versions previously published and involved air generated by an air pump passed through a charcoal filter before entering the system.[17]. Air flow was regulated and maintained constant using rotameters (Dwyer VFB™). The olfactometer had six odor channels that allowed the presentation of up to six different odors or different dilutions of the same odorant. Each odor channel was connected to a borosilicate odor jar (40 mL) by piercing the septa of the jar with a polytetrafluoroethylene (PTFE) tubing connected to a stainless-steel push to connect fitting. The activation and deactivation of the valves was conducted by a custom computer program. When a valve was activated, air from

the odor line (2 L/m) entered the odor vial and carried the headspace of the jar through another PTFE tubing that carried the headspace to a PTFE manifold where it was mixed with a continuous air stream (8 L/m). Check valves in the manifold prevented back flow of air to the odor jar. The final air dilution (20 % v/v) of the odorant was then presented to the dog in an odor port mounted into a polypropylene panel. This panel had a wood frame that supported it on top of the treadmill (Dogtread Pz-1703) at a height of 55 cm. Infrared (IR) sensors were located at the side of the odor port to measure if a dog responded to the odor presented during a trial. Dogs were trained to respond to the target odor by poking the odor port and thus breaking the IR beam with their nose. A small fan (40 x 40 x 10 mm; Sunon, HA40101V4-0000-C99) was on top of the odor port. This was activated at the end of a trial to help with odor clearance. All testing was conducted double blind. Odor randomization, odor presentation, and data collection was conducted by the olfactometer program.

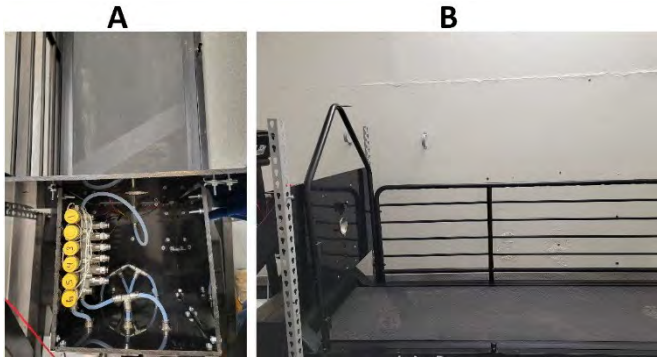


**Figure 1. Testing apparatus. A: Olfactometer mounted on the panel in front of the treadmill. B: Side view of the apparatus including the treadmill and the panel containing the odor port (silver circle on the panel).**

### 2.3 Odor delivery validation

A photoionization detector (PID) (200B miniPID, Aurora Scientific, Canada) was used to validate odor delivery of the system and ensure an odor signal was detectable at different points within the treadmill. We utilized limonene (CAS # 5989-54-8) diluted in mineral oil (5 x $10^{-2}$ v/v) as the trace odorant for this analysis to facilitate odor detection by the sensor. For analysis, the sensor was mounted on a stand at odor port height and the stand was placed on the treadmill at different distances from the odor port (i.e., 7–76 cm). During testing, the experimenter placed the PID at a specific distance and activated the computer program that controlled the odor valve. The program ran a loop that activated the odor valve for 45 s and deactivated the valve for 60 s to allow for odor clearance between cycles. In addition, the program sent a voltage signal that marked when the odor valve was activated. This cycle was repeated ten times (i.e., ten trials or rep at each distance). The odor line was set at 2 L/m and the continuous line at 8 L/m. The different distances evaluated were tested in random order. The voltage reading of the PID at 500 Hz was recorded during the activation and deactivation cycles. To graph the voltage signal obtained from the PID, the raw readings were filtered with a low-pass Butterworth filter at a scalar of 0.01 of the Nyquist frequency using the signal package in R studio. The voltage signal indicating the activation of the odor valve was superimposed to better visualize periods where the odor valve was activated or deactivated. To address sensor drift from baseline (i.e., negative voltage values) we calculated the average voltage reading during baseline (no odor valve activation) from the average value during odor valve activation. A positive voltage indicates that the sensor detected the odorant. A regression analysis was conducted to evaluate the effect of distance on changes in voltage when the odor valve was activated.

### 2.4 Training

Dogs were conditioned to walk and trot on the treadmill without the olfactometer and without incline. Dogs were gradually acclimatized until trotting on the treadmill at 8 Km/h following an acclimatization plan.[18] For dogs' safety, the experimenter always had the leash on hand (with no pressure on the dog) and the leash was attached to the harness.

After dogs were conditioned to the treadmill, we introduced the olfactometer panel. Dogs were trained to perform a Go/No-go task while walking (4 Km/h) and trotting (8 Km/h) on the treadmill. We used 1-Bromooactane (CAS # 111-83-1) diluted in food grade mineral oil ($10^{-1}$ v/v) as the target odor during training (CS+). Olfactometer training was divided into distinct phases. The first phase of training consisted of training dogs to the "Go" response. Herein the "Go" response consisted of poking the odor port (breaking the IR beam) when the target odor was presented

while simultaneously walking or trotting on the treadmill. For this we gave dogs 20 trial sessions at a target odor prevalence of 100 % (i.e., all 20 trials contained the target odor) while they were walking. A trial consisted of the activation of the odor valve for 20 seconds followed by a 10 second intertrial interval (ITI) where the odor valve was deactivated. During the 20 seconds where the odor valve was activated the experimenter reinforced successive approximations to the odor port (i.e., shaping). This was repeated until dogs were triggering the IR sensor in front of the port within the 20 seconds the odor valve was activated. Responses during the ITI were not reinforced (i.e., extinction). This was repeated until dogs learned to activate the IR sensor for at least 0.4 consecutive seconds while simultaneously walking.

Once dogs were triggering the IR consistently at the presentation of the CS+ stimulus, we initiated the second training phase. The second phase of training consisted of training the "No-go" response. The "No-go" response was not poking the odor port for a predetermined amount of time when distractor odors or diluent were presented (CS-). For training the No-go response, dogs received 20 trial sessions at a target odor frequency of 50 % (i.e., target odor was presented only in 10 trials). A blank vial, mineral oil, Limonene (CAS # 5989-54-8; $10^{-2}$ v/v), Hexanal (CAS # 66–25–1; $10^{-2}$ v/v), and Isobutyl propionate (CAS # 540-42-1; $10^{-2}$ v/v) were used as distractor odors (CS-). Odor presentation was randomized by the computer program and on CS- trials each distractor odor had equal probability of being selected. The duration of a trial was as described in phase one. During initial training, "Go" responses to the CS- did not result in the termination of the trial. Responses to CS- were ignored (i.e., not reinforced) and the trial continued until the dog stopped showing the "Go" response for at least 3 consecutive seconds. Not responding to the CS- for three consecutive seconds was reinforced by the experimenter and resulted in the termination of the trial. Training in this phase continued until the number of trials within a session was gradually increased from 20 to 60 and the time criterion for recording a "No-go" response from 3 to 8 consecutive seconds. Within a session, a dogs' pace was alternated between walking (4 Km/h) and trotting (8 Km/h) until they were able to perform all 60 trials trotting (~15–20 minutes).

At the end of training, the final reinforcement rate for correct rejections (i.e., correct "No-go" responses) was 40 % and false alerts (i.e., "Go" response to CS-) and false rejections (i.e., "No-go" response to CS+) resulted in the termination of the trial with no reinforcement. A dog was considered trained once all training parameters were met and their proportion of correct responses was ≥ 80 % within a session.

### 2.5 Testing

A testing session consisted of 100 trials in the "Go"/"No-go" paradigm at a target odor frequency of 50 % and a reinforcement rate of 40 % for correct rejections and 100 % for correct "Go" responses (Hits). The order in which odors (i.e., CS+ or CS-) were presented and the trails to be reinforced were randomized by the computer program each session. A trial consisted of the activation of the odor valve (CS+ or CS-) for 20 seconds and an ITI of 10 seconds to allow for odor clearance before the following trial. The "Go" response consisted of poking the odor port and breaking the IR beam for at least 0.4 seconds. The "No-go" response consisted of not showing the "Go" response for 8 consecutive seconds after an odor valve was activated. All testing was conducted double blind. The computer utilized different tones to indicate if dogs' responses were correct or incorrect and when to deliver the reinforcer. False alerts, and odor misses were marked by the computer program with a "buzzer" sound. These responses were not reinforced and resulted in the immediate termination of the trial. Hits and correct rejection preprogrammed to be reinforced were marked with a "bleep" sound. These responses were reinforced by the handler. Unreinforced correct rejections were not marked with a tone. For all dogs, food was used as the reinforcer. The duration of a testing session ranged from 28–32 minutes.

For threshold assessment, we presented dogs with four different half-log liquid dilutions of 1-Bromooctane (CS+) within a session at random order while they were simultaneously at a trotting (8 Km/h) or walking (4 Km/h) pace on the treadmill (see Figure 2). Diluent mineral oil was used as the CS-. The threshold assessment was divided into different descending steps to accommodate the four-dilution capacity of the olfactometer (see Figure 2). The CS- (mineral oil) and each concentration of 1-Bromooctane were presented randomly within a session. The computer program also balanced the number of times each concentration was presented (i.e., each concentration was presented 12–13 times per session). Dogs received a total of 4 testing sessions in each step. Two of these sessions were walking (4 Km/h) and two were trotting (8 Km/h). We defined threshold as the concentration at which dogs Hit rate was ≤ 50 %. If a dog's average Hit rate to the lowest concentration tested in a step was > 50 % at a walk and a trot pace, they moved to the next step. During the next step we tested dogs with the lowest concentration of the previous step and with 3 new lower half-log concentrations. We included the lowest concentration from the previous step to ensure

at least one of the concentrations was above the dogs' threshold. This process was repeated until dogs reached threshold criteria at either a walk or a trot pace.

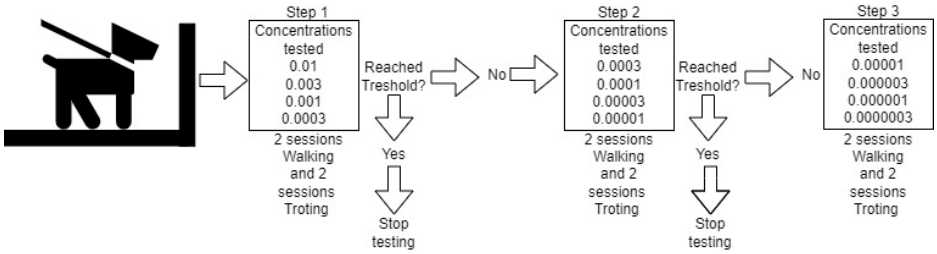


**Figure 2. Testing Paradigm. Dogs' detection threshold was tested in a descending series of odor concentrations ("steps").**

During each session we calculated dogs' latency to respond during trials where CS+ was presented, their Hit, False, miss, and correct rejection rates. Attached to the dogs' harness was the Actigraph GT3X accelerometer (Actigraph) to measure accelerometry. We also measured dogs' heart rate (HR) using the Polar® H10. The HR sensor was attached to dogs' chest using the manufacture's strap and vet wrap was used to maintain it in place during the session. Ultrasound gel was applied to improve HR readings. Measures from the 3-axis of the accelerometer and the Polar® H10 were collected every second for the duration of the session using the Actilife® software.

### 2.6 Statistical analysis

Hit rates were calculated for each concentration and pace. For this we divided the number of times a dog responded to a concentration over the number of times that concentration was presented. Similarly, the False alert rate was calculated by dividing responses to the CS- over the number of times CS- was presented to the dog. An odor miss was calculated as the number of no responses to a concentration over the number of times the concentration was presented. Correct rejections were calculated as the number of no responses to the CS- over the number of times the CS- was presented. Latency to respond was defined as the amount of time a dog required to trigger the IR sensor after the odor valve was activated. If a dog did not respond to the CS+ within a trial, we assigned a latency score of 10 s. This was to numerically reflect that the dog did not respond in the allotted time.

HR and accelerometry data was collected using the Actigraph (wGT3X-BT) Polar H10 and Actilife® software. Using timestamps from the Actilife software and the olfactometer program we were able to calculate an average HR reading, an average accelerometry count per trial and a sum of vector magnitude. Subsequently we calculated the cumulative accelerometry values from the trial averages for each of the three axes and vector magnitude. These cumulative values reflected total activity over the session up until the trial in question.

To evaluate the relationship amongst the physiological measures with olfactory performance, we conducted a series of exploratory analyses on trials in which odor was present (excluding no odor trials). We used Pearson correlations and correlation matrices to evaluate correlations amongst the measures obtained and computed from the heart rate monitor and accelerometer. To reduce the number of variables and reduce redundancy in measures, a Principal Component Analysis (PCA) was performed to identify uncorrelated components that optimally summarize the physiological measures.

Lastly, a support vector machine (SVM) was used to evaluate whether it could classify the probability of a correct hit, or a miss, based on the physiological measures. First, a PCA was conducted on the predictor data set (ten physiological measures from Polar and Actigraph and session time of the trial). Next, the data sample was split into a training data set (80 % of data or 960 trials) and a test data set (20 % of trials or 251 trials). The SVM was trained on the training set using the principal components and evaluated for prediction accuracy on the test data set. Using a re-sampling procedure, the training and test data set were re-sampled for 1,000 runs and the SVM mean test accuracy, sensitivity and specificity are reported.

## 3. RESULTS

To validate the overall setup, distribution of target odor was measured using the PID. With an airflow of 10 L/m, and an air dilution of 20 %, limonene volatiles were readily detected at 45.72 cm away from the odor port or less. Even at this distance, the PID showed noticeable voltage increments immediately after the odor valve was activated. Odor

concentration, as measured by voltage increment, versus distance followed the expected logarithmic relationship ($P < 0.001$; $R^2 = 0.92$ with the linear regression model $y = -0.0795\ln(x) + 0.255$).

In the next step, three dogs (Dasty, Charles, Ziggy) were trained to indicate the odor. All three dogs learned the "Go"/"No-go" task successfully. Dasty and Charles met training criterion withing 15 and 14 training sessions, respectively. Ziggy met training criterion within 26 training sessions. Prior to testing, false alerts and misses were 5.0% ± 1.7 (SE) and 2.0% ± 1.0 (SE), respectively. The percentage of correct responses to 1-Bromooctane (CS+) for all dogs was ≥ 90 %.

We then measured each dog' olfactory performance during a walk and a trot (Figure 3). All dogs reached threshold (≤ 50 % hit rate) at a trotting pace first. Dasty and Ziggy's threshold at a trot was at a dilution $10^{-5}$ v/v. Charles' threshold at a trot was at a dilution of $10^{-6}$. Contrasting the trot, at a walk, hit rates of all dogs for all the concentrations were over 70 %. Thus, dogs were still able to detect even the lowest concentrations tested at a walk with proficiency. Overall, Ziggy showed lower hit rates during a walk relative to Charles and Dasty. Dogs' latency to respond increased with an increase in odor dilution at a walk and a trot pace. However, the increment in latency was greater at a trot. Data also show how the latency to respond was different between dogs. Overall Ziggy required more time to respond than Dasty and Charles. These differences in Ziggy's performance could have been due to her previous inexperience in odor detection. Taken together, these results show that the performance in the detection tasks correlates with physical exercise (walk vs. trot). Furthermore, the show that the general setup enables the detection and quantification of performance differences between individual dogs.

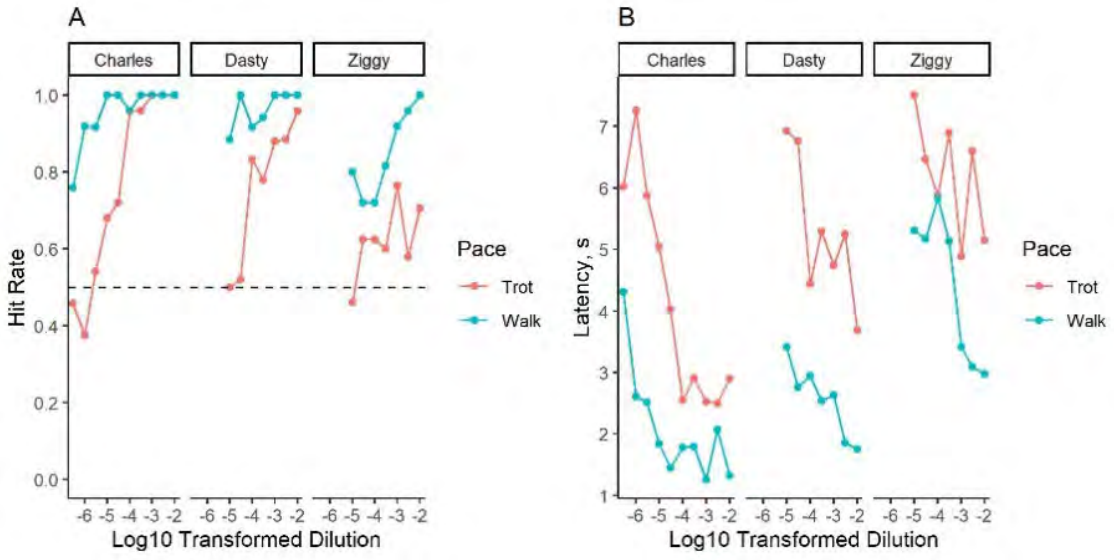


**Figure 3. Performance decrement under physical exertion. A: Dashed lined indicates a hit rate of 0.50, our threshold criterion. B: Change in latency to respond on an odor present trial. Latency to respond increases with dilution and is greater under a trot pace.**

To enable the identification of common features despite individual differences, we analyzed the performance in relation to each dog's individual threshold as defined above (Figure 4). We found that the dogs maintained hit rates > 80 % during both a trot and walk pace at concentrations at least 2 log steps (100-fold) above threshold. Hit rates at concentrations below 2 log steps above threshold remained above 80 % at a walk. Contrasting, they gradually declined to < 50 % at a trot. On the same line, the latency of an indication increased with lower concentrations at a trot but not at a walk.

To evaluate when dogs started showing this decrement in hit rates and an increase in latency, data were grouped in blocks of 25 trials (Figure 4 C, 4D). The hit rate decreased with trial at both paces. However, at a walking pace, the average hit rate for all concentration tested was never < 76 %, even during the last 25 trials. At a trot, dogs showed robust response rate (≥ 80 %) to all concentrations tested during the first 25 trials. An initial decrement in response rate to dogs' threshold concentration was observed after trial 25 (~ 7.22 ± 0.14 minutes after the beginning of the session). Response rate to the threshold concentration continued decreasing with trial at a trot pace and after trial 75

(~ 22.72 ± 0.28 minutes after the beginning of the session) dogs' response rate to the threshold concentration was 0 % (although at a walking pace hit rate was at 76 %). A similar but less pronounced effect was observed for concentrations below 2 log steps above threshold. These results indicate that the decrement in olfactory sensitivity was not instantaneous, but rather was a result of increased physical activity (i.e., exertion) with time.

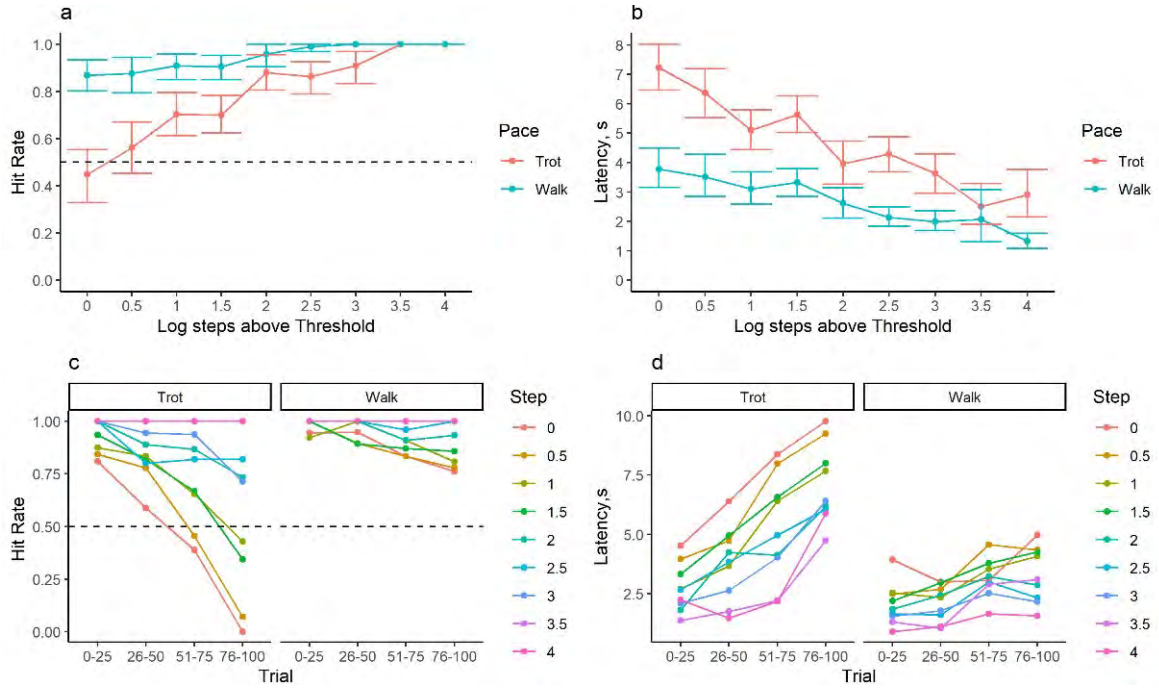


**Figure 4. Performance decrement in reference to threshold and session duration. A: Average Hit rate ± 95 % confidence interval for the CS+ at varying concentrations using dog threshold as reference point. Dashed lines indicate a hit rate of 50 %, which was our threshold criterion. B: Average latency to respond to the different concentrations tested using each dog's threshold as reference point. C: Average Hit rate to the different concentrations tested divided by 25 trials blocks within a session. D: Latency to respond increases across trials and at lower concentrations.**

To quantify the physical activity, we equipped the dogs with sensors tracking the acceleration in three axes (Actigraph) as well as the HR (Polar H10). Cumulative accelerometry values or counts increased linearly with trials and the effect was more pronounced at a trot. A trotting pace generated higher cumulative values for Axis 1, Axis 2, and VM (Vector Magnitude). Axis 3 did not show any difference in cumulative accelerometry counts between paces. These results show that the accelerometer data were able to detect differences in pace and that this difference was more pronounced for Axis 2 and for the VM.

Heart rate values did not increase with trial and remained relatively constant throughout the session, indicating dogs were not reaching their cardiovascular limits within the session. The average HR at a walk was 96.29 beats per minute (bpm) whereas it was 121.11 bpm during the trot. Dasty' s and Ziggy's HR at a walk were 86.55 ± 0.70 bpm and 88.01 ± 0.84 bpm, respectively. In contrast Charles' average HR at a walk was 117.83 ± 1.07 bpm. Despite HR differences between Charles and the other dogs at a walk, all dogs had similar HR at a trot. At a trot, Dasty showed the highest average HR (125.29 ± 0.15 bpm). Ziggy and Charles HR were 119.66 ± 0.39 bpm and 119.12 ± 0.27 bpm, respectively.

To evaluate the relationship amongst the measures recorded with olfactory performance, we first conducted a correlation matrix using data from trials where the CS+ was presented to identify the correlates of increased misses (Figure 5). We included HR, accelerometry measures, trial length (i.e., duration of the trial), latency to respond, the time at which a trial occurred after the begining of the session (trial minutes), concentration step above threshold, and trial accuracy (see Figure 5). Dogs' accuracy in the model was represented as a binary variable using 1 for hit and 0 for miss. The vector sum variable was calculated by adding all the VM measures within a trial. As expected all accelerometry variables were highly correlated between each other ($R>0.50$). Cumulative accelerometry measurements were also highly correlated with trial minutes, and showed a moderate correlation with trial length ($0.30<R<0.50$). This was expected because as the duration of the session increases the cumulative accelerometry also

increases. Trial length was correlated with odor misses and highly correlated with latency as expected (i.e., increased latency will increase the duration of the trial). Heart rate did not show any high or moderate correlation with any of the variables measured. Overall, accuracy was negatively correlated with cumulative accelerometry, trial minutes, trial length, and latency.

Given the important differences in accuracy based on concentration (Figure 4), we next explored the Pearson correlation analysis of when the odor concentration was within 2 log steps (i.e., peri-threshold) of threshold (Figure 5, right panel). Similar results were found but correlation coeffecients increased in relationship, which further confirms the importance of odor concentration.

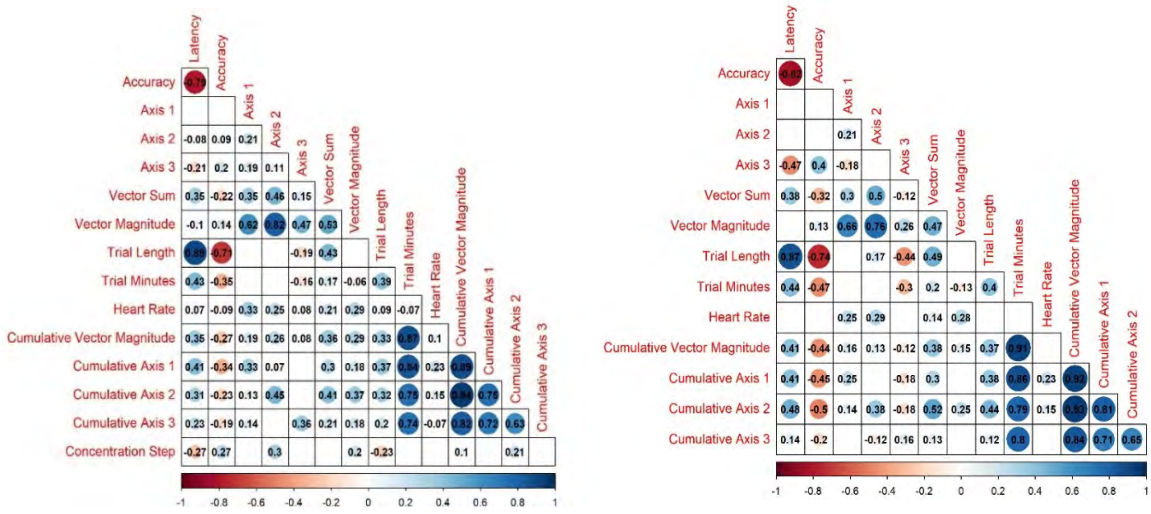


**Figure 5. Correlation matrix between all the accelerometry measurements, heart rate, and olfactory performance on odor present trials. Left shows all odor present trials. Right shows odor present trials where the concentration was within 100-fold of threshold.**

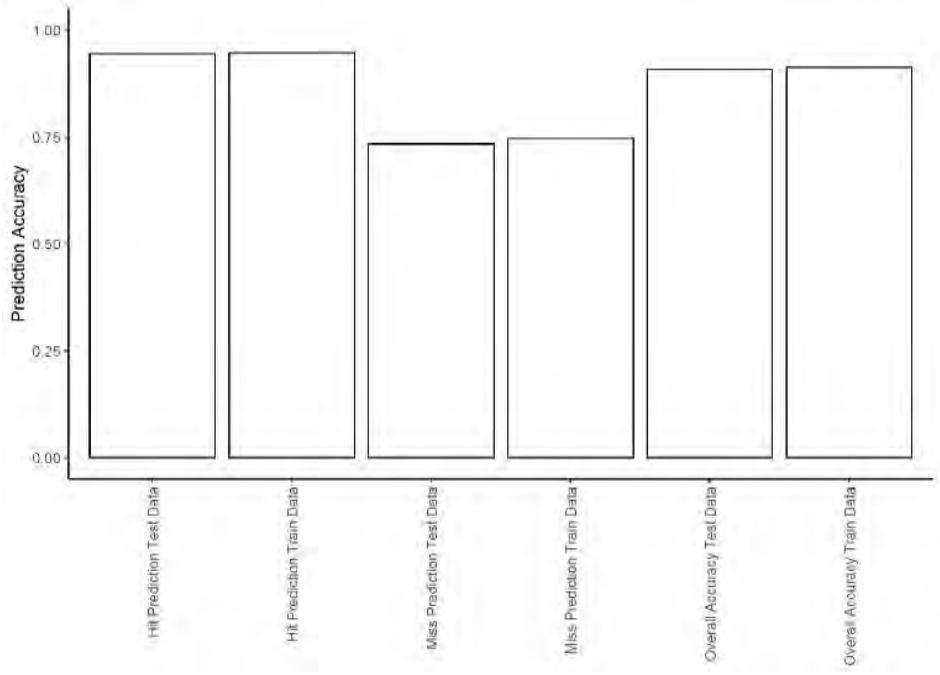


**Figure 6. Support VM prediction accuracy. The results averaged over 1,000 resamples are presented here.**

To further evaluate the predictive value of the independent variables measured, we conducted a principal component analysis (PCA) on all the trials in which odor was present (~ 1,200 trials). Only accelerometry, heart rate, and trial

minutes were included in the PCA model. We did not include latency and trial duration because these two measures are highly correlated between each other and are variables dependent on the paradigm. We also did not include step above threshold or odor concentration because these variables cannot be accurately measured outside of a laboratory setting. PC1-6 explained 97 % of the variance in the data.

A support vector machine was used to predict whether an odor present trial would end in a miss or a hit using the first six principal components as the predictor variables. Figure 6 shows the performance of the SVM over 1,000 re-samples of selecting the training (960 trials) and testing data set (250 trials). Overall, accuracy was highest in prediction of a hit, with >90 % accuracy. Prediction of miss could be made with ~75 % accuracy. Due to the fewer misses that occurred for SVM training, accuracy was lower in miss prediction. Nonetheless the SVM did lead to adequate overall accuracy in being able to predict a miss or hit.

## 4. DISCUSSION

To date, little is known about the effect of physical activity on dogs' olfactory sensitivity and detection performance. Due to the essential role detection dogs play in our national security, greater understanding of the effects of physical activity on dogs' olfactory sensitivity is imperative to maximize dogs' performance and ensure national security. Thus, the basic research conducted in this experiment is one of the first works to close the existing knowledge gaps.

Overall, we found that increased physical activity was negatively correlated with olfactory sensitivity. This was noted by an increase in the number of odor misses and latency after dogs were trotting for over 20 minutes. Surprisingly, the effect of physical activity on dogs' olfactory sensitivity was heavily dependent on the target odor concentration. For instance, a negative effect was only observed at odor concentrations within 100-fold of dogs' threshold. Unexpectedly, our study shows that a drop in performance happens in critical trace odor detection even when heart rate indicates only minor effort (~ 120 bpm) suggesting this research could lead to important implications on how and when to deploy dogs for low concentration odors.

We further found a significant correlation between the accelerometer sensor data and the performance of the dog. In particular, the cumulative accelerometry was highly correlated with the latency, sensitivity (as measured by detected odor concentration), and accuracy (number of false negatives) of the detection task. This result is a first indication that it indeed might be possible to use sensors to gain sufficient information about the physiological status of a working dog to predict performance.

This was further confirmed by the Support Vector Machine (SVM) which predicted whether a dog would indicate an odor with more than 90 % accuracy. More importantly, for a real mission scenario, the model was able to predict a miss (a false negative) with about 75 % accuracy based on physical activity and heart rate data. Although the quality of the prediction can still be improved, this clearly shows that prediction of detection performance based on sensor data is feasible.

We expect that the addition of further data covering the internal physiological status like the core body temperature, electrocardiogram or even heart rate variability as well as external observables like breathing pattern, mouth opening angle or even gait anomalies will increase the predictive value of the model. It is a strong advantage of the setup presented in this study that all measures can be performed in a highly controlled environment. This enables the evaluation of sensors as well as the isolation of physiological parameters which would not otherwise be possible.

This pilot study revealed that detection dog performance can drop within 20 mins of trotting at 8 Km/h, and that electronic sensors might be able to predict when this drop will happen. Although further studies covering more dogs as well as exploring additional sensor types are needed, it provides initial proof of principle that it might be possible to assist the dog handler in their decision on when to rest a detection dog. This could significantly improve the efficiency of bomb detection dog teams. Most importantly, this has the potential to reduce the risk to soldiers' lives by effectively minimizing the threat of explosive devices.

## ACKNOWLEDGMENTS

The authors would like to acknowledge Dr. Patricia McDaniel for mentorship, guidance, and indirect technical assistance. We would also like to acknowledge Dasty, Charles, and Ziggy for their hard work and effort. Funding was provided by the U.S. Army via the Chemical Biological Advanced Materials and Manufacturing Science (CBAMMS) Program (PE 0601102A Project VR9) at the Combat Capabilities Development Command Chemical Biological Center.

## REFERENCES

[1] Fjellanger, R. Remote Explosive Scent Tracing. In *Vapour and Trace Detection of Explosives for Anti-Terrorism Purposes*; NATO Science Series II: Mathematics, Physics and Chemistry; Springer Netherlands: Dordrecht, **2004**, pp 63–68.

[2] Lazarowski, L.; Dorman, D.C. Explosives Detection by Military Working Dogs: Olfactory Generalization from Components to Mixtures. *Appl. Anim. Behav. Sci.* **2014**, *151*, pp 84–93.

[3] Mendel, J.; Burns, C.; Kallifatidis, B.; Evans, E.; Crane, J.; Furton, K.G.; Mills, D. Agri-Dogs: Using Canines for Earlier Detection of Laurel Wilt Disease Affecting Avocado Trees in South Florida. *HortTechnology.* **2018**, *28* (2), pp 109–116.

[4] Gazit, I.; Terkel, J. Domination of Olfaction over Vision in Explosives Detection by Dogs. *Appl. Anim. Behav. Sci.* **2003**, *82* (1), pp 65–73.

[5] Furton, K.G.; Myers, L.J. The Scientific Foundation and Efficacy of the Use of Canines as Chemical Detectors for Explosives. *Talanta.* **2001**, *54* (3), pp 487–500.

[6] Ballard, J.C. Computerized Assessment of Sustained Attention: A Review of Factors Affecting Vigilance Performance. *J. Clin. Exp. Neuropsychol.* **1996**, *18* (6), pp 843–863.

[7] Hubal, R.; Mitroff, S.R.; Cain, M.S.; Scott, B.; DeWitt, R. Simulating a Vigilance Task: Extensible Technology for Baggage Security Assessment and Training. In *2010 IEEE International Conference on Technologies for Homeland Security (HST)*; **2010**; pp 543–548.

[8] Matthews, G.; Davies, D.R.; Holley, P.J. Cognitive Predictors of Vigilance. *Hum. Factors* **1993**, *35* (1), pp 3–24.

[9] Pattyn, N.; Neyt, X.; Henderickx, D.; Soetens, E. Psychophysiological Investigation of Vigilance Decrement: Boredom or Cognitive Fatigue? *Physiol. Behav.* **2008**, *93* (1), pp 369–378.

[10] Altom, E.K.; Davenport, G.M.; Myers, L.J.; Cummins, K.A. Effect of Dietary Fat Source and Exercise on Odorant-Detecting Ability of Canine Athletes. *Res. Vet. Sci.* **2003**, *75* (2), pp 149–155.

[11] Jenkins, E.K.; Lee-Fowler, T.M.; Angle, T.C.; Behrend, E.N.; Moore, G.E. Effects of Oral Administration of Metronidazole and Doxycycline on Olfactory Capabilities of Explosives Detection Dogs. *Am. J. Vet. Res.* **2016**, *77* (8), pp 906–912.

[12] Brustkern, M.; Thompson, R.; Lawhon, S.; Good, K.; Bunker, P.; Prada-Tiedemann, P.; Hall, N.J. Effect of Rapid Changes in Environmental Conditions on Canine Detection of Methyl Benzoate. *Appl. Anim. Behav. Sci.* **2023**, *264*, p 105924.

[13] Gazit, I.; Terkel, J. Explosives Detection by Sniffer Dogs Following Strenuous Physical Activity. *Appl. Anim. Behav. Sci.* **2003**, *81* (2), pp 149–161.

[14] Aviles-Rosa, E.O.; DeChant, M.T.; Prada-Tiedemann, P.A.; Hall, N.J. A Laboratory Model of Canine Search Vigilance Decrement, I. *J. Exp. Anal. Behav.* **2023**, *120* (1), pp 103–119.

[15] Essner, A.; Sjöström, R.; Ahlgren, E.; Gustås, P.; Edge-Hughes, L.; Zetterberg, L.; Hellström, K. Comparison of Polar® RS800CX Heart Rate Monitor and Electrocardiogram for Measuring Inter-Beat Intervals in Healthy Dogs. *Physiol. Behav.* **2015**, *138*, pp 247–253.

[16] Yam, P.S.; Penpraze, V.; Young, D.; Todd, M.S.; Cloney, A.D.; Houston-Callaghan, K.A.; Reilly, J.J. Validity, Practical Utility and Reliability of Actigraph Accelerometry for the Measurement of Habitual Physical Activity in Dogs. *J. Small Anim. Pract.* **2011**, *52* (2), pp 86–91.

[17] Aviles-Rosa, E.O.; Gallegos, S.F.; Prada-Tiedemann, P.A.; Hall, N.J. An Automated Canine Line-Up for Detection Dog Research. *Front. Vet. Sci.* **2021**, *8*, p 775381.

[18] Stigall, A.R.; Farr, B.D.; Ramos, M.T.; Otto, C.M. A Formalized Method to Acclimate Dogs to Voluntary Treadmill Locomotion at Various Speeds and Inclines. *Animals.* **2022**, *12* (5), p 567.

# Production of an iridescent surface using synthetic biology and a membrane sculpting protein

Daniel A. Phillips[a]*, John R. Biondo[a,b], Cheri M. Hampton[c,d], Christian L. Jednorski[e], Lily McCloskey[c], Jill B. Harland[f], Danielle L. Kuhn[a], Lawrence F. Drummy[c], Patricia E. Buckley[a], Aleksandr E. Miklos[a]
[a]U.S. Army Combat Capabilities Development Command Chemical Biological Center, Research & Operations Directorate, 8198 Blackhawk Rd, Aberdeen Proving Ground, MD 21010
[b]Excet Inc., 6225 Brandon Ave, Suite 360, Springfield, VA 22150
[c]Materials and Manufacturing Directorate, Air Force Research Laboratory, Wright-Patterson Air Force Base, Dayton, OH, 45433
[d]UES, Inc., 4401 Dayton Xenia Rd, Dayton, OH, 45433
[e]Oak Ridge Institute for Science and Education, 1299 Bethel Valley Rd, Oak Ridge, TN 37830
[f]National Research Council, 500 5th St NW, Washington, DC 20001

## ABSTRACT

Biology naturally excels at building precise structures at nanometer scales using a variety of biopolymers. Utilizing proteins to control the formation of these nanoscale structures can enable development of biomaterials with metamaterial properties like those found in nature, such as structural coloration. Membrane curvature formation mediated by Bin/Amphiphysin/Rvs domain proteins generates high aspect ratio tubule particles with dimensions that could be useful for making an obscurant. Here, we build on previous work investigating the *in vitro* membrane binding and remodeling activity of the Bin/Amphiphysin/Rvs domain-like protein BdpA by using these sculpted tubules as templates for plasmonic nanoparticles. Membranes sculpted with engineered BdpA constructs were incubated with gold salts and reduced to form metallic nanoparticles. The resultant tubule-templated nanoparticles changed visible color and shifted the absorbance spectra. BdpA protein bound to hydrophobic plastic produced structural coloration in the form of an iridescent film. Through synthetic biology and further investigation into forming and patterning high aspect ratio conductive materials, this work provides early steps toward the possibility of lightweight, adaptable biological metamaterials and next generation obscurants.

**Keywords:** Metamaterials, synthetic biology, membrane sculpting, Bin/Amphiphysin/Rvs domain, cell-free, tunable, obscurants, iridescence, biomaterials, biomanufacturing

## 1. INTRODUCTION

Examples of structural coloration exist throughout nature, from the brilliant blue color of the blue morpho butterfly's wings, the metallic blue marble berries, and to the tunable iridescent biofilms of *Cellulophaga lytica*.[1-4] Patterns of constructive and destructive interference, known as the thin film interference effect, can result in the production of an array of colors in the absence of pigment. Structural coloration, size, and patterning of particles, films, or membranes is essential to produce a specific effect, in a similar manner to modern, inorganic metamaterials.[5] This can be achieved through localized plasmonic effects that selectively reflect, cancel out, or steer wavelengths of incident electromagnetic radiation.

Because nature is already an expert at patterning optical metamaterials (OMMs) in the form of structural coloration, synthetic biology could be used to produce similar optical effects if the tools and design rules are properly understood. For example, the marble berry's metallic blue color is formed through a series of lipid stacks that give rise to the macroscale structural coloration.[2,3] Lipids are natural scaffolds and membrane structures in living cells, but forming lipids into these precisely ordered structures with the requisite dimensions to produce optical effects likely requires the assistance of membrane sculpting proteins or other scaffolding polymers. In eukaryotic cells, membrane sculpting mechanisms are tightly controlled and ubiquitous due to the necessity of membrane trafficking,

receptor recycling, organelle biogenesis, vesicle transport, and protein-lipid scaffolding.[6-9] The Bin/Amphiphysin/Rvs (BAR) domain family of proteins are protein dimers that induce membrane curvature through electrostatic interactions between positively charged residues on the protein and negatively charged lipids.[7] The BAR protein dimers can oligomerize on lipids and form high aspect ratio tubules.[6] To make an OMM, high aspect ratio structures less than 100 nm in diameter, but greater in length than the incoming incident wavelength of electromagnetic radiation are needed,[10] so the protein:lipid structures formed through BAR domain-mediated membrane sculpting were chosen to engineer a biological OMM.

A biological OMM could have the advantage of being lightweight, self-healing, tunable, and inexpensive to produce compared to modern, inorganic OMMs. Here, we show progress into investigation of a bacterial BAR domain-like protein BdpA[11] and its interactions with lipids and hydrophobic surfaces. The high aspect ratio tubule structures formed through BAR domain protein interactions with lipids serve as our templates and scaffolds for nanoparticle formation. We investigated the potential for using BdpA as a film or coating through a serendipitous finding involving interactions with plastics and continue efforts to solve the protein structure towards the goal of a tunable biological OMM or next generation obscurant material for spectral overmatch.

## 2. RESULTS

### 2.1 Production of an iridescent surface using BdpA

#### *2.1.1 BdpA sample loss after centrifugal concentration*

BdpA protein constructs were purified by immobilized metal ion affinity chromatography as previously reported[12] and were concentrated by centrifugal spin concentrators. Rather than concentrating the protein as expected, minimal protein was recoverable after using the centrifugal devices. When the filter concentrator was examined more closely, a thin, iridescent film was observed at the plastic slope near the top of the filter (Figure 1). The same iridescent film was not observed when the centrifugal filter device was exposed to the BdpA purification buffer. We suspected that the observed protein loss was due to direct binding of BdpA to the polyethylene (PET) plastic.

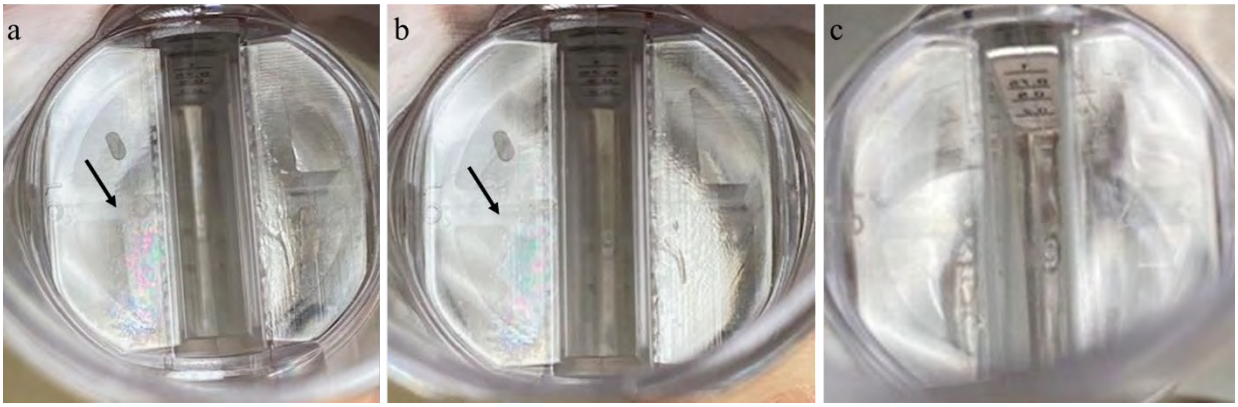


**Figure 1. Iridescent film following centrifugal spin concentration of maltose binding protein (MBP)-BdpA. a) Spin concentrator after centrifugation with an immobilized-metal affinity chromatography (IMAC)-purified sample of MBP-BdpA. An arrow points to the iridescent film on the PET plastic. b) The same spin concentrator and film, but slightly tilted to demonstrate surface iridescence. c) A spin concentrator after centrifugation with the IMAC purification buffer alone.**

#### *2.1.2 BdpA binds to hydrophobic plastic*

We suspected that the iridescent film bound to the plastic in the spin concentrator device was the purified protein. To test this theory, sheets of PET were acquired, and serial dilutions of purified BdpA were spotted onto the surface of the sheets. The highest concentration of BdpA improved surface wetting of the hydrophobic plastic compared to spots containing decreasing concentrations of BdpA or the buffer alone (Figure 2). Iridescence was observable in the 500 μg/mL and 50 μg/mL dilution spots.

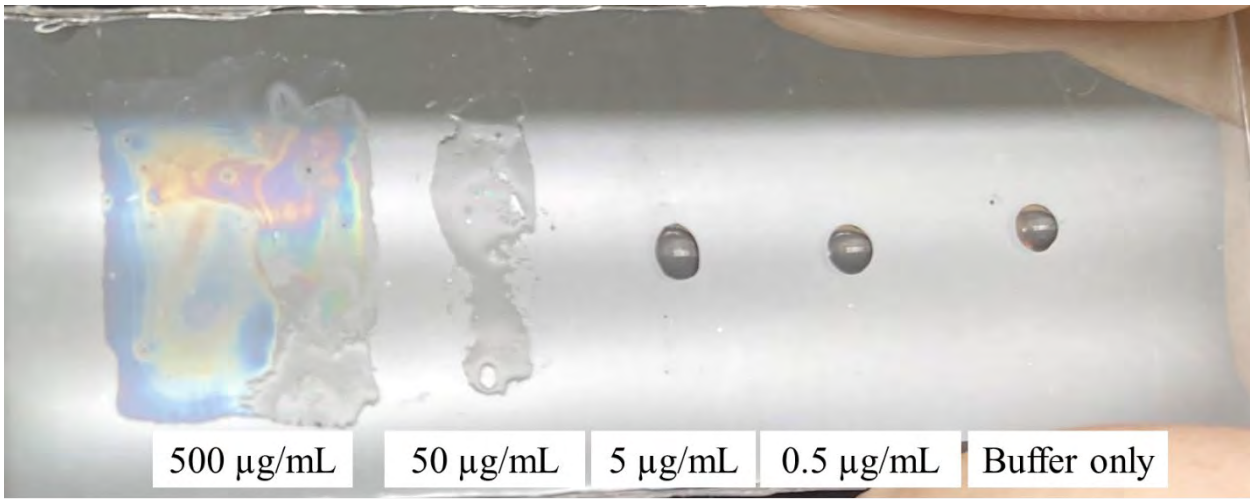


**Figure 2. BdpA concentration-dependent surface wetting and iridescence on PET. A 10 µL droplet of each of the protein serial dilutions was spotted onto the PET sheet and spread with a pipette tip.**

Serial dilutions of purified BdpA, the BAR-only BdpA protein construct, and MBP-only were spotted onto PET sheets as in Figure 2 to determine if the surface wetting and iridescence phenotypes were unique to BdpA, and more specifically, to the predicted BAR domain-containing region of the protein. The 500 µg/mL and 50 µg/mL protein spots containing either BdpA or the BAR-only fragment formed iridescent films and had improved surface wetting (Figure 3). None of the protein spots containing MBP-only had either iridescent films or improved surface wetting, suggesting that PET-binding phenotype of BdpA is associated with the BAR domain region of the protein. The serial dilution binding assay was repeated with polyethylene terephthalate glycol (PET-G) sheets to determine if plastic binding was achievable with different hydrophobic plastic or if the phenotype is PET-specific, and similar iridescence and surface wetting was observed (Figure 4).

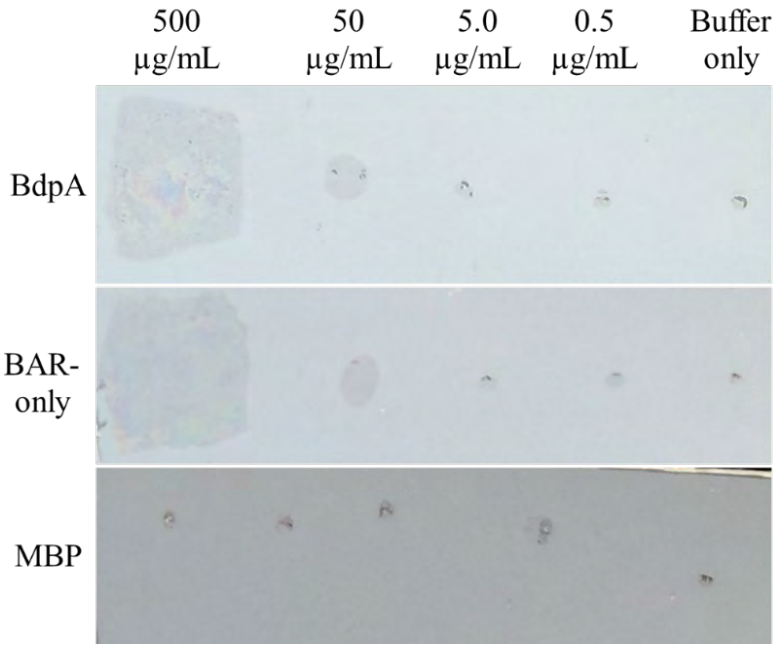


**Figure 3. The BAR domain region of BdpA is required for iridescence and binding to PET. The 10 µL droplets were spotted onto the PET sheets and spread using a pipette tip.**

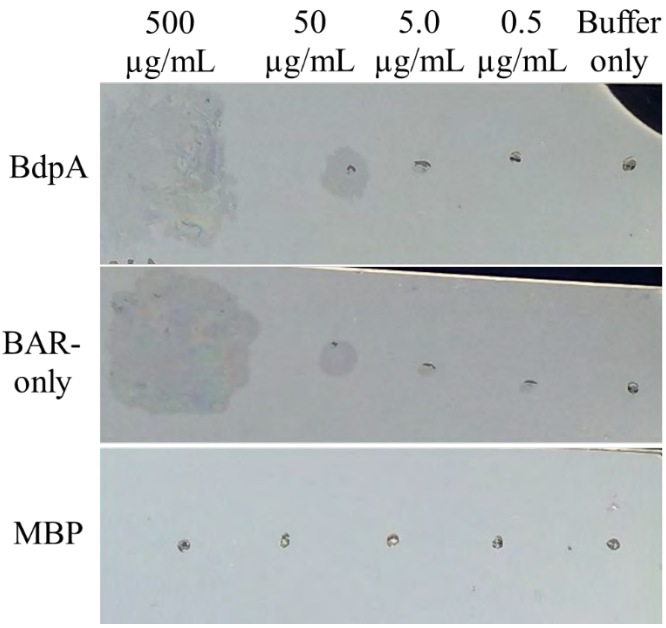


**Figure 4. BdpA BAR domain-mediated surface wetting and iridescence on hydrophobic PET-G sheets. The 10 µL protein serial dilution droplets were spotted onto the PET-G sheets and spread using a pipette tip.**

### 2.2 Phospholipid binding by BdpA through electrostatic interactions

Previously, we demonstrated that BdpA could sculpt membranes of *Shewanella oneidensis* MR1, *Marinobacter altanticus* CP1, and *Eschericia coli* BL21(DE3) cells into lipid structures of varying morphologies *in vivo*.[11] Likewise, BdpA was shown to bind to purified *S. oneidensis* MR1 lipopolysaccharide (LPS) liposomes through electrostatic interactions.[12] The observation that the BAR domain-containing region of BdpA bound to hydrophobic plastic sheets suggested that BdpA could bind to more lipids than LPS alone. Liposomes were made using POPC and labeled with the fluorescent lipophilic dye FM 4-64 for visualization. Liposome cosedimentation analysis was performed using the fluorescently labeled POPC liposomes incubated with the purified BAR-only fragment of BdpA in buffer containing increasing concentrations of NaCl (Figure 5). The BAR-only fragment remained bound to the liposomes after multiple washes. BAR-only protein fragment binding decreased with higher concentrations of NaCl, consistent with previous LPS cosedimentation results.[12]

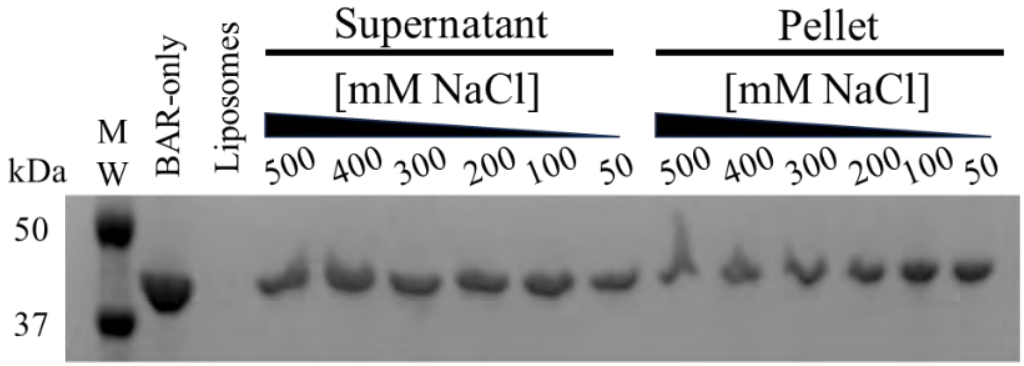


**Figure 5. The BAR domain-containing region of BdpA binds POPC liposomes through electrostatic interactions. The Coomassie-stained SDS-PAGE gel shows the 42 kDa BAR-only fragment of BdpA in either the supernatant or pellet fractions from liposome cosedimentation after incubation in a range of NaCl concentrations.**

### 2.3 Structural analysis of BdpA

#### *2.3.1 Improvements in transmission electron microscopy (TEM) sample preparation*

Previous attempts to solve the structure of BdpA by cryo-TEM were hindered by lipid contamination in the protein samples, protein aggregates, and an inability of the protein to stick to the TEM grids. Graphene grids were tested to see if protein adherence to the grids could be improved. Protein adherence and monodispersity were analyzed by negative stain TEM, and individual particles corresponding to the predicted protein dimer size and shape were observed (Figure 6a, 6b). BdpA protein samples on graphene grids were then frozen in liquid ethane for cryo-TEM imaging. Electron-dense regions in the cryo-TEM images also resembled the predicted model of the BdpA dimer (Figure 6c, 6d).

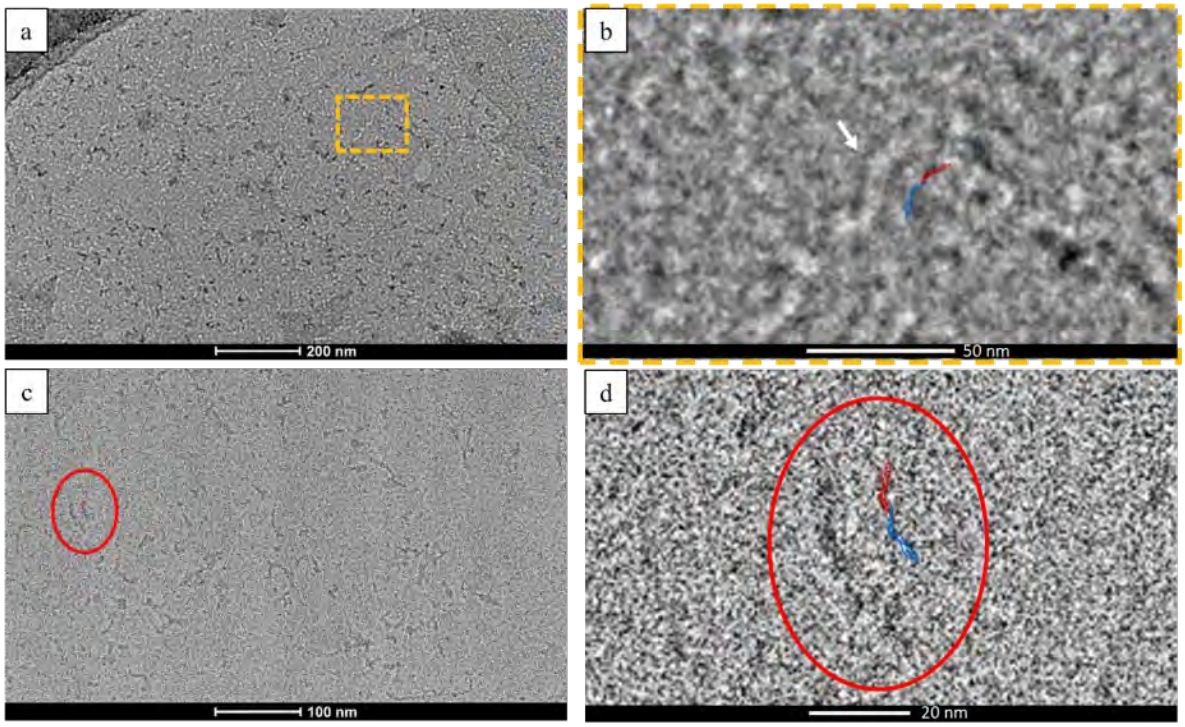


**Figure 6. Negative stain TEM and cryo-TEM images show particles resembling the BdpA dimer predicted model. a) Negative stain TEM images of monodisperse BdpA protein on graphene grids. The dashed yellow box is enlarged in b) to show detail of the predicted BdpA dimer model (red and blue crescent shape) juxtaposed to a similarly shaped negatively stained particle. c) Cryo-TEM images of BdpA samples on graphene grids. Dark, electron-dense particles highlighted in the red circle are enlarged in d) and juxtaposed to the predicted BdpA protein dimer model.**

### *2.3.2 Automated image collection and analysis of BdpA cryo-TEM images*

With the grid conditions optimized, the BdpA cryo-TEM samples were ready for automated, high throughput data collection. A total of 2668 images were collected and aligned. Each image was segmented for individual particles, normalized, and 2D class averages were generated (Figure 7). The 2D class averages are ranked according to the frequency that the particle was observed in a specific orientation out of the total number of particles analyzed. In these averages, the ten most frequently observed particles resembled the crescent-shaped dimer of the BdpA predicted model,[11] as well as other BAR domain-containing protein dimers.[7] After this 2D classification, a 3D model can be generated and iteratively refined to solve the structure of BdpA.

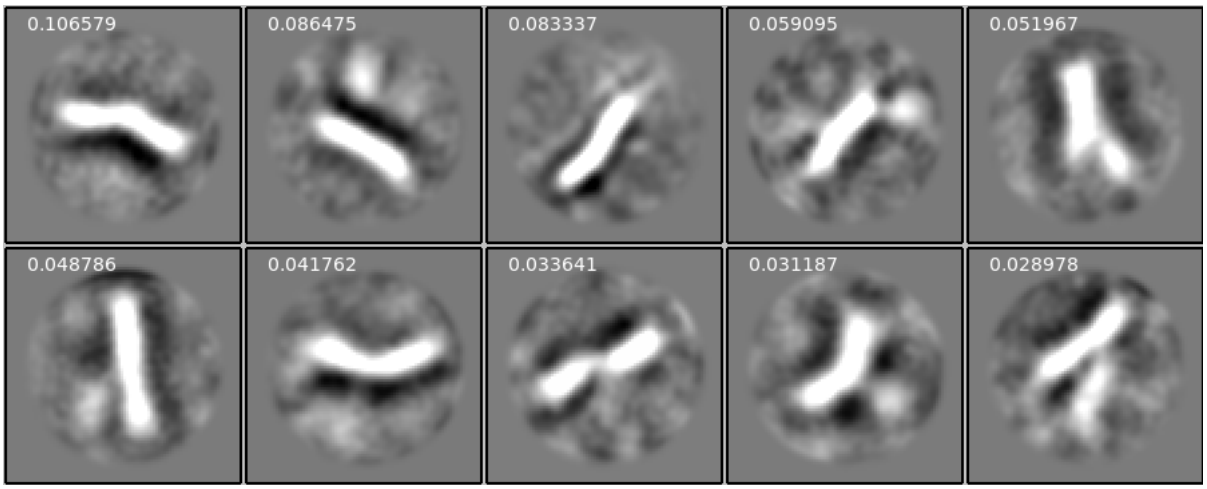


**Figure 7. 2D class averages of BdpA. The ten most frequent orientations of averaged particles from automated collection and analysis of cryo-TEM images of BdpA samples frozen on graphene grids.**

## 2.4 Protein-sculpted membranes as scaffolds for nanoparticle synthesis

### *2.4.1 Formation of gold nanoparticles in tubes*

Previously, BdpA-mediated membrane sculpting was used to aggregate preformed nanoparticles and shift the absorbance spectra. Here, citrate reduction was used for *de novo* synthesis of gold nanoparticles from gold(iii) chloride-laden LPS liposomes alone or with membrane sculpting proteins (BdpA and the BAR-only fragment region of BdpA) to see if high aspect ratio conductive nanoparticles would form. MBP was selected as the control protein as it does not bind the hydrophobic plastic sheets (Figures 3, 4) and is not known to form tubules from liposomes. Gold(iii) chloride in buffer without protein or liposomes was included to control for the reduction of free gold ions in solution. The resultant nanoparticles in tubes displayed a range of colors (Figure 8a). The nanoparticles formed with BdpA and the BAR-only fragment presented as a bluish purple, while the MBP and nanoparticles formed without lipids or protein were a peach-orange color. Liposome alone nanoparticles were a magenta. The absorbance spectra of the nanoparticles were measured by UV-Vis spectrometry (Figure 8b). The absorbance peaks for the BdpA, BAR-only fragment, and MBP liposome nanoparticles red-shifted in comparison to liposome-only nanoparticles. The MBP peak shifted from the liposomes alone peak at 555–560 nm. BdpA and BAR-only fragment liposome nanoparticles shifted to a broader peak at 580 nm that remained elevated to near infrared, and the BAR-only fragment liposome nanoparticle spectra resembled a rounded plateau, suggesting either increased aggregation or higher aspect ratio particle formation.

### *2.4.2 Formation of gold nanoparticles in a flow cell*

Formation of a metamaterial or structural coloration depends on ordered structures. A flow channel was constructed to attempt to form the nanoparticles and orient them in the same direction. Nanoparticles were formed using the same proteins and liposomes from Figure 8a, but this time they were incubated within the individual channels of the flow chamber prior to citrate reduction (Figure 8c). The flow channel nanoparticles similar in color except for the BAR-only fragment liposome nanoparticles. These nanoparticles appeared a brighter blue color, while previously in the tubes they were a bluish purple. When observed by light microscopy, the BAR-only fragment liposome nanoparticles appeared as spiderweb tubules (Figure 8d). Similar tubules were present in the BdpA liposome nanoparticles, but with less abundance. MBP liposome and liposome alone nanoparticles appeared as larger, distributed aggregates, and the nanoparticles alone without protein or liposomes were small and dispersed.

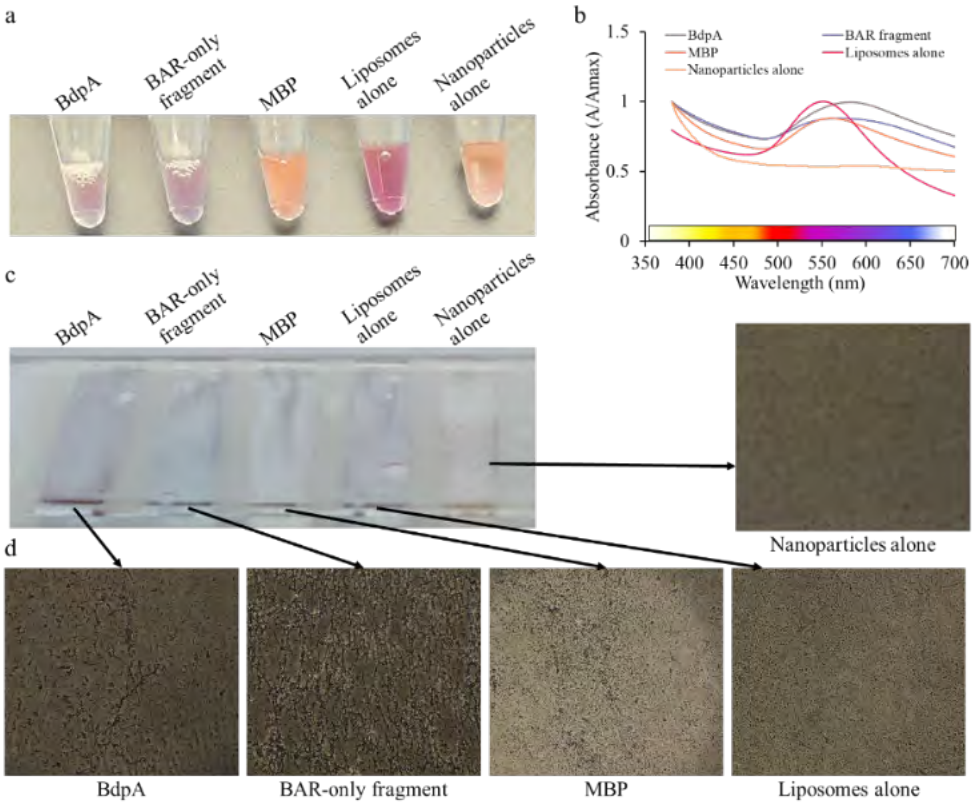


**Figure 8. Gold nanoparticles formed with of BdpA-sculpted membranes have red-shifted absorbance spectra. a) Photograph of gold(iii) chloride-containing LPS liposomes incubated with either BdpA, the BAR domain-only fragment of BdpA, MBP, or buffer (liposomes alone), then reduced with sodium citrate. Gold(iii) chloride in buffer without liposomes was also reduced into nanoparticles using citrate as protein and liposome-free control (nanoparticles alone). b) Absorbance spectra of the nanoparticle solutions measured by UV-Vis spectrometry. The color spectrum associated with the x-axis indicates the perceived color of a particle with higher absorbance at each wavelength of visible light. c) Photograph of protein:lipid scaffolded nanoparticles formed in a glass slide flow chamber in an attempt to orient particles in the same direction. d) Light microscopy images of the corresponding nanoparticles taken at 10x optical zoom.**

## 3. DISCUSSION

Here we present data showing that BdpA can be used to make a surface that alters reflected light through different methods. First, an iridescent film was produced by accident because of protein binding directly to hydrophobic plastic. The two most likely explanations for the observed iridescence on the PET and PET-G films are either 1) thin film interference, or 2) an ordered liquid crystal lattice. BdpA has both a hydrophilic and a hydrophobic interface. It is possible that the hydrophobic interface bound to the hydrophobic plastic, keeping the hydrophilic region oriented in solution towards the buffer. This interaction could explain the increased surface wetting on PET and PET-G we observed at higher protein concentrations. The surface wetting would promote the formation of a thin film of buffer. Future experiments could aim to control the precise amount of liquid dispersed over an area by spin coating to attempt to tune the resultant coloration to specific wavelengths relative to the thickness of the film. Further, BdpA forms oligomers with itself. At higher protein concentrations, a thin film could promote the formation of an ordered liquid crystal lattice. This phenomenon and ordered structure could explain the iridescent effect and color change relative to the incident angle of observation from Figure 1. The two explanations for the iridescence on plastic are not necessarily mutually exclusive. Atomic force microscopy of the BdpA films on PET could provide insight into this phenomenon.

The BdpA protein structure is nearly solved. The 2D class averages resemble BAR domain protein dimers[7] and the BdpA predicted structure model.[11] It is possible that the 3D model of BdpA will reveal the first solved structure of a bacterial BAR domain protein. This finding could have interesting evolutionary implications, such as the possibility

for additional bacterial BAR domain-containing proteins waiting to be discovered, glimpses into the evolutionary origin of membrane trafficking in cells, or evidence of either convergent evolution or horizontal gene transfer from a eukaryote.

Finally, this project set out to produce an optical effect using membrane sculpting. Through interaction of the BAR domain-containing region of BdpA with liposomes, nanoparticles with red-shifted absorbance were produced. Alignment of these nanoparticles was attempted using a flow system during synthesis. To optimize the patterning of these nanoparticles, liposomes could be tethered to a surface, then exposed to BdpA during flow. After sufficient length tubules are formed, reduction of the nanoparticles could be achieved electrochemically. This technique could improve uniformity of the particles for a more tunable material, and this degree of precision is likely to be necessary to build towards the goal of using membrane sculpting as a template to pattern a biological metamaterial. For now, we have demonstrated structural coloration with BdpA films, but more research is needed to form a negative refractive index metamaterial using synthetic biology.

## 4. METHODS

### 4.1 Protein purification

BdpA constructs were prepared as previously described, with few modifications.[12] MBP-tagged constructs were ordered and cloned into the pET-28(a) expression vector with an N-terminal MBP tag, 6x-His tag, GSSGSS linker, and a thrombin cleavage site by Twist Bioscience. Plasmid constructs were transformed into chemically competent *E. coli* Rosetta2(DE3) pLysS cells for protein expression. Protein purification of BdpA constructs was performed as previously described.[12] Protein purification of MBP was performed by amylose resin affinity chromatography from *E. coli* Rosetta2(DE3) pLysS cells harboring the pMAL-c6t MBP expression vector. Expression and purification conditions for MBP were performed as indicated in the manufacturer's instructions (New England Biolabs Inc.).

### 4.2 Iridescent protein films

Serial dilutions of the indicated proteins were made in 50 mM Tris, 50 mM NaCl, pH 8.0 buffer. A 10 µL droplet was applied to either PET or PET-G sheets and spread using the same 20 µL pipette tip. Samples were allowed to dry completely prior to imaging, except for the film in Figure 2. Protein films were imaged using the camera of a Microsoft Surface 9 tablet.

### 4.3 Liposome preparation

For cosedimentation with DOPC liposomes, 10 mg/mL DOPC (Avanti Polar Lipids, Inc) in chloroform was evaporated until dry overnight to form a film, then rehydrated with 50 mM Tris, 50 mM NaCl, pH 8.0 buffer. Rehydrated lipids were sonicated for 10 minutes in a water bath to form liposomes.

For gold nanoparticle formation experiments, LPS was purified from *S. oneidensis* MR1 cultures using the LPS Isolation Kit according to the manufacturer's instructions (MAK339, Sigma-Aldrich). A solution of 6 mg/mL of LPS was prepared in chloroform and allowed to evaporate overnight to form the lipid film. The LPS film was rehydrated in a solution containing 1 mM $HAuCl_4 \cdot 3H_2O$ in 500 mM glucose at pH 8.0. This solution was vortexed and passed through sequentially smaller filters of a liposome extruder kit (Avanti Polar Lipids, Inc).

### 4.4 Nanoparticle formation

The 6 mg/mL LPS liposomes containing the gold(iii) chloride salt were incubated with 5 mg/mL of the indicated protein or buffer in a 1:1 ratio in a total volume of 20 µL for 10 minutes. The protein:lipid:gold salt mixture was reduced with 10 µL of a 40 mM sodium citrate solution in 30 µL. The mixture was left at room temperature overnight. Nanoparticle absorbance was measured in clear bottom 384 well plates via Biotek Neo2 reader.

Glass slide flow chambers were prepared by cutting 5 mm strips of parafilm, placing them at 8 mm distances apart on the glass slide, and placing a no. 1 cover glass over top of the films. The glass chambers were heated to 70 °C for 5 minutes to melt the parafilm and form the channel. Into these channels, 5 µL of the gold salt glucose liposomes was added first, followed by 5 µL of the indicated protein or buffer. This was allowed to incubate at room temperature for 5 minutes before adding 5 µL of the sodium citrate solution. Glass flow chambers were sealed with acrylic nail polish to prevent evaporation. The nanoparticles were imaged on an Olympus upright light microscope.

### 4.5 Transmission electron microscopy

For negative stain TEM and cryo-TEM of the protein samples, samples were spotted onto graphene monolayers supported on Quantifoil holey carbon grids. Grids were frozen for cryo-TEM as described previously[11] and imaged on a Titan Krios (Thermo Scientific).

## ACKNOWLEDGMENTS

Daniel Phillips and Aleksandr Miklos wrote the proposal, acquired funding, planned and supervised research. Daniel Phillips, John Biondo, and Christian Jednorski purified proteins. Daniel Phillips, John Biondo, Jill Harland, and Danielle Kuhn performed nanoparticle absorbance measurements. Daniel Phillips and John Biondo prepared liposomes, made iridescent films, and performed light microscopy imaging experiments. John Biondo performed liposome cosedimentation experiments. Cheri Hampton, Lily McCloskey, and Lawrence Drummy performed TEM experiments. Patricia Buckley and Aleksandr Miklos provided guidance and troubleshooting. Daniel Phillips wrote the report. Funding was provided by the U.S. Army via the Chemical Biological Advanced Materials and Manufacturing Science Program (PE 0601102A Project VR9) at the Combat Capabilities Development Command Chemical Biological Center.

## REFERENCES

[1] Vignolini, S.E.; Catón, L.; Hamidjaja, R.; Oosterink, E.; Wilts, B.D.; Rasmussen, T.S.; Sherlock, M.M.; Ingham, C.J.; Vignolini, S. Genetic manipulation of living bacterial color. *Proc. Natl. Acad. Sci. U.S.A.* **2018**, *115* (11), pp 2652–2657.

[2] Vignolini, S.; Rudall, P.J.; Rowland, A.V.; Reed, A.; Moyroud, E.; Faden, R.B.; Baumberg, J.J.; Glover, B.J.; Steiner, U. Pointillist structural color in *Pollia* fruit. *Proc. Natl. Acad. Sci. U.S.A.* **2012**, *109* (39), pp 15712–15715.

[3] Middleton, R.; Sinnott-Armstrong, M.; Ogawa, Y.; Jacucci, G.; Moyroud, E.; Rudall, P.J.; Prychid, C.; Conejero, M.; Glover, B.J.; Donoghue, M.J.; Vignolini, S. *Viburnum tinus* Fruits Use Lipids to Produce Metallic Blue Structural Color. *Curr. Biol.* **2020**, *30* (19), pp 3804–3810.

[4] Sullivan, C.J.; Brown, K.; Hung, C.-S.; Tang, J.K.-H.; DeSimone, M.; Chen, V.; Lloyd, P.F.; Gupta, M.; Juhl, A.; Crookes-Goodson, W.; Vasudev, M.; Dennis, P.B.; Kelley-Loughnane, N. Iridescent biofilms of *Cellulophaga lytica* are tunable platforms for scalable, ordered materials. *Sci. Rep.* **2023**, *13*, p 13192.

[5] Yang, W.; Xiao, S.; Song, Q.; Liu, Y.; Wu, Y.; Wang, S.; Yu, J.; Han, J.; Tsai, D. All-dielectric metasurface for high performance structural color. *Nat. Commun.*, **2020**, 11, p 1864.

[6] Daum, B.; Auerswald, A.; Gruber, T.; Hause, G.; Balbach, J.; Kühlbrandt, W.; Meister, A. Supramolecular organization of the human N-BAR domain in shaping the sarcolemma membrane. *J. Struc. Bio.*, **2016**, *194* (3), pp 375–382.

[7] Daumke, O.; Roux, A.; Haucke, V. BAR domain scaffolds in dynamin-mediated membrane fission. *Cell*. **2014**, *156* (5), pp 882–892.

[8] Frost, A.; Perera, R.; Roux, A.; Spasov, K.; Destaing, O.; Egelman, E.H.; De Camilli, P.; Unger, V.M. Structural basis of membrane invagination by F-BAR domains. *Cell*. **2008**, *132* (5), pp 807–817.

[9] Simunovic, M.; Evergren, E.; Callan-Jones, A.; Bassereau, P. Curving Cells Inside and Out: Roles of BAR Domain Proteins in Membrane Shaping and Its Cellular Implications. *Annu. Rev. Cell Dev. Bio.* **2019**, *35* (1), pp 111–129.

[10] DuFort, C.C.; Dragnea, B. Bio-enabled synthesis of metamaterials. *Annu. Rev. Phys. Chem.* **2010**, 61, pp 323–344.

[11] Phillips, D.A.; Zacharoff, L.A.; Hampton, C.M.; Chong, G.W.; Malanoski, A.P.; Metskas, L.A.; Xu, S.; Bird, L.J.; Eddie, B.J.; Miklos, A.E.; Jensen, G.J.; Drummy, L.F.; El-Naggar, M.Y.; Glaven, S.M. A bacterial membrane sculpting protein with BAR domain-like activity. *eLife*. **2021**, 10, e60049.

[12] Phillips, D.A.; Biondo, J.R.; Lee, J.A.; Buckley, P.E.; Miklos, A.E. Protein-sculpted membrane scaffolds as templates for conductive materials towards the development of biological metamaterials. FY22 *Proceedings of the Edgewood Chemical Biological Center In-House Laboratory Independent Research and Surface Science Initiative Programs*; U.S. Army Edgewood Chemical Biological Center: Edgewood, MD, **2022**.

This page left intentionally blank

# Controlling the heterogeneous catalysis of zirconium clusters within a porous SBA-15 scaffold

Ann M. Kulisiewicz[a]*, Sergio J. Garibay[a,b], Trenton B. Tovar[a], Matthew A. Browe[a]
[a]U.S. Army Combat Capabilities Development Command Chemical Biological Center, Research & Operations Directorate, 5183 Blackhawk Rd, Aberdeen Proving Ground, MD 21010
[b]Leidos, Inc., 3465 Box Hill Corporate Center Dr., Abingdon, MD 21009

## ABSTRACT

Metal-organic frameworks (MOFs) with Zr-based secondary building units (SBUs) are promising materials for degradation of chemical warfare agents. The Zr-based SBUs have been determined to be the primary reactive component for catalytic hydrolysis. However, the variables inherent to MOF structures complicate the understanding reactivity of the material, especially the role of the SBU. Here, the reactivity of a simplified system consisting of $Zr_6$ and $Zr_{12}$ clusters grafted onto silica supports was explored to understand the reactivity of the SBU independent of the variables inherent to MOF structures. Silica supports (SBA-15) with sulfuric acid groups were used to tether individual Zr clusters to the surface. Final products were characterized by powder x-ray diffraction and $N_2$ isotherm to confirm porosity and retained crystallinity of the Zr cluster post-attachment. Hydrolysis reactivity was assessed through $^1$H Nuclear Magnetic Resonance experiments under buffered and non-buffered conditions in the presence of dimethyl nitrophosphate. The $SO_3$H-SBA-15 bound $Zr_{12}$ clusters performed hydrolysis while the $SO_3$H-SBA-15 bound $Zr_6$ clusters produced a mixture of the hydrolyzed product and undesired product, 4-methylnitrophosphate. Computational modeling gives insight into this trend through electrostatic potential mapping of the $Zr_6$ and $Zr_{12}$ clusters and calculated pKa and bond strength data for the monocarboxylic acid modulators.

**Keywords:** metal-organic framework, catalysis, acid-modified silica

## 1. INTRODUCTION

Metal-organic frameworks (MOFs) have shown immense promise for the catalytic degradation of chemical warfare agents. MOFs consist of metal nodes, referred to as secondary building units (SBUs), bridged in a crystalline arrangement by organic linkers to create a porous framework. By varying the SBU and linker, a wide array of MOFs can be synthesized with different structural or chemical properties tailored to a specific application. MOFs containing $Zr_6O_4(OH)_4^{12+}$ SBUs have recently shown promise as catalytically active materials for nerve agent hydrolysis. This includes UiO-66, UiO-67, NU-1000, NU-901, MOF-808, and many variants of these structural topologies with functionalized linkers. For each of these MOFs, the hydrolysis reaction mechanism of VX and GB depends only on the SBU and not the linker.[1] Despite having the same reaction site and mechanism, the reaction rate varies based on the MOF and the agent. Currently, why some Zr-MOFs perform better for agent hydrolysis is not understood.

A key limitations for why reactivity is poorly understood is the inability to quantify the number of active sites within a MOF. Different Zr-MOFs can have connectivity of 6, 8, or 12 linkers per SBU, possibly revealing more active Zr sites. Due to pore size, it is hypothesized that some agents cannot access the interior of some MOFs based on steric constraints, thus reactivity is limited only to sites on the surface causing crystal size to become the main determinant for reactivity. However, crystal sizes are determined by synthesis conditions and can vary. In some MOFs, the presence of defect sites, which cannot be quantified and depends on synthesis conditions, have been shown to impact reactivity.

MOF linkers can further complicate the understanding of reactivity profiles. While linkers do not participate in the hydrolysis reaction, linker topology can create steric effects at the SBU which can affect the adsorption and subsequent reactivity of the MOF with chemical warfare agents. In addition, functionalized linkers could induce electronic effects on the SBU thereby affecting reactivity. In this study, we explore hydrolysis reactions on Zr-MOF SBU clusters independent of the MOF structure to better understand the reactivity of the Zr cluster and the role of the local chemical environment on reactivity. To generate a suite of standardized materials for this study, $Zr_6$ and $Zr_{12}$ clusters with varying monocarboxylic acid modulators (MCAMs) were synthesized. The MCAMs varied in pKa, steric, and

electronic properties to mimic the effect of the MOF linker on the Zr cluster reactivity. The reactive material consists of an inert, mesoporous silica support functionalized with a sulfuric acid group to tether a quantifiable number of Zr clusters to the surface. This material was then assessed for hydrolysis activity when reacted with dimethyl nitrophosphate (DMNP), a nerve agent simulant, under buffered and non-buffered aqueous conditions.

## 2. EXPERIMENTAL METHODS

### 2.1 Synthesis

#### *2.1.1 Zirconium cluster synthesis*

All reagents were purchased from commercial sources and used without further purification. $Zr_6$-acetic acid, $Zr_6$-glycine, and $Zr_{12}$-SBUs were synthesized according to modified literature procedures.[2–4]

$[Zr_6(O)_4(OH)_4(H_2O)_8(Gly)_8]$ 12Cl $8H_2O$ cluster synthesis: In an 8-dram vial $ZrOCl_2 \cdot 8H_2O$ (0.403 g, 1.25 mmol) was dissolved with $H_2O$ (12 mL). Glycine (0.375 g, 5 mmol) and 0.1 mL of an 8 mM HCl (aq) solution were then added to the vial. After briefly stirring the solution (5 min) the vial was heated at 98 °C for 4 days, slowly evaporating the water. The gel was recrystallized with 4–6 mL of hot DI water at 100 °C on a hot plate. Upon heating to 100 °C, the water evaporated, leaving ~3 mL . The vial was removed from the hot plate and allowed to cool. After 2 hours, the vial generated a white solid which was then solvent exchanged with $CHCl_3$ (3 mL x 3).

$[Zr_6(O)_4(OH)_4(FA)_8]$ 3Cl $2H_2O$ cluster synthesis: $ZrCl_4$ (2 g, 8.58 mmol) and a stir bar were added to a 50 mL round-bottom flask along with isopropanol (5 mL) and 88% formic acid (2 mL, 52.35 mmol). The flask was fitted with a reflux condenser and heated to 120 °C for 18 hours. After cooling to room temperature, the SBU was then filtered and washed with acetone.

$[Zr_6(O)_4(OH)_4(AA)_8]$ 3Cl $2H_2O$ cluster synthesis: $ZrCl_4$ (2 g, 8.58 mmol) was added to a 50 mL round-bottom flask along with isopropanol (5 mL) and acetic acid (3 mL, 53 mmol). The flask was fitted with a reflux condenser and heated at 120 °C for 1 hour. After cooling to room temperature, the SBU was then filtered and washed with acetone.

$[Zr_6(O)_4(OH)_4(PA)_8]$ 3Cl $2H_2O$ cluster synthesis: In a 50 mL round-bottom flask, $ZrCl_4$ (2 g, 8.58 mmol) and a stir bar were added, followed by isopropanol (5 mL) and propanoic acid (3.9 mL, 52.35 mmol). The flask was fitted with a reflux condenser and heated at 120 °C for 18 hours. After cooling to room temperature, the isopropanol was evaporated and the SBU was precipitated by trituration with acetone.

$[Zr_6(O)_4(OH)_4(BA\text{-}CH_2NH_2)_{10}]$ 5Cl cluster synthesis: Zr6-AA-SBU (0.1 g, 0.07 mmol) was added to an 8-dram vial with a stir bar. $BA\text{-}CH_2NH_2$ (0.140 g, 0.927 mmol) was dissolved in 12 mL $H_2O$ and added to the vial. The vial was heated at 50 °C and stirred for 30 minutes then capped and heated at 80 °C for 18 hours in an oven. The solution was removed through rotary evaporation.

$[Zr_6(O)_4(OH)_4(BA\text{-}CH_2\text{-}Morph)_{12}]$ 5Cl cluster synthesis: Zr6-AA-SBU (0.1 g, 0.07 mmol) was added to an 8-dram vial with a stir bar. $BA\text{-}CH_2$ -Morph (0.204 g, 0.924 mmol) was dissolved in 12 mL $H_2O$ and added to the vial. The vial was heated to 80 °C and stirred for 30 minutes then capped and heated to 80 °C for 18 hours in an oven. The solution was removed through rotary evaporation.

$[Zr_6(O)_4(OH)_4(BA)10]$ 2Cl $2H_2O$ cluster synthesis: In a 50 mL round-bottom flask, $ZrCl_4$ (2 g, 8.58 mmol) and a stir bar were added followed by isopropanol (10 mL) and benzoic acid (6.39 g, 52.35 mmol). The flask was fitted with a reflux condenser and heated at 120 °C for 18 hours. After cooling to room temperature, the SBU was then filtered and washed with acetone.

$Zr_{12}O_8(OH)_8(FA)_{24}$ cluster synthesis: $ZrOCl_2 \cdot 8H_2O$ (1.16 g, 3.6 mmol) was dissolved with DMF (1.8 mL) in an 8-dram vial with magnetic stir bar. Formic acid (5.24 mL, 139 mmol) was added to the vial and the solution was stirred for 5 minutes until becoming solution clear. The vial was capped and placed in a pre-heated oven at 110 °C for 24 hours. The white crystalline solid was filtered and washed with acetone. Residual acetone was evaporated with $N_2$ (g) at room temperature.

$Zr_{12}O_8(OH)_8(AA)_{24}$ cluster synthesis: $ZrOCl_2 \cdot 8H_2O$ (1.16 g, 3.6 mmol) was dissolved with DMF (1.8 mL) in an 8-dram vial with magnetic stir bar. Acetic acid (7.95 mL, 139 mmol) was added to the vial and the solution was stirred for 5 minutes until becoming clear. The vial was capped and placed in a pre-heated oven at 110 °C for 24 hours. The white crystalline solid was filtered and washed with 50 mL of a 1:1 DMF:Acetic acid solution. The solid was

transferred to an 8-dram vial and solvent exchanged with $CHCl_3$ (3 mL x 3). Residual chloroform was evaporated with $N_2$ (g) at room temperature.

$Zr_{12}O_8(OH)_8(PA)_{24}$ cluster synthesis: 70 wt% $ZrO(CH_2CH_2CH_3)_4$ in 1-propanol (2.35 g, 5.2 mmol) was added to an 8-dram vial with magnetic stir bar. Propanoic acid (3.13 mL, 41.8 mmol) was then added to the vial and the solution was stirred for 5 minutes until becoming clear. The vial was capped and placed in a pre-heated oven at room temperature for 24 hours. The white crystalline solid was filtered and washed with 50 mL of a 1:3 isopropanol:propanoic acid solution.

#### *2.1.2 Synthesis of sulfuric acid treated SBA-15*

Sulfuric acid treated SBA-15 was synthesized according to literature procedures from Crisci et al.[5] 0.67 g Pluronic 123 was dissolved in 23 mL 1.6 M HCl at 35 °C. 1.4 mL of TEOS and 140 mg NaCl were added, and the solution was stirred for 1 h. The solution was then equally divided into 3 vials. In 1 vial, 12 µL of 3-mercapto-trimethoxysilane (MPTMS) was added. In another vial, 48 µL of MPTMS were added in 12 µL increments every 15 minutes. $H_2O_2$ (1.4 mmol) was added to all 3 vials and the solutions were stirred for 24 hours. The three samples were put in Parr bombs and heated at 100 °C for 24 h before being filtered and washed with water. From each sample, the Pluronic surfactant was extracted with ethanol under reflux. The samples were washed with ethanol and the extraction was repeated. The 2 samples with MPTMS were washed with water and suspended in HCl for 3 h. The HCl treated samples were filtered and washed with water, dried in air at 60 °C overnight, and then dried under vacuum at 150 °C.

#### *2.1.3 Synthesis of phosphoric acid treated SBA-15*

The sample that did not contain MPTMS detailed in section 2.1.2 was suspended in a $H_3O_4$/acetone solution. The sample was stirred at 60 °C until the acetone evaporated. The sample was dried in air at 60 °C overnight and then dried under vacuum at 150 °C.

#### *2.1.4 Synthesis of zirconium cluster treated acid functionalized SBA-15*

Phosphoric or sulfuric acid functionalized SBA-15 (70 mg) of was added to an 8-dram vial. A solution of Zr-SBU cluster (70 mg) in 12 mL of DMF was added to the vial and capped. The vial sulfuric acid functionalized SBA-15 was placed in a 55 °C oven while the phosphoric acid functionalized SBA-15 was placed in a 100 °C pre-heated oven for 18 hours. The vials were solvent exchanged with fresh DMF and acetone (12 mL x 3).

#### *2.1.5 Synthesis of acid-base functionalized SBA-15*

A bifunctional acid-base SBA-15 support was synthesized according to previous methods.[6] P123 (1 g) was dissolved in 40 mL of water and 5 mL of HCl at 40 °C. Following the initial step, 5 mL of TEOS, 200 µL of MPTMS, and 3-tert-butyloxycarbonylaminopropyltrimethoxysilane (NHBoc) were added and the solution was stirred for 24 h at 40 °C. The protecting group on the amino of NHBoc was necessary as post synthetic grafting of aminopropyltrimethoxysilane was unsuccessful for producing a bifunctional support. The solution was then put in a Parr bomb apparatus and heated at 100 °C for an additional 24 h. The product was washed with water and extracted with ethanol under reflux. The material was then treated with $H_2O_2$ to oxidize the mercapto groups to form sulfonic acid sites. The sample was then heated at 185 °C under vacuum for 24 h to remove the protecting group and leave basic amino sites.

#### *2.1.6 Synthesis of zirconium cluster treated acid-base functionalized SBA-15*

Propylamine-propylsulfuric acid-functionalized SBA-15 (70 mg) was added to an 8-dram vial. A solution of $Zr_{12}$-acetic acid-SBU cluster (70 mg) in 12 mL of DMF was added to the vial and capped. The vial was placed in a 55 °C oven for 18 hours. The vials were solvent exchanged with fresh DMF and acetone (12 mL x 3).

#### *2.2.1 Powder X-ray diffraction*

Powder x-ray diffraction (PXRD) patterns were measured on a Rigaku MiniFlex 600 diffractometer equipped with a D/teX Ultra detector with Cu-Kα radiation (λ = 1.5418 Å) over a range of 2θ = 3-50° at a scan rate of 5 deg $min^{-1}$.

#### *2.2.2 ATR-IR*

Attenuated total reflectance-Fourier transform infrared (ATR-FTIR) spectra were measured on a Bruker Tensor 27 spectrometer from 4000–400 $cm^{-1}$ at a resolution of 2 $cm^{-1}$.

#### *2.2.3 $N_2$ physisorption*

$N_2$ isotherms were measured using a Micromeritics ASAP 2420 analyzer at 77 K. Samples were off gassed at 120 °C under vacuum for ~16 h. The Brunauer-Emmett-Teller method was used to calculate specific surface area in $m^2/g$.

#### *2.2.4 X-Ray Photoelectron Spectroscopy experiments*

All X-Ray Photoelectron Spectroscopy (XPS) measurements were performed using a Physical Electronics VersaProbe II photoelectron spectrometer outfitted with an AlKα x-ray source. The base pressure in the analyzer chamber was 1 x $10^{-9}$ mbar. High-resolution scans were taken with a pass energy of 23.5 eV and a step size of 0.05 eV. The elemental analysis does not reveal contamination in the studied compounds beyond the adventitious contamination, which corresponds to hydrocarbon species present in all air-exposed materials. The peak-fitting procedures were carried out using CasaXPS software using a Shirley-type background.

#### *2.2.5 Catalysis experiments*

Cluster modified SBA-15 (12 mol% ~8.6 to 8.7 mg) were added to a vial. A mixture (9:1) of $H_2O$:$D_2O$ (0.9/0.1 mL) was added to the vial and capped. The vial was briefly (1 min) sonicated then transferred to an Nuclear Magnetic Resonance (NMR) tube. N-ethylmorpholine (50 µL) was added to the solution within the NMR tube. DMNP (4 µL, 25 µmol) was added to the top sidewalls of the NMR tube. The tube was capped and carefully inverted thrice to mix the components. The tube was inserted into the NMR instrument and conversion was monitored by $^{31}$P NMR.

#### *2.2.6 Computational modeling of zirconium clusters*

Electrostatic potential mapping was evaluated for all optimized zirconia clusters from Gaussian 16 calculations at the B3LYP/lanl2dz level of theory for Zr and the B3LYP/6-31g(d,p) level of theory for all other atom types. X-ray diffraction data was computed for the DFT-optimized clusters using Debyer, a code that uses the Debye formula to compute scattering intensity versus scattering vector for nonperiodic systems.[7] Modulator hydrophilicity was computed through calculating solvation free energy in water using the Bennett Acceptance Ratio (BAR) method implemented in the Gromacs molecular dynamics code. pKa was calculated for each of the modulators from quantum chemical calculations using the method of Cabellero-Garcia.[8] The method consisted of a DFT-optimized structure at the ωB97X-D/cc-pVDZ level of theory and electrostatic mapping performed as discussed previously, at constant electron density of 0.001 atomic units. An algebraic equation, equation x, was used to compute the pKa from the maximum electrostatic potential on the hydrogen atom of the carboxylic acid group of the modulators.

## 3. RESULTS

The zirconium clusters were synthesized following a modified literature procedure using a thermal synthesis of a zirconium source with excess mono-carboxylic acid modulators (MCAMs). The PXRD patterns of the synthesized clusters closely resembled that of their simulated patterns derived from their single crystal X-ray diffraction structures (Figure 1). With both $Zr_6$- and $Zr_{12}$-clusters in hand, we explored their catalytic properties in the hydrolysis of DMNP under aqueous conditions through $^{31}$P NMR spectroscopy. Like many Zr-MOFs, hydrolysis of DMNP with the Zr clusters requires basic conditions or amine co-catalyst for effective reactivity. As expected, the Zr clusters which have mono-carboxylic acids bound to zirconium sites do not facilitate DMNP hydrolysis under strictly aqueous (pH = 7) conditions. However, the use of N-ethylmorpholine (NEM) engenders the Zr clusters to facilitate DMNP hydrolysis (Figure 2, Table 1). Presumably, the NEM facilitates the dissociation of MCAMs which induces DMNP access to the resulting Zr-OH, -$H_2O$ catalytic sites for hydrolysis. When $Zr_{12}$-(acetic acid) was activated with HCl to form open Zr-OH sites, the reactivity of the material increased with a shortened half-life of 7 minutes versus 12 minutes for the activated and non-activated materials, respectively.

The MCAMs on the Zr clusters used in this study varied in pKa and chemical functionality to aid in determining trends between reactivity and the overall chemical environment of the Zr center imparted by the MCAM. When cluster reactivity was compared to the pKa of the MCAMs, the $Zr_6$ clusters showed a clear trend in which the clusters with higher pKa values had enhanced reaction rates. This trend is consistent with the observation made in the comparison between activated and non-activated samples as the increased pKa indicates a more labile MCAM facilitating the formation of Zr-OH reactive sites in solution. However, the $Zr_{12}$ clusters did not show a clear trend based on the pKa.

When looking at the binding motifs of both clusters, the $Zr_{12}$ clusters contain three MCAM binding motifs (bridging, chelating, inter-cluster bridging) as compared to the two potential binding motifs in the $Zr_6$ clusters (bridging, chelating). The presence of these different binding motifs is supported by XPS data which shows a difference in peak shape for Zr, C, and O between the $Zr_6$ and $Zr_{12}$ clusters. Computational modeling determined that the $\mu_3$-OH adjacent to a bridging MCAM had a higher electrostatic potential as compared to that of a chelating MCAM in the case of the $Zr_6$ clusters (Figure 3).[9-10] Since the $Zr_6$ clusters presumably contain only bridging MCAMs, all MCAMs on the cluster are essentially chemically equivalent, making pKa the driving factor for reactivity. However, the $Zr_{12}$ clusters exhibit

a gradient of electrostatic potential, with an increased electrostatic potential adjacent to the inter-cluster bridging MCAMs. This indicates the electrostatic potential of the MCAMs is a potential factor in the reactivity of the cluster with DMNP. When the electrostatic potentials of the MCAMs were calculated, the MCAMs with lower electrostatic potential on the $Zr_{12}$ cluster exhibited faster reactivity (Table 2). Interestingly, the $Zr_6$ clusters showed the opposite trend in reactivity and electrostatic potential of the MCAMs. Hydrophobicity of the MCAM was considered as a factor in this trend as the ability of the MCAM to facilitate water coordination could potentially overcome the electrostatic potential barrier in facilitating reactivity. However, computational data to determine the hydrophilicity of the individual MCAMs was inconclusive in terms of establishing a trend among both the $Zr_6$ and $Zr_{12}$ clusters.

Both $Zr_6$ and $Zr_{12}$ clusters show selectivity towards the formation of the desired DMP product over the formation of the 4-methylnitrophosphate (M4NP) product. However, XPS data revealed a significant difference in chlorine content between the $Zr_6$ and $Zr_{12}$ clusters (Figure 4). The $Zr_6$ clusters contained a greater degree of chloride content presumably bound to the zirconium indicating the presence of residual starting material. The $Zr_6$ clusters also exhibit slower reactivity overall compared to the $Zr_{12}$ clusters indicating that this impurity likely plays a role in that trend.

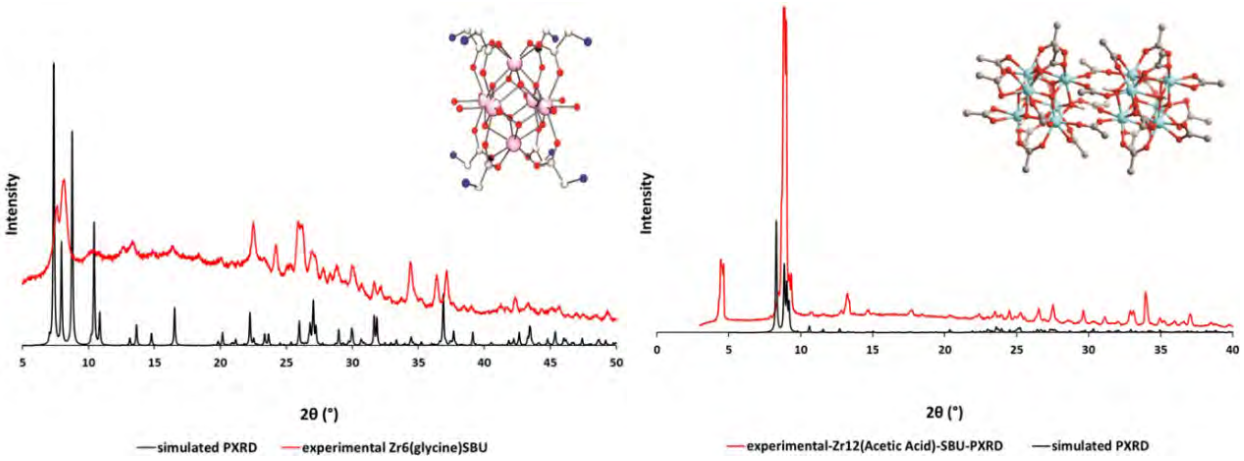


**Figure 1. (Left) Simulated PXRD pattern of $Zr_6$-(glycine) (bottom, black) and experimental PXRD pattern of $Zr_6$(glycine) SBU (top, red) with the representation of the $Zr_6$ cluster derived from single X-ray diffraction data. (Right) Simulated PXRD pattern of $Zr_{12}$-(acetic acid) (bottom, black) and experimental PXRD pattern of $Zr_{12}$-(acetic acid) (top, red) note that simulated spectra begins at 5° with the representation of the $Zr_{12}$-(acetic acid) cluster derived from single X-ray diffraction data.**

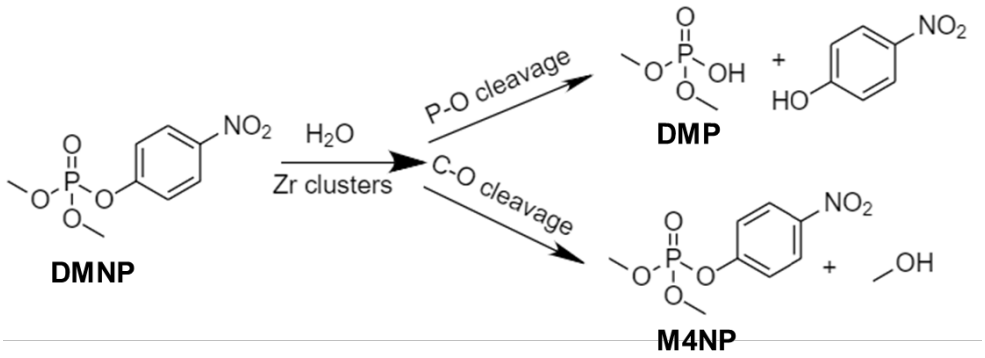


**Figure 2. DMNP hydrolysis reaction scheme showing the formation of the desired product (DMP) and undesired product (M4NP).**

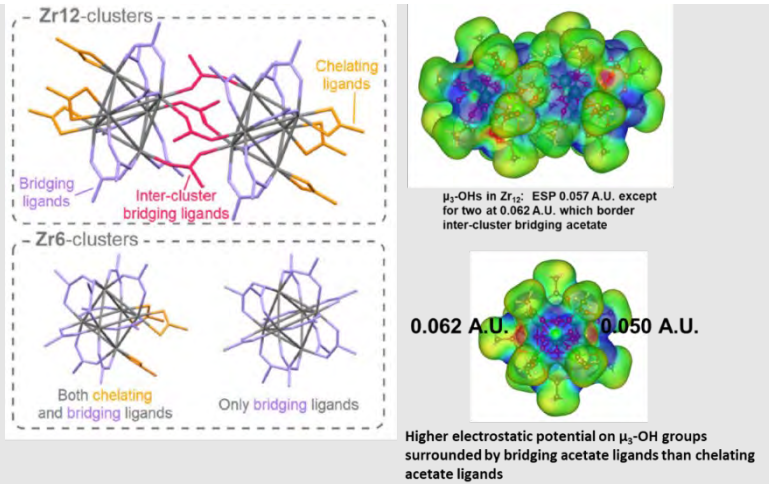


**Figure 3. Electrostatic potential maps at constant electron density of 0.001 a.u. for a (top) Zr12 cluster with bridging, chelating, and inter-cluster bridging ligands and a (bottom) Zr6 cluster with bridging and chelating ligands.**

**Table 1. DMNP hydrolysis by zirconium clusters in 0.45 M N-ethyl morpholine buffer and aqueous conditions**

| Material | pKa (calculated) | Half-life (min.), DMNP, 0.45 NEM buffer | DMNP:DMP:4-MNP (%, at 18 hours) | dG solvation, water (kJ/mol, more negative, more hydrophilic) |
|---|---|---|---|---|
| $Zr_6$-glycine | 3.97 | 69 | 0:100:0 | -31.84 |
| $Zr_6$-formic acid | 3.77 | 27 | 0:100:0 | -36.34 |
| $Zr_6$-benzoic acid | 4.20 | 20 | 0:100:0 | -19.96 |
| $Zr_6$-acetic acid | 4.76 | 17 | 0:100:0 | -21.42 |
| $Zr_6$-propanoic acid | 4.87 | 8 | 0:100:0 | -18.19 |
| $Zr_{12}$-acetic acid | 4.76 | 12 | 0:100:0 | -21.42 |
| $Zr_{12}$-propanoic acid | 4.87 | 9 | 0:100:0 | -18.19 |
| $Zr_{12}$-formic acid | 3.77 | 7 | 0:100:0 | -36.34 |

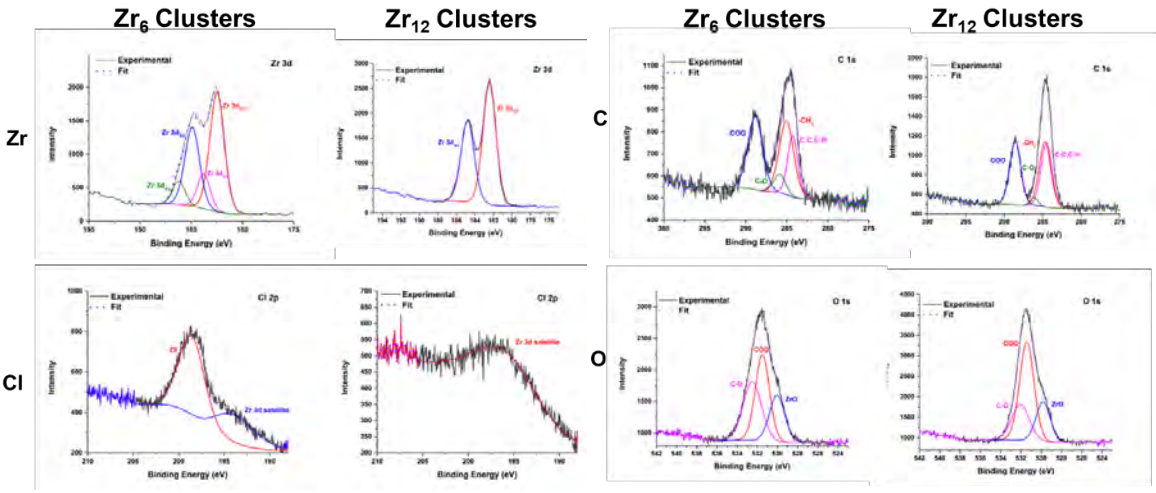


**Figure 4. High-res XPS data for Zr6 clusters (left) and Zr12 clusters (right)**

**Table 2. Binding energies of MCAMs on Zr6 and Zr12 clusters and respective hydrolysis rates of DMNP in 0.45 M N-ethyl morpholine buffer and aqueous conditions**

| Sample | Max ESP at 0.001 A.U. electron density, A.U., $u_3$-OH | DMNP hydrolysis in 0.45 M NEM buffer (half life, min.) |
|---|---|---|
| $Zr_6$-(glycine) | 0.0814 | 69 |
| $Zr_{12}$-(formic acid) | 0.0788 | 7 |
| $Zr_6$-(formic acid) | 0.0786 | 27 |
| $Zr_{12}$-(acetic acid) | 0.0637 | 12 |
| $Zr_6$-(acetic acid-bridging/chelating) | 0.0628 | 17 |
| $Zr_6$-(acetic acid) | 0.0621 | 17 |
| $Zr_6$-(propanoic acid) | 0.0589 | 8 |
| $Zr_6$-(hydroxyl) | 0.0563 | -- |
| $Zr_6$-(benzoic acid) | 0.0482 | 20 |

Silica particles (SBA-15) were modified with sulfuric acid to tether the zirconium clusters to silica. SBA-15 was modified with different amounts of $SO_3H$ and $PO_3H$ to generate H-$SO_3H$-SBA-15, L-$SO_3H$-SBA-15, and $PO_3H$-SBA-15, respectively (H = high, L = low). $Zr_{12}$-(acetic acid)-P-SBA-15 facilitates fast, selective hydrolysis of DMNP to DMP under 0.45 M NEM aqueous conditions while $PO_3H$-SBA-15 produces a mixture (Table 4). The stark contrast in DMNP hydrolysis reactivity and selectivity is attributable to $Zr_{12}$-(acetic acid) clusters into SBA-15, similar to the $SO_3H$-SBA-15 samples. EDX-SEM analysis indicates that H-$SO_3H$-SBA-15 has a 3.9-fold greater sulfide content than L-$SO_3H$-SBA-15 (Figure 5, Table 3). However, it was determined that the L-SO3H-SBA-15 sample had enhanced reactivity relative to H-$SO_3H$-SBA-15 sample when $Zr_{12}$-(acetic acid) was tethered and reactivity with DMNP was assessed under buffered conditions. Therefore, L-$SO_3H$-SBA-15 was reacted with the suite of $Zr_6$ and $Zr_{12}$ clusters to generate $Zr_6$- and $Zr_{12}$-modified SBA-15 materials, respectively. Synthesized particles were characterized by ATR-IR and $N_2$ isotherms to determine crystallinity and porosity The IR spectrum of L-$SO_3H$-SBA-15 peaks at 688 $cm^{-1}$ corresponding to the S-OH stretch (Figure 6). Upon introduction of the $Zr_{12}$-(acetic acid) clusters, the S-OH stretch disappears and new stretches at 1586 $cm^{-1}$ and 1480 $cm^{-1}$ correspond to the acetic acid within the $Zr_{12}$-(acetic acid). A similar trend is observed for $Zr_{12}$-(formic acid) and $Zr_{12}$-(propanoic acid).

L-$SO_3H$-SBA-15 primarily generates M4NP in the hydrolysis of DMNP in 0.45 M NEM aqueous conditions. Zr clusters bound to SBA-15 and the resulting materials were assessed for reactivity with DMNP. While $Zr_6$ and $Zr_{12}$ clusters are crystalline, SBA-15 is amorphous. Consequently, clusters bound to L-$SO_3H$-SBA-15 show limited

crystallinity by PXRD (Figure 7). The introduction of the $Zr_6$ or $Zr_{12}$-clusters into L-$SO_3$H-SBA-15 changes the properties of the materials with respect to the hydrolysis of DMNP under buffered aqueous conditions (Table 4). When $Zr_6$ or $Zr_{12}$ clusters are bound to SBA-15, the reaction rates increased relative to the native materials based on the zirconium loading for each reaction. However, M4NP is produced in reactions with the $Zr_6$ clusters bound to SBA-15 indicating that the hybrid materials are less selective. The $Zr_{12}$ clusters, however, retain selectivity when incorporated into the hybrid materials. When the materials were analyzed by SEM-EDX, zirconium content was higher for the $Zr_6$ clusters as compared to the $Zr_{12}$ clusters corresponding with the XPS data indicating the presence of $ZrCl_4$ starting material in the $Zr_6$ cluster samples. Since the native $Zr_6$ clusters show selectivity while the bound $Zr_6$ clusters do not, the decrease in selectivity is due to the silica strut changing the chemical environment around the Zr cluster.

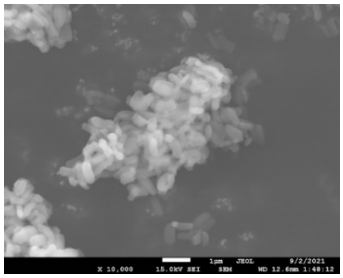

**Figure 5. SEM image of Zr12-SBU-L-SO3H-SBA-15.**

**Table 3. EDX analysis of zirconium clusters bound to silica surfaces. Atomic percentage ratios of key elements are tabulated for each sample.**

| Sample | %Si | %O | %S | %P | %Zr |
|---|---|---|---|---|---|
| L-$SO_3$H-SBA-15 | 23.8 | 76 | 0.20 | | 0 |
| $Zr_{12}$-acetic acid-L-$SO_3$H-SBA-15 | 80 | | | | 20 |
| H-$SO_3$H-SBA-15 | 24 | 75.4 | 0.6 | | 0 |
| $Zr_{12}$-acetic acid-H-$SO_3$H-SBA-15 | 94 | | | | 6 |
| $PO_3$H-SBA-15 | 63 | 32 | | 5 | |
| $Zr_{12}$-acetic acid- $PO_3$H-SBA-15 | 96 | | | | 4 |

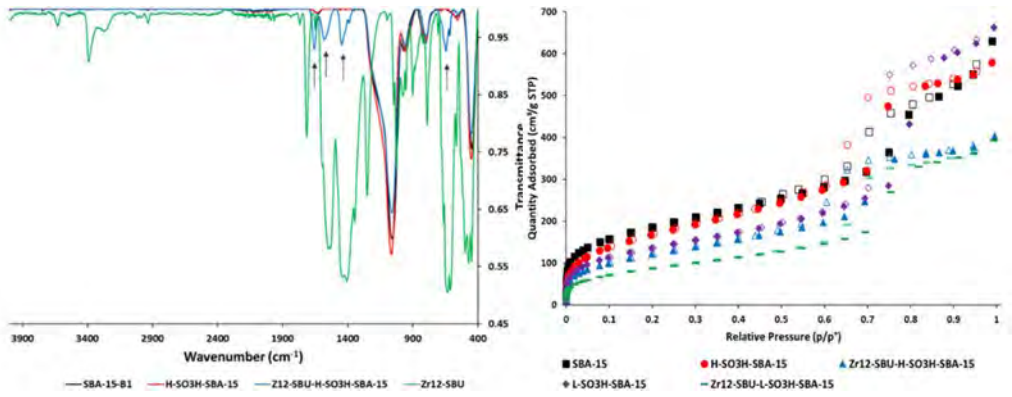


**Figure 6. (Left) IR spectra of SBA-15 (black), H-SO3H-SBA-15 (red), Zr12-SBU- H-SO3H-SBA-15 (blue), and Zr12(acetic acid) SBU (green). (Right) N2 adsorption isotherms of SBA-15 (black squares), H-SO3H-SBA-15 (red circles), Zr12-SBU-H-SO3H-SBA-15 (blue triangles), L-SO3H-SBA-15 (purple diamonds), and Zr12-SBU-L-SO3H-SBA-15 (green line). Solid symbols represent adsorption, empty symbols represent desorption.**

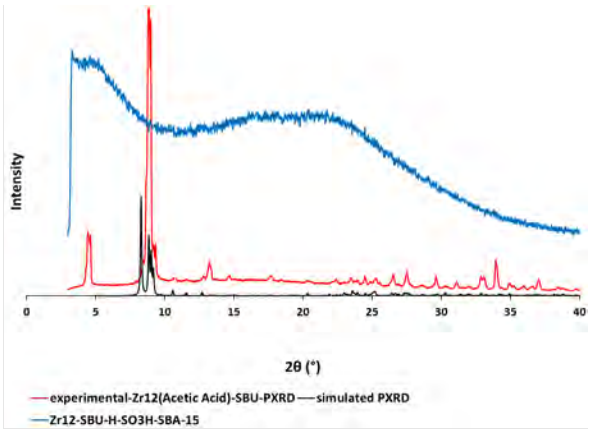


**Figure 7. Simulated PXRD pattern of Zr12(acetic acid) SBU (bottom, black) and experimental PXRD pattern of Zr12(acetic acid) (middle, red) and experimental PXRD pattern of Zr12-SBU-H-SO3H-SBA-15 (top, blue).**

**Table 4. DMNP hydrolysis of bound Zr clusters in 0.45 M N-ethyl morpholine buffer and aqueous conditions[11]**

| Material | Half-life (min), DMNP, water | Half-life (min.), DMNP, 0.45 M NEM buffer | DMNP:DMP:4-MNP (%, at 18 hours) | Zr:S ratio (SEM-EDX) |
|---|---|---|---|---|
| P-SBA-15 | | >220 | 4:14:82 | -- |
| $Zr_{12}$-acetic acid-P-SBA-15 | | 69 | 0:95:5 | |
| H-$SO_3$H-SBA-15 | | >1080 | 43:14:43 | -- |
| L-$SO_3$H-SBA-15-$(CH_2)_3NH_2$ | ~20% (18 h) | 550 | | -- |
| SBA-15-$(CH2)_3NH_2$ | >1080 | >1080 | 25:37:38 | -- |
| $Zr_{12}$-acetic acid-SBA-15-$(CH2)_3NH_2$ | >1080 | >1080 | 11:43:46 | |
| Zr-SBA-15 | | >550 | 34:36:29 | 0.09:1 (Zr:Si) |
| SBA-15 + $Zr_{12}$-acetic acid | | 69 | 16:68:15 | -- |
| $Zr_6$-acetic acid-L-$SO_3$H-SBA-15 | | 89 | 5:86:9 | 5.6:1 |
| $Zr_6$-propanoic acid-L-$SO_3$H-SBA-15 | | 197 | 13:71:16 | 5.68:1 |
| $Zr_6$-benzoic acid-L-$SO_3$H-SBA-15 | | 407 | 15:64:21 | 5.25:1 |
| $Zr_6$-formic acid-L-$SO_3$H-SBA-15 | | 717 | 25:54:21 | 8.03:1 |
| $Zr_{12}$-formic acid-L-$SO_3$H-SBA-15 | | 85 | 7:93:0 | 4.3:1 |
| Zr12-acetic acid-L-$SO_3$H-SBA-15 | | 221 | 31:69:0 | 2.8:1 |
| Zr12-propanoic acid-L-SO3H-SBA-15 | | 283 | 18:81:0 | 1.9:1 |
| $Zr_{12}$-acetic acid-L-$SO_3$H-SBA-15 | ~10% (18 h) | 15 (+/- 2) | 2:98:0 | |
| $Zr_{12}$-acetic acid-L-$SO_3$H-SBA-15-PEI | ~20% (18 h) | | | |
| $Zr_{12}$-acetic acid-L-$SO_3$H-SBA-15-$(CH_2)_3NH_2$ | ~50% (18 h) | | 44:56:0 | |

## 4. CONCLUSIONS/FUTURE WORK

Novel sulfuric acid modified SBA-15 materials decorated with $Zr_6$ and $Zr_{12}$ clusters were developed and shown to selectively hydrolyze DMNP to DMP in less than 10 minutes under buffered conditions. The native SBA-15 shows hydrolysis to the less desired product, M4NP. However, incorporation of $Zr_{12}$ clusters leads to selective hydrolysis while buffered, indicating Zr clusters are imparting reactivity and selectivity within hybrid materials. When analogous $Zr_6$ clusters were synthesized, they did not show the same trend in reactivity or selectivity as the $Zr_{12}$ clusters when bound to sulfuric acid modified SBA-15. This is attributed to the environment imparted on the clusters by modified support. There is a difference in the electrostatic potential map of the $Zr_6$ clusters versus the $Zr_{12}$ clusters, which shows few areas of increased potential on the $Zr_{12}$ clusters as compared to the $Zr_6$ clusters, contributing to the decrease in selectivity. These initial experiments demonstrate the potential of this silica platform to study and optimize zirconia clusters for chemical warfare agent decontamination. In addition, these novel materials are scalable and can be readily transitioned into relevant form factors including fibers and polymer coatings. These materials will be incorporated into polymer components containing buffer moieties onto the $SO_3H$-modified SBA-15 to enhance reactivity of material under neutral aqueous conditions and transitioning these materials into engineered forms and variations in the amount of zirconia clusters on particles to determine reactivity. Once materials are optimized and a route for incorporation of these porous materials into fibers or coatings is determined, reactivity with CWAs will be evaluated.

## ACKNOWLEDGEMENTS

Funding was provided by the U.S. Army via the Chemical Biological Advanced Materials Manufacturing Science Program (PE 0601102A Project VR9) at the Combat Capabilities Development Command Chemical Biological Center.

## REFERENCES

[1] Troya, D. Reaction Mechanism of Nerve-Agent Decomposition with Zr-Based Metal Organic Frameworks. *J. Phys. Chem. C.* **2016**, *120* (51), pp 29312–29323.

[2] Dai, S.; Simms, C.; Dovgaliuk, I.; Patriarche, G.; Tissot, A.; Parac-Vogt, T.N.; Serre, C. Monodispersed MOF-808 Nanocrystals Synthesized via a Scalable Room-Temperature Approach for Efficient Heterogeneous Peptide Bond Hydrolysis. *Chem. Mater.* **2021**, *33* (17), pp 7057–7066.

[3] Pappas, I.; Fitzgerald, M.; Huang, X-Y.; Li, J.; Pan, L. Thermally Resolved in Situ Dynamic Light Scattering Studies of Zirconium(IV) complex formation. *Cryst. Growth Des.* **2009**, *9* (12), pp 5213–5219.

[4] Bezrukov, A.A.; Törnroos, K.W.; Le Roux, E.; Dietzel, P.D.C. Incorporation of an intact dimeric $Zr_{12}$ oxo cluster from a molecular precursor in a new zirconium metal-organic framework. *Chem. Commun.* **2018**, *54* (22), pp 2735–2738.

[5] Crisci, A.J.; Tucker, M.H.; Lee, M.-Y.; Jang, S.G.; Dumesic, J.A.; Scott, S.L. Acid-Functionalized SBA-15-Type Silica Catalysts for Carbohydrate Dehydration. *ACS Catal.* **2011**, *1* (7), pp 719–728.

[6] Shao, Y.; Liu, H.; Yu, X.; Guan, J.; Kan, Q. Synthesis, characterization and catalytic activity of acid-base bifunctional materials through protection of amino groups. *Mater. Res. Bull.* **2012**, *47* (3), pp 768–773.

[7] Farrow, C.L.; Billinge, S.J.L. Relationship between the atomic pair distribution function and small-angle scattering: implications for modeling of nanoparticles. *Acta Cryst.* **2009**, *A65*, pp 232–239.

[8] Cabellero-Garcia, G.; Mondragon-Solorzano, G.; Torres-Cadena, R.; Diaz-Garcia, M.; Sandoval-Lira, J.; Barroso-Flores, J. Calculation of $Vs_{max}$ and Its Use as a Descriptor for the Theoretical Calculation of pKa Values for Carboxylic Acids. *Molecules.* **2019**, *24* (1), pp 79–93.

[9] Bader, R.F.W.; Carroll, M.T.; Cheeseman, J.R.; Chang, C. Properties of atoms in molecules: atomic volumes. *J. Am. Chem. Soc.* **1987**, *109* (26), pp 7968–7979.

[10] Murray, J.S.; Politzer, P. The electrostatic potential: an overview. *Wiley Interdiscip. Rev.: Comput. Mol. Sci.* **2011**, *1* (2), pp 153–163.

[11] Gargiulo, N.; Peluso, A.; Aprea, P.; Pepe, F.; Caputo, D. $CO_2$ Adsorption on Polyethyleneimine-Functionalized SBA-15 Mesoporous Silica: Isotherms and Modeling. *J. Chem. Eng. Data*. **2014**, *59* (3), pp 896–902.

# Molecular modeling of toxic industrial chemicals on metal-organic frameworks for next-generation filtration applications

Matthew A. Browe[a]*, Adam R. Hinkle[ab], Ivan O. Iordanov[a], Wesley O. Gordon[a], John Landers[ac], Shivam Parashar[d], Alex Neimark[d]
[a]U.S. Army Combat Capabilities Development Command Chemical Biological Center, Research & Operations Directorate, 8198 Blackhawk Rd, Aberdeen Proving Ground, MD 21010
[b]DCS Corporation, 4696 Millennium Dr, Suite 450, Belcamp, MD 21017
[c]Leidos, Inc., 1750 Presidents St, Reston, VA 20190
[d]Rutgers University, 57 U.S. Highway 1, New Brunswick, NJ 08901

## ABSTRACT

Advances in supercomputing resources and algorithmic development have enabled chemical reaction to be simulated on porous materials used in filtration applications, enabling the chance for accelerated materials discovery. Adsorption and chemical reaction of zirconium-based metal-organic frameworks UiO-66, UiO-66-$NH_2$, MOF-808, and selected MOF-74 materials against guest molecules of interest are simulated using Monte Carlo methods and molecular dynamics methods utilizing chemically reactive force fields allowing for bond breaking and formation to occur. A range of structural modifications have been simulated for UiO-66, UiO-66-$NH_2$, and MOF-808, and results have led to which computed isotherms closely matching experiments. Reactive molecular dynamics simulations were performed in detail simulating the hydrochloric acid solution activation of MOF-808 to remove formate modulators, which dynamic reaction product statistics computed as a function of temperature and hydrochloric acid concentration. Introductory screening efforts of toxic industrial chemical exposure on UiO-66, MOF-808, and MOF-74 commenced and selected results were considered for pursuing potential follow-on experimental studies.

**Keywords:** Monte Carlo, molecular dynamics, metal-organic frameworks, molecular simulation, adsorption, chemical reaction, ReaxFF

## 1. INTRODUCTION

Removal of toxic industrial chemicals (TICs) is a prominent concern in military filtration applications. Their high vapor pressure precludes removal via noncovalent interactions such as physical adsorption, mandating that a variety of reaction chemistries be incorporated into any filtration media for removal of a broad spectrum of threats. Currently fielded filtration media, such as metal-incorporated activated carbon, cannot adequately address the full spectrum of chemical threats. Metal-organic frameworks (MOFs) have been extensively investigated for this purpose.[1] Their high surface area, porosity, and tunable physical and chemical properties enable a range of reaction chemistries to be incorporated into the structure for chemical removal. Additionally, zirconium-based MOFs are of high interest due to their wide stability under a range of environmental and synthetic conditions,[2] which is a deficiency of other MOFs.

Among the zirconium-based MOFs, UiO-66, UiO-66-$NH_2$, and MOF-808 have been studied in the literature.[3] Additionally, MOFs can be readily tuned physically and chemically for enhancing guest molecule removal. The UiO-66 and UiO-66-$NH_2$ MOFs can be modified through induced defects in the structure, where a linker molecule is removed and the resulting site is terminated through a formate group (in the traditional synthesis involving formic acid) or hydroxyl groups.[4] The UiO-66 family of MOFs can vary chemically through functionalization of the linker, represented by UiO-66-$NH_2$ in which an amine moiety is incorporated onto the benzene dicarboxylic acid linker through synthesis variation, using aminoterephthalic acid instead of terephthalic acid.[2] The MOF-808 MOF can be chemically modified through modulator incorporation on the node, a feature not available on pristine UiO-66 due to all possible node sites bonded to linker molecules.[5] Additionally, all MOFs are subject to contamination from residual solvent, consisting, in their traditional synthesis, of dimethylformamide (DMF) and water.[2]

This effort aims to build on previous efforts to utilize computational techniques to determine the effect of various physical and chemical modifications of zirconium-based MOFs on adsorption and chemical reaction against guest

molecules. Adsorption properties are evaluated by simulating an adsorption isotherm, measuring uptake of an inert gas as a function of applied pressure, and can be evaluated using Monte Carlo methods. Chemical reactions can be evaluated using molecular dynamics simulations incorporating reactive force fields (ReaxFF[5]), which allow explicit bond breaking and bond formation phenomena. Results can guide design strategies towards improving and optimizing these materials for filtration applications.

## 2. METHODS

Crystallographic information files for UiO-66, UiO-66-$NH_2$, and MOF-808 were obtained from the Cambridge Structural Database. Defects were induced into the structure using the Avogadro molecular editor, and the resulting structure was subsequently geometry optimized with the Quantum Espresso code[6] using the "relax" option of the pw.x executable of Quantum Espresso, which adjusts bond lengths and bond angles but not unit cell parameters. Simulation settings used a kinetic energy cutoff distance of 60 Ry for wavefunctions, a kinetic energy cutoff distance of 480 Ry for charge density, Gaussian smearing for metals with a degauss parameter of 0.002, the semiempirical Grimme's DFT-D2 van der Waals dispersion correction, the BFGS quasi-newton algorithm for ion dynamics, and a mixing factor of 0.7 for self-consistency. Default settings for convergence were used.

Nitrogen adsorption isotherms of all MOFs were simulated using the Monte Carlo code RASPA[7] with assistance from Shivam Parashar and Dr. Alex Neimark of Rutgers University. A total of 20,000 Monte Carlo cycles and 5,000 initialization cycles were used, with a cutoff distance of 17 Å at 77 K with equal probabilities of translation, rotation, reinsertion, and swap. Selected results with all computed with adsorbate probes of Ar and $CO_2$ at their respective normal boiling temperatures of 87.3 K and 195 K. All simulations assumed a rigid framework structure; no framework flexibility was accounted for. Electrostatic effects were not accounted for when using nitrogen as the adsorbate. A cutoff distance of 12 angstroms was used for both force fields. A representative configuration of water loading corresponding to 1 wt% concentration in the MOF and representative DMF loadings corresponding to 1 wt% and 5 wt% concentrations in the MOF were saved from their Monte Carlo simulations and subsequently subjected to nitrogen adsorption in a follow-on Monte Carlo simulation, treating the preadsorbed molecules as extra-framework species in the force field definitions in line with previous studies.[8] Simulations for UiO-66 and UiO-66-$NH_2$ used a 2 x 2 x 3 unit cell domain, and simulations for MOF-808 used a 2 x 2 x 2 unit cell domain.

Molecular dynamics simulations were conducted by Dr. Adam Hinkle using the LAMMPS[9] code. In the codes, for production runs analyzing the HCl solution activation process of MOF-808, a 2 x 2 x 2 unit cell simulation domain of MOF-808 was utilized. For other screening runs on UiO-66 and MOF-74 with other guest molecules, a 1 x 1 x 1 unit cell simulation domain was used. The ReaxFF[5] reactive force field jz0c02930,[10] trained on the zirconium-based MOF MIL-140C was used for UiO-66 and MOF-808, as it was parameterized and trained on structurally similar materials to the MOFs used in this study. The ReaxFF reactive force field CHONSSiCaCsKSrNaMgAlClIFLiX[11] was used for simulating Mg-MOF-74. A Langevin thermostat was used in the NVE ensemble with a time step of 0.1 fs in all simulations. In the simulations, each atom is assigned a unique identifier number, with its bonding explicitly tracked roughly every 1 % of the total simulation time, including its total number of bonds and the identifier number of the atoms that it is bonded to. This information was then converted by a postprocessing code into time-dependent species population data to quantify reaction product data.

## 3. RESULTS AND DISCUSSION

Monte Carlo simulations were finalized through simulating isotherms of other probe gases such as argon and carbon dioxide in the pristine MOFs and through trying to match nitrogen isotherms of experimental materials by making structural modifications to the pristine framework, optimizing the new structure through quantum chemical calculations and simulating nitrogen adsorption equilibria on the resulting material. Probe gases argon and carbon dioxide offer different steric dimensions than nitrogen and shed light on accessible pore volume for a range of probe molecule sizes. For simulations where a zirconium oxide cluster defect was implemented, the unit cell was replicated twice in the x direction and four times in the y direction to avoid adjacent vacant node sites in the simulation upon implementation of periodic boundary conditions.

Results on pristine UiO-66 with argon and carbon dioxide are shown in Figure 1 and compared to previously simulated nitrogen isotherms. Isotherms are decomposed on a pore type basis, compartmentalizing by tetrahedral and octahedral

pores in the MOF, as discussed in the 2022 report on this program. For all adsorbates, it is shown that the two inflection points in the total isotherm correspond to filling of the two pore types in the order of their pore sizes, with the smaller tetrahedral pores preferentially filled at lower pressures.

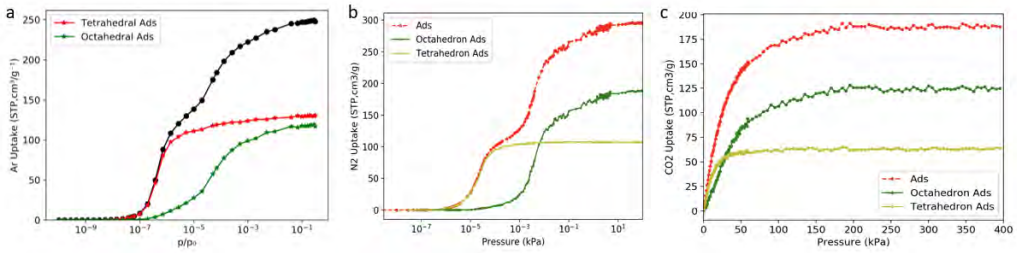


**Figure 1. Adsorption isotherms of (a) Ar, (b) $N_2$, and (c) $CO_2$ on UiO-66 crystallographic structure calculated using the grand canonical Monte Carlo simulations at 87.3 K, 77.4 K, and 195 K respectively.**

Results with UiO-66-$NH_2$ are shown in Figure 2. The argon and nitrogen isotherms on UiO-66-$NH_2$ with the unmodified UiO-66. It is shown that due to addition of $NH_2$ group, the low-pressure adsorption increases for both argon and nitrogen and more substantially for argon, due to increased solid-fluid interaction energy. At the same time, the larger $NH_2$ group causes the high-pressure adsorption capacity to be reduced compared to the unmodified UiO-66, more substantially reduced for nitrogen.

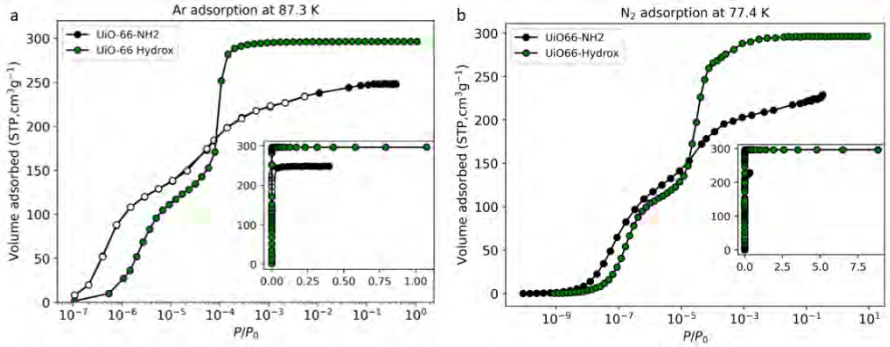


**Figure 2. Comparison of simulated isotherms of (a) Ar, and (b) $N_2$ on hydroxylated UiO-66 vs UiO-66-$NH_2$.**

In-house UiO-66 and UiO-66-$NH_2$ samples were shown from thermogravimetric analysis to contain four missing linker molecules per node and two missing linker molecules per node, respectively, and so this property was implemented into the corresponding structure files. Further, pore size distribution analysis from experimental nitrogen isotherms showed the presence of a missing cluster defect in the structure, and so one missing cluster per 8-unit cell domain was induced as well. Further, infrared spectroscopy data showed contamination of the UiO-66 experimental sample with dimethylformamide, though this was minimal for the UiO-66-$NH_2$ experimental sample, so 1 wt% residual solvent was implemented into the UiO-66 sample as well (Figure 3). Further efforts to make structural modifications to the isotherms to match experimental data were carried out. These previous efforts focused on gauging the impact of individual structural modifications on the nitrogen isotherm of the MOFs, namely induction of missing linker defects with hydroxyl group termination, presence of residual dimethylformamide solvent in the pores (from synthesis, through running a separate Monte Carlo simulation of dimethylformamide adsorption prior to nitrogen adsorption), induction of missing cluster defects for the UiO-66 and UiO-66-$NH_2$ family, and variation of modulator type for the MOF-808 family (hydroxyl, acetate, and formate modulation). Additional efforts focused on implementing combinations of these features in a single structure and isotherm in the effort to try to match data from experimental materials at CBC (Figures 4, 5, 6). Results show that these modifications closely represent the experimental isotherms for both UiO-66 and UiO-66-$NH_2$ (Figures 4 and 5), with the correlation closest for UiO-66-$NH_2$, as the isotherms are nearly identical between simulation and experiment. Lastly, for MOF-808, nuclear magnetic resonance spectroscopy experiments showed full modulation of acetate groups on the node and applying a scaling factor of 0.7 to the simulated acetate-modulated structure closely matched experiments (Figure 6). The interpretation of this from previous literature is that only 70 % of the pores are accessible to adsorbate, with the rest filled with residual solvent or structurally collapsed.

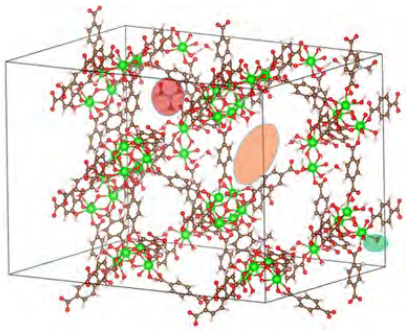

**Figure 3. Representative structure of UiO-66 used in simulations which most closely resembles the experiment. Modifications include missing cluster defect (orange), missing linker defects (green) and presence of residual dimethylformamide solvent (red).**

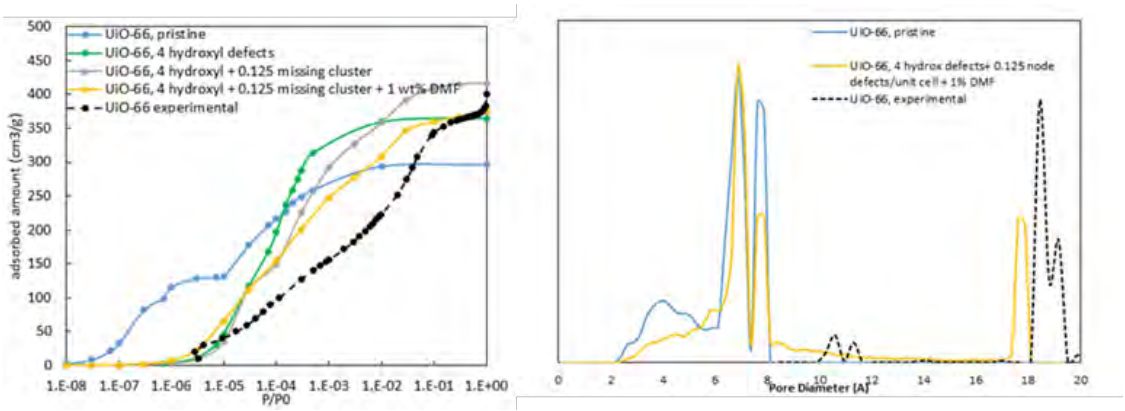


**Figure 4. Simulated nitrogen isotherms for the following UiO-66 derivatives: UiO-66 pristine, UiO-66 with four hydroxyl defects per unit cell, UiO-66 with four hydroxyl defects and one missing cluster per 8-unit cells, UiO-66 with four hydroxyl defects and 1 missing cluster per 8-unit cell + 1 wt% DMF, and experimental sample (left). Pore size distribution of the closest matching sample to experiments (right).**

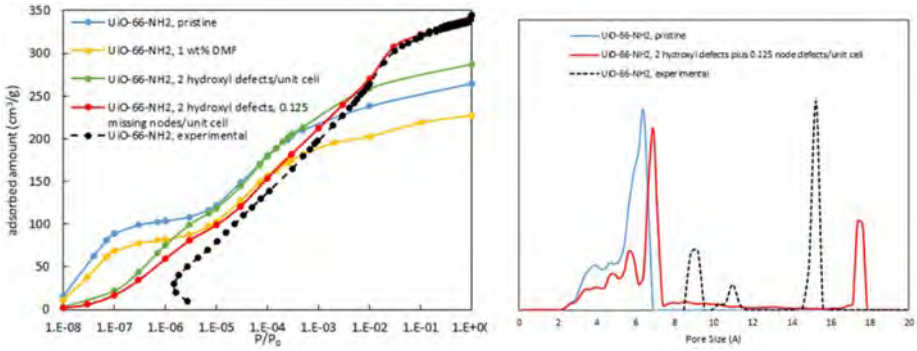


**Figure 5. Simulated nitrogen isotherms for the following UiO-66-$NH_2$ derivatives: pristine, two hydroxyl defects per unit cell, two hydroxyl defects, and one missing cluster per 8-unit cells, one weight percent dimethylformamide preadsorbed, two hydroxyl defects and one missing cluster, and experimental sample (left). Pore size distribution of the closest matching sample to experiments (right).**

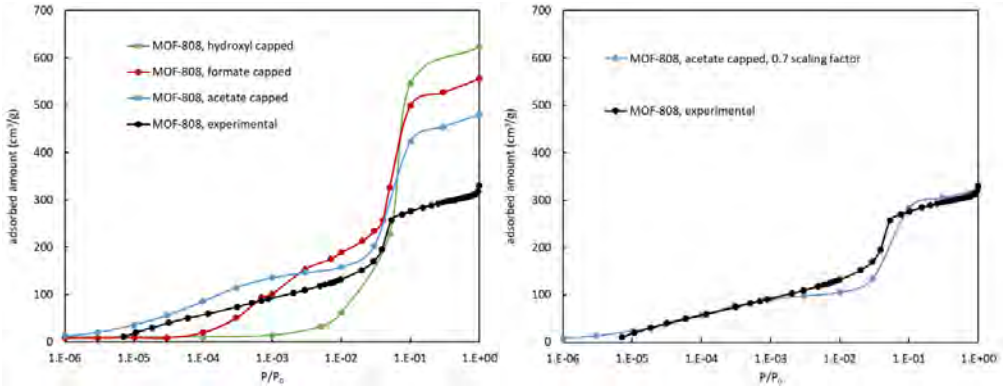


**Figure 6. Simulated nitrogen isotherms for MOF-808 with formate, acetate, and hydroxyl node capping (left) and MOF-808 acetate capping with scaling factor of 0.7 applied to match experiments (right).**

The focus of the project then turned fully to reactive molecular dynamics simulation. In addition to the UiO-66 and MOF-808 family of MOFs, simulations were also performed with the MOF-74 family, as a greater number of ReaxFF force fields were found to be compatible with this family of MOFs. Each family consists of a structure considered the "baseline" representation, with wide ability for modification. For UiO-66, the principal modification considered was functionalization of the linker component. For MOF-808, the principal modification considered was modulation of the node. For MOF-74, the principal modification considered was substitution of the metal, with the magnesium analogue considered the baseline version of the material (Figure 7).

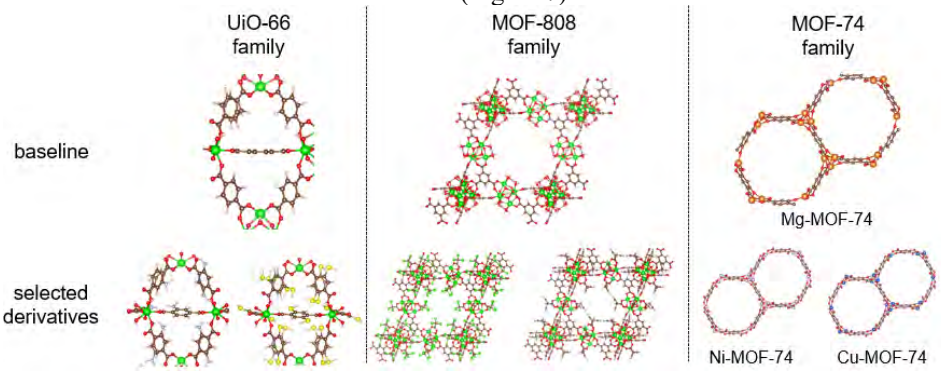


**Figure 7. MOF classes and selected derivatives investigated in reactive molecular dynamics simulations. Left: UiO-66 family, Middle: MOF-808 family, Right: MOF-74 family.**

Among force field testing, several phenomena were observed in the unexposed zirconium MOFs. Namely, for formate-modulated MOF-808 and UiO-66 with formate-terminated missing linker defects, it was seen that two principal phenomena tend to occur. First, some of the formate groups seemed to partially detach from the zirconium sites with no external driving force for this. Further, some of the $\mu_3$-OH groups migrated to a $\mu_2$-OH configuration, switching from being bonded to three zirconium atoms to being bonded to two zirconium atoms (Figure 8). These processes/phenomena are both observed in ab-initio molecular dynamics simulation in Quantum Espresso, which explicitly accounts for the electronic structure of the material, supporting our observation of these phenomena which has strong implications for interpretation of the modulated structure of these materials.

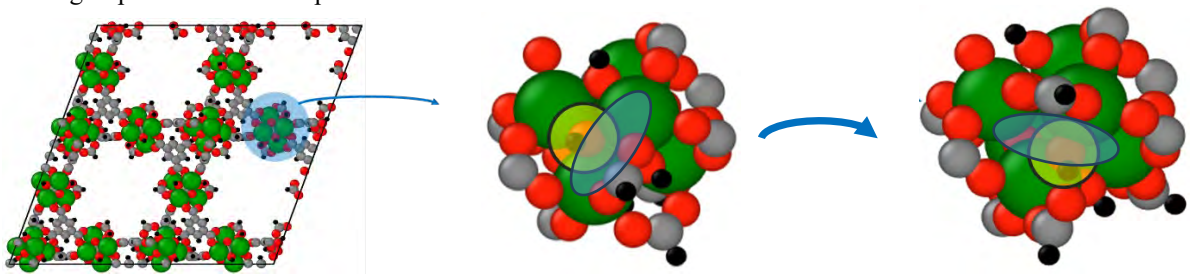

**Figure 8. Migration behavior of $\mu_3$-OH observed in MOF-808 cluster to transition to $\mu_2$-OH observed in both reactive molecular dynamics and ab-initio molecular dynamics simulations.**

Several studies were then performed introducing guest molecules into the structure. In addition to explicit bond parameters defined in the force field files, the ability of the ReaxFF force field to represent a given bond in question can be determined through simulating a dimer of interest and computing the total potential energy of the system. If the opposite of the calculated potential energy is equal to the literature value for the bond dissociation energy of the dimer, then the bond in question can be properly described by the force field. Taking this into account and using chemical intuition on the types of bonds that must be described by any potential reaction pathways, it was determined that the hydrochloric acid (HCl) activation process of removing hydrocarbon modulators from the zirconium MOFs could be properly described by the force field (Figure 9). In this process, formate groups present on the node from residual dimethyl formamide in synthesis are removed, exposing hydroxyl groups on the node which are favorable for many guest molecule reactions. Understanding the mechanism, reaction products, and effect of synthesis conditions on this process would be valuable in improving it.

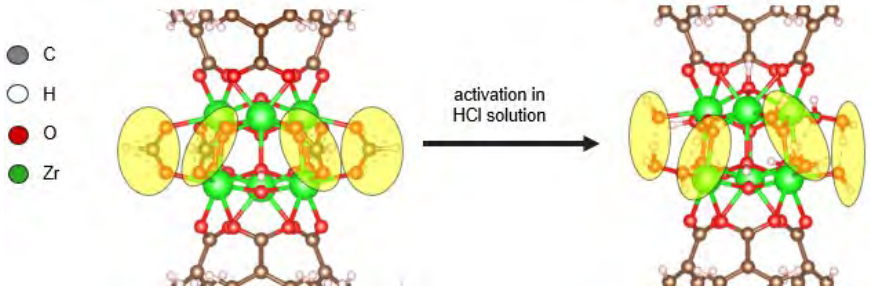


**Figure 9. Hydrochloric acid activation of MOF-808 with formate modulation.**

The simulation setup is shown in the right of Figure 10, and one of the mechanisms determined is shown in Figure 11. The mechanism consists of proton transfer from the HCl molecule to a neighboring free water molecule, resulting in concomitant proton transfer from the free water molecule to one of the oxygen atoms of a formate modulator, leading to immediate detachment as formic acid. Further, one of the $\mu_3$-OH groups then transitions to a $\mu_2$-OH configuration, leading to partial detachment of a second formate and transfer of a proton from the previously detached formic acid to the oxygen atom of the $\mu_2$-OH. This results in a free formate group and a partially desorbed formate group.

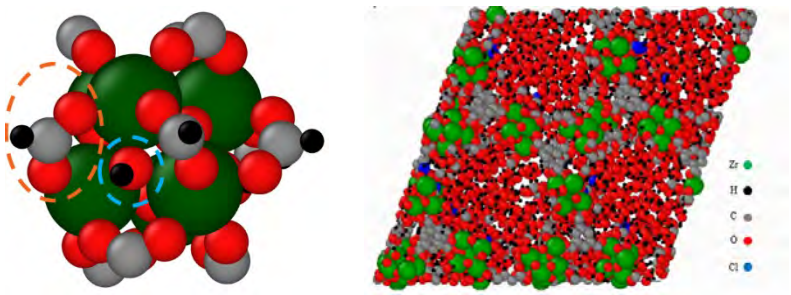


**Figure 10. Left: MOF-808 cluster with formate modulator and $\mu_3$-OH group circled (left) and MOF-808 with its pores saturated with HCl solution (right).**

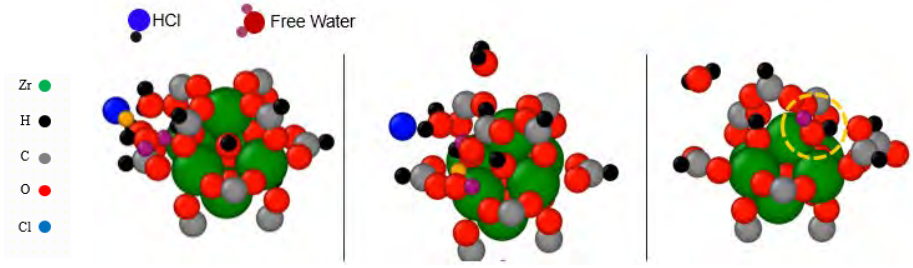


**Figure 11. HCl activation mechanism determined from reactive molecular dynamics simulations on MOF-808. Participating hydrogen atoms on the HCl and free water molecules are distinctly colored yellow and purple. Left: starting configuration. Center: Dissociation of HCl, proton transfer to $H_2O$, and protonating formate group as formic acid. Right: $\mu_3$-OH transition to $\mu_2$-OH, partial desorption of second formate.**

Reaction product species quantification was then performed on a system scale for run times up to equilibrium (3 nanoseconds) for a temperature of 300K (Figure 12) and for a range of temperatures (300K, 400K, 600K, 1200K) (Figure 13), all for the lowest HCl concentration analyzed. Fates of the formate species included remaining fully attached, being partially desorbed (only one oxygen atom bonded to a zirconium atom), being fully desorbed as a formate group, and being fully desorbed as a formic acid group. The ideal scenario is being fully desorbed as a formic acid group, as this frees all zirconium sites for hydroxyl speciation from neighboring water molecules and leaves the desorbed product in a neutrally charged state with a lower propensity for subsequent reaction. Results show that free formate decreases and free formic acid increases from 300K to 600K, with partially attached formate remaining the same. At 1200K, all species are present as free CO or $CO_2$, reflecting full decomposition of the organic component of the MOF structure. Therefore, for the HCl concentration evaluated, 600K could be considered as an optimum temperature for the activation process. Further efforts being pursued involve collecting equivalent reaction product speciation data for a range of HCl concentrations in MOF-808 and comparing the statistics to formate-capped defecting UiO-66 (Figure 14). This represents a similar modulation environment with slightly different zirconium oxide configuration in the node.

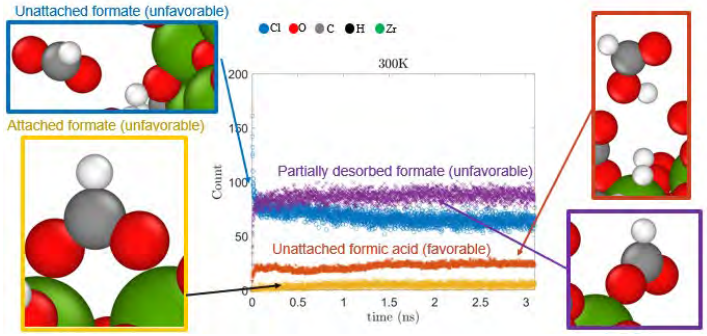


**Figure 12. Species identification and quantification for formate groups involved in HCl activation of MOF-808 at 300K.**

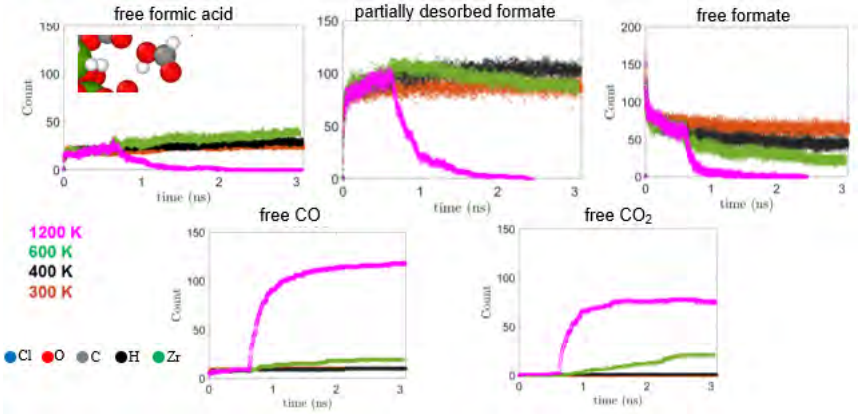


**Figure 13. Species identification and quantification for formate groups involved in HCl activation of MOF-808 at a range of temperatures: 300K, 400K, 600K, and 1200K.**

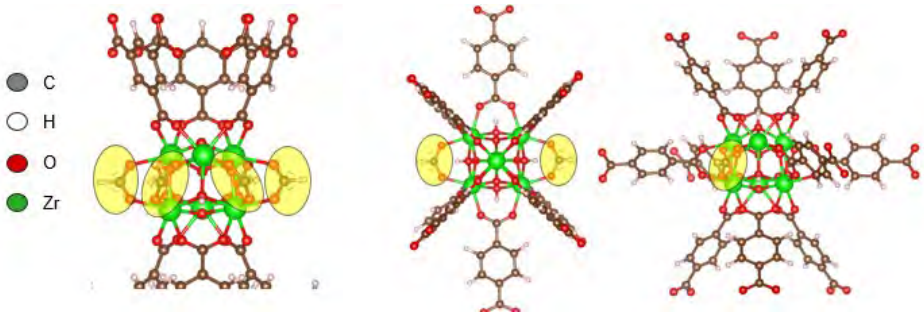


**Figure 14. Formate modulation on MOF-808 (left) and on UiO-66 with two formate-terminated missing linker defects per unit cell (middle, right).**

Screening for additional guest molecule reactions on the zirconium MOFs was then explored (Figure 15). Several structural analogues of UiO-66 and MOF-808 were optimized via quantum chemical calculations, incorporating functional groups shown in Figure 15 on the terephthalic acid ligand of UiO-66 and as a carboxylic acid-based modulator for MOF-808. A range of guest molecule studies, annotated in Figure 15, were explored at 5 molecules per unit cell for UiO-66 and 10 molecules per unit cell for MOF-808 using simulations of 1 nanosecond length.

| Toxic industrial chemicals | Functional groups in MOFs |
|---|---|
| CO | -COOH |
| $CO_2$ | -OH |
| $NH_3$ | $-NO_2$ |
| $NO_2$ | $-NH_2$ |
| $SO_2$ | $-SO_3H$ |
| $H_2S$ | -SH |
| HCl | -C≡N |
| HCN | -N=C=S |

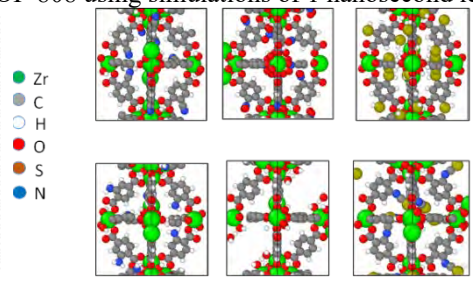


**Figure 1. Functional groups and toxic industrial chemicals incorporated into and exposed to zirconium-based MOFs (left) and structures of selected derivatives generated from quantum calculations (right).**

Among these reactivity data, promising results were shown with hydrogen sulfide. Mechanistic data with baseline UiO-66 (Figure 16) shows the hydrogen atom protonating the oxygen atom of one of the linkers, leading to partial detachment and hydrogen bonding to the $\mu_3$-OH moiety of the node. Subsequently, the linker fully detaches from the node and the $HS^-$ anion bonds covalently to a vacant site on the corresponding zirconium atom.

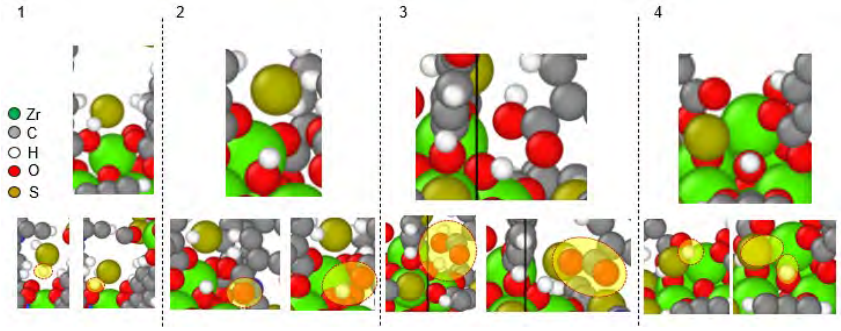


**Figure 16. Hydrogen sulfide reaction mechanism observed on UiO-66, featuring protonation of linker oxygen molecule from hydrogen atom of hydrogen sulfide, partial desorption of linker and hydrogen bonding to μ3-OH, then full detachment and HS chemisorption to zirconium site.**

The mechanism changes upon incorporating cyano groups into the structure. In MOF-808, cyano groups deprotonate the $H_2S$ molecule, in addition to oxygen atoms on the modulator, leading to formation of a $S^{-2}$ anion. This coordinates with the node in a $\mu_2$-S configuration, with the sulfur atom bonded to two zirconium atoms.

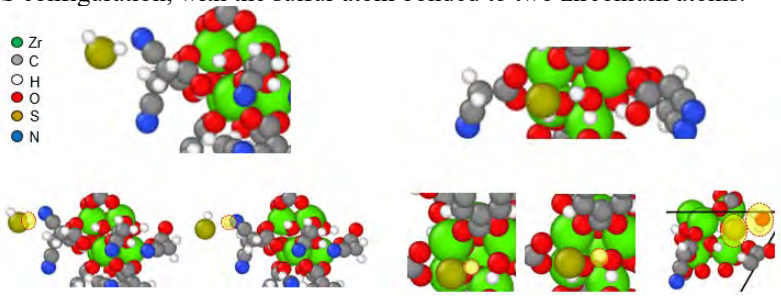


**Figure 17. Hydrogen sulfide reaction mechanism observed on cyanoacetic acid-modulated MOF-808.**

Steric factors among participating functional groups appear to play a role in mechanistic data. With UiO-66, in contrast to MOF-808, while hydrogen sulfide is still deprotonated by the cyano groups, the proximity of the functional groups seems to favor the $HS^-$ reaction intermediates reacting with each other to form dihydrogen disulfide and then trisulfur (Figure 18). This type of reaction to a higher-molecular-weight product would be favorable for filtration, as such products would have greater propensity for removal via physical adsorption than the toxic reactant molecule due to lower vapor pressure. This will be explored in greater detail in fiscal year 2024.

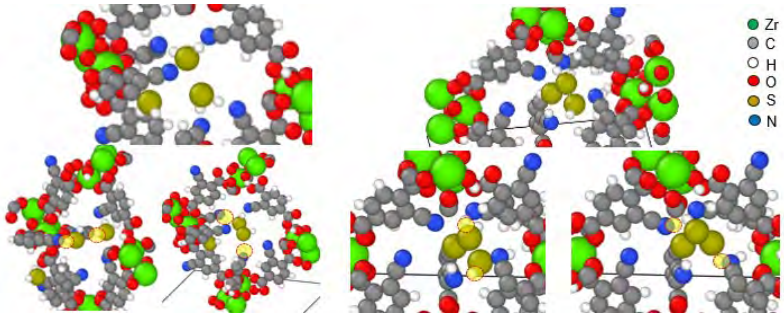


**Figure 18. Hydrogen sulfide reaction mechanism observed with cyano-functionalized UiO-66.**

Lastly, selected guest molecule interactions were explored with Mg-MOF-74 due to the wider availability of potential ReaxFF force fields for describing the constitutive atoms of the structure. Among the results observed that reflect previous experimental data are decomposition of the structure in water (Figure 19) and nitrogen dioxide chemisorption consisting of the oxygen atom of $NO_2$ chemisorbing to the Mg atom of Mg-MOF-74[12] (Figure 20). This will be further explored in fiscal year 2024 to gauge the effect of chemical modifications to the structure on these phenomena.

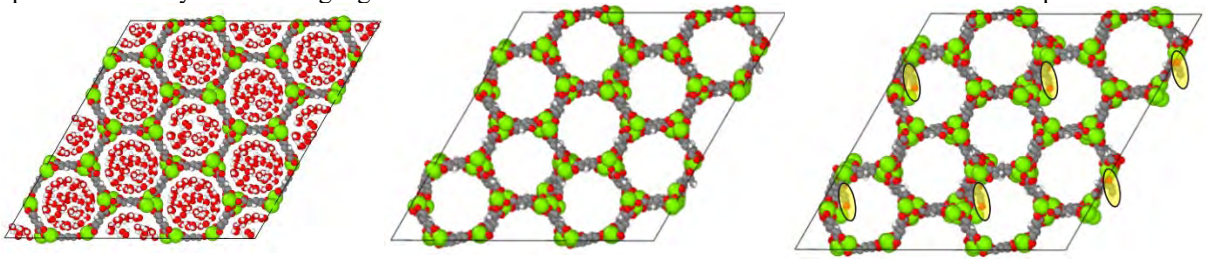

**Figure 19. Water interaction with MOF-808. Left: Starting configuration. Middle: starting configuration with water molecules removed. Right: ending configuration with water molecules removed, clearly depicting structural collapse through linker detachment from the node.**

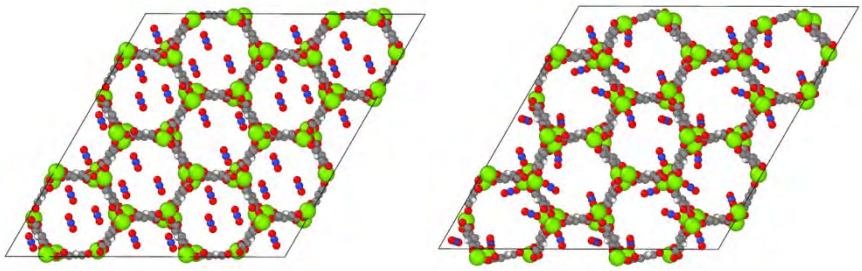

**Figure 20. Nitrogen dioxide reaction on Mg-MOF-74, with the oxygens of nitrogen dioxide chemically adsorbing to the magnesium sites of the MOF.**

## CONCLUSIONS

Monte Carlo and molecular dynamics simulations have been used to simulate adsorption and chemical reactions on zirconium-based metal-organic frameworks UiO-66, UiO-66-$NH_2$, MOF-808, and MOF-74. It has been shown that experimental adsorption data can be closely reproduced from simulations upon incorporating structural deviations to the MOF supported by characterization data. Reactive molecular dynamics simulations have been performed to determine optimal conditions facilitating the HCl activation reaction removal of formate modulators from MOF-808 and are in progress with formate-modulated missing-linker-defective UiO-66. Other promising results involving hydrogen sulfide reaction on cyano functionalized UiO-66 and MOF-808 and nitrogen dioxide reaction on Mg-MOF-74 have been identified with chemically reactive force fields and will be pursued further in fiscal year 2024.

## ACKNOWLEDGMENTS

Funding was provided by the U.S. Army via the Chemical Biological Advanced Materials and Manufacturing Science Program (PE 0601102A Project VR9) at the Combat Capabilities Development Command Chemical Biological Center.

## REFERENCES

[1] Bobbitt, N.S.; Mendonca, M.L.; Howarth, A.J.; Islamoglu, T.; Hupp, J.T.; Farha, O. K.; Snurr, R.Q. Metal-organic frameworks for the removal of toxic industrial chemicals and chemical warfare agents. *Chem. Soc. Rev.* **2017**, *46* (11), pp 3357–3385.

[2] Kandiah, M.; Nilsen, M. H.; Usseglio, S.; Jakobsen, S.; Olsbye, U.; Tilset, M.; Larabi, C.; Quadrelli, E. A.; Bonino, F.; Lillerud, K. P. Synthesis and Stability of Tagged UiO-66 Zr-MOFs. *Chem. Mater.* **2010**, *22*, pp 6632–6640.

[3] Winarta, J.; Shan, B. H.; McIntyre, S. M.; Ye, L.; Wang, C.; Liu, J. C.; Mu, B. A Decade of UiO-66 Research: A Historic Review of Dynamic Structure, Synthesis Mechanisms, and Characterization Techniques of an Archetypal Metal-Organic Framework. *Cryst. Growth Des.* **2020**, *20* (2), pp 1347–1362.

[4] Liu, L. M.; Chen, Z. J.; Wang, J. J.; Zhang, D. L.; Zhu, Y. H.; Ling, S. L.; Huang, K. W.; Belmabkhout, Y.; Adil, K.; Zhang, Y. X.; Slater, B.; Eddaoudi, M.; Han, Y. Imaging defects and their evolution in a metal-organic framework at sub-unit-cell resolution. *Nat. Chem.* **2019**, *11* (7), pp 622–628.

[5] Senftle, T.P.; Hong, S.; Islam, M.M.; Kylasa, S.B.; Zheng, Y.X.; Shin, Y.K.; Junkermeier, C.; Engel-Herbert, R.; Janik, M.J.; Aktulga, H.M.; Verstraelen, T.; Grama, A.; van Duin, A.C.T. The ReaxFF reactive force-field: development, applications and future directions. *npj Comput. Mater.* **2016**, *2*, p 15011.

[6] Giannozzi, P.; Andreussi, O.; Brumme, T.; Bunau, O.; Nardelli, M. B.; Calandra, M.; Car, R.; Cavazzoni, C.; Ceresoli, D.; Cococcioni, M.; Colonna, N.; Carnimeo, I.; Dal Corso, A.; de Gironcoli, S.; Delugas, P, Distasio Jr, R.A.; Ferretti, A.; Floris, A.; Fratesi, G.; Fugallo, G.; Gebauer, R.; Gerstmann, U.; Giustino, F.; Gorni, T.; Jia, J.; Kawamura, M.; Ko, H.-Y.; Kokalj, A.; Kucukbenli, E.; Lazzeri, M.; Marsili, M.; Marzari, N.; Mauri, F.; Nguyen, N.L.; Nguyen, H.-V.; Otero-de-la-Roza, A.; Paulatto, L.; Ponce, S.; Rocca, D.; Sabatini, R.; Santra, B.; Schlipf, M.; Seitsonen, A.P.; Smogunov, A.; Timrov, I.; Thonhauser, T.; Umari, P.; Vast, N.; Wu, X.; Baroni, S. Advanced capabilities for materials modelling with QUANTUM ESPRESSO. *J. Phys.: Condens Matter.* **2017**, *29* (46), p 465901.

[7] Dubbeldam, D.; Calero, S.; Ellis, D.E.; Snurr, R.Q. RASPA: molecular simulation software for adsorption and diffusion in flexible nanoporous materials. *Mol. Simul.* **2016**, *42* (2), pp 81–101.

[8] Jajko, G.; Kozyra, P.; Gutierrez-Sevillano, J.J.; Makowski, W.; Calero, S. Carbon Dioxide Capture Enhanced by Pre-Adsorption of Water and Methanol in UiO-66. *Chem.-Eur. J.* **2021**, *27* (59), pp 14653–14659.

[9] Thompson, A.P.; Aktulga, H.M.; Berger, R.; Bolintineanu, D.S.; Brown, W.M.; Crozier, P.S.; Veld, P.J.I.; Kohlmeyer, A.; Moore, S.G.; Nguyen, T.D.; Shan, R.; Stevens, M.J.; Tranchida, J.; Trott, C.; Plimpton, S.J. LAMMPS-a flexible simulation tool for particle-based materials modeling at the atomic, meso, and continuum scales. *Comput. Phys. Commun.* **2022**, *271*, p 108171.

[10] Dwivedi, S.; Kowalik, M.; Rosenbach, N.; Alqarni, D.S.; Shin, Y.K.; Yang, Y.J.; Mauro, J.C.; Tanksale, A.; Chaffee, A.L.; van Duin, A.C.T. Atomistic Mechanisms of Thermal Transformation in a Zr-Metal Organic Framework, MIL-140C. *J. Phys. Chem. Lett.* **2021**, *12* (1), pp 177–184.

[11] Muraleedharan, M.G.; Herz-Thyhsen, R.; Dewey, J.C.; Kaszuba, J.P.; van Duin, A.C.T. Understanding the chemistry of cation leaching in illite/water interfacial system using reactive molecular dynamics simulations and hydrothermal experiments. *Acta Mater.* **2020**, *186*, pp 564–574.

[12] Tan, K.; Zuluaga, S.; Wang, H.; Canepa, P.; Soliman, K.; Cure, J.; Li, J.; Thonhauser, T.; Chabal, Y.J. Interaction of Acid Gases $SO_2$ and $NO_2$ with Coordinatively Unsaturated Metal Organic Frameworks: M-MOF-74 (M=Zn, Mg, Ni, Co). *Chem. Mater.* **2017**, *29 (10)*, pp 4227–4235.


SEEDLING
PROJECTS

# Simple Modular Aptamer Response Test (SMART)

Mia Seergae[a], Aleksandr E. Miklos[b], Daniel A. Phillips[b], Elizabeth S. Dhummakupt[b], Kimberly L. Berk[b]*
[a]Army Educational Outreach Program (AEOP) Undergraduate Apprenticeship, 8198 Blackhawk Rd, Aberdeen Proving Ground, MD 21010
[b]U.S. Army Combat Capabilities Development Command Chemical Biological Center, Research & Operations Directorate, 8198 Blackhawk Rd, Aberdeen Proving Ground, MD 21010

## ABSTRACT

A fieldable, low size, weight, and power technology for small molecule detection was created by blending an oligo-based fluorescent reporting system with a published qualitative polymerase chain reaction based aptamer detection method. This design employs a simple isothermal toxin:aptamer competition scheme that would release a barcoded molecular tag ("sensor oligo") upon the binding of the target toxin to an aptamer, activating a fluorescent reporter system that can be visualized using a blue light and orange filter or glasses. This system can detect as little as 100 ng of Aflatoxin M1.

**Keywords:** aptasensor, aptamer, small molecule detection, toxin detection, aflatoxin

## 1. INTRODUCTION

Detection and identification of toxins in rugged or austere environments at point-of-contact is currently not possible. This is a huge gap in our ability to ensure safe environments and resources for both military operations and in public health situations. Detection and identification of toxins, or other small molecules, requires complex equipment and specialized laboratory space as well as highly trained personnel. The advancement of detection of toxins in the field has been hard to obtain due to the size and structure of small molecules. This project was an attempt to establish new methodology for identification by combining two approaches.

### 1.1 Aflatoxin detection assays

A step forward in performing specific toxin identification in a less specialized, but still a laboratory environment was identified when assays were designed for detection of Aflatoxin by qualitative polymerase chain reaction (qPCR).[1,2] These assays leveraged the specific recognition ability of aptamers and the intrinsic properties of DNA to, upon aptamer binding aflatoxin, release a DNA oligo. The DNA oligos bound to the aptamer were used as template for the qPCR reaction and were designed to overlap with the 3'-end of the aptamer in increasing lengths. Primers were designed specifically against the overhang sequence alone, which allowed for generation of an amplicon in a qPCR when the oligo is present. The aptamer was anchored to the wall of a polymerase chain reaction (PCR) tube, allowed the DNA oligo to anneal with the aptamer, and after performing an incubation with the toxin, then they performed qPCR on the bound aptamer in the PCR tube. The increase in cycle threshold (Ct) value (decrease in detection quantity) was confirmation of a binding event between the aptamer and toxin and thus detection of the toxin. When alternative toxins were used for the test, their Ct values were near the same low Ct value as the control (no toxin incubation) sample.

### 1.2 DNA taggants reporter system

Previous efforts were made to design a fluorescent reporter system that would allow users to tag items in a supply chain so they could be verified for authenticity further down the line.[3] DNA is easily embedded into various substrates (ink, textiles, grease, etc.) that can be used to covertly mark an item. A total of 32 sequence sets were developed and tested for their ability to multiplex. Three oligos involved with each set of sequences for this system: a fluorophore bound oligo, a quencher bound oligo, and an unmodified oligo. The fluorophore oligo is 22 bp long with a 30 bp poly–T tail and a 3'-FAM fluorophore. The quencher oligo is 16 bp long, partially complementary to the fluorophore

oligo on the 3'-end and has a 5'-Black-Hole Quencher. The unmodified oligo is fully complementary to the fluorophore oligo except for the poly-T tail. The unmodified oligo is the tag component in the system. The fluorophore and quencher oligo sets would be bound to a ticket. The activation would occur after placing the ticket, Tris-Mg buffer, and a swab collected from the tagged item into a pouch and mixing. Only the tagged item-specific spots recover fluorescence and can be visualized using commercial-off-the-shelf available blue flashlight and orange glasses.

## 2. METHODOLOGIES

### 2.1 Aptasensor and oligo design

This system is comprised of an aptasensor and reporter complex (Figure 1). The aptasensor is made up of an anti-toxin DNA aptamer (in this case against aflatoxin M1 (AFM1)) bound to a partially complementary sensor oligo. The reporter complex contains two partially complimentary oligos, one modified with a fluorescence quencher and the other with a fluorescein isomer (FAM). The colocalization of the quencher and FAM due to complimentary oligo binding suppresses the emission of FAM, thus in the absence of AFM1 there is no fluorescent signal. When AFM1 is present, it competes with the sensor oligo for binding with the aptamer. The aptamer has a higher affinity for the toxin, so the sensor oligo is released, allowing it to interact with the reporter complex, displace the quencher oligo, and fluoresce.

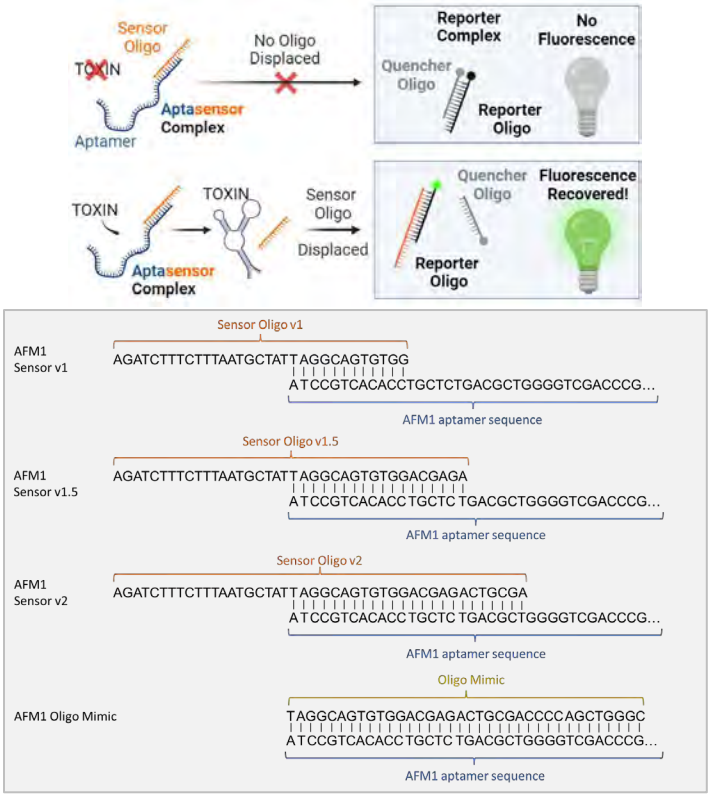


**Figure 1. Aptasensor scheme and sensor oligo design.**

Multiple versions of the sensor oligo were designed and tested to mirror the experiments performed in literature for a PCR-based detection system.[1,2] These sensor oligos overlapped 12, 18, or 24 bp of the aptamer for versions 1, 1.5, and 2, respectively (Figure 1). Adjusting the amount of overlap was hypothesized to balance between specificity (requiring strong binding of toxin to aptamer to release the signal) and sensitivity (allowing the signal to be released more readily). Finally, an oligo mimic was designed to compete with the sensor oligos to mimic the effects of a toxin binding event by releasing the sensor oligos into solution. This oligo mimic was used to verify the system worked before introducing toxin. A second aptasensor complex was designed using an aflatoxin B1 (AFB1) specific aptamer but, while successful, data is not shown here. All versions of the aptasensor were designed to work with one reporter complex.

### 2.2 Oligo and Tris-Mg buffer preparation

The aptamer and sensor oligos were resuspended in nuclease-free water (2000 µM) while the reporter and quencher oligos were similarly suspended at a concentration of 100 µM. The Tris-Magnesium (Tris-Mg) buffer used for all reactions was a 10 mM Tris-HCl, 10 mM $MgSO_4$ solution in Milli-Q water.

### 2.3 Reporter ticket generation

The reporter system was created by combining the reporter and quencher oligos in a 1:7 ratio in Tris-Mg buffer. Oligos were incubated at room temperature for 15 minutes. The loss of fluorescence was verified by using an E-gel rig. The reporter complex solution was deposited on nitrocellulose tickets at 3 µL per spot and contained 14 pmol of the reporter oligo and 100 pmol of the quencher oligo. These tickets were allowed to dry for 30–60 minutes at 60 °C. After thoroughly dried, the tickets were washed in Tris-Mg buffer for 5 minutes on each side for a total of 15 minutes. The tickets were dried again for a minimum of 60 minutes at 60 °C or at room temperature overnight. All tickets generated contained one spot of the reporter system for the aflatoxin detection assay and one spot containing an orthogonal reporter system to act as a negative control. Tickets were stored at room temperature in the dark until ready for use.

### 2.4 Aptasensor ticket generation

The aptasensor system was created by depositing both aptamer and sensor oligos. The aptamer was diluted 1:1 in Tris-Mg buffer and 2 µL was deposited on 4 spots. Each spot contained 2000 pmol with one ticket containing 8000 pmol of aptamer total. These tickets were dried for 30–60 minutes at 60 °C. Once dry, the tickets were washed in Tris-Mg buffer for 5 min on each side for a total of 15 min. Tickets were dried for a minimum of 60 min at 60 °C.

Next, the sensor oligo (v1, v1.5, and v2 were used on separate tickets) was diluted 1:1 in Tris-Mg buffer and 2 µL was deposited per spot across same 4 spots containing the aptamer sequence. Each spot contained 2000 pmol with one ticket containing 8000 pmol of sensor oligo total. These tickets were allowed to dry for at least 60 min at 60 °C then washed in Tris-Mg buffer for 5 min on each side. The Tris-Mg buffer was replaced with fresh buffer, and the wash protocol was repeated for an additional 15 minutes. As the sensor oligo will trigger the reporter system, it is essential this wash remove unbound sensor oligos. Tickets were dried for 60 minutes at 60 °C or overnight at room temperature.

## 3. RESULTS

### 3.1 Verification of reporter and aptasensor complexes

First, the combination of the aptasensor complex with the reporter complex was tested (Figure 2). The reporter complex and aptasensor complex were prepared on separate tickets. Both the toxin specific reporter system and negative control (responsive to an orthogonal signal) were added to each reporter ticket. The tickets were placed in the same baggie with Tris-Mg buffer. Tickets were incubated in buffer for more than one hour. The toxin oligo (target) mimic was then added and allowed to react, followed by a negative control orthogonal trigger oligo which showed the reporter complexes responded properly. The aptasensor complex does not activate the reporter unless the sensor oligo is released. The negative control reporter complex has been verified to work in the presence of its orthogonal oligo but was not activate in the presence of the aptasensor complex, toxin oligo mimic, or released sensor oligo.

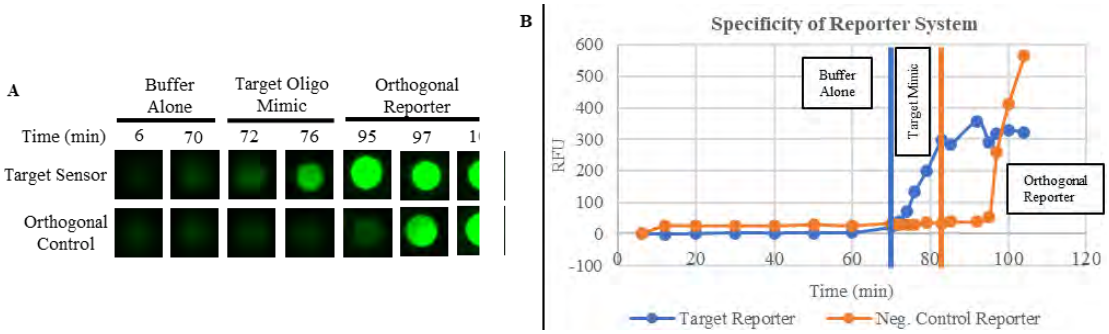


**Figure 2. Time lapse of reporter system after exposure to specific and orthogonal control. A) Images from LI-COR Odyssey imaging system. B) Analysis of pixel intensity performed using LI-COR Image Studio software.**

Next, the aptasensor complex was verified for specificity (Figure 3). The sensor oligo should not be released except in the presence of its specific oligo mimic (AFM1). To test this, an oligo mimic designed for a different aptasensor complex (AFB1 oligo mimic) was incubated with the AFM1 aptasensor and reporter complex. After approximately one hour, the AFM1 aptasensor oligo mimic was added and incubated. Fluorescence was not recovered until the correct oligo mimic was added.

### 3.2 Aptasensor comparison

Each aptasensor was prepared on separate tickets at the same concentration. The reporter complex tickets were prepared at the same time, using the same reagent working stocks. The aptasensor and reporter tickets were placed into a baggie together with the Tris-Mg buffer. A total of 8000 pmol of the different versions of AFM1 oligo mimics were added and imaging of the ticket was performed over 30–60 minutes. The results in Figure 3 indicate that smaller aptasensor overlaps lead to faster activation of the reporter complexes when displaced by the oligo mimic, with the 'v2' aptasensor requiring twice the amount of time to trigger the reporter complex.

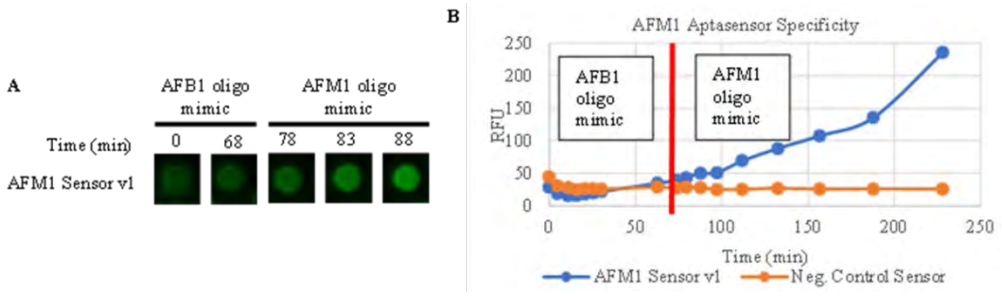


**Figure 3. AFM1 aptasensor specificity. Time lapse of reporter system activation after exposure to non-target (AFB1 aptasensor) and target (AFM1 aptasensor) oligo mimics. A) Images from LI-COR Odyssey imaging system. B) Analysis of pixel intensity performed using the LI-COR Image Studio software.**

### 3.3 Aptasensor detection of AFM1 toxin

The aptasensor systems were assayed with AFM1 toxin. All versions of the aptasensor worked to trigger the reporter system in less than 20 minutes using 500 ng of AFM1 toxin (Figure 5A, 5B). This contrasts with the AFM1 oligo mimic finding (Figure 4) and may indicate that toxin binding is much more effective at releasing the sensor oligos. To test the specificity of the AFM1 aptamer, estradiol was selected as a 'simulant' for AFM1 based on very roughly similar structures. A total of 500 ng of estradiol, while slow (Figure 5C), does eventually trigger the reporter system. The AFM1 aptasensor v1 system was further tested with 100 ng of AFM1 toxin (Figure 5D). Ultimately, we successfully recovered fluorescence, but it took nearly an hour to see a distinguishable difference between the negative control and the sensor, roughly comparable to the estradiol control.

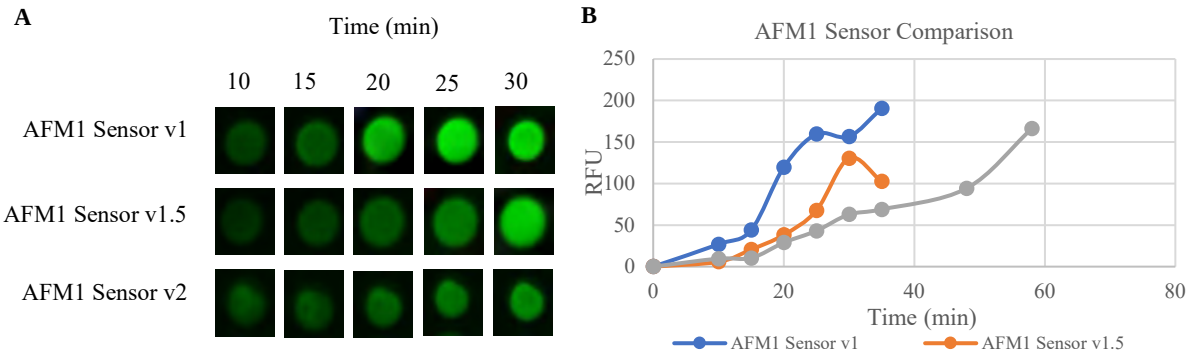


**Figure 4. AFM1 sensor system evaluation. Time lapse of AFM1 system after exposure to target mimic. A) Images from LI-COR Odyssey imaging system for AFM1 Sensor v1, AFM1 Sensor v1.5, and AFM1 Sensor v2. B) Analysis of pixel intensity performed using LI-COR Image Studio software for AFM1 Sensor v1, AFM1 Sensor v1.5, and AFM1 Sensor v2.**

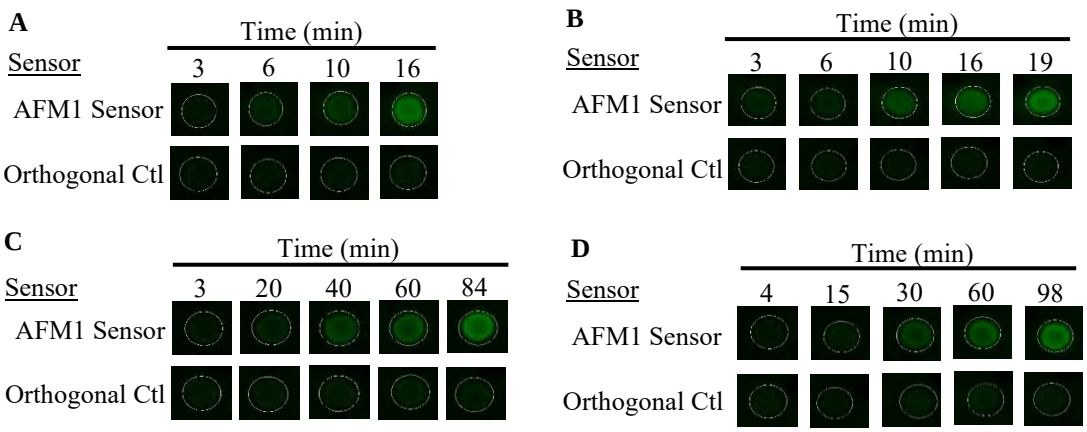


**Figure 5. A total of 500 ng AFM1 toxin assayed against A) AFM1 Sensor v1.5 and B) AFM1 Sensor v2. C) Conversely, 500 ng Estradiol assayed against AFM1 Sensor v1. D) Finally, 100 ng AFM1 toxin assayed against AFM1 Sensor v1.**

The AFM1 aptasensor was tested using AFB1 toxin (data not shown) and the toxin did activate the reporter system, indicating the aptamer was not specific for AFM1. Inspection of the structure for AFB1 and AFM1 show they differ by only a hydroxyl group. This highlights how important aptamer specificity is to the overall system.

## 4. CONCLUSIONS

We have demonstrated that the aptasensor system is specific (to the limits of the parent aptamer) as well as rapid and perhaps most importantly isothermal and eye-readable for field use. Detection of aflatoxin in the nanogram (ppb) range means this system is within an order-of-magnitude for the Food and Drug Administration actionable level detection. With additional optimization, this system could exceed current detection standards.

## ACKNOWLEDGMENTS

Funding for this Seedling project was made available through the Department of Defense Funding Laboratory Enhancements Across (X) Four Categories (FLEX 4) in accordance with the Army, Navy, and Air Force efforts funded under the authority in 10 U.S.C. § 4123.

## REFERENCES

[1] Guo, X.; Wen, F.; Zheng, N.; Li, S.; Fauconnier, M.-L.; Wang J. A qPCR aptasensor for sensitive detection of aflatoxin M1. *Anal. Bioanal. Chem.* **2016**, *408* (20), pp 5577–5584.

[2] Guo, X.; Wen, F.; Zheng, N.; Luo, Q.; Wang, H.; Wang, H.; Li, S.; Wang, J. Development of an ultrasensitive aptasensor for the detection of aflatoxin B1. *Biosens. Bioelectron.* **2014**, *56*, pp 340–344.

[3] Berk, K.L.; Blum, S.M.; Funk, V.L.; Sun, Y.; Yang, I.-Y.; Gostomski, M.V.; Roth, P.A.; Liem, A.T.; Emanuel, P.A.; Hogan, M.E.; Miklos, A.E.; Lux, M.W. Rapid Visual Authentication Based on DNA Strand Displacement. *ACS Appl. Mater. Interfaces.* **2021**, *13* (16), pp 19476–19486.

This page left intentionally blank

# Reactive molecular dynamics simulations of sarin and diisopropyl fluorophosphate on Zirconium metal-organic frameworks

Matthew A. Browe[a]*, Adam R. Hinkle[a,b], Ivan O. Iordanov[a], Adri van Duin[c],
[a]U.S. Army Combat Capabilities Development Command Chemical Biological Center, Research & Operations Directorate, 8198 Blackhawk Rd, Aberdeen Proving Ground, MD 21010
[b]DCS Corporation, 4696 Millennium Dr., Suite 450, Belcamp, MD 21017
[c]Pennsylvania State University, 201 Old Main, University Park, PA 16802

## ABSTRACT

Force fields describe the interactions between atoms in molecular simulation. In a reactive force field, chemical bonds can be created or dissociated based on the local environment, allowing different reactions to occur in the simulation. Initially developed for hydrocarbons, the ReaxFF reactive force field method has been expanded for use on a wide range of materials, from metals to ceramics to ionic materials consisting of elements spanning the periodic table. This project is focused on ReaxFF force field development for zirconium-based metal-organic framework/sarin interactions for predicting chemical reaction events in these systems.

**Keywords:** molecular dynamics, metal-organic frameworks, molecular simulation, chemical reaction, ReaxFF

## 1. INTRODUCTION

Metal-organic frameworks (MOFs) are a class of materials that has shown promising capabilities for a wide range of chemical threat decontamination applications.[1] Zirconium-based MOFs are of high interest due to their wide stability under a range of environmental and synthetic conditions.[2] Ability to predict reactivity of guest molecules with MOFs through the use of chemically-reactive molecular dynamics simulation is a growing field due to advances in computational tools for crafting suitable force fields describing their interatomic interactions and for simulating these interactions. Force fields predicting chemical reactions are specific to certain atom types and bond types; currently, no chemically reactive force field exists describing the P–F bond, a key bond in decontamination reaction mechanisms of nerve agents such as sarin (GB). This project focuses on developing a force field suitable for describing GB interaction with the zirconium-based MOF MOF-808 and a common simulant of GB, diisopropyl fluorophosphate (DFP).

## 2. METHODS

The ReaxFF force field development effort consisted of combining previously developed parameters with new parameters determined from density functional theory (DFT) calculations on the system of interest. First, the ReaxFF descriptions for Zr-based MOF materials[3] were merged with ReaxFF parameter sets for molecules containing hydrogen/carbon/phosphorus/oxygen[4] [H/C/P/O], carbon/nitrogen/hydrogen[5] [C/N/H], and carbon/sulfur/oxygen/hydrogen[6] [C/S/O/H] to enable simulations of GB interactions with zirconium-based MOFs functionalized with $–NH_2$ and $–SO_3H$ groups. Since no phosphorus–fluorine [P–F] ReaxFF parameters existed previously, the ReaxFF H/C/P/O description was extended with P–F parameters by training ReaxFF against DFT simulations describing P–F bond dissociation and associated valence and dihedral angles of GB/DFP.

For DFT calculations, the Amsterdam Modeling Suite AMS2022 software application from Software for Chemistry and Materials was used. Calculations used the PBE–D3 functional with the Triple Zeta basis set and frozen core electrons. Specifically, bond and angle scans were run for the following systems: $ZrF_4$, evaluating Zr–F bonds and F–Zr–F angles; $P(–F)(=O)(–OH)_2$, evaluating P–F bonds and O–P–F and O=P–F angles, and $P(–F)(=O)(–CH_3)(–O–CH_3)$, evaluating P–C bonds and O–P–C, O=P–C, and C–P–F angles. Starting structures for the zirconia cluster and associated GB bonding configurations in the reaction mechanism were taken from Troya.[7] Molecular dynamics simulations of the resulting force field were subsequently run using the Large-Scale

Atomic/Molecular Massively Parallel Simulator code.[8] For GB and DFP, a $C_{11}H_{14}O_{30}Zr_6$ zirconia cluster system with 20 GB/DFP molecules and 20 water molecules was used. Simulations were run for 250 ps at 800 K, 1000 K, and 1200 K.

## 3. RESULTS AND DISCUSSION

DFT simulations describing P–F bond dissociation and associated valence and dihedral angles are shown for $ZrF_4$ in Figure 1. Potential energies are computed for this system for a range of bond length and bond angle values around the equilibrium value (adjusted to a value of 0 kcal in all figures) by fixing these parameters at specified values, with the goal of the ReaxFF-force-field-calculated values to match the DFT calculations. There is good/very good agreement between DFT and ReaxFF for the F–Zr–F bond angle and for the Zr–F bond scan except at high compressions.

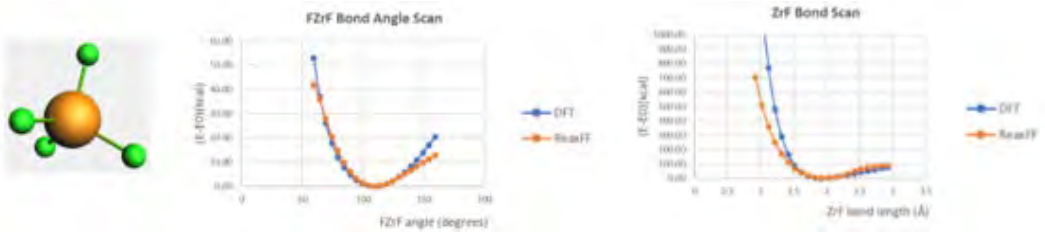


**Figure 1. ReaxFF vs DFT data in $ZrF_4$. Zr–F bond scan and F–Zr–F bond angle scan.**

Results for the $P(–F)(=O)(–OH)_2$ system are shown in Figure 2. There is generally good agreement between DFT and ReaxFF for the bond angle scans in $P(–F)(=O)(–OH)_2$. For the P–F bond scan, the agreement is very good around equilibrium; however, it deviates significantly during compression.

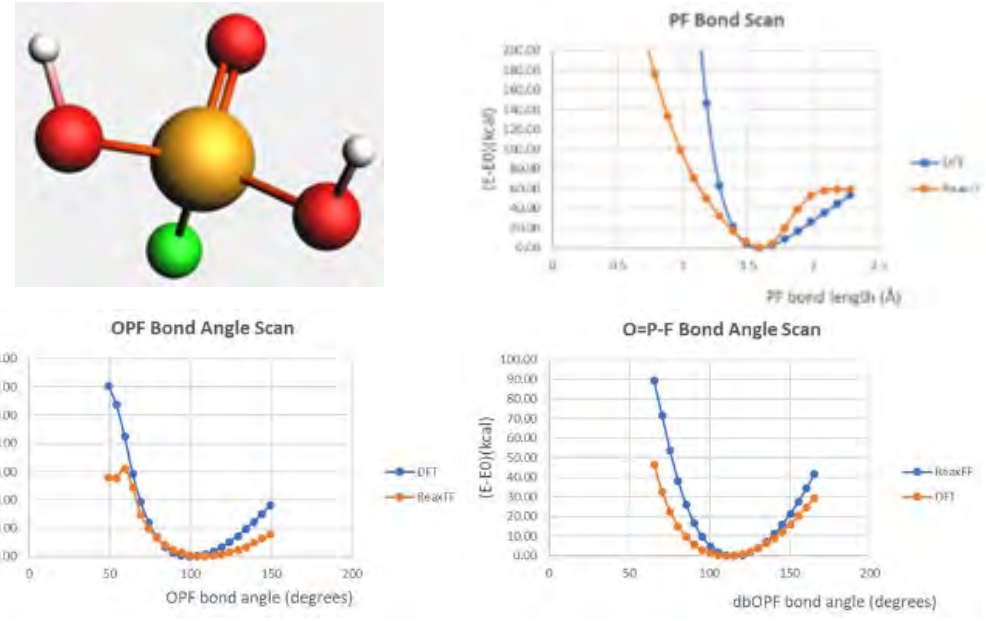


**Figure 2. ReaxFF vs DFT data in $P(–F)(=O)(–OH)_2$. P–F bond scan, O–P–F, and O=P–F bond angle scans.**

Results for the $P(–F)(=O)(–CH_3)(–O–CH_3)$ system are shown in Figure 3. There is good agreement between DFT and ReaxFF for the bond angle scans in $P(–F)(=O)(–CH_3)(–O–CH_3)$, while for the P–C bond scan, the agreement is very good around equilibrium and during bond expansion; however, it deviates significantly during compression.

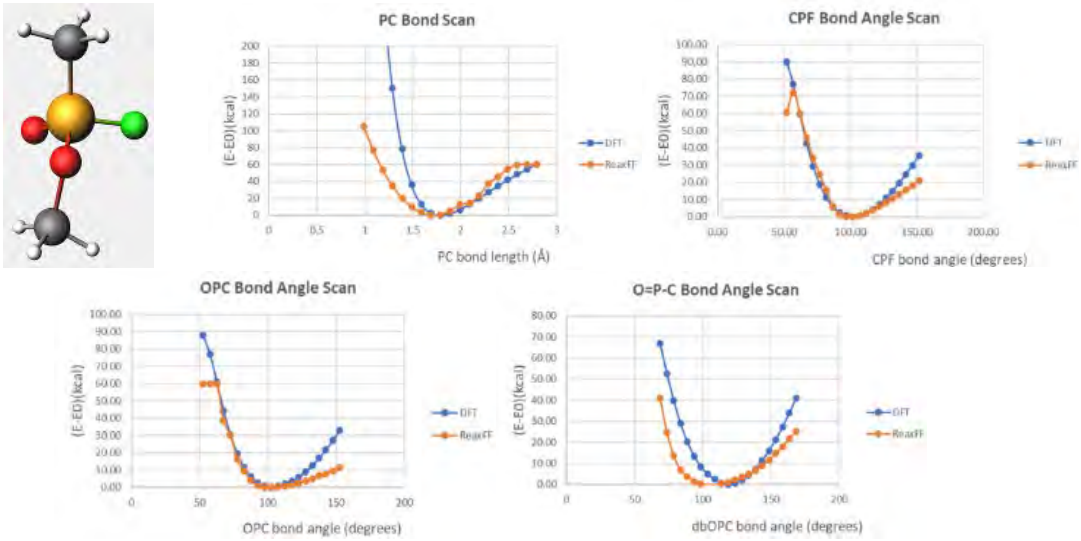


**Figure 3. ReaxFF vs DFT data in P(–F)(=O)(–$CH_3$)(–O–$CH_3$): P–C bond scan and O–P–C, O=P–C, and C–P–F angles.**

As a next step, the GB-zirconia reaction mechanism intermediate and final structures from Troya[7] were used for further force field training. The objective was to match the computed energy at every step of the reaction mechanism of GB and water with zirconia, scaling the starting configuration (all reactants in isolation) to an energy of 0 kcal. There is very good agreement between ReaxFF and DFT for the reaction energies and transition states (Figures 4, 6, 9 and S6 of Troya (Figure 4–7)).

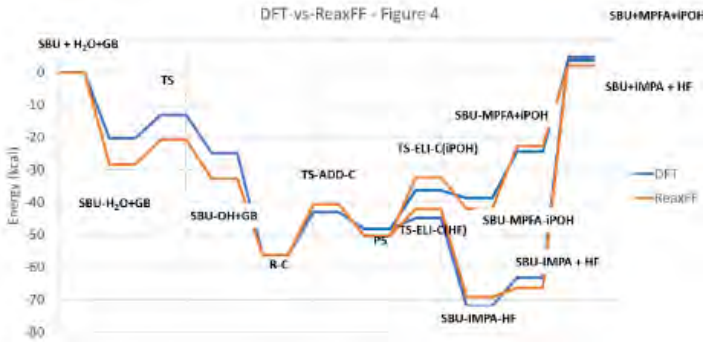


**Figure 4. DFT vs ReaxFF for the energies and transition state energies as previously reported.[7]**

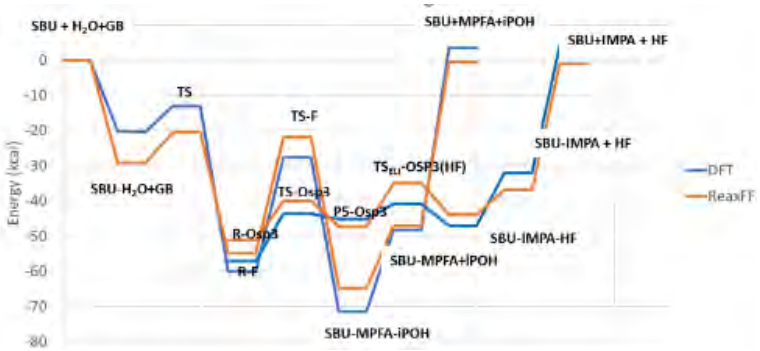


**Figure 5. DFT vs ReaxFF for the energies and transition state energies as previously reported.[7]**


**Figure 6. DFT vs ReaxFF for the energies and transition state energies shown in Figure S6 in the supplemental information from Troya.[7]**

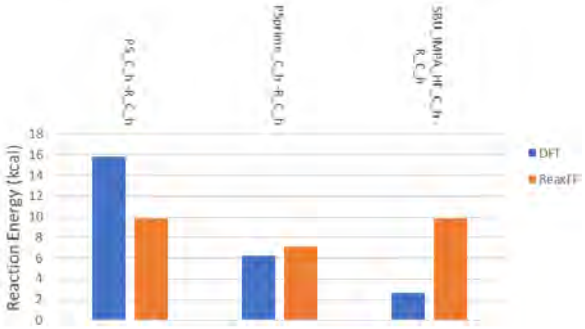


**Figure 7. DFT vs ReaxFF for the energies shown in Figure 9 from Troya.[7]**

During initial molecular dynamics simulations, unexpected reactions were observed, and so further DFT data for those reactions was used for additional force field training (Figure 8). After retraining, good agreement was obtained between ReaxFF and DFT for all these reactions, while the force field quality for Figures 1–7 was retained.

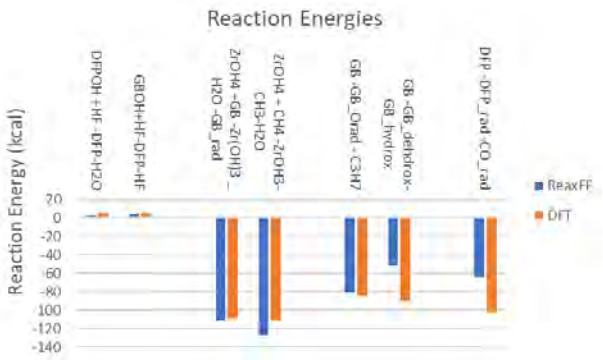


**Figure 8. Supplemental reactions for the final force field training.**

Molecular dynamics simulations were then performed using the force field developed. Three systems were evaluated. The first system involved separate test simulations of DFP/water and GB/water, with DFP/water run at 800 K and GB/water run at 1000 K. Both DFP and Sarin seemed stable in water at those temperature during the 25 ps of the simulation. At higher temperatures, DFP and Sarin became unstable. The second system involved simulations of the zirconia/water system with either DFP or GB, again with the DFP system at 800 K and the GB system at 1000 K. For GB at 1000 K no reaction was observed. The Sarin molecule does not attach to the SBU within the 25 ps timescale of the simulation. The SBU/water system with DFP at 800 K showed a significant number of H–bonding, leading unexpectedly to H–F cluster formation (Figure 9) which was not observed with GB.

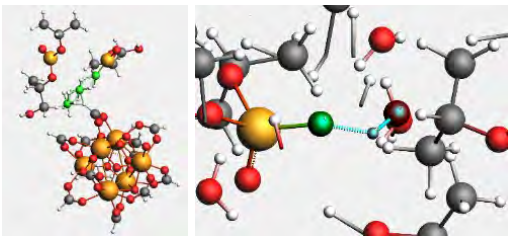

**Figure 9. Zirconia and DFP: (left) final results at the end of the simulation, and (right) interactions between DFP and water.**

A third system consisting of simulation of the zirconia/GB and zirconia/DFP complexes was run to learn more about the dissociation of F on the zirconia unit. Five of these complexes were placed in a box and simulations were run at 750 K for 250 ps. The zirconia/GB complex can dissociate, and the zirconia gets fluorinated (Figure 10 right), or HF formation can occur (Figure 10 left).

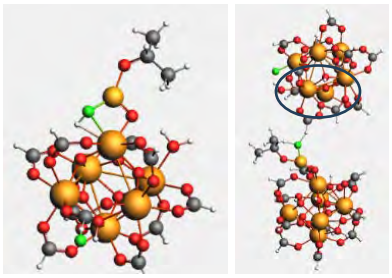

**Figure 10. Dissociation on the zirconia/GB complex: (left) HF formation and (right) F dissociation.**

The mechanism for HF formation or direct dissociation of F from GB on zirconia (Figures 11 and 12). In Figure 11, F attracts a H atom from an O atom on the zirconia structure, forming HF, and then F attaches further to the zirconia unit through a Zr atom. Figure 12 shows F dissociation from GB, with F binding to the Zr atom. Hydrogen bonds seem to hold the F atom in the right position for it to attach to the zirconia structure.

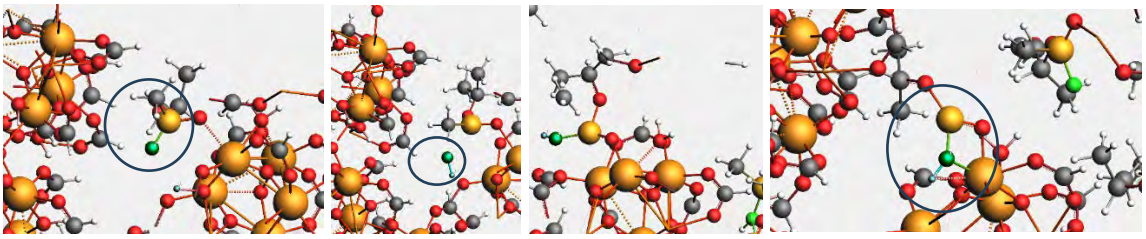

**Figure 11. Mechanism for HF formation from GB on zirconia.**

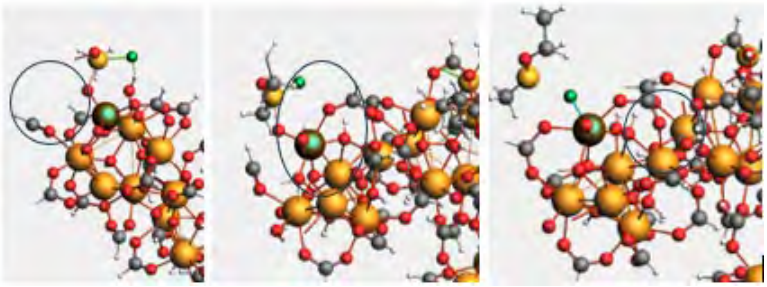

**Figure 12. F dissociation from GB to zirconia.**

A simulation of 5 molecules of the DFP-zirconia complex was then run at 750 K for 250 ps. In this case no F dissociation was observed on zirconia; however, H–F formation was observed (Figure 13). Again, some unusual $HF_2$ formation occurred when DFP was used.

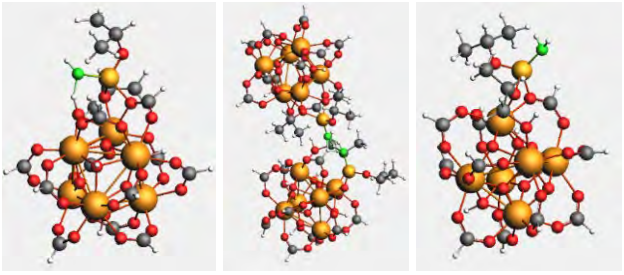

**Figure 13. HF formation and H bond interactions within the zirconia-DFP complex.**

Simulations were then run with GB on a 2x2x2 system of zirconium-based MOF-808 with node sites not bonded to linker molecules being terminated with hydroxyl groups (Figure 14). In the system, 25 molecules of GB were added. GB did not attach to MOF when the simulation was run at 800 K or 1000 K for 250 ps. At 1200 K, GB started to dissociate.

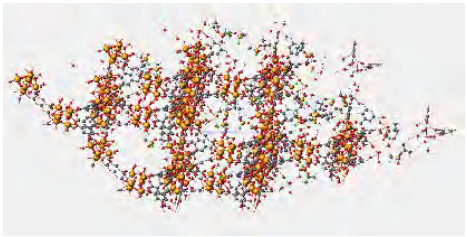

**Figure 14. Expanded MOF unit with 25 GB molecules.**

Similarly, 28 molecules of DFP were added to the MOF-808 structure with hydroxyl groups on the node sites not bonded with linker molecules. At the end of the simulation, 8 molecules of DFP attached to the MOF unit via H–bonds as shown below (Figure 15 left). Some unexpected fluorine clustering can be observed in this case as well (Figure 15 right, green circle).

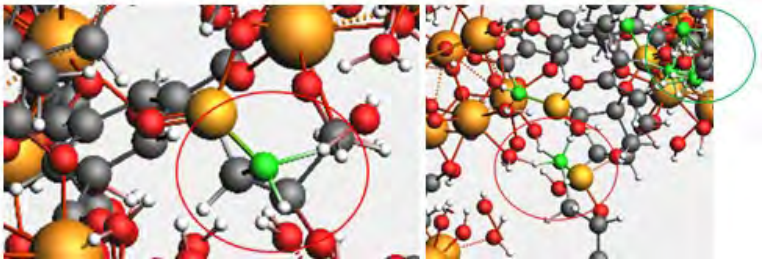

**Figure 15. DFP attached to MOF-808 via H–bonds.**

The hydrogen bonds are formed preferentially with the H atoms present on the water molecule attached to the MOF unit. The MOF unit cannot be fully shown since the molecule attachment crosses periodic boundaries (Figure 16). Overall, the number of DFP molecules in the gas phase was depleted during the simulation (Figure 17).

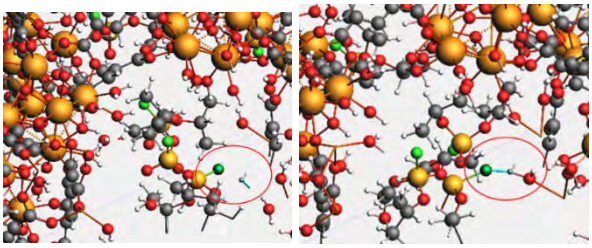

**Figure 16. Mechanism for DFP attachment to MOF-808 unit via H bonds.**

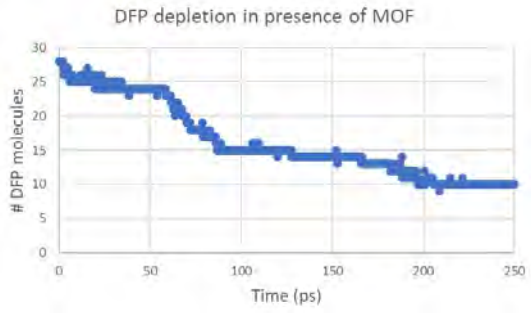


**Figure 17. Plot of unbonded DFP molecules versus simulation time during exposure to MOF-808.**

## 4. CONCLUSIONS

A ReaxFF force field was trained using DFT calculations from Troya on the GB decomposition mechanism on zirconia, and additional DFT calculations performed at RxFF Consulting. ReaxFF simulations of GB decomposition on zirconia show very good agreement with DFT calculations. Molecular dynamics simulations show HF formation and F dissociation for Sarin and HF formation for DFP. Sarin and DFP seem to behave very differently, with DFP being more reactive and unstable. The formation of fluorine clusters and $H_2F$ formation in presence of DFP is questionable and should be further validated with additional DFT calculations.

## ACKNOWLEDGMENTS

Funding for this Seedling project was made available through the Department of Defense Funding Laboratory Enhancements Across (X) Four Categories (FLEX 4) in accordance with the Army, Navy, and Air Force efforts funded under the authority in 10 U.S.C. § 4123.

## REFERENCES

[1] Bobbitt, N.S.; Mendonca, M.L.; Howarth, A.J.; Islamoglu, T.; Hupp, J.T.; Farha, O.K.; Snurr, R.Q. Metal-Ooganic frameworks for the removal of toxic industrial chemicals and chemical warfare agents. *Chem. Soc. Rev.* **2017**, *46* (11), pp 3357–3385.

[2] Kandiah, M.; Nilsen, M.H.; Usseglio, S.; Jakobsen, S.; Olsbye, U.; Tilset, M.; Larabi, C.; Quadrelli, E.A.; Bonino, F.; Lillerud, K.P. Synthesis and Stability of Tagged UiO-66 Zr-MOFs. *Chem. Mater.* **2010**, *22* (24), pp 6632–6640.

[3] Dwivedi, S.; Kowalik, M.; Rosenbach, N.; Shin, Y.K.; Chaffee, A.L.; Mauro, J.C.; van Duin, A.C.T. Molecular insights to the thermal decomposition of a Zr-Metal Organic Framework, MIL-140c. *J. Phys. Chem. Lett.* **2021**, *12* (1), pp 177–184.

[4] Quenneville, J.; Taylor, R.S.; van Duin, A.C.T. Reactive Molecular Dynamics Studies of DMMP Adsorption and Reactivity on Amorphous Silica Surfaces. *J. Phys. Chem. C.* **2010**, *114* (44), pp 18894–18902.

[5] Yang, Y.; Shin, Y.K.; Li, S.; Bennett, T.D.; van Duin, A.C.T.; Mauro, J.C. Enabling high-throughput computational design of ZIFs using ReaxFF. *J. Phys. Chem. B.* **2018**, *122* (41), pp 9616–9624.

[6] Shin, Y.K.; Kwak, H.; Vasenkov, A.; Sengupta, D.; van Duin, A.C.T. Development of a ReaxFF Reactive Force Field for Fe/Cr/O/S and Application to Oxidation of Butane over a Pyrite-covered $Cr_2O_3$ Catalyst. *ACS Catal.* **2015**, *5* (12), pp 7226–7236.

[7] Troya, D. Reaction Mechanism of Nerve-Agent Decomposition with Zr-Based Metal Organic Frameworks. *J. Phys. Chem. C.* **2016**, *120* (51), pp 29312–29323.

[8] Thompson, A.P.; Aktulga, H.M.; Berger, R.; Bolintineanu, D.S.; Brown, W.M.; Crozier, P.S.; Veld, P.J.I.; Kohlmeyer, A.; Moore, S.G.; Nguyen, T.D.; Shan, R.; Stevens, M.J.; Tranchida, J.; Trott, C.; Plimpton, S.J. LAMMPS-a flexible simulation tool for particle-based materials modeling at the atomic, meso, and continuum scales. *Comput. Phys. Commun.* **2022**, *271*, p 108171.

This page left intentionally blank

# MXene-enabled bacterial DNA extraction for PCR analysis

Stephanie D. Cole[a]*, Grace E. Rawlett[b], Shaun M. Debow[a]
[a]U.S. Army, Combat Capabilities Development Command Chemical Biological Center, Research & Operations Directorate, 8198 Blackhawk Rd, Aberdeen Proving Ground, MD 21010
[b]Oak Ridge Institute for Science and Education, 1299 Bethel Valley Rd, Oak Ridge, TN 37830

## ABSTRACT

Biological detection assays rely on an initial cell lysis and DNA extraction procedure to free genetic material for analysis and identification. Current extraction methods are difficult to deploy in the field due to their requirement for powered laboratory equipment, multiple steps, or disruptive detergents that interfere with downstream detection assays. Recently, reports on the antibacterial properties of two-dimensional nanomaterials have suggested MXenes disrupt the membranes of both Gram-positive and Gram-negative bacteria, and release DNA into solution. This can be achieved with a simple incubation of the bacterial culture with MXenes without the need for specialized, powered equipment. However, using MXenes to extract DNA for detection assays has not yet been reported in the scientific literature. In this project, we investigated if MXenes can be used to extract genetic material from bacterial cells for downstream analysis by PCR. Despite detection of free DNA from bacteria lysed by MXenes, qPCR reactions were unsuccessful compared to control assays. Further optimization may mitigate inhibitory effects of MXenes and advance them as candidates for genomic extraction in biodetection assays.

**Keywords:** MXene, biodetection, genomic extraction, lysis

## 1. INTRODUCTION

Biological detection assays require DNA to be released from cells for extraction and analysis. Releasing genetic material from cells typically requires cellular membranes to completely rupture or undergo physical lysis, thus releasing their DNA-containing cytoplasm. Many existing methods are not well-suited for field use and require powered laboratory equipment, caustic reagents, and/or special handling procedures. In this work, we investigated a novel approach to release genetic material from bacterial cells through physical lysis enabled by a two-dimensional (2D) material, MXene. MXenes are a family of very thin, layered two-dimensional carbides, carbonitrides and nitrides formed from early transition metals that are very conductive and have rich surface terminations.[1,2] The unique properties inherent to MXenes have enabled diverse applications, such as super capacitors,[3] water filtration,[4] photocatalysts,[5] electrocatalysts,[6] composites for lithium batteries,[7] light-emitting diodes,[8] viral decontamination,[9] and antibacterial agents.[10,11] Previous reports have demonstrated that $Ti_3C_2T_x$ MXene is a potent antimicrobial material[12] that disrupts bacterial cell membranes and walls of both Gram positive and Gram-negative species, and thus releases the cytosolic contents of the cell, including genomic DNA.[13] The size of the MXene nanosheet is critical for this process and requires sub-micron sized particles to produce this antimicrobial effect.[13,14]

## 2. MATERIALS AND METHODS

### 2.1 $Ti_3C_2T_x$ MXene preparation

MXenes are formed by etching a sacrificial layer from a layered MAX phase material, where M represents an early transition metal; A is a sacrificial layer (such as Al, Si); and X is C, N, or CN. Upon etching away the sacrificial layer from the MAX phase, an accordion-like, multi-layer structure remains having a composition of $M_{n+1}X_nT_x$, where T is a variable surface termination (such as F, Cl, O, OH) and $n$ = 1, 2, or 3.[15] The resulting accordion-like phase is further delaminated to yield single to few-layer sheets with thickness of several nanometers, and lateral dimensions from sub-100 nanometers to several microns. In this study, $Ti_3C_2T_x$ MXene was etched from a $Ti_3AlC_2$ MAX phase utilizing the HF-HCl/LiCl procedure as previously described.[16] Briefly, 1 g of 500 mesh $Ti_3AlC_2$ MAX phase was pre-etched with HCl, then etched with a combination of HCl and HF, washed with deionized (DI) water through serial

centrifugation steps until a near-neutral pH was obtained, LiCl intercalation was utilized to aid with delamination, followed by washing with DI water and serial centrifugation. All reaction steps and delamination were performed under a continuous Argon purge.

MXene was delaminated via sonication using several strategies. Initially, a 5 mL solution of 1 mg/mL MXene was sonicated on ice using a QSonica q125 sonicator for three seconds on and one second off at 60 % amplitude for 30 minutes. This sample was centrifuged at 1,900 x g for one hour and the supernatant was used in subsequent cell viability assays. Later efforts at delamination exposed ~0.5 mL of 3 mg/mL MXene to eight hours of sonication in either a Cole-Parmer Ultrasonic Cleaner or a Branson 5510 Ultrasonic Cleaner without subsequent centrifugation.

### 2.2 Cell viability assays

Single colony isolates of *Escherichia coli* 1946 were used to inoculate approximately 7 mL of nutrient broth, which was incubated overnight at 37 °C with shaking at 250 rpm. The next morning, 2 mL of the overnight culture was added to 100 mL of nutrient broth in a 500 mL baffled flask and grown as before until the culture reached exponential phase, (an optical density at 600 nm (OD600) of approximately 0.1–0.7). The bacterial culture was pelleted via centrifugation at 6,000 x g for 5 minutes. To remove residual culture medium, the pellet was resuspended in 1X phosphate buffered saline (PBS) (Invitrogen AM9624) and pelleted again as described for a total of three washes with PBS. After the final wash, the bacterial pellet was resuspended in sterile water in an equivalent volume to the starting culture volume.

The cell culture was exposed to MXene by adding 20 µL of MXene to 180 µL of the culture in a 1.5 mL Eppendorf tube. The tubes were capped, wrapped in foil to avoid light exposure, and placed in a 250 rpm shaking incubator at 37 °C for four hours.

Viability of the MXene-exposed bacterial cells was measured by both colony counting and by monitoring OD600 over time. Colony counting was conducted by diluting the MXene-bacteria mixture in nutrient broth and then plating 50 µL onto nutrient broth agar plates in triplicate. The plates were incubated overnight at 37 °C, the resulting colonies were counted the following morning and then converted to colony forming units per milliliter (CFU/mL). Optical density was monitored by combining 20 µL of the MXene-bacteria mixture with 180 µL of nutrient broth per well in a sterile, clear 96-well microplate and OD600 was read by a BioTek Synergy H1 Microplate Reader every five minutes for sixteen hours while shaking at 37 °C.

### 2.3 qPCR

The *E. coli* 23S rRNA gene was quantified via qPCR using a QuantStudio Real-Time PCR System and previously published primers.[17] Briefly, 20 µL reactions containing Fast SYBR Green Master Mix, 1 µM of each primer, and 6 µL of sample containing either reference genetic material or experimentally extracted *E. coli* genomic DNA in the presence and absence of MXenes were amplified using the following cycling conditions: 10 minutes at 95 °C, 40 cycles of 3 seconds at 95 °C and 20 seconds at 60 °C. Serial dilutions of reference *E. coli* genomic DNA were included on each plate to generate a standard curve for quantitation, along with a no template control. Experimental samples were derived from *E. coli* cells exposed to MXenes as described in Section 2.2. The samples were centrifuged at 6,000 x g for 5 min to remove live cells. The resulting supernatant was analyzed by qPCR.

### 2.4 Gram staining and microscopy

*E. coli* cells with and without MXene exposure were prepared as described in Section 2.1. Following MXene exposure, the cells were fixed to a slide and Gram stained using Sigma-Aldrich Gram Stain Kit and following the manufacturer's protocol. Slides were imaged using a Keyence VHX-7000N light microscope equipped with variable magnification lenses from 20–2000 X.

## 3. RESULTS

### 3.1 Impact of MXenes on cell viability

Previous reports have demonstrated MXenes are cytotoxic to *E. coli* cells,[12] and we sought to recapitulate the published data using both colony counting and monitoring the culture's optical density as metrics for cell viability post-MXene exposure. This proved to be more challenging than anticipated. Multiple approaches were attempted to induce cell death via MXenes, including two distinct MXene preparations, different delamination procedures, heating or vortexing

cells in the presence of MXenes, and altered bacterial washing procedures before MXene exposure, none of which had any impact on cell viability (data not shown). Finally, cell viability was reduced using MXene that had been delaminated via sonication in a Branson 5510 Ultrasonic Cleaner for eight hours (Figure 1). Based on visual observation, we believe that this approach produced smaller MXene particles compared to previous delamination methods that we attempted, thus producing the desired effect of reduced cell viability.

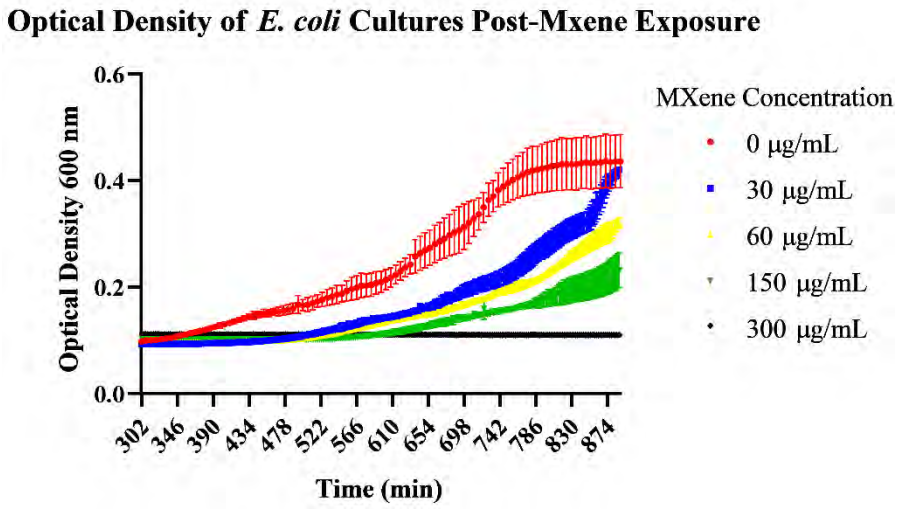


**Figure 1. Optical density over time of liquid *E. coli* cultures after exposure to various concentrations of MXenes. Cultures exposed to higher concentrations of MXenes were slower to recover, and no recovery was observed in the sample exposed to the highest concentration of MXene (*n=3*).**

Colony counting also revealed a significant decrease in *E. coli* cell viability after MXene exposure. With no MXene present we observed 4.19E6 +/- 0.53 CFU/mL, while exposure to 300 µg/mL MXene reduced the number of colonies to 3.05E4 +/- 0.73 CFU/mL.

### 3.2 Detection and quantification of genomic DNA by qPCR

To determine whether genomic DNA released from MXene-exposed *E. coli* cells could be measured in a biodetection assay, we used qPCR to detect the genomic 23S gene from MXene-exposed *E. coli* (Table 1). Supernatants derived from the cell cultures were used so that remaining live cells were removed from the samples. Several dilutions of the samples were used in the qPCR assays.

**Table 1. qPCR analysis of MXene-lysed *E. coli* cells, reported in genomic equivalents (GE). Reported values are corrected for dilution; error is standard error. *N/A: No amplification was detected in the sample.**

| | **Undiluted** | | **Diluted 10X** | | **Diluted 100X** | | **Diluted 1000X** | |
|---|---|---|---|---|---|---|---|---|
| **[MXene]** | Mean GE | Error | Mean GE | Error | Mean GE | Error | Mean GE | Error |
| **0 µg/mL** | 11,438.07 | 338.07 | 14,206.42 | 710.82 | 12,346.8 | 1,104.8 | 12,828 | 1,441 |
| **30 µg/mL** | 4,267.61 | 1,163.38 | 4,508.13 | 250.96 | 3,021.5 | 424.4 | 2,531 | 594 |
| **60 µg/mL** | 1,066.10 | 183.78 | 1,525.77 | 122.02 | 1,372.0 | 237.9 | 1,602 | 418 |
| **150 µg/mL** | 175.74 | 47.83 | 4,419.04 | 1,529.55 | 2,592.8 | 540.6 | 2155 | 989 |
| **300 µg/mL** | *N/A | *N/A | 3,409.51 | 528.09 | 2,313.6 | 333.9 | 1,845 | 409 |

Despite of the higher amount of genomic material present in the solution as a result of greater cell lysis, lower GE values were observed in samples exposed to greater amounts of MXene. One possible explanation for these results is MXenes partially inhibit qPCR reactions, as PCR inhibition is a common phenomenon with various sample matrices.[18] To determine if MXenes inhibit the qPCR reaction, we repeated the qPCR analysis using reference genomic *E. coli* DNA at known quantities in the presence of different MXene concentrations. We observed that cycle threshold (Ct) values increased with higher MXene concentrations, indicating that the MXenes do inhibit the qPCR reaction (Table 2).

**Table 2. qPCR analysis of reference *E. coli* genomic material in the presence of MXene. Error is standard error. *N/A: No amplification was detected in the sample.**

| | No MXene (Ct) | | 300 µg/mL MXene (Ct) | | 30 µg/mL MXene (Ct) | | 3 µg/mL MXene (Ct) | |
|---|---|---|---|---|---|---|---|---|
| **GE** | Mean | Error | Mean | Error | Mean | Error | Mean | Error |
| **6.00E6** | 8.408 | 0.028 | N/A* | N/A* | 14.129 | 0.906 | 8.584 | 0.040 |
| **6.00E5** | 11.593 | 0.029 | N/A* | N/A* | 15.423 | 0.498 | 11.684 | 0.026 |
| **6.00E4** | 15.023 | 0.004 | N/A* | N/A* | 18.718 | 0.309 | 15.169 | 0.115 |
| **6.00E3** | 19.292 | 0.032 | N/A* | N/A* | 23.332 | 1.509 | 19.277 | 0.029 |
| **6.00E2** | 22.892 | 0.023 | N/A* | N/A* | 27.041 | 0.438 | 22.939 | 0.013 |
| **6.00E1** | 24.802 | 0.018 | N/A* | N/A* | 27.270 | 0.328 | 28.188 | 5.865 |
| **6.00E0** | 29.459 | 0.138 | N/A* | N/A* | 32.643 | 0.735 | 29.402 | 0.547 |

### 3.3 Microscopy of MXene-exposed bacterial cell

*E. coli* cells in the presence and absence of 100 µg/mL MXene were Gram stained and imaged via light microscopy (Figure 2). While we did not observe any morphological changes to the cells to suggest membrane rupture or death, the bacterial cells associated more with the MXene than with other bacterial cells when MXene was present in the solution. This is an indication that, with further optimization, MXenes can be used for cell lysis applications.

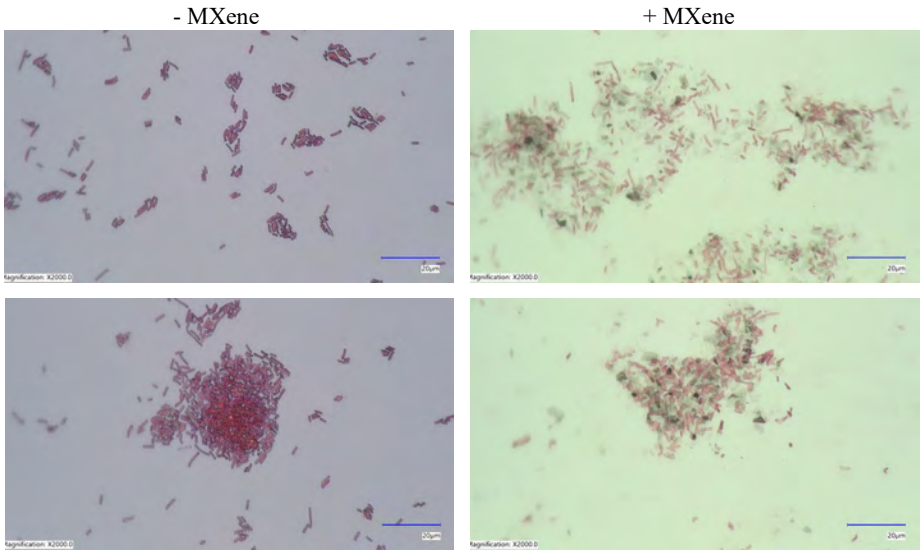


**Figure 2. Light microscopy images of *E. coli* cells in the presence and absence of 100 µg/mL MXene. Scale bar is 20 µm.**

## 4. CONCLUSIONS

After several delamination strategies were attempted, we were able to recapitulate published reports demonstrating that MXenes associate with *E. coli* cells and induce lysis. We hypothesize that delamination of the MXenes to smaller particle sizes lead to increased cell lysis. In addition, although we were able to successfully detect *E. coli* gDNA via qPCR, we found that MXenes significantly inhibit the reaction and thus reduce sensitivity. We believe this effect could be mitigated by removing MXene from the solution after lysis via filtration or by immobilizing the MXene on a surface during cell lysis and then washing the genomic DNA from the surface. Future work will aim to address these factors to better enable the use of MXene as an extraction tool for biodetection assays.

## ACKNOWLEDGMENTS

Funding for this Seedling project was made available through the Department of Defense Funding Laboratory Enhancements Across (X) Four Categories (FLEX 4) in accordance with the Army, Navy, and Air Force efforts funded

under the authority in 10 U.S.C. § 4123. The authors extend their sincere gratitude to the Senior Research Scientists, internal and external senior scientists, and professionals who invested their time to evaluate the initial proposal.

## REFERENCES

[1] Naguib, M.; Mashtalir, O.; Carle, J.; Presser, V.; Lu, J.; Hultman, L.; Gogotsi, Y.; Barsoum, M.W. Two-Dimensional Transition Metal Carbides. *ACS Nano*. **2012**, *6* (2), pp 1322–1331.

[2] Naguib, M; Kurtoglu, M.; Presser, V.; Lu, J.; Niu, J.; Heon, M.; Hultman, L.; Gogotsi, Y.; Barsoum, M.W. Two-Dimensional Nanocrystals Produced by Exfoliation of $Ti_3AlC_2$. *Adv. Mater.* **2011**, *23* (37), pp 4248–4253.

[3] Liang, C.M.; Meng, Y.; Zhang, Y.; Zhang, H.; Wang, W.; Lu, M.; Wang, G. Insights into the impact of interlayer spacing on MXene-based electrodes for supercapacitors: A review. *J. Energy Storage*. **2023**, *65*, p 107341.

[4] Lim, G.P.; Soon, C.F.; Al-Gheethi, A.A.; Morsin, M.; Tee, K.S. Recent progress and new perspective of MXene-based membranes for water purification: A review. *Ceram. Int.* **2022**, *48* (12), pp 16477–16491.

[5] Im, J.K.; Sohn, E.J.; Kim, S.; Jang, M.; Son, A.; Zoh, K.D.; Yoon, Y. Review of MXene-based nanocomposites for photocatalysis. *Chemosphere*. **2021**, *270*, p 129478.

[6] Heo, J.; Her, N.; Jang, M.; Park, C.M.; Son, A.; Han, J.; Yoon, Y. Photocatalytic and electrocatalytic reduction of $CO_2$ by MXene-based nanomaterials: A review. *Crit. Rev. Environ. Sci. Technol*. **2023**, *53* (9), pp 987–1008.

[7] Folorunso, O.; Kumar, N.; Hamam, Y.; Sadiku, R.; Ray, S.S. Recent progress on 2D metal carbide/nitride (MXene) nanocomposites for lithium-based batteries. *FlatChem*. **2021**, 29, p 100281.

[8] Ahn, S.; Han, T.H.Maleski, K.; Song, J.N.; Kim, Y.H.; Park, M.H.; Zhou, H.Y.; Yoo, S.; Gogotsi, Y.; Lee, T.W. A 2D Titanium Carbide MXene Flexible Electrode for High-Efficiency Light-Emitting Diodes. *Adv. Mater*. **2020**, *32* (23), p 2000919.

[9] Khatami, M.; Iravani, P.; Soufi, G.J.; Iravani, S. MXenes for antimicrobial and antiviral applications: recent advances. *Mater. Technol*. **2022**, *37* (11), pp 1890–1905.

[10] Abbasi, F.; Hajilary, N.; Rezakazemi, M. Antibacterial properties of MXene-based nanomaterials: A review. *Mater. Express.* **2022**, *12* (1), pp 34–48.

[11] Gogotsi, Y.; Anasori, B. The rise of MXenes. *ACS Nano.* **2019**, *13* (8), pp 8491–8494.

[12] Rasool, K.; Helal, M.; Ali, A.; Ren, C.E.; Gogotsi, Y.; Mahmoud, K.A. Antibacterial activity of $Ti_3C_2T_x$ MXene. *ACS Nano.* **2016**, *10* (3), pp 3674–3684.

[13] Shamsabadi, A.A.; Sharifian Gh., M.; Anasori, B.; Soroush, M. Antibacterial Mode-of-Action of Colloidal $Ti_3C_2T_x$ MXene Nanosheets. *ACS Sustainable Chem. Eng*. **2018**, *6* (12), pp 16586–16596.

[14] Pandey, R.P.; Rasheed, P.A.; Gomez, T.; Rasool, K.; Ponraj, J.; Prenger, K.; Naguib, M.; Mahmoud, K.A. Effect of Sheet Size and Atomic Structure on the Antibacterial Activity of Nb-Mxene Nanosheets. *ACS Appl. Nano Mater.* **2020**, *3* (11), pp 11372–11382.

[15] Naguib, M.; Mochalin, V.N.; Barsoum, M.W.; Gogotsi, Y. 25th Anniversary Article: MXenes: A New Family of Two-Dimensional Materials. *Adv. Mater.* **2014**, *26* (7), pp 992–1005.

[16] Thakur A.; Chandran B.S.N.; Davidson K.; Bedford A.; Fang H.; Im Y.; Kanduri V.; Wyatt B.C.; Nemani S.K.; Poliukhova V.; Kumar R.; Fakhraai Z.; Anasori B. Step-by-Step Guide for Synthesis and Selamination of $Ti_3C_2T_x$ MXene. *Small Methods.* **2023**, *7* (8), p 2300030.

[17] Ahmed, W.; Richardson, K.; Sidhu, J.P.S.; Toze, S. Escherichia coli and Enterococcus spp. in rainwater tank samples: comparison of culture-based methods and 23S rRNA gene quantitative PCR assays. *Environ. Sci. Technol.* **2012**, *46* (20), pp 11370–11376.

[18] Schrader, C.; Schielke, A.; Ellerbroek, L.; Johne, R. PCR inhibitors - occurrence, properties, and removal. *J. Appl. Microbiol.* **2012**, *113* (5), pp 1014–1026.

This page left intentionally blank

# MXene electrochemical detoxification of VX

Shaun Debow[a]*, Stephen P. Harvey[a], Michael J. Chesebrough[b], Vanessa L. Funk[a], Mallory Liebes[c], Zachary B.S. Zander[a], Yi Rao[c]
[a]U.S. Army, Combat Capabilities Development Command Chemical Biological Center, Research & Operations Directorate, 8198 Blackhawk Rd, Aberdeen Proving Ground, MD 21010
[b]Oak Ridge Institute for Science and Education, 1299 Bethel Valley Rd, Oak Ridge, TN 37830
[c]Department of Chemistry and Biochemistry, Utah State University, 300 Old Main Hill, Logan, Utah 84322

## ABSTRACT

Electrochemical processes are used to treat recalcitrant chemicals present in waste streams, including landfill leachate, pharmaceutical byproducts, industrial chemical and textile dying processes. Some electrochemical treatment processes proceed by applying an electrical current to an electrocatalyst in the presence of a recalcitrant chemical, thus directly reacting with the chemical or creating reactive species to further react with the chemical. VX nerve agent is one such recalcitrant chemical which has a long environmental fate and presents challenges with detoxification. In this study, we aimed to increase VX degradation kinetics and explore VX degradation by utilizing electro-Fenton reactions through in-situ hydrogen peroxide generation using an oxygen reduction reaction catalyst combined with an oxygen evolution reaction catalyst in a dual-electrode configuration. Both oxygen evolution reaction and oxygen reduction reaction catalysts were fabricated in-house and based on FeCo-MXene chemistry. We found VX nerve agent degradation kinetics were similar for both the dual electro-catalyst configuration, utilizing both an oxygen evolution reaction and oxygen reduction reaction catalyst configuration, when compared to a single oxygen evolution reaction catalyst for electro-chemical advanced oxidation reactions.

**Keywords:** MXene, VX, organophosphorus, nerve agent

## 1. INTRODUCTION

### 1.1 Background

Chemical agent detoxification for decontamination or destruction has traditionally relied upon the transportation, storage, and management of caustic solids and liquids.[1] These caustic materials create secondary chemical hazards for operators and the environment, which are beyond the primary hazards posed by the original chemical agent. Our goal is to develop a safer method for chemical agent detoxification that reduces secondary risks to both the operator and environment. In this study, we investigated FeCo-$Ti_3C_2$ MXene-based electrochemical catalysts for chemical agent detoxification that can improve availability of chemical agent detoxification anytime and anywhere detoxification is needed. We hypothesize reactive peroxide and hydroxyl radical species, electrochemically generated in situ through a combination of oxygen evolution reaction (OER) catalysis to produce oxygen in solution, then followed by a 2-electron process to reduce the as-generated oxygen through an oxygen reduction reaction (ORR) catalysis, will improve detoxification kinetics.

### 1.2 O-ethyl-S-[2-(diisopropylamino)ethyl]-methylphosphonothioate (VX) chemical agent

VX chemical agent is a persistent, low vapor-pressure organophosphorus molecule that interferes with the enzyme acetylcholinesterase, prevents hydrolysis of the neurotransmitter acetylcholine and results in its toxic accumulation at the neuron-muscle cell junction; cutaneous exposure to approximately 5 mg can be lethal. VX degradation typically follows several pathways. These pathways frequently include scission of the P–S bond and the P–O bond. When the latter occurs, it can result in a very toxic and stable byproduct, EA-2192, that retains nearly the same toxicity of the parent VX molecule and is difficult to degrade.[1,2] Identifying methods to safely detoxify VX while preventing formation of other toxic byproducts during chemical destruction is essential for detoxification.

### 1.3 $Ti_3C_2$ MXene-supported electrocatalyst

$Ti_3C_2$ MXene is a two-dimensional carbide wth rich polar surface terminations, such as F, Cl, O, and OH.[3-6] These polar surface terminations allow MXene to form stable colloidal suspensions in aqueous systems, and act as nucleation sites for organic ligands or grow inorganic guest particles.[7,8] Carbide layers along its basal plane promote high electroconductivity.[9] These unique properties enable $Ti_3C_2$ MXene to be an excellent electrochemical support for heterogeneous bi-metallic catalysts in OER and hydrogen evolution reactions (HER).[10,11] Reports suggest that MXene-supported electrocatalysts can generate hydrogen peroxide through ORR electrochemistry.[12] We fabricated MXene-based electrodes for OER and ORR electrochemistry to enable both in-situ oxygen generation and oxygen reduction to peroxide through a two-electron transfer process.[13,14] Our catalysts further promote improved reaction kinetics by utilizing iron and cobalt-based catalysts for Fenton and Fenton-like electrochemical reactions.[15-18]

## 2. MATERIALS AND METHODS

### 2.1 $Ti_3C_2T_x$ MXene preparation

MXenes are formed by etching a sacrificial layer from a layered MAX phase material, where M represents an early transition metal, A is a sacrificial layer (such as Al, Si), and X is C, N, or CN. Upon etching the sacrificial layer from the MAX phase, an accordion-like, multi-layer structure remains with a composition of $M_{n+1}X_nT_x$, where T is a variable surface termination (such as F, Cl, O, OH) and an n = 1, 2, or 3.[19] The resulting structure is further delaminated to yield single to few-layer sheets with thickness of several nanometers, and lateral dimensions from sub-100 nm to several microns. In this study, $Ti_3C_2T_x$ MXene was etched from a $Ti_3AlC_2$ MAX phase utilizing the HF-HCl/LiCl procedure previously reported.[20] Briefly, 1 g of 500 mesh $Ti_3AlC_2$ MAX phase was pre-etched with HCl, etched with a combination of HCl and HF, washed with deionized (DI) water through serial centrifugation steps until near-neutral pH was obtained, LiCl intercalation was utilized to aid with delamination, followed by DI washes water and serial centrifugation. All steps and delamination were performed under continuous Argon purge.

### 2.2 FeCo-MXene carbon paper electrodes

FeCo-MXene carbon-paper electrodes were fabricated for electrochemical reactions with VX. Two FeCo-based catalysts were produced, for OER or ORR. FeCo-MXene layered double hydroxides (LDH) catalysts are superior for OER compared to the platinum-group catalyst, $RuO_2$.[13,21] A metal-nitrogen-carbon (M-N-C) catalyst, having iron and cobalt as active metals, was selected as the ORR catalyst based upon high efficiencies of M-N-C-based catalysts.[14] Fabrication of the electrodes involved multi-step processes where FeCo-MXene inks were prepared, drop cast onto carbon paper affixed to copper conductive tape, and sealed with Parafilm. Catalyst inks maintained the FeCo-MXene catalyst as a suspension, while promoting quick solvent evaporation for electrode fabrication upon drop casting.

#### *2.2.1 Oxygen evolution reaction catalyst ink*

The FeCo-MXene OER catalyst was formed by nucleating and growing FeCo LDH on the surface of $Ti_3C_2$-MXene. Briefly, 0.125 g $CoCl_2{\cdot}6H_2O$, 0.047 g $FeCl_3{\cdot}6H_2O$, 1.72 g urea, 2.8 mL $H_2O$ (18.2 MΩ), and 2.8 mL anhydrous ethanol were combined and stirred for 60 minutes at room temperature. Separately, 10 mg MXene was sonicated in 4.5 mL dimethylformamide (DMF) for 90 minutes at room temperature. Once thoroughly mixed, the reagents and MXene substrate were combined, stirred for an additional 30 minutes, and then transferred to a 20 mL polytetrafluoroethylene autoclave vessel. The autoclave vessel was heated to 120 °C and held for 16 hours. Next, 6.0 mg FeCo-MXene LDH catalyst, 1160 µL ethanol (anhydrous), 800 µL DI $H_2O$ (18.2 MΩ), and 40 µL Nafion (5%) were combined to form the FeCo-MXene ink. Generation of the catalyst ink allows for maintaining a stable suspension of the FeCo-MXene catalyst, while promoting quick solvent evaporation for electrode fabrication.

#### *2.2.2 Oxygen reduction reaction catalyst ink*

The FeCo-MXene ORR catalyst was formed by sequentially adding 0.298 g 2-aminotherephathalic acid, 0.72 mL 2M NaOH, 0.324 g $FeCl_3{\cdot}6H_2O$ to 9 mL DMF solution at room temperature. Care was taken to ensure each component had dissolved, prior to adding each the next component. Separately, 10 mg MXene was sonicated in 4.0 mL DMF for 120 minutes at room temperature. Once mixed, the reagents and MXene substrate were combined, stirred for an additional 30 minutes, and transferred to a 20 mL polytetrafluoroethylene autoclave vessel. The autoclave vessel was heated to 100 °C for 18 hours. Next, the reaction product was washed with DMF two times, washed with DI water

three times, and ethanol once. Each wash cycle was accomplished by centrifugation at 4000 rpm for 5-minutes. The reaction product was dried in a vacuum oven for 60 minutes at 65 °C. After drying, the resulting powder calcined at 750 °C for 120 minutes under flowing nitrogen. The calcined product was washed in 1M HCl, followed by another ethanol wash. Each wash cycle was accomplished by centrifugation at 4000 rpm for 5-minues. The washed product was dried in a vacuum oven at 65 °C for 60 minutes. Next, 5.0 mg FeCo-MXene ORR catalyst, 1160 µL ethanol (anhydrous), 800 µL DI $H_2O$ (18.2 MΩ), and 40 µL Nafion (5%) were combined to form the FeCo-MXene ink. Finally, FeCo-MXene carbon-paper electrodes were fabricated by drop-casting 80 µL of the FeCo-MXene ink onto carbon paper fixed onto conductive copper tape. The carbon paper was allowed to air dry until no liquid was visible. The electrodes were transferred to a vacuum oven and held at 30 °C for 16 hours and reached a surface area of approximately 0.5 $cm^2$. Each electrode was fixed to folded copper-tape and the interface was sealed with Parafilm.

**Table 1. HPLC-MS Parameters.**

| **LC Parameters** |
|---|
| Mobile Phase A: 0.1% Formic Acid and 5 mM Ammonium Acetate in 95 % Deionized Water / 5% Isopropanol |
| Mobile Phase B: 0.1% Formic Acid and 5 mM Ammonium Acetate in 5 % Deionized Water / 95% Isopropanol |
| Gradient:<br>Time (min): %A %B<br>0.00 50.0 50.0<br>4.00 50.0 50.0 |
| Flow Rate: 0.2 mL/min |
| Analytical Column: Phenomenex Synergi Hydro-RP, 4 µm, 2 x 150 mm |
| Typical Column Pressure: 180 bar |
| Analytical Column Temperature: 40 ºC |
| Injection Volume: 10 µL |
| Autosampler Temperature: 5 ºC |
| Post-injection Needle Wash: 10 seconds of Mobile Phase B |
| **Mass Spectrometer Parameters** |
| Scan Type: Multiple Reaction Monitoring (MRM) |
| Polarity: Positive Mode |
| Curtain Gas: 30 |
| CAD Gas: Medium |
| Source Temperature: 300 ºC |
| GS1: 40 |
| GS2: 50 |
| Declustering Potential: 100 |
| Exit Potential: 10 |
| Collision Energy: 25 (for all analytes) |
| MRM for VX: 268.1 > 128.0<br>MRM for EA2192: 240.1 > 128.0<br>MRM for VX Sulfonic Acid: 210.1 > 126.2<br>MRM for EMPA: 125.1 > 97.1<br>MRM for VX-d5 Internal Standard: 273.1 > 128.0 |

### *2.2.3 Electrochemical reactions*

Electrochemical reactions were performed using Gamry electrochemical workstations, model 1010E, in a Gamry Dr. Bob's electrochemical cell fitted with a Saturated Calomel Electrode (SCE) as the reference electrode, a 5-mm diameter graphite rod as the counter electrode, and FeCo-MXene catalyst electrode as the working electrode. The OER method utilized one electrochemical workstation operating in chronoamperometry mode with an FeCo-MXene OER catalyst electrode held at a constant potential of +1.5V. The OER + ORR method utilized two electrochemical workstations that were connected and synchronized to simultaneously perform OER and ORR reactions with one working electrode per each workstation, one FeCo-MXene OER catalyst electrode and one FeCo-MXene ORR catalyst electrode, respectively. The synchronized workstations were operated in chronoamperometry mode, potentials were held at + 1.5V (OER) and -0.5 V (ORR). Chronoamperometry mode was selected due to limitations within the Gamry Framework Software, when operating in the bi-potentiostat mode. The reaction liquid phase was formed by diluting neat VX to a concentration of 3 mM in 25 mL of a 0.5 M potassium phosphate buffer at pH 8. The liquid phase was stirred inside the electrochemical cell using a stir plate. All electrodes were positioned approximately 2 cm apart to prevent physical contact while stirring. FeCo-MXene electrodes were positioned so only the FeCo-MXene catalyst and carbon paper support contacted the liquid phase with each FeCo-MXene catalyst surface facing the counter electrode, care was taken to prevent the copper-tape conductor from contacting the liquid phase.

### *2.2.4 Analysis*

VX was quantified using an Applied Biosystems 5500 QTrap Triple-Quadrupole Mass Spectrometer, equipped with a TurboV Ion Source. Sample introduction and chromatography were performed with an Agilent 1200 series high-performance liquid chromatography, including an Agilent Binary Pump, Degasser, Thermal Column Compartment (TCC), High Performance Automatic Liquid Sampler (ALS), and an ALS Thermostat. Sample effluent was directed from the LC directly to the TurboV ion source of the API5500 MS. Operation and analysis were performed with Applied Biosystems Analyst software package (v. 1.5.1.) (Table 1). Aliquots of the reaction were drawn from the reaction cell and diluted into anhydrous isopropyl alcohol (IPA). All analytes were transferred from the pipette tip by rinsing the pipette tip with the diluted IPA-analyte solution. Just prior to analysis, a second 100 x serial dilution was made in IPA to bring the VX concentration into the calibration range of the analysis platform.

## 3. RESULTS

Electrochemical reactions were performed according to the described methodology using OER and ORR FeCo-MXene catalysts. OER catalysts had a constant applied potential of +1.5 V, while the ORR catalyst had a constant applied potential of -0.5 V. An additional reaction, without applied potential, was acquired to determine the effect of non-electrochemical degradation. Each reaction lasted 90 minutes (Figure 1) but no difference was observed between methods (Figure 1). No toxic byproduct was detected by HPLC-MS for any of the experimental methods.

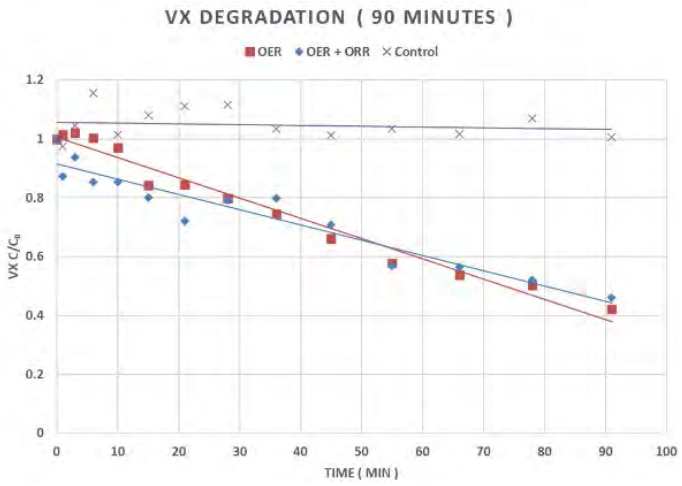


**Figure 1. VX Degradation by OER + ORR and OER electrochemical methods.**

## 4. CONCLUSION

VX chemical agent electrochemical detoxification by FeCo-MXene ORR and FeCo-MXene OER catalysts was demonstrated for both the OER + ORR and the OER electrochemical methods. Each method resulted in an approximate 60 % decrease in VX concentration at 90 minutes. Elucidating the similarities in reaction kinetics was beyond the scope of this project. We hypothesize that the peroxide generation rate by ORR at near-neutral pH was insufficient to substantially increase reaction kinetics through Fenton and Fenton-like reactions. A follow-on effort should aim to increase ORR catalyst efficiency and peroxide generation rates at near-neutral pH, then repeat the study to determine rate dependence based upon increased peroxide generation rates and hydroxyl radical formation.

## ACKNOWLEDGMENTS

Funding for this Seedling project was made available through the Department of Defense Funding Laboratory Enhancements Across (X) Four Categories (FLEX 4) in accordance with the Army, Navy, and Air Force efforts funded

under the authority in 10 U.S.C. § 4123. The authors wish to thank the Senior Research Scientists, internal and external senior scientists, and professionals who invested their time to evaluate the initial proposal.

## REFERENCES

[1] Yang, Y-C.; Szafraniec, L.L.; Beaudry, W.T.; Rohrbaugh, D.K. Oxidative detoxification of phosphonothiolates. *J. Am. Chem. Soc.* **1990**, *112* (18), pp 6621–6627.

[2] Smith, B.M. Catalytic methods for the destruction of chemical warfare agents under ambient conditions. *Chem. Soc. Rev.* **2008**, *37* (3), pp 470–478.

[3] Naguib, M.; Mashtalir, O.; Carle, J.; Presser, V.; Lu, J.; Hultman, L.; Gogotsi, Y.; Barsoum, M.W. Two-Dimensional Transition Metal Carbides. *ACS Nano*. **2012**, *6* (2), pp 1322–1331.

[4] Naguib, M.; Kurtoglu, M.; Presser, V.; Lu, J.; Niu, J.; Heon, M.; Hultman, L.; Gogotsi, Y.; Barsoum, M.W. Two-Dimensional Nanocrystals Produced by Exfoliation of $Ti_3AlC_2$. *Adv. Mater.* **2011**, *23* (37), pp 4248–4253.

[5] Gogotsi, Y.; Anasori, B. The rise of MXenes. *ACS Nano* **2019**, *13* (8), pp 8491–8494.

[6] Naguib, M.; Mochalin, V.N.; Barsoum, M.W.; Gogotsi, Y. 25th Anniversary Article: MXenes: A New Family of Two-Dimensional Materials. *Adv. Mater.* **2014**, *26* (7), pp 992–1005.

[7] Mahmud, S.T.; Hasan, M.M.; Bain, S.; Rahman, S.T.; Rhaman, M.; Hossain, M.M.; Ordu, M. Multilayer MXene Heterostructures and Nanohybrids for Multifunctional Applications: A Review. *ACS Mater. Lett.* **2022**, *4* (6), pp 1174–1206.

[8] Jung, S.; Zafar, U.; Achary, L.S.K.; Koo, C.M. Ligand chemistry for surface functionalization in MXenes: A review. *EcoMat.* **2023**, *5* (10), p e12395.

[9] Hu, T.; Hui, Z.; Wang, J.; Li, Z.; Hu, M.; Tan, J.; Hou, P.; Li, F.; Wang, X. Anisotropic electronic conduction in stacked two-dimensional titanium carbide. *Sci. Rep.* **2015**, *5*, p 16329.

[10] Zhang, T.; Debow, S.; Song, F.; Qian, Y.; Creasy, W.; DeLacy, B.; Rao, Y. Interface Catalysis of Nickel Molybdenum (NiMo) Alloys on Two-Dimensional (2D) MXene for Enhanced Hydrogen Electrochemistry. *J. Phys. Chem. Lett.* **2021**, *12* (46), pp 11361–11370.

[11] Song, F.; Debow, S.; Zhang, T.; Qian, Y.; Huang-Fu, Z.; Munns, K.; Schmidt, S.; Fisher, H.; Brown, J.; Su, Y.; Zander, Z.; DeLacy, B.; Mirotznik, M.; Opila, R.; Rao, Y. Interface Catalysts of $Ni_3Fe_1$ Layered Double Hydroxide and Titanium Carbide for High-Performance Water Oxidation in Alkaline and Natural Conditions. *J. Phys. Chem. Lett.* **2023**, *14* (24), pp 5692–5700.

[12] Peera, S.; Liu, C.; Sahu, A.; Selvaraj, M.; Rao, M.; Lee, T.; Koutavarapu, R.; Shim, J.; Singh, L.; Recent Advances on MXene-Based Electrocatalysts toward Oxygen Reduction Reaction: A Focused Review. *Adv. Mater. Interfaces.* **2021**, *8* (23), p 2100975.

[13] Hoo, C.; Wu, Y.; An, Y.; Cui, B.; Lin, J.; Li, X.; Wang, D.; Jiang, M.; Cheng, Z.; Hu, S. Interface-coupling of CoFe-LDH on MXene as high-performance oxygen evolution catalyst. *Mater. Today Energy*. **2019**, *12*, pp 453–462.

[14] Yoo, R.; Pranada, E.; Johnson, D.; Qiao, Z.; Djire, A. Review—The Oxygen Reduction Reaction on MXene-Based Catalysts: Progress and Prospects. *J. Electrochem. Soc.* **2022**, *169*, p 063513.

[15] Chen, N.; Zhao, Y.; Li, M.; Wang, X.; Peng, X.; Sun, H.; Zhang, L. $FeC_2O_4 \cdot 2H_2O$ enables sustainable conversion of hydrogen peroxide to hydroxyl radical for promoted mineralization and detoxification of sulfadimidine. *J. Haz. Mat.* **2022**, *436*, p 129049.

[16] Guo, Y.; Tang, C.; Cao, C.; Hu, X. N-doped carbon-based catalysts in situ generation hydrogen peroxide via 2-electron oxygen reduction for degradation of organic contaminants of heterogeneous electro-Fenton process: A mini review. *Surf. Interfaces.* **2023**, *38*, p 102879.

[17] Amor, C.; Marchao, L.; Lucas, M.; Peres, J. Application of Advanced Oxidation Processes for the Treatment of Recalcitrant Agro-Industrial Wastewater: A Review. *Water*. **2019**, *11* (2), p 205.

[18] Ahman, A.; Zarel, M.; Hassani, A.; Ebratkhahan, M.; Olad, A. Facile synthesis of iron(II) doped carbonaceous aerogel as a three-dimensional cathode and its excellent performance in electro-Fenton degradation of ceftazidime from water solution. *Sep. Purif. Rev.* **2021**, *278*, p 119559.

[19] Hope, M.; Forse, A.; Griffith, K.; Laukatskaya, M.; Ghidu, M.; Gogotsi, Y.; Grey, C. NMR reveals the surface functionalisation of $Ti_3C_2$ MXene. *Phys. Chem. Chem. Phys.* **2016**, *18*, p 5099.

[20] Thakur, A.; Chandran, B.S.N.; Davidson, K.; Bedford, A.; Fang, H.; Im, Y.; Kanduri, V.; Wyatt, B.C.; Nemani, S.K.; Poliukhova, V.; Kumar, R.; Fakhraai, Z.; Anasori, B. Step-by-step guide for synthesis and delamination of Ti3C2Tx MXene. *Small Methods.* **2023**, *7* (8), p 2300030.

[21] Tian, M.; Jiang, Y.; Tong, H.; Xu, Y.; Xia, L. MXene-Supported FeCo-LDHs as Highly Efficient Catalysts for Enhanced Electrocatalytic Oxygen Evolution Reaction. *ChemNanoMat*. **2020**, *6*, pp 154–159.

# Modeling the lymphatic vessel using microfluidic technology to study immune response *in vitro*

Priscilla Lee[a]*, Sarfaraz A. Ejazi[b], Ann Ramirez[b], Morgan Minyard[a], Katharina Maisel[b]
[a]U.S. Army Combat Capabilities Development Command Chemical Biological Center, Research & Operations Directorate, 8198 Blackhawk Rd, Aberdeen Proving Ground, MD 21010
[b]Fischell Department of Bioengineering, University of Maryland, 3102 A. James Clark Hall, College Park, MD 20742

## ABSTRACT

Immune response to chemical and biological toxins of interest is understudied due, in part, to the complexity of the immune system. A core physical component of the immune system, the lymphatic vessels, is of particular interest as its function is understudied *in vivo* and limited by external factors, such as lymphatic fluid flow, in current *in vitro* models. These vessels have a significant role in transporting key molecules, with potential to transport chemical and biological agents throughout the body. This study developed a microfluidic device for a lymphatic vessel using additive manufacturing techniques, including computer aided design and biomaterial manufacturing. To create the structure of a lymphatic vessel with human lymphatic endothelial cells, a collagen hydrogel was optimized under static and flow conditions. With the introduction of flow, the human lymphatic endothelial cells expressed more junction proteins and formed more physiologically relevant cell morphology within the vessel in the device. Rather than relying on a commercially available system, this work developed a platform for assessing lymphatic vessels under flow conditions. This model can be used in future toxicity studies, specifically looking at permeability of particles across lymphatic vessels.

**Keywords:** lymphatics, microfluidic device, *in vitro*, immunoengineering

## 1. INTRODUCTION

The field of immunoengineering is a rapidly developing scientific field that focuses on developing tools to investigate the immune system.[1] There is little data on the effects chemical or biological warfare agents have on the immune system due to its complexity, but immunoengineering tools can provide insight into assessing toxicological characteristics of existing and emerging toxin threats. Together, organ-on-a-chip technologies, microfluidic platforms, and microphysiological systems are areas of interest for screening chemical and biological threats.[2] Stemming from traditional two-dimensional cell culture methods, these systems sustain microenvironments for cell viability which is necessary for understanding the multifaceted nature of an organ or organ system, especially in context of human lymphatics.

The lymphatic system is responsible for maintaining homeostasis in the body by transporting fluid, macromolecules, and particulates via initial lymphatics in peripheral tissues into collecting vessels towards lymph nodes. From there, particulates join systemic circulation via the thoracic duct. Initial lymphatics have characteristic button-like junctions that allow for easy diffusion from tissue and into initial lymphatics.[3] Collecting vessels have more zipper-like junctions that ensure the fluid does not leak out into peripheral tissue. Lymphatic vessel physiology is unique in that collecting vessels are collapsed during steady-state conditions and are pushed open by interstitial flow.[4,5] While research has gone into exploring lymphatic physiology including transport phenomenon, cell morphology, and cellular junctions, studying lymphatics *in vivo* is extremely difficult. Lymphatic vessels are extremely thin and are buried deep within tissue. To circumvent this, researchers have begun developing *in vitro* models to visualize and study lymphatics.

Current lymphatic vessel models are created in a 2D Transwell model format. Cells are cultured on a semi-permeable membrane and allowed to culture until they reach confluency, and a monolayer is confirmed.[6] These models can be used to study cell morphology, migration, and permeability. However, 3D models are considered more physiologically relevant as these vessels can capture physiological conditions including barrier integrity while exposed to luminal and interstitial fluid flow.[7]

# 2. METHODOLOGY

## 2.1 Microfluidic device design

For the lymphatic vessel chip design, computer aided design (CAD) was used to design a simple vessel-like structure. The ends of the design were rounded to allow ports for flow insertions. A laser cutter was then used to cut molds from an acrylic sheet (Figure 1). Polydimethylsiloxane (PDMS), a silicone elastomer, was used to create the devices due to its biocompatible, inert, non-toxic properties and its status as the gold standard for microfluidic devices. A 10:1 PDMS mixture of elastomer base to curing agent ratio was used to create the device. The acrylic mold pieces were placed in the center of PDMS to allow room for a vessel, collagen hydrogel and the lymphatic endothelial cells (Figure 1).

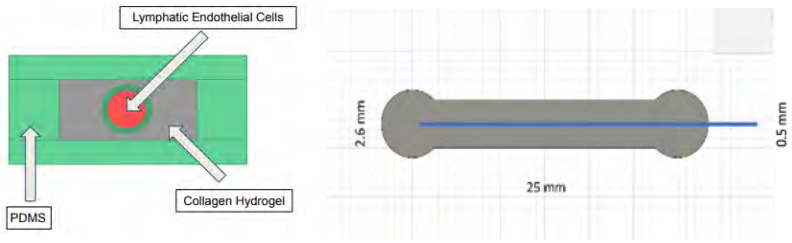


**Figure 1. CAD drawing of lymphatic microfluidic device. A 2D sketch (right) was used to then be used to laser cut the design on a 5 mm clear acrylic sheet. The cross section of the device (right) shows a PDMS casting, collagen hydrogen, and lymphatic endothelial cells.**

## 2.2 Lymphatic endothelial cell culture

Human dermal lymphatic endothelial cells (hLECs) (Promocell, C-12217) were used to seed the vessel throughout the channel in the device. hLECs were cultured in T-75 flasks in endothelial cell growth medium MV2 (EGM-MV2) with a provided supplement mix containing 5 % fetal calf serum and growth factors, including vascular endothelial growth factor, epidermal growth factor, and basic fibroblast growth factor, until they reached 70–80 % confluency and were lifted off using Accutase. Cells were used at passages 5–10 and 2.5 x $10^5$ cells were seeded in each device.

## 2.3 Collagen preparation

Prior to collagen loading, the devices were treated with 0.01 % poly-L-ysine and 1 % glutaraldehyde to sustain collagen formation within the device. A 25G needle (0.514 mm outer diameter) was placed into the channel to create a lumen within the collagen layer. A collagen hydrogel was prepared using 3 mg/mL of rat-tail collagen I, and adjusted the pH to 7.2 with 1N NaOH, 1M HEPES, 10 x PBS solution and deionized water. Once the collagen was loaded into the devices around the needle, the devices were placed in sterile petri dishes in the incubator under cell culture conditions for an hour to allow the collagen to solidify. Needles were removed from the device and media was pipetted into the device until cell seeding.

## 2.4 Seeding cells into device

The hLECs were delivered into the device through the inlet port and incubated for one hour at 37 °C and 5 % $CO_2$. During this time, devices were tilted 45° every 15 minutes to ensure the full vessel lumen was covered in cells. The device was immersed in supplemented Endothelial Cell Growth Medium MV2 media and incubated for 2–3 days until cells reached confluency. Cell confluency was confirmed by brightfield microscopy. The lymphatic vessel was exposed to luminal flow by an external pump for another 1–2 days. hLECs were grown under flow for 1–2 days after cells were adhered to the surface at rates of 5 µL/min and 30 µL/min through a syringe pump.

## 2.5 Staining of hLECs for junction protein markers

When cells under static or flow conditions reach confluency, they were fixed using a 4 % paraformaldehyde solution for 15 minutes. Fixed cells were then permeabilized with 0.1 % Triton X-100 for 5 minutes and blocked for 30 minutes in 2 % fetal bovine serum, diluted in 1x PBS. Primary antibodies specific to ZO-1 (Abcam, 216880) and Vascular Endothelial-cadherin (BD Biosciences 555661) proteins (1:200 dilutions) were used for overnight incubation. After washing the device with phosphate-buffered saline (PBS) and Tween, Alexa fluor 555 (Invitrogen, A31572) and Alexa fluor 488 (Invitrogen, A37114) conjugated secondary antibodies (1:400 dilutions) were incubated for 2 hours at room

temperature (25 °C) with agitation before counterstaining with Hoechst dye. Images were taken using an Olympus FV300 laser scanning confocal microscope.

## 3. RESULTS

### 3.1 Lymphatic cells monolayer on a 2D transwell system

A collagen-coated (50 µg/mL) 0.4 µm transwell insert was used to confirm the cell confluency and monolayer capacity. Cells were grown on the bottom layer of the transwell and allowed to adhere to the membrane surface as previously described.[7] Lymphatic cells show complete confluency on day three to become a monolayer (Figure 2).

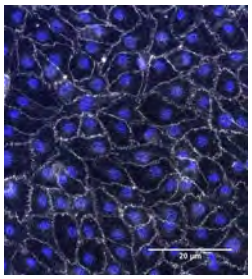

**Figure 2. Human dermal lymphatic primary endothelial cells with a complete confluent monolayer on 2D transwell culture. Blue: Hoechst dye, Gray: ZO-1 junction protein stain.**

### 3.2 Fabrication of the microfluidic device

To ensure collagen hydrogel formed in the channel of the device, surface treatment of PDMS channel was optimized for collagen adherence. Using a 0.01 % Poly-L-lysine solution, the surface was treated with 1–3 % of glutaraldehyde; however, higher percentages of glutaraldehyde were toxic against the cells. Therefore, 2 % glutaraldehyde with overnight washing was used to maintain healthy cell growth within the channel and kept intact with hydrogel.

### 3.3 Optimization of collagen gel

Different concentrations, 1 mg/mL, 2 mg/mL, 2.5 mg/mL, or 3 mg/mL, of the collagen hydrogel were tested for gelling within the channel. The collagen hydrogel was most stable at a concentration of 3 mg/mL and pH 7.4. Prior to collagen loading, a 25G needle treated with 0.1 % bovine serum albumin (BSA) was inserted into the hollow channel to form a lumen structure with a 42 $mm^2$ surface. Removing the needle from the hydrogel is critical to avoid disturbing the collagen layer. The device and hydrogel were incubated under cell culture conditions for 1 hour before removing the needle and seeding cells.

### 3.4 Seeding hLECs in the device

To test the viability of the culture, 0.5–3 x $10^5$ cells/device were loaded within the channel for analysis. Ultimately, 2.5 x $10^5$ cells were determined to be the optimal number of cells to seed and incubate for 1 hour at 37 °C. Culture condition within the lumen were similarly optimized. Typically, 15 minutes of incubation of each side of the lumen with 15° tilt showed sufficient adherence of hLECs. The device was then immersed in EGM-MV2 media and kept in static condition for one day. Cells were stained with 4',6-diamidino-2-phenylindole (DAPI) to locate the cell spread within the channel and observed to form a vessel-like structure inside the lumen of a microfluidic device (Figure 3).

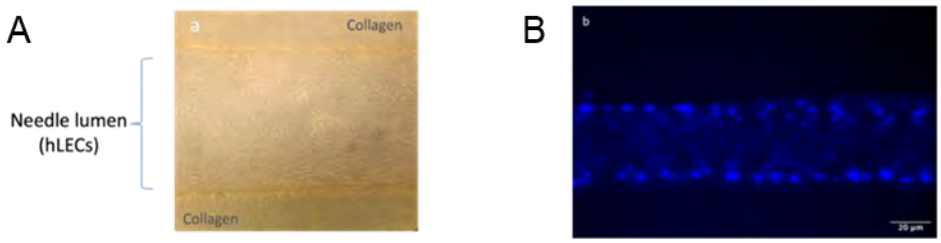


**Figure 3. A) hLECs seeded into the channel lumen surrounded by collagen. B) hLECs vessel stained with DAPI.**

### 3.5 Confocal imaging of hLECs within the channel

Two days after seeding hLECs in the device, cells were fixed for staining purposes. Anti-ZO-1 and Vascular Endothelial-cadherin (VE-cadherin) antibodies were used with Hoechst counterstain to visualize the junction morphology under a 3D hLEC vessel. Both the junction proteins were expressed within the channel with good confluency (Figure 4 left). We found that expression of junction proteins does not change to form a vessel inside the lumen. Cells were found to be confluent and formed a complete monolayer, though some gaps where cells were missing were still apparent. Figure 3a confirmed the vessel-like culture of hLECs. hLECs nuclei showed a circular vessel like structure of cells (Figure 4 right).

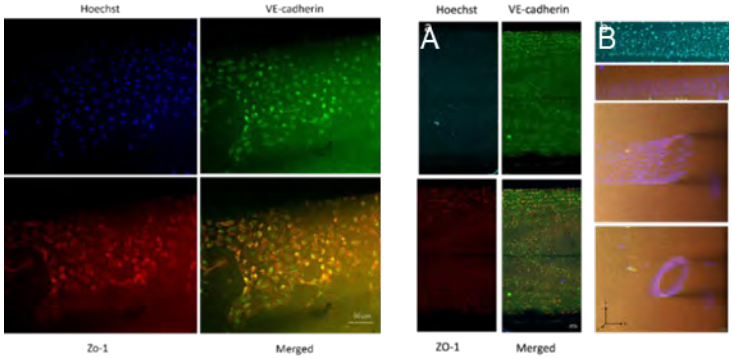


**Figure 4. Left) hLECs vessel stained for junction proteins, VE-cadherin, and ZO-1 with Hoechst. (Right) Figure 6. Z-stack confocal images of hLECs stained for junction proteins, VE-cadherin and ZO-1 with Hoechst (a). The lymphatic vessel within the device with nuclei stain (b).**

### 3.6 Testing static versus flow conditions

To mimic the natural fluid flow found in lymphatic vessels in the human body, we introduced luminal flow into the device. To compare static and flow conditions, hLECs were incubated for three days in static condition and two days under flow (5 µL/min) conditions after a day in static conditions. After fixing, cells were stained with ZO-1 and VE cadherin and counterstained with Hoechst for imaging. Introducing luminal flow did not affect the overall adherence of the cells with the hydrogel and formed a vessel like those under static conditions, however, cells under the flow were found to be stretched and elongated in shape in the direction of the flow (Figure 5).

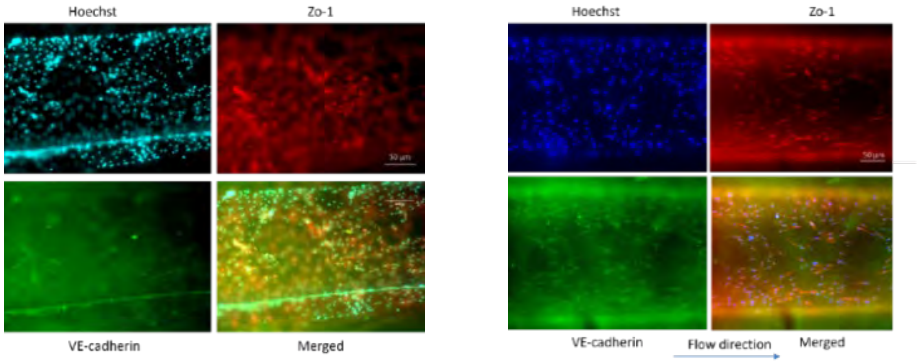


**Figure 5. hLECs under three days in static media condition stained with ZO-1, VE-cadherin, and Hoechst (left). hLECs under two days of flow at a rate of 5 µL/min (right).**

In another experiment, hLECs were incubated for either three days in static condition or two days in static conditions with a subsequent day under luminal flow (30 µL/min). After three days, cells were found confluent within the channels. The lymphatic vessel with the introduction of flow have shown comparatively better vessel formation with tight cell to cell contact. Junction protein analysis of hLECs showed a clear difference in the intensity of the proteins under flow conditions. Cells in the static condition showed less expression of ZO-1 and VE-cadherin (Figure 6 left).

Additionally, cells are loosely packed with adherent cells but, when flow was introduced, cells were more compact as monolayers with higher expression of VE-cadherin and ZO-1 proteins. While the flow expression of VE-cadherin was

confined to the membrane while cells in the static condition had protein mostly localized in the cytoplasm. A confocal image of hLEC culture under flow showed a vessel-like structure with junction and adherent proteins (Figure 6 right).

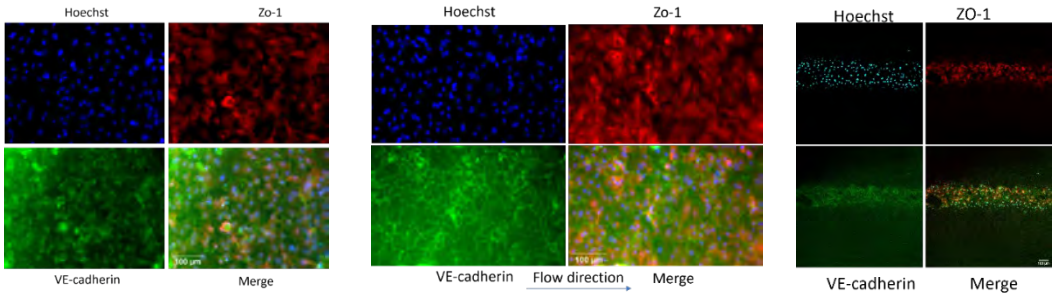


**Figure 6. (Left) hLECs under three days in static media condition stained with ZO-1 (tight junctions), VE-cadherin (endothelial cell adhesions), and Hoechst (DNA). (Right) hLECs under one day of luminal flow after two days in static condition (middle). Confocal image of lymphatic vessel under flow.**

## 4. CONCLUSIONS

This study established protocols for forming a vessel within a microfluidic device and optimized collagen hydrogels for lymphatic endothelial cell seeding. hLECs formed in a vessel-like structure and their structures were analyzed within the device under both static and flow conditions within the device. The addition of flow showed that hLECs formed a tightly packed structure and formed more junction proteins when compared to the cells under static conditions. This study suggests that lymphatic vessel permeability changes with the addition of continuous flow. Future work could include testing more flow rates within the 5–30 µL/min range for better cell morphology as a compact pushed-upon vasculature, unlike collapsed cellular morphology under static conditions. This platform could also enhance the *in vitro* toolbox for predictive toxicology as it is a customizable platform that can be easily setup with in-house resources. The results from this study have also produced preliminary results for further immunotoxicity research proposals in collaboration with the University of Maryland.

## ACKNOWLEDGMENTS

Funding for this Seedling project was made available through the Department of Defense Funding Laboratory Enhancements Across (X) Four Categories (FLEX 4) in accordance with the Army, Navy, and Air Force efforts funded under the authority in 10 U.S.C. § 4123.

## REFERENCES

[1] Green, J.J. Immunoengineering has arrived. *J. Biomed. Mater. Res. A.* **2021**, *109* (4), pp 397–403.
[2] Yeo, L.Y.; Chang, H.-C.; Chan, P.P.Y.; Friend, J.R. Microfluidic devices for bioapplications. *Small*. **2011**, *7* (1), pp 12–48.
[3] Zhang, F.; Zarkada, G.; Yi, S.; Eichmann A. Lymphatic Endothelial Cell Junctions: Molecular Regulation in Physiology and Diseases. *Front. Physiol*. **2020**, *11*, pp 1–17.
[4] Tammela, T.; Alitalo, K. Lymphangiogenesis: Molecular mechanisms and future promise. *Cell*. **2010**, *140* (4), pp 460–76.
[5] Petrova, T.V.; Koh, G.Y. Biological functions of lymphatic vessels. *Science*. **2020**, *369* (6500), eaax4063.
[6] Triacca, V.; Güç, E.; Kilarski, W.W.; Pisano, M.; Swartz, M.A. Transcellular Pathways in Lymphatic Endothelial Cells Regulate Changes in Solute Transport by Fluid Stress. *Circ. Res.* **2017**,*120* (9) , pp 1440–1452.
[7] Bogseth, A.; Ramirez, A.; Vaughan, E.; Maisel, K. In Vitro Models of Blood and Lymphatic Vessels–Connecting Tissues and Immunity. *Adv. Biol*. **2023**, *7* (5), p 2200041.
[8] McCright, J.; Skeen, C.; Yarmovsky, J.; Maisel, K. Nanoparticles with dense poly(ethylene glycol) coatings with near neutral charge are maximally transported across lymphatics and to the lymph nodes. *Acta Biomater*. **2022**, *145*, pp 146–158.

This page left intentionally blank

# Leveraging engineered allosteric transcription factors for the detection of small molecule threats

Jessica T. Paradysz[a,b]*, Alena Calm[a], Nathan Novy[c], Vatsan Raman[c]
[a]U.S. Army Combat Capabilities Development Command Chemical Biological Center, Research & Operations Directorate, 8198 Blackhawk Rd, Aberdeen Proving Ground, MD 21010
[b]Excet, Inc, 6225 Brendan Ave, Springfield, VA 22150
[c]University of Wisconsin-Madison, 433 Babcock Dr, Madison, WI 53706

## ABSTRACT

Microcystin is a hepatotoxin produced by harmful algal blooms globally. Tools are necessary to aid scientists and warfighters in detecting microcystin and other toxins in freshwater systems. This project focuses on the use of a genetically engineered bacterial transcription factor library used to identify potential binders of microcystin-leucine arginine, a common microcystin congener and small molecule toxin produced by cyanobacteria. Transcription factors bind to DNA to regulate DNA transcription in bacteria and form unique structures. Additionally, transcription factors can form binding pockets that, when bound, cause the transcription factor to undergo a conformational change and be released from DNA. In this study, we aimed to determine whether microcystin-leucine arginine can bind in any of the binding pockets of transcription factors within the synthesized library created by the Raman lab at the University of Wisconsin-Madison. If microcystin-leucine arginine can bind a unique transcription factor in the library, an RNA-barcode corresponding to that transcription factor would be transcribed and identified via deep sequencing. The initial incubation and analysis have been performed; however, sequencing analysis is ongoing.

**Keywords:** microcystin, small molecules, transcription factors, detection

## 1. INTRODUCTION

Cyanobacteria, also known as blue-green algae, are single-celled, photosynthetic organisms. These organisms can accumulate to dangerous levels, causing algal blooms in aquatic environments. Blooms of toxic cyanobacteria have become a global concern, as environmental factors contribute to proliferation events. Small molecule toxins secreted by cyanobacteria and dinoflagellates are a threat to warfighters both at home and abroad due to the high concentration of toxins released into water systems. *Microcystis*, *Anabaena*, and *Oscillatoria* are prominent genera responsible for harmful algal blooms (HABs), as species within these genera can biosynthesize the cyanotoxin microcystin. Recent reports suggest that microcystin-producing cyanobacteria are distributed worldwide and can produce the predominant cytotoxin in water systems. Microcystin is a very well-studied cyanotoxin because of its wide distribution and high toxicity and is a toxin of interest to the Department of Defense (DoD). This specific cyanotoxin inhibits eukaryotic protein serine and threonine phosphatases 1 and 2A and causes oxidative stress in liver tissue through phosphatase inhibition. Microcystin is water soluble; therefore, it is unlikely to passively diffuse into host systems through the water. Humans are usually exposed to microcystin through ingestion of contaminated water or food.[1] Structurally, microcystin is a cyclic hepatotoxin with more than 200 different congeners due to substitutions in a few prominent amino acids. Microcystin-leucine arginine (MC-LR) is the most common and one of the most toxic congeners. In mice, the median lethal dose for oral MC-LR exposure is 8–20 mg/kg and 25–65 µg/kg for intraperitoneal injection.[2] Nearly 95 % of microcystin blooms contain multiple microcystin congeners, and the toxicity of other congeners varies depending on the compound's hydrophilic nature.[1]

Microcystin is a hepatotoxin that destroys or damages tissue directly. For this reason, prophylaxis (pretreatment to negate the effects of the toxin) is important because irreversible pathological changes occur within minutes to hours after exposure. Humans can be exposed to microcystin through ingestion of toxin-containing water or food. For example, during recreational activities, dissolved microcystin from HABs can affect those swimming in contaminated water sources. Additionally, livestock and pets are prone to microcystin exposure from drinking contaminated water. Microcystin dissolved in potable water is also a concern as many municipal water treatment plants do not have effective technologies for removal of cyanotoxins. In 2022, the U.S. Environmental Protection Agency added

cyanotoxins to the Contaminant Candidates List, which is a list of drinking water contaminants that are known or anticipated to occur in public water systems and are not currently subject to EPA drinking water regulations.[3]

Because the most common threat of microcystin exposure occurs from HABs, many of the detection methods described are employed in the context of detection in recreational waters or municipal water supplies. Sample collection and processing is a critical first step in any detection method. Microcystin is an intracellular toxin; therefore, it is important to test samples only after completing a lysis step. Lysis is accomplished by freeze-thaw cycles, lyophilization, or mechanical disruption using sonication.[4] Other detection methods that can be used include reversed-phase high-performance liquid chromatography coupled with mass spectrometry or ultraviolet photodiode array detectors and protein phosphatase inhibition assays; however, these instruments are costly, time-consuming, and not field forward.[4]

The work described in this effort provides proof-of-principle, preliminary data for the future use of engineered allosteric transcription factors (aTF) to detect molecules of interest to the DoD. In this effort, as described in Figure 1, microcystin-LR was chosen as an initial target, as the Combat Capabilities Development Command Chemical Biological Center has recently completed an effort to understand the production, purification, and toxicity of MC-LR. The use of transcription factors for detection purposes can be leveraged towards additional targets that lack effective detection mechanisms for scientists in the lab and for troops in the field.

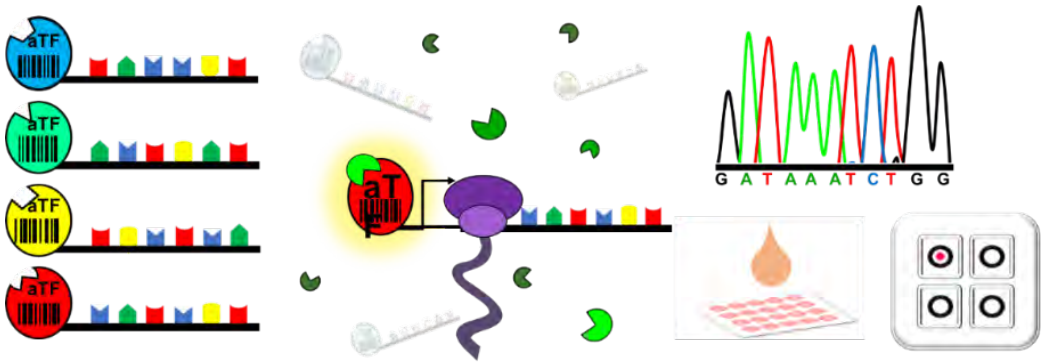


**Figure 1. Overall schematic of effort. An *E. coli* aTF library was created encoding thousands of transcription factors, each containing a unique RNA barcode. The engineered aTF library is incubated with MC-LR to see which aTFs binds to MC-LR and transcribes the RNA barcode. RNA barcode sequencing is used to identify unique aTFs that bind MC-LR. This technology can be assessed in the future using detection platforms (i.e., "Dial-a-threat", paper-based, etc.).**

## 2. METHODS AND RESULTS

### 2.1 MC-LR, *E. coli* viability assay

To verify that the *E. coli* strain containing the transcription factor library can grow in the presence of MC-LR, we grew *E. coli* in the presence of various concentrations of MC-LR. Method development was transferred from the Raman Lab at University of Wisconsin-Madison. *E. coli* NEB10β was grown in Lysogeny Broth (LB) 1 % NaCl for 16 hours. After the culture grew to stationary phase, it was used to inoculate a plate-based growth assay of *E. coli* in LB. This strain did not possess vectors housing the transcription factor library, so no antibiotics were used. Once inoculated, plate-based cultures were grown in duplicate with various concentrations of MC-LR: 10, 50, 100, or 200 µM. Two cultures were grown without inoculum as a negative growth control, while two cultures were grown without MC-LR as a positive growth control. The plates were grown for 24 hours while measuring absorbance every hour. Based on the results of this growth curve, it was determined that 100 µM of MC-LR is the appropriate concentration of toxin to use in the future incubation assay. Growth of *E. coli* incubated with 100 µM of MC-LR did not show signs of growth inhibition prior to the targeted optical density (OD) for this study (0.6 OD) (Figure 2). Incubation of the *E. coli* containing the transcription factor library, described in the next section, was completed with 100 µM of MC-LR.

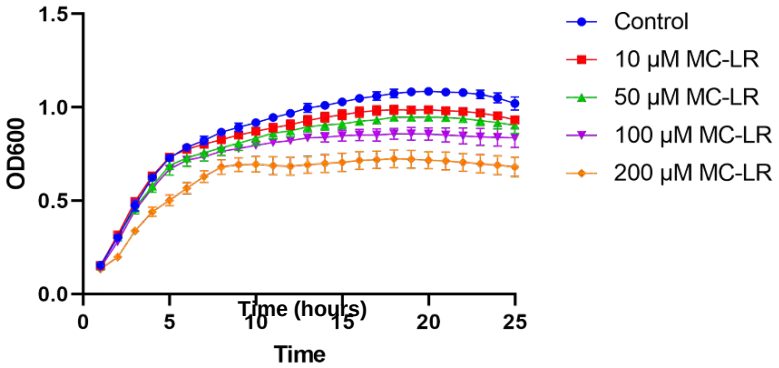


**Figure 2. *E. coli* growth curve incubated with various concentrations of MC-LR: 10, 50, 100, or 200 µM. Overnight cultures were grown without MC-LR and used to inoculate growth curve cultures in triplicate. Cultures were grown for 24 hours with shaking and the OD600 was read every hour.**

### 2.2 MC-LR library incubation

Cultures of *E. coli* DH10β containing the transcription factor library were incubated with MC-LR. Standards of MC-LR were dissolved at 2 mg/mL. Three 25 mL cultures were inoculated with 100 µM final concentration of MC-LR and allowed to grow to optical density at 600 nm (OD600) of 0.6. Once the desired OD600 was reached, cells were separated in two 1-mL and two 10-mL aliquots, centrifuged, and stored for future processing. A positive control ligand that has previously been shown to bind to transcription factors in the library was run alongside MC-LR cultures. The positive control naringenin, a ligand previously identified as a positive control, was added to cultures at a final concentration of 200 µM.

### 2.3 RNA and plasmid isolation

Plasmid preparations of cultures incubated with each ligand (MC-LR and naringenin) were performed in triplicate using the ZymoPURE Plasmid Miniprep kit. Plasmids were isolated as a positive DNA control and used to confirm that a single plasmid (containing a single-coded transcription factor) overtook any of the cultures, therefore skewing results. Isolated plasmids were used as template to amplify a unique region of the plasmid, indicating which transcription factor it encoded. These PCR products will be sequenced as analyzed as part of a larger, ongoing effort.

RNA was isolated from the same cultures that were incubated with either MC-LR or naringenin. RNA was isolated using the Qiagen RNeasy Mini Kit. As shown in Figure 3, if a ligand, such as MC-LR or naringenin can bind to a transcription factor within the transcription factor library, a promoter site is exposed allowing for transcription of a unique barcode. Such barcodes will be identified during sequencing.

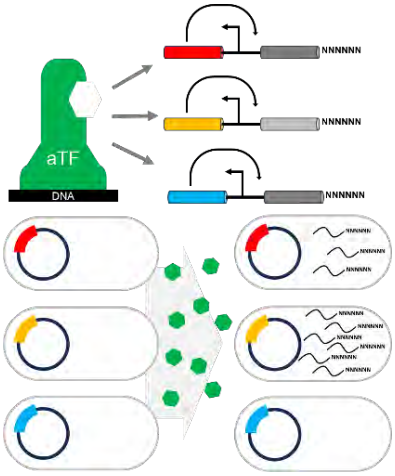


**Figure 3. Transcription regulation schematic. If MC-LR allosterically binds to an allosteric transcription factor, transcription of reporter sequence is activated. Unique barcodes correspond to each transcription factor and can be identified during sequencing.**

RNA isolated from the cells was used as a template for cDNA synthesis using a Maxima H Minus cDNA synthesis kit. A maximum of 1 µg of RNA, measured via nanodrop, was used in each cDNA reaction to ensure coverage. Instead of using random hexamers for cDNA synthesis, specifically designed primers were used to target the barcoded region. cDNA synthesis was performed in triplicate per ligand and then pooled for sequencing. Deep sequencing was conducted using NovaSeq 600 at the Next Generation Sequencing Core at the University of Wisconsin-Madison Biotechnology Center. Sequencing results will indicate if any transcription factors within the library were able to bind to the targeted ligand MC-LR.

## 3. CONCLUSIONS AND DISCUSSION

Microcystin-LR is a small molecule toxin produced in large concentrations by freshwater cyanobacteria. This toxin is of interest to the DoD due to its abundance and wide distribution. This effort focused on the use of novel and unique approached at identifying and detecting MC-LR. In this effort, MC-LR was chosen as an initial target, as DEVCOM CBC has recently completed an effort to understand the production, purification, and toxicity of MC-LR. The use of transcription factors for detection purposes can be leveraged towards additional targets that lack effective detection mechanisms for scientists in the lab and for troops in the field.

After sequencing of the plasmid and cDNA samples using the NovaSeq6000, the Raman lab at the University of Wisconsin-Madison will determine whether any transcription factors within the library were able to bind to MC-LR. This workflow was completed with a positive control ligand that successfully binds transcription factors within the library to confirm that any positive results are true positives, or negative results are true negatives. The work executed in this Seedling project highlights the need to identify and develop detection platforms for targets of interest to the DoD. The engineered transcription factor library can be leveraged towards other molecules, such as peptides or rare earth elements that could be targeted by transcription factors. Additional effort is required to expand the number and array of targets exposed to this novel genetic technology through a larger basic research effort.

## ACKNOWLEDGMENTS

Funding for this Seedling project was made available through the Department of Defense Funding Laboratory Enhancements Across (X) Four Categories (FLEX 4) in accordance with the Army, Navy, and Air Force efforts funded under the authority in 10 U.S.C. § 4123. Thank you to Kelley Betts for assistance in writing and figure creation.

## REFERENCES

[1] Ren, X.; Wang, Y.; Zhang, K.; Ding, Y.; Zhang, W.; Wu, M.; Xiao, B.; Gu, P. Transmission of Microcystins in Natural Systems and Resource Processes: A Review of Potential Risks to Humans Health. *Toxins*. **2023**, *15* (7), p 448.

[2] Yoshida, T.; Makita, Y.; Nagata, S.; Tsutsumi, T.; Yoshida, F.; Sekijima, M.; Tamura, S.I.; Ueno, Y. Acute Oral Toxicity of Microcystin-LR, a Cyanobacterial Hepatotoxin, in Mice. *Nat. Toxins*. **1997**, *5* (3), pp 91–95.

[3] *Contaminant Candidate List 5 (CCL 5).* U.S. Environmental Protection Agency, **2022**. https://www.epa.gov/ccl/contaminant-candidate-list-5-ccl-5 (accessed 2023-07-31).

[4] *Drinking Water Health Advisory for the Cyanobacterial Microcystin Toxins;* U.S. Environmental Protection Agency, **2015**. https://www.epa.gov/sites/default/files/2017-06/documents/microcystins-report-2015.pdf (accessed 2023-08-01).

# Probing chemical parameters for enhanced vat polymerization 3D printing

Chase B. Thompson[a], Jordan A. Mack[b], and Kristian M. Van de Voorde[c]*
[a]Leidos Inc., 1750 Presidents St, Reston, VA 20190
[b]Tuskegee University, Department of Electrical and Computer Engineering, 1200 W Montgomery Rd, Tuskegee, AL 36088
[c]U.S. Army Combat Capabilities Development Command Chemical Biological Center, Research & Operations Directorate, 8198 Blackhawk Rd, Aberdeen Proving Ground, MD 21010

## ABSTRACT

Additive manufacturing offers on-demand production of precision parts with tunable properties based upon both print parameters and chemical feedstock. In this work, a model monomer resin is formulated using either a difunctional or tetrafunctional crosslinker where the total number of crosslinking acrylate groups is held constant, changing only the connectivity of the network while leaving the theoretical number of crosslinks unchanged. It is demonstrated that increasing crosslink functionality increases the network heterogeneity and leads to a stiffer, more brittle material. Furthermore, the concentration of photoinitiator is changed to control the polymerization rate of the 3D prints, highlighting how network connectivity is influenced by the polymerization rate while the overall conversion is controlled by the post-cure process. In this case, the difunctional system's thermal behavior is relatively unaffected by the change in initiator concentration, but the mechanics show significant differences due to a more rapid gelation. Finally, the utility of these minute changes in monomer formulation are highlighted in the development of a 3D printed bilayer hygromorph, where it is demonstrated that the bilayer printed with difunctional crosslinker has a stronger shape change response than a print containing the stiffer tetrafunctional crosslinker.

**Keywords:** Additive manufacturing, photopolymerization, 3D printing, crosslink density, heterogeneity

## 1. INTRODUCTION

Additive manufacturing is a high-throughput production technique that has drawn interest due to its ability to provide on-demand parts and materials in the field. Vat photopolymerization 3D printing such as digital light processing (DLP) operates by polymerizing a reactive resin in a layer-by-layer photopolymerization process to yield the bulk part. Resin chemistry, print parameters, and post-cure processing all dictate the final thermal and mechanical properties of the printed object.[1–3] However, there is still a lack of understanding of how the photopolymerization and layer-by-layer printing control the structure and connectivity of the final thermoset. In thermoset chemistry—especially those based on the free radical polymerization of acrylates and methacrylates—the network connectivity controls the thermal and mechanical properties of the resultant network. Network heterogeneity, which includes dangling ends, loops, and microgel formation,[4] can alter the glass transition temperature ($T_g$), relaxation time, and stiffness of a material.[5–7] As such, understanding how resin formulation and print parameters dictate thermomechanics in printed parts is crucial to applying 3D printers into the field.

In this work, we design a series of model 3D printing resins based upon commercially available acrylate monomers and crosslinkers. Through altering the functionality of the crosslinker from a difunctional to tetrafunctional system without changing the total number of crosslinking acrylates, we can tune the heterogeneity of the final thermoset network. Additionally, we explore how the concentration of photoinitiator controls print properties by increasing the mole percentage of Irgacure 651 from 0.2 to 1.0 mol%. Through this methodology, we can begin to understand how polymerization kinetics dictate the thermoset network structure and, as a result, the thermal and mechanical properties of the final material including its utility in the production of stimuli-responsive systems.

## 2. EXPERIMENTAL

All materials were purchased from Millipore Sigma with the exception of 2-propanol (IPA) which was purchased from Fisher Scientific. All resins were pre-mixed in a fume hood in covered bottles to minimize premature photopolymerization. All 3D printing was performed on an Anycubic Photon system using a layer thickness of 100 μm at a layer cure time of 12 s with no base layer. Rectangles of dimensions 20 mm x 5 mm x 1 mm (LxWxT) were used for most characterization techniques. Prints were removed from the print head and washed with IPA to remove excess resin prior to post-cure. All prints were post-cured inside of an Anycubic washing and post-curing station for 20 min. Printed parts were pressed between glass slides held shut with binder clips to ensure that the printed objects stayed flat. For the hygromorphic bilayer printing, a vat exchange process was used. The print process was stopped at 50 % completion and the vat was exchanged for the 2-hydroxy ethyl acrylate chemistry then printing was continued as normal.

Dynamic mechanical analysis (DMA) was performed on a DMA 850 (TA Instruments) with liquid nitrogen. All DMA measurements were conducted from -50–150 °C at a heating rate of 5 °C/min. All runs were conducted in triplicate and data was processed in TRIOSsoftware. The glass transition temperature ($T_g$) of the samples was determined from the peak position of the tanδ curve. Representative runs are shown in places where raw data is plotted to highlight trends. The kinetic study was based upon the time it took for a 50 μL droplet of resin on a glass slide to form a tack-free solid when exposed to a 405-nm light source with an intensity of 5.5 mW/cm$^2$. Gel fraction measurements were conducted by swelling and extracting printed parts in chloroform for 24 hours. The solvent was exchanged once for fresh chloroform after 16 hours. Samples were removed from the solvent and dried *in vacuo*. Printed bilayers were submerged in distilled water for 3 hours and photographs were taken to compare their state of curvature.

## 3. RESULTS AND DISCUSSION

### 3.1 Print optimization and polymerization kinetics

The resin developed in this study was formulated to allow for controlling crosslink density and initiator concentration while producing prints that were easy to work with and remove from the print head. For this reason, tBA and BA were chosen as monomers to control the overall molecular weight between crosslinks and influence the $T_g$ of the samples. HDDA and PETA were selected as the difunctional and tetrafunctional crosslinker, respectively (Figure 1). All formulations consisted of 70 mol% tBA, 20 mol% BA, and 10 mol% crosslinking acrylate groups. The total number of crosslinking acrylates was held constant and, as such, the molar amounts of HDDA and PETA were adjusted by their functionalities of 2 and 4, respectively. Additionally, different molar concentrations of initiator were added to alter the polymerization kinetics during printing. As such, the nomenclature for the samples is chosen as XF-YI where X refers to the functionality of the crosslinker used in the formulation (2 for HDDA, 4 for PETA), and Y is replaced by the mol% of BAPO used in that formulation (0.2, 0.5, or 1.0 mol%). For example, 2F-0.5I refers to a resin employing HDDA and 0.5 mol% BAPO. Initial printing studies highlighted that extensive washing caused the prints to crack and curl upon drying likely due to their relatively low conversion. For this reason, washing with IPA was kept brief and post-curing was conducted between two glass slides clamped shut with binder clips to yield flat samples.

A)

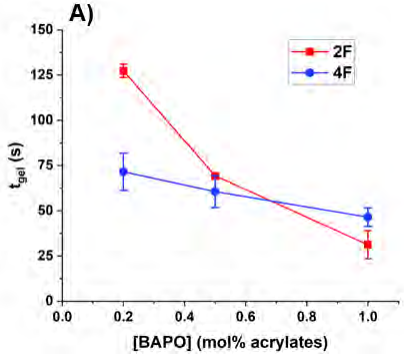


B)

| | Gel (%) |
|---|---|
| 2F-0.2I | 87 |
| 2F-0.5I | 100 |
| 2F-1.0I | 100 |
| 4F-0.2I | 97 |
| 4F-0.5I | 100 |
| 4F-1.0I | 91 |

**Figure 1. A) Gelation time versus photoinitiator concentration for the 2F (squares) and 4F (circles) sample series. B) Gel fraction calculated for each of the printed samples.**

To gain an understanding of the underlying kinetics that control the print properties, studies were conducted that compared the time to tack-free gelation ($t_{gel}$) and its dependence on initiator loading (Figure 2). Interestingly, the 2F sample series shows a substantial decrease in $t_{gel}$ with increasing loading of BAPO, decreasing from 127 ± 3.7 s to 31 ± 7.8 s between 2F-0.2I and 2F-1.0I, respectively. On the other hand, the 4F sample series shows a smaller variation in $t_{gel}$ with increasing initiator concentration, with $t_{gel}$ only decreasing from 72 ± 10.3 s to 47 ± 5.1 s from 4F-0.2I to 4F-1.0I. The primary driving force for this lack of variation is attributed to the higher propensity of the 4F samples to form microgels in early stages of the polymerization. It has been previously demonstrated that increasing crosslinker functionality increases the network heterogeneity and formation of microgels.[6,8] During the early stages of polymerization when microgels occur, local regions of high crosslinker density polymerize from the initiator sites; as polymerization progresses, the continuous network is formed when long, less-crosslinked reactive chains link these microgels together, resulting in heterogeneous systems with areas of high and low crosslink density. Because the critical point of gelation is driven by interconnecting microgels, an increase in initiator concentration wouldn't drastically shift this gelation point when compared to the more homogeneous polymerization of the 2F system. It should be noted that the gelation times here are much longer than the layer cure times for printing due to the much larger resin-air interface in the gelation studies and the greater thickness of the resin droplet when compared to the print layer thickness. Gel fraction measurements were conducted to probe the bulk conversion of the different prints through a simple solvent extraction process. Samples were swollen in chloroform for 24 hours with the solvent exchanged for fresh chloroform after ~16 hours. The extracted samples were then rinsed, dried, and weighed to calculate their mass before ($m_i$) and after ($m_f$) extraction, where any uncrosslinked monomer is removed by dissolution in chloroform. The gel fraction is then calculated using equation (1):[9]

$$\text{gel fraction (\%)} = 100\left[1-\left(\frac{m_i - m_f}{m_i}\right)\right] \quad (1)$$

Gel fraction values for the different prints are listed in Figure 2B. Here, it becomes apparent that while the polymerization kinetics are different as indicated by $t_{gel}$: the total conversion between networks is similar as indicated by gel fractions >95% for most samples. This points to the fact that the post-cure process is important for offering a stable, high-conversion material after the rapid photopolymerization that occurs during print. The effects of this two-stage cure process are detailed in Section 3.2.

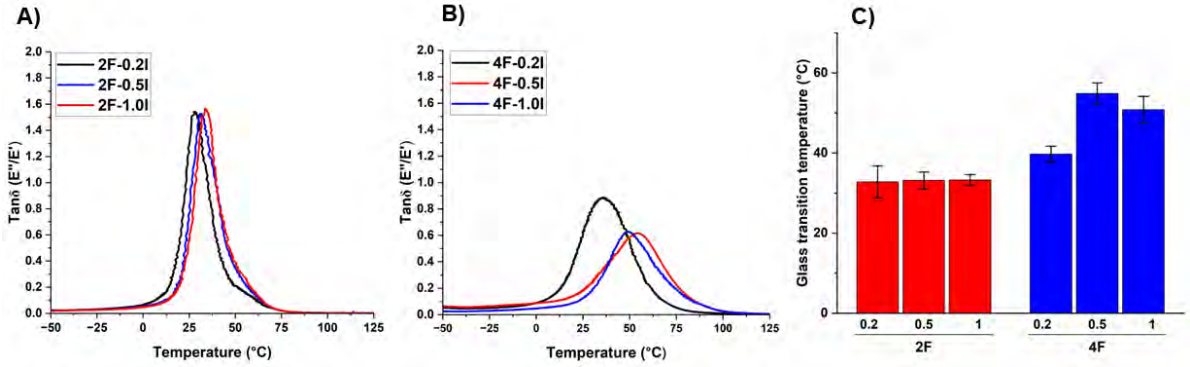


**Figure 2. A) Representative tanδ plots of 2F sample series. B) Representative tanδ plots of 4F sample series. C) Comparison of glass transition temperature between 2F and 4F samples.**

### 3.2 Thermal properties of printed objects

The thermal properties of acrylate thermosets have been shown to be strongly influenced by the connectivity and heterogeneity of the polymer chains.[5] For this reason, DMA is a powerful tool for characterizing the network topology. Representative tanδ versus temperature curves for the 2F and 4F samples are shown in Figure 2A and 2B, respectively. In the 2F system, there does not appear to be a substantial shift in the $T_g$ of the samples with increasing BAPO concentration (Figure 2C, Table 1). However, there is an apparent high-temperature shoulder present that increases with increasing initiator content (Figure 2A). The presence of this shoulder indicates a non-uniform chain distribution that occurs at high temperatures—corresponding to a less mobile (i.e., more highly crosslinked) section of the network. This network heterogeneity is driven by the more rapid gelation of the print as indicated by established gelation time data discussed above. Because the network connects faster, conversion becomes diffusion limited more rapidly and, as a result, larger molecules—either growing strands or crosslinkers—are frozen in place. These larger molecules

cause more densely crosslinked regions to be created locally. However, it is important to again note that the gel fraction, and therefore the conversion, of these samples is nearly identical, indicating that these small differences are not the result of changes in conversion.

The 4F series, on the other hand, shows some dependence of the $T_g$ upon the initiator concentration. The $T_g$ increases above an initiator loading of 0.2 mol% with similar values observed in 4F-0.5I and 4F-1.0I. This increase in $T_g$ above 0.2 mol% may be caused by the lower density of microgels that form when the BAPO concentration is lower. Since most microgels are formed around the site of initiation, a lower concentration of initiator would also lower the concentration of densely crosslinked microgels, contributing to a more homogeneous network (Table 1). This is supported both by the reduced peak width (full width at half maximum) of 4F-0.2I when compared to other 4F samples (Table 1) and by the similarity of the 4F-0.2I $T_g$ value to the values measured in the 2F samples. It is important to note that even though the starting initiator concentrations were different, the gel fraction data (Figure 2) indicates that the total number of crosslinks/overall conversion of the networks is similar. This data suggests that polymerization kinetics play a large role in the properties of 3D prints: when more reactive and higher functionality crosslinkers are used, heterogeneous network structures are formed. While post-curing can enhance the overall conversion and crosslinking of the print, the network formed during the print process still heavily influences the overall behavior of the network.

**Table 1. Values derived from DMA data for the printed samples.**

| | $T_g$ (ºC) | FWHM (ºC) |
|---|---|---|
| **2F-0.2I** | 32.8 ± 4.0 | 43.4 ± 2.2 |
| **2F-0.5I** | 33.2 ± 2.1 | 46.2 ± 1.4 |
| **2F-1.0I** | 33.3 ± 1.3 | 50.3 ± 2.9 |
| **4F-0.2I** | 39.7 ± 2.0 | 53.1 ± 3.3 |
| **4F-0.5I** | 54.9 ± 0.4 | 64.4 ± 2.0 |
| **4F-1.0I** | 50.8 ± 3.3 | 65.2 ± 2.8 |

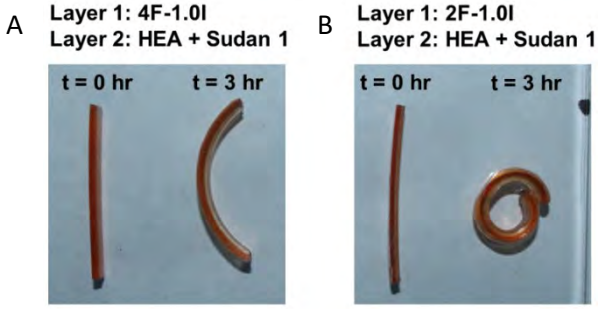


**Figure 3. Photographs showing the comparison between actuating behavior of the bilayer containing 4F-1.0I (left) and 2F-1.0I (right) before and after 3 hours of soaking the bilayers in distilled water.**

### 3.3 Hygromorphic bilayer actuators

One interesting area of growth for 3D printed materials is the production of complex geometries that incorporate functional materials. 3D printing offers an avenue to spatially control material chemistry using either vat swapping or resin swapping methods or dual wavelength 3D printing.[10] In either protocol, spatial control over the chemistry offers changes in local thermomechanics and can be used to create functional, stimuli-responsive materials. In cases where a specific response is required, the properties of the printed layers will control the functional output of the system. To demonstrate the utility of our formulated resin, we used it as a passive layer in a 3D printed hygromorphic bilayer actuator. First, the resin vat was loaded with either 2F-1.0I or 4F-1.0I resin and 5 layers of a rectangle was printed. Printing was paused and the resin vat was exchanged for a vat containing HEA, 1.0 mol% BAPO, and 0.2 wt% of Sudan III as a red dye for identifying the layers. The HEA print layer was adapted from prior literature. Printing was resumed for five more identical layers and the resulting rectangles were post-cured for 20 minutes. The bilayer prints were then submerged in water for 3 hours and their behavior was tracked. The hydrophilic HEA resin absorbed water while the passive 2F-1.0I and 4F-1.0I resins did not, resulting in the bilayer curving toward the passive layer as the swollen active HEA layer picked up water.

After 3 hours, the bilayer with the 2F-1.0I passive layer had curled into a complete circle while the active print with the 4F-1.0I layer showed substantially less curvature. This is due to the increased $T_g$ of the 4F prints when compared to the 2F prints resulting in a greater stiffness at room temperature, causing the force imposed by the swelling HEA layer to be more strongly resisted in the 4F-1.0I sample when compared to the softer 2.0I layer.

## 4. CONCLUSION

In this study, we formulated and applied a model resin to understand how network connectivity is influenced by small changes to the resin chemistry. It was shown that increasing crosslinker functionality from 2 to 4 increases the network heterogeneity while decreasing the dependence of gelation time on initiator concentration. The 4F system also has a higher $T_g$ than the 2F counterpart due to the greater mobility restriction imposed by the higher functionality PETA crosslinker. Furthermore, the 4F system $T_g$ showed a greater dependence on the initiator concentration than the 2F system due to the concentration of microgels being directly proportional to the concentration of BAPO, resulting in a greater disparity in local versus global crosslink density when compared to the more homogeneous 2F sample series. Finally, it was demonstrated the resins formulated here could be incorporated into a functional bilayer actuator as a passive layer to resist the swelling of a hydrophilic printed HEA layer. The stiffer and higher $T_g$ 4F-1.0I bilayer more greatly resisted the actuation than the more elastomeric 2F-1.0I layer.

## ACKNOWLEDGMENTS

We would like to thank Dr. Susan Kozawa for providing technical insight and assistance with photographing bilayer actuators. Funding for this Seedling project was made available through the Department of Defense (DoD) Funding Laboratory Enhancements Across (X) Four Categories (FLEX 4) in accordance with the Army, Navy, and Air Force efforts funded under the authority in 10 U.S.C. § 4123.

## REFERENCES

[1] Higgins, C.I.; Brown, T.E.; Killgore, J.P. Digital light processing in a hybrid atomic force microscope: *In situ*, nanoscale characterization of the printing process. *Addit. Manuf.* **2021**, *38*, p 101744.

[2] Caplins, B.W.; Higgins, C.I.; Kolibaba, T.J.; Arp, U.; Miller, C.C.; Poster, D.L.; Zarobila, C.J.; Zong, Y,Y.; Killgore, J.P. Characterizing light engine uniformity and its influence on liquid crustal display based vat photopolymerization printing. *Addit. Manuf.* **2023**, *62*, p 103381.

[3] Ge, Q.; Jian, B.; Li, H. Shaping soft materials via digital light processing-based 3D printing: A review. *Forces in Mechanics*. **2021**, *6*, p 100074.

[4] Lin, T.-S.; Wang, R.; Johnson, J.A.; Olsen, B.D. Topological Structure of Networks Formed from Symmetric Four-Arm Precursors. *Macromolecules*. **2018**, *51* (3), pp 1224–1231.

[5] Tsige, M.; Lorenz, C.D.; Stevens, M. J. Role of Network Connectivity on the Mechanical Properties of Highly Cross-Linked Polymers. *Macromolecules.* **2004**, *37* (22), pp 8466–8472.
[6] Elliott, J.E.; Bowman, C.N. Monomer Functionality and Polymer Network Formation. *Macromolecules*. **2001**, *34* (13), pp 4642–4649.
[7] Wen, M.; Scriven, L.E.; McCormick, A.V. Kinetic Gelation Modeling: Kinetics of Cross-Linking Polymerization. *Macromolecules.* **2003**, *36* (11), pp 4151–4159.
[8] Elliott, J.E.; Bowman, C.N. Kinetics of Primary Cyclization Reactions in Cross-Linked Polymers: An Analytical and Numerical Approach to Heterogeneity in Network Formation. *Macromolecules*. **1999**, *32* (25), pp 8621–8628.
[9] Matolyak, L.E.; Thompson, C.B.; Li, B.; Keum, J.K.; Cowen, J.E.; Tomazin, R.S.; Korley, L.T.J. Secondary-Structure-Mediated Hierarchy and Mechanics in Polyurea-Peptide Hybrids. *Biomacromolecules.* **2018**, *19* (8), pp 3445–3455.
[10] Thrasher, C.J.; Schwartz, J.J.; Boydston, A.J. Modular Elastomer Photoresins for Digital Light Processing Additive Manufacturing. *ACS Appl. Mater. Interfaces*. **2017**, *9* (45), pp 39708–39716.

# Investigating scalable materials production pathways for biodefense applications

Susan K. Kozawa[a,b], Jennifer A. Lee[a,c], Sanchao Liu[d], Hong Dong[d], Anne Y. Walker[a]*
[a]U.S. Army Combat Capabilities Development Command Chemical Biological Center, Research & Operations Directorate, 8198 Blackhawk Rd, Aberdeen Proving Ground, MD 21010
[b]Oak Ridge Institute for Science and Education, 1299 Bethel Valley Rd, Oak Ridge, TN 37830
[c]Defense Threat Reduction Agency, 2800 Bush River Rd, Gunpowder MD 21010
[d]U.S. Army Combat Capabilities Development Command Army Research Laboratory, Army Research Directorate, 2800 Powder Mill Rd, Adelphi, MD 20783

## ABSTRACT

This investigation focused on strategies to create filtration media for use in biodefense-oriented personal protective equipment. Strategies were centered around identifying materials and fabrication methods for a *bio-prefilter* concept. This bio-prefilter will be used as a multistage set of nonwoven nanofibrous filters overlaid on commercially available respiratory protection materials, expanding the range of biothreats the products can protect against and enable protection from a wide range of Warfighter and public health-related threats without the need to embark on costly and time-consuming product redesigns. This study evaluated the viability of solution blow spinning to produce functionalizable fibers from poly(acrylic acid). This study assessed the suitability of modified poly(acrylic acid) for use with bioconjugation techniques to produce materials that could be modified with biocapture moieties such as biotin-streptavidin binding system at high binding efficiencies. Success with this model system demonstrates the viability of the bio-prefilter strategy and its suitability for further evaluation with real-world relevant biocapture biomolecules.

**Keywords:** personal protective equipment, biodefense, respiratory protection, bioconjugation, filtration, bioconjugation, poly(acrylic acid), solution blow spinning

## 1. INTRODUCTION

Biodefense in public health and defense spheres is a critical responsibility of chemical, biological, radiological, or nuclear researchers. Development of biodefense materials that detect, capture, or detoxify biological threats is a major area of focus, yet facile methods for incorporating these functionalities into easily scaled materials systems remain elusive. This study seeks to lay the groundwork for developing straightforward production methods by exploring pathways for imparting functionalities on commercial, off the shelf (COTS) textile materials and exploring scalable fiber fabrication techniques to create functional protective materials from readily available commodity polymers. Rather than starting from square one, finding methods for combining reliable mass-manufacturing techniques and COTS materials with flexible advanced fabrication processes can speed up the product development timeline and more quickly supply the warfighter with advanced personal protective equipment (PPE) with new functionalities.

The pursuit of broadly effective biodefense materials relies on identifying strategies for imparting antimicrobial or microbe capture behaviors onto materials and the use of similar strategies employed by adjacent industries.[1,2] It is unlikely a single antimicrobial functionality will cover all relevant biothreats in the defense and public health landscapes and identifying simplified schemes for attaching many antimicrobial moieties onto materials is imperative for the development of a truly multispectral PPE system.[3,4] This study focused on a system based around a common bioconjugation technique to provide a flexible, efficient methodology for functionalizing polymeric material.[5] Coupling this system with a scalable fiber fabrication technique (solution blow spinning) and easily functionalizable commodity polymers, is a route for enabling the creation of versatile, multispectral biodefense materials.

# 2. RESULTS AND DISCUSSION

## 2.1 Biodefense filtration media and respirator design (bio-prefilter system)

### *2.1.1 Design constraints*

The primary methods for capture in commercial respiratory PPE are mechanical or electrostatic, and the filtration media used in PPE is composed of nonwovens created through melt, carding, wetlay, or airlay processes.[6,7] Filtration strategies consider biological threats an aerosol problem.[8] The efficacy of fibrous filtration media for aerosol capture is governed by fiber characteristics (size, density, orientation, and distribution). Design of fiber-based media must strike a balance between collection efficiency and pressure drop.[9,10] Strategies for imparting specific biological capture functionality rely on surface functionalization and trend toward creation of hydrophobic or metal-loaded antimicrobial fibers are not easily biofoul instead of focusing on specific capture strategies.[11,12] High efficiency, specific biocapture requires introduction of high surface area fibers with packed binding moieties, requiring fibers to achieve the necessary binding moiety density. The pressure drop makes this strategy a non-starter unless nanofibers can be dispersed among larger fibers. Straightforward commercial processes may struggle to provide a balance between manufacturability and intercalation of small, functionalized fibers and large, mechanical/electrostatic fibers. From a manufacturing standpoint, even a 1:10 ratio by weight of nanofiber to large fiber in a nonwoven mat yields a material that is 60 % nanofiber/40 % larger fiber, resulting in a material that is neither efficient nor mechanically robust with prohibitive pressure drop. It is necessary to pursue alternative strategies for incorporation of fibers with high biocapture capacity.

### *2.1.2 Materials design constraints, evaluation, and down selection*

Pursuing a versatile, scalable, application-appropriate prefilter material requires careful polymer selection. Many materials are inappropriate as a first line component of biofiltration media with fouling due to nonspecific protein binding.[12] Common filtration media materials all suffer from such issues.[13] These issues prevent techniques from being useful. Adding specific binding moieties to a nonspecific surface, without removing the parts of the surface that are nonspecific does not suddenly yield an extra specific surface, it simply yields a waste of time, capital, and confusion within the scientific community. Moreover, for ease of scaling, identifying a material that could be functionalized using widely known bioconjugation strategies was a critical consideration. For this reason, poly(acrylic acid) (PAA) emerged as the main polymer platform for this study. The availability of multiple forms and molecular weights of PAA and the abundance of carboxylate groups made it the best candidate for this investigation.

### *2.1.3 Filter media system (bio-prefilter)*

Given the constraints and material selection, a device consisting of multiple micron or, submicron-scale “prefilter” layers modified with binding moieties was pursued which will be placed in line with a main COTS filter. In filtration devices, a prefilter to capture particles is placed in front of the main filtration media to prevent loading and prolong efficacy. The prefilter approach here is an analogue, with micro- and nanoscale fibers with biocapture functionality placed before the primary COTS filter. This prevents primary filter bombardment and heavy, nonspecific binding and premature failure and introduces mission-specific flexibility. Both the COTS primary filter and the specific biothreat capture moieties bound to the prefilter can be selected based on need, potentially allowing for on-the-fly modifications.

## 2.2 Polymer formulations

Though PAA was the focus of this study, 1-ethyl-3-(3-dimethylamino) propyl carbodiimide/N-hydroxysuccinimide (EDC/NHS) conjugate is not 100 % efficient, with undesirable anhydride groups making up 40 % post treatment.[14] The efficacy of the bio-prefilter concept relies on bioconjugation to prevent bombardment of biological material and nonspecific binding. The more specific binding groups on the prefilter, the less likely contaminants reach and foul the primary filter. Therefore, PAA must be modified with 1,4 diaminobutane for higher bioconjugation.

## 2.3 Functional polymer films

PAA formulations were tested for successful functionalization in a solvent cast film format. The PAA was readily cast into the film form and fluorescence imaging showed successful binding of fluorescently labeled streptavidin-AF568 by the biotin moieties conjugated to the polymer (Figure 1). Given these results, the next phase of the study was to move from the film form into fibrous media more suitable for use in the bio-prefilter. The biotin can also be blocked using bovine serum albumin, as seen by a decrease in fluorescence compared to film with biotin-streptavidin.

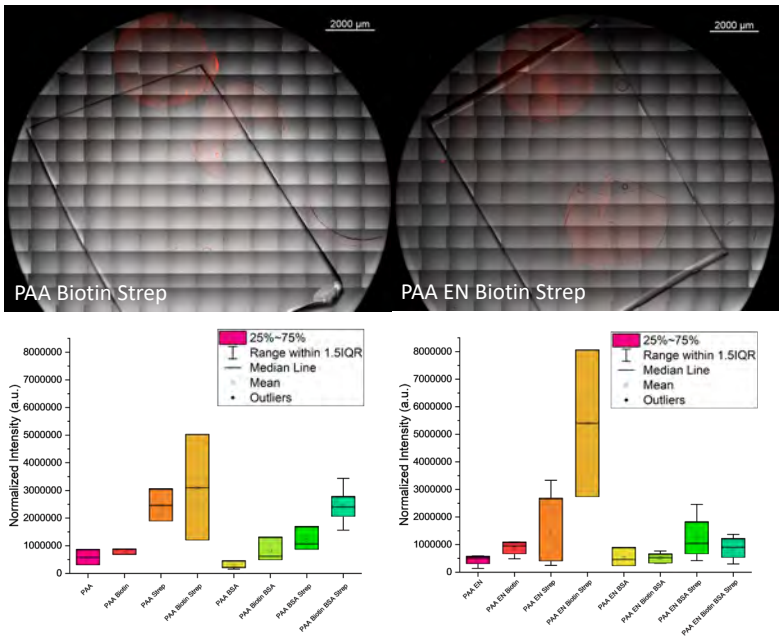


**Figure 1. Fluorescence of PAA conjugated and unconjugated films with biotin streptavidin. The left figures depict unconjugated PAA with all conditions and the right figures depict conjugated PAA with all conditions.**

## 2.4 Functional polymer fibers

### *2.4.1 Solution blow spinning of fibers*

Fiber mats were successfully spun from PAA solution. Fibers showed size scales and distributions common to solution blow spinning processes with a roughly measured average diameter of 2.47 ± 1.1 µm (Figure 2). Effective fiber diameter measured from permeation studies are planned for the next phase of the study after which optimization of fiber morphology will take place. Successful fiber mat formation was sufficient to proceed to the next phase of the study to assess viability of these materials for modification with the biotin streptavidin system.

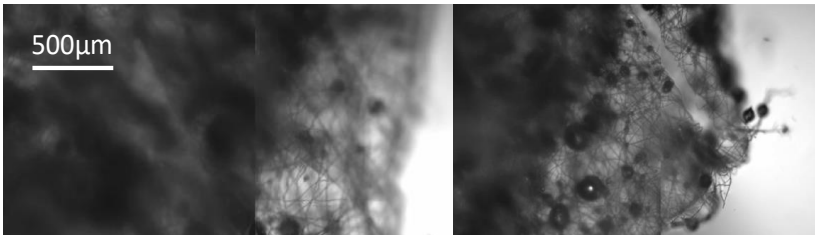


**Figure 2. Microscopy image of PAA fiber mats in PBS.**

### *2.4.2 Functionalized fiber mats*

Biotin-conjugated PAA fiber mats were incubated with labeled streptavidin-AF568 to test binding efficacy of the binding system. Fluorescence imaging showed successful binding, demonstrating that the solution blow spinning technique and PAA material selection are suitable for the bio-prefilter (Figure 3). This successful conjugation is promising, as it opens the door for exploration of a wide range of binding moieties. Unconjugated PAA with biotin and streptavidin appears to increase fluorescence compared to conjugated PAA with biotin and streptavidin due to bubbles in the imaging and entrapment within the fiber matrix. Increasing time and washes will be further explored.

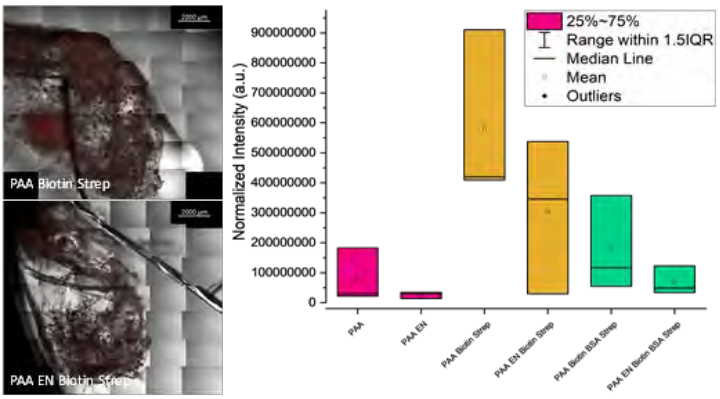


**Figure 3. Activity of biotin-functionalized PAA mats.**

## 3. METHODOLOGY

### 3.1 Film casting and solution blow spinning

Previously published PAA formulations were used.[15] Polymer solution included 3 wt% solution of PAA (MW ~450,000) in ethanol with 10 % ethylene glycol relative to the solution and 50 µL/mL of 1 M sulfuric acid. Films were cast and crosslinked at 130 °C for 30 minutes and punched with a 5 mm pin punch. Solution blow spinning was performed with a custom system consisting of a syringe pump fed to a capillary inserted into a die designed to direct a constant flow of compressed air. Fiber mats were spun from 3 wt% PAA solution. The solution was spun at 0.3 mL/min at 40 psi using a blunted 20 gauge needle with the surrounding air heated to 100 °C and suspended 250 mm above a perpendicular platform to form fibers. A surrounding cylinder confined the spun area to prevent any fibers from escaping the base. Fibers were captured on aluminum and crosslinked at 130 °C for 30 minutes.

### 3.2 EDC/NHS bioconjugation on PAA

N-ethyl-N'-(3-(dimethylamino)-propyl)carbodiimide/N-hydroxysuccinimide (EDC/NHS)-mediated biotin coupling is a technique taken from the literature.[5,15] EDC (341006) and NHS(130672) (Millipore Sigma) were used to couple PAA with 1,4-diaminobutane (D13208, Sigma Aldrich) overnight to provide an amine group to couple with biotin (Figure 4). EDC/NHS was then recoupled to biotin for 2 hours at room temperature under constant shaking.

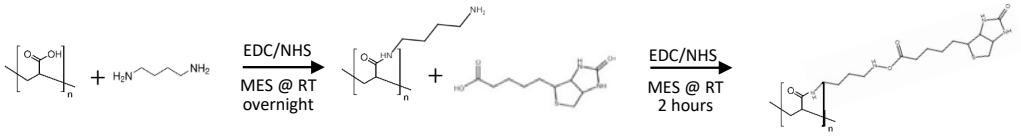


**Figure 4. Schematic of PAA coupling to 1,4-diaminobutane then biotin.**

### 3.3 Protein capture

To determine if biotin conjugated PAA films and fibers were capable of protein capture, PAA samples were incubated with streptavidin, Alexa Fluor™ 568 conjugate (2 µg/mL) (S11226, Thermo Fisher Scientific) overnight at 4 °C or for 1 h at room temperature with constant shaking. Samples were rinsed with PBS for 5 minutes three times at room temperature, placed into glass bottom plates, and imaged using fluorescence microscopy to evaluate protein capture.

### 3.4 Microscopy imaging

A Zeiss Axio Observer Z1 inverted microscope was used to image fluorescently labeled streptavidin-AF568 (ex/em 578/603 nm) binding to biotin-conjugated PAA films and fibers. Images were taken with an Axiocam 506 camera using a Plan-Apochromat 10 x/0.45 M27 objective. A Colibri 7 light source was used with a lime LED (567/100 nm). Endpoint tiled images of streptavidin binding were taken using differential interference contrast (DIC) and AF568 channels. Fluorescence images were quantified using ImageJ software.[16] Fiber diameter was obtained from the DIC images and analyzed in ImageJ using General Image Fiber Tool.[17]

## 4. CONCLUSIONS

This study laid the groundwork for explorations of antimicrobial strategies for biospecific filtration media. Evaluating limitations of nonwoven manufacturing processes and current strategies for specific biodefense equipment led to a filtration concept based on COTS filtration media with a series of "bio-prefilters" composed of micron-scale fibers functionalized with binding moieties. Selecting a fiber fabrication technique that can functionalize materials with favorable properties imparted by micro/nanofibers that can be used as prefilters for easily obtainable COTS materials provides design flexibility and agility against the biothreat landscape. PAA is mechanically robust, readily spinnable into micron-scale fibers, and functionalizable using bioconjugation strategies. Findings in this study are encouraging and suggest the bio-prefilter concept is a viable strategy for biodefense materials. Future work should evaluate design considerations such as pressure drop as the bioprefilter is layered on materials, biocapture efficacy as layers are increased, and viability of incorporating capture moieties into a filter layer or development of "one-pot" modifications.

## ACKNOWLEDGMENTS

Funding for this Seedling project was made available through the Department of Defense Funding Laboratory Enhancements Across (X) Four Categories (FLEX 4) in accordance with the Army, Navy, and Air Force efforts funded under the authority in 10 U.S.C. § 4123.

## REFERENCES

[1] Clifford, A.; Das, J.; Yousefi, H.; Mahmud, A.; Chen, J.B.; and Kelley, S.O.; Strategies for Biomolecular Analysis and Continuous Physiological Monitoring. *J. Am. Chem. Soc.* **2021**, *143* (14), pp 5281–5294.
[2] Khater, I.; Nassar, A. Potential antiviral peptides targeting the SARS-CoV-2 spike protein. *BMC Pharmacol. Toxicol.* **2022**, *23*, p 91.
[3] Stokes. K.; Peltrini, R.; Bracale, U.; Trombetta, M.; Pecchia, L.; Basoli, F. Enhanced Medical and Community Face Masks with Antimicrobial Properties: A Systematic Review. *J. Clin. Med.* **2021**, *10* (18), p 4066.
[4] Pullangott, G.; Kannan, U.; Gayathri, S.; Kiran, D.V.; Maliyekkal, S.M. A comprehensive review on antimicrobial face masks: an emerging weapon in fighting pandemics. *RSC Adv.* **2021**, 11, pp 6544–6576.
[5] de Mol, N.; Fischer, M. (eds.). Amine Coupling Through EDC/NHS: A Practical Approach, *Surface Plasmon Resonance Methods and Protocols*, Springer Science Business Media, **2010**, pp 55–73.
[6] Chapman, R. *Applications of Nonwovens in Technical Textiles*, Woodhead Publishing, **2010**, pp 65–84.
[7] Pourmohammadi, A. *Joining Textiles: Principles and Applications*, Woodhead Publishing Series in Textiles, **2013**, pp 565–581.
[8] Miaskiewicz-Peska, E.; Lebkowska, M. Comparison of aerosol and bioaerosol collection on air filters. *Aerobiologia,* **2012**, *28* (2), pp 185–193.
[9] Hutten, I., *Handbook of Nonwoven Filter Media*, Butterworth-Heinemann, **2015**, pp 451–519.
[10] Jung, S.; Kim, J. Advanced Design of Fiber-Based Particulate Filters: Materials, Morphology, and Construction of Fibrous Assembly. *Polymers*. **2020**, *12* (8), p 1714.
[11] Mohan, T.R.; Kumar, M.S.M.; Rao, L. Biofouling of hollow fiber ultrafiltration membranes: A novel multiphase CFD – Porous - CES model and experimental study, *J. Membr. Sci.* **2022**, *663*, p 121034.
[12] Etemadi, H.; Fonouni, M.; Yegani, R. Investigation of antifouling properties of polypropylene/$TiO_2$ nanocomposite membrane under different aeration rate in membrane bioreactor system. *Biotechnol. Rep*. **2019**, *25* (4), e00414.
[13] Bixler, G. D.; Bhushan, B. Biofouling: Lessons from Nature. *Philos. Trans. R. Soc., A.* **2012**, *370* (1967), pp 2381–2417.
[14] Wang, C.; Yan, Q.; Liu, H.-B.; Xiao, X.-H.; Xiao, S.-J. Different EDC/NHS Activation Mechanisms between PAA and PMAA Brushes and the Following Amidation Reactions. *Langmuir.* **2011**, *27* (19), pp 12058–12068.
[15] Meng, L.; Klinkajon, W.; K-hasuwan, P.-r.; Harkin, S.; Supaphol, P.; Wnek, G.E. Electrospun crosslinked poly(acrylic acid) fiber constructs: towards a synthetic model of the cortical layer of nerve. *Polym. Int*. **2015**, *64* (1), pp 42–48.
[16] Schindelin, J.; Arganda-Carreras, I.; Frise, E.; Kaynig, V.; Longair, M.; Pietzsch, T.; Preibisch, S.; Rueden, C.; Saalfeld, S.; Schmid, B.; Tinevez, J.Y.; White, D.J.; Hartenstein, V.; Eliceiri, K.; Tomancak, P.; Cardona, A. Fiji: an Open-Source platform for biological-image analysis. *Nat. Methods.* **2012**, *9* (7), pp 676–682.
[17] Götz, A.; Senz, V.; Schmidt, W.; Huling, J.; Grabow, N.; Illner, S. General image fiber tool: A concept for automated evaluation of fiber diameters in SEM images. *Measurement.* **2021**, *177*, p 109265.

This page left intentionally blank

# Bioaerosol release profiles and spectra of vegetative bacteria for methodology development

Angela M. Zeigler[a]*, Ashish Tripathi[a], Daniel McGrady[b], Aime P. Goad[a]
[a]U.S. Army Combat Capabilities Development Command Chemical Biological Center, Research & Operations Directorate, 8198 Blackhawk Rd, Aberdeen Proving Ground, MD 21010
[b]Tech(X), 210 Research Blvd Suite 130, Aberdeen, MD, 21001

## ABSTRACT

Vegetative bacteria have been of high interest to the intelligence community as a credible bioaerosol threat; however, historically there has been a consistent problem with detection technologies in the ability to detect and correctly identify bioaerosols of vegetative bacteria, due to the fragile nature of the aerosol and maintaining its viability for testing and analysis. This research effort tackled technical and practical challenges with the ability of vegetative bacteria, like *Pantoea agglomerans*, to remain viable during laboratory aerosolization processes. Efforts also included utilizing results from this effort to develop aerosol methodologies for the evaluation of biological detection and identification technologies. The observed outcomes are reported of the aerosolization phenomena as well as evaluating samples with Raman microscopy, as Raman based technologies have gained interest in the detection community. Results indicate that additional study is required to further develop methods to separate individual vegetative aerosol particles. Assessment of sampling strategies and methodologies is required while at the same time keeping realistic concept of operations threat scenarios in mind.

**Keywords:** Vegetative bacteria, aerosols, viability, biodetection testing, laboratory methodology

## 1. INTRODUCTION

Emerging bioterrorism events in recent years has highlighted the importance of bioaerosol research and the need for monitoring technologies to enable advanced warning of potential biological threats. Predominantly, vegetative bacteria have been of high interest to the intelligence community as a credible bioaerosol threat. However, there has been a historically consistent problem with detection technologies and their ability to detect and correctly identify bioaerosols of vegetative bacteria due to the fragile nature of the organism and the damage they can endure during aerosolization which can affect viability during subsequent testing and analysis. To develop advanced detection and identification technology for early warning of any biothreat, a rigorous evaluation of a technology's abilities throughout the technology readiness level milestones is required. This means, early stages of testing and evaluation involved bioaerosol exposure in a controlled laboratory environment.

This research effort set out to characterize how different growth protocols, storage times, and aerosolization techniques of vegetative bacteria, specifically *Pantoea agglomerans* (Pa), affects bacterial survivability. Aerosolized bacterial samples were deposited on a surface and characterized using Raman spectra profiling. The results provide valuable input for concept of operations scenarios and development and evaluation of biological threat monitoring technologies, particularly those that are Raman based. Furthermore, the impact of these results provide input into building a standardized methods for overall biodetection technology assessment utilizing vegetative bacteria.

## 2. MATERIALS AND EQUIPMENT

### 2.1 *Pantoea agglomerans* (Pa)

The simulant Pa, formerly known as *Erwinia herbicola*, is a Gram negative bacteria with poor viability characteristics when sampled with traditional methods and subsequently cultured due to its fragile nature. Viability loss due to aerosolization and sampling processes can reach up to 70 % after sampling with impingers, and up to 99 % after collected on filters.[1] Four different stock solutions were utilized in this study. Stock solutions 1–3 (S1, S2, and S3) of

Pa was cultured from the American Type Culture Collection (ATCC) Cat. #33243. S1 was prepared in May 2018 via the shaker flask growth as recommended by ATCC. Samples were cultured in 0.8 % nutrient agar and broth (pH 7.0) (Difco™ Nutrient Broth, BD) and grown to a concentration of 1.0 x $10^9$ CFU/mL at the time of production. S2 was prepared in a similar manner in March 2023 and grown to a concentration of 1.82 x $10^8$ colony forming units (CFU)/mL. Finally, S3 was prepared in March 2023 via microbial fermentation growth method and grown to a concentration of 1.04 x $10^{10}$ CFU/mL at the time of production. Stock solution 4 (S4) was cultured from ATCC Cat. #27155 and prepared in July 2023 according to the recommended protocol from ATCC in nutrient agar and broth to a concentration of 1.19 x $10^9$ CFU/mL.

### 2.2 Sono-Tek aerosol nozzle

Sono-Tek ultrasonic nozzles were used to produce micrometer-sized aerosol droplets of liquid or suspensions that can evaporated down to narrowly dispersed residue particles. The carrier liquid is water-based and may have nutrients/media depending on the biological particle. The final particle size was dependent on the solid/liquid content ratio in the suspension/solution and on the characteristic size of the primary Sono-Tek droplet. The rate of aerosol generation is dependent on the delivery speed of the external syringe pump. The primary particle ranged from 23–70 μm (120–25 kHz operating frequencies) and flow rates from a few microliters per second to about 6 gal/h. Through the evaporation process, a uniform residue aerosol particle resulted in the range of 1–10 μm in size. Sono-Tek nozzles are typically considered a more ‘gentle’ aerosolization technique for sensitive biological particles.

### 2.3 Controlled aerosol delivery system

The controllable aerosol delivery (CAD) system was an in-house development by the Sensors, Signatures, & Aerosol Technologies Branch to quickly generate and switch aerosol outputs between an instrument inlet and a reference filter at a controlled rate without releasing aerosol to the environment. Originally built for potential use in a BSL-3 laboratory, this system is 13 inches tall and has a 4 × 3-inch cross-sectional area. A Sono-Tek aerosol generator connected to a syringe pump was used to generate the aerosols. A heated tube, which is temperature variable, warmed the air to dry the particles, and carried the particles out of the system through an insulated tube. The particles were generated at a very low rate (10 μL/min), and the airflow rate was low (approximately 5 L/min) to ensure the particles had enough time to dry before they exited the aerosol generator.

### 2.4 Aerodynamic particle sizer

The aerodynamic particle sizer (APS) model 3321 (TSI Inc., St. Paul, MN) is a high-performance general-purpose particle spectrometer that measures the aerodynamic diameter of aerosol particles in response to an accelerated airflow. Smaller particles accelerate faster, and time of flight of an aerosol particle is measured between two laser beams. The amount of time was recorded and converted to an aerodynamic diameter using an internal calibration table. Light-scattering information was also obtained and plotted against the aerodynamic size to gain additional information. The APS provides accurate particle count and size distributions for particles with aerodynamic diameters of 0.5–20 μm, detects light-scattering intensity for particles 0.3–20 μm, and is specifically engineered to perform aerodynamic size measurements in real time using low particle acceleration rates. The APS categorized the particles over 52 particle size bins. The sample flowrate of the APS was 1.0 liters per minute (LPM) with a sheath flow rate of 4.0 LPM.[2] The APS was used to measure the size and concentration of the aerosolized Pa at the location of aerosol generation.

### 2.5 Lab-based Raman chemical imaging microscopy (L-RCIM)

Lab-based Raman chemical imaging microscopy (L-RCIM) provides Raman imaging on a bacterial sample. It allows for obtaining a Raman spectrum per cell or spore and assigning the spectrum to the image of that cell or spore. This isolation provides the advantage of analyzing samples which may contain impurities or even a complex mixture of various bacterial cells.

A WiTec R300 Microscope was utilized, and operation conditions included a 633-nm excitation laser, 15-mW laser power, with 1.0 sec integration time/spectra. A 100 x magnification objective was used, and one spectra every 0.5 x 0.5 mm area was acquired. A Raman hyperspectral cube was sent through a cosmic ray correction and baseline removal module for the Raman imaging analysis. Basis vector analysis was performed to determine the independent component Raman spectra.

For the sample preparation, if the sample was suspended in liquid, a 5 µL aliquot of each sample was spotted from an aqueous suspension onto an aluminum coated slide and allowed to dry in a biosafety cabinet. For the aerosolized sample preparation, samples were directly generated from the aerosol source onto the aluminum coated slides. The field of view for all experiments were chosen in the near central regions of the dried spot. The edge of a spot experienced bacteria aggregation while the central regions of a spot displayed a dispersion of bacteria.

## 3. RESULTS

Initial steps were first taken to compare how S1–S4 were prepared and how the concentrations at the time of production differed to current date of use by directly pipetting the liquid solutions onto filters. Filters were processed and grown to obtain S1–S4 cultures. The results obtained from the liquid deposition yielded similar production concentrations except for S1 (2018) which had decreased in concentration to 1 x$10^8$ CFU/mL, most likely due to the aging and breakdown of the Pa in the solution over time. Raman spectroscopy did show that the solution was 'dirtier' with dead cells present in the solution, however, there was enough viable Pa in each solution independent of the solution age.

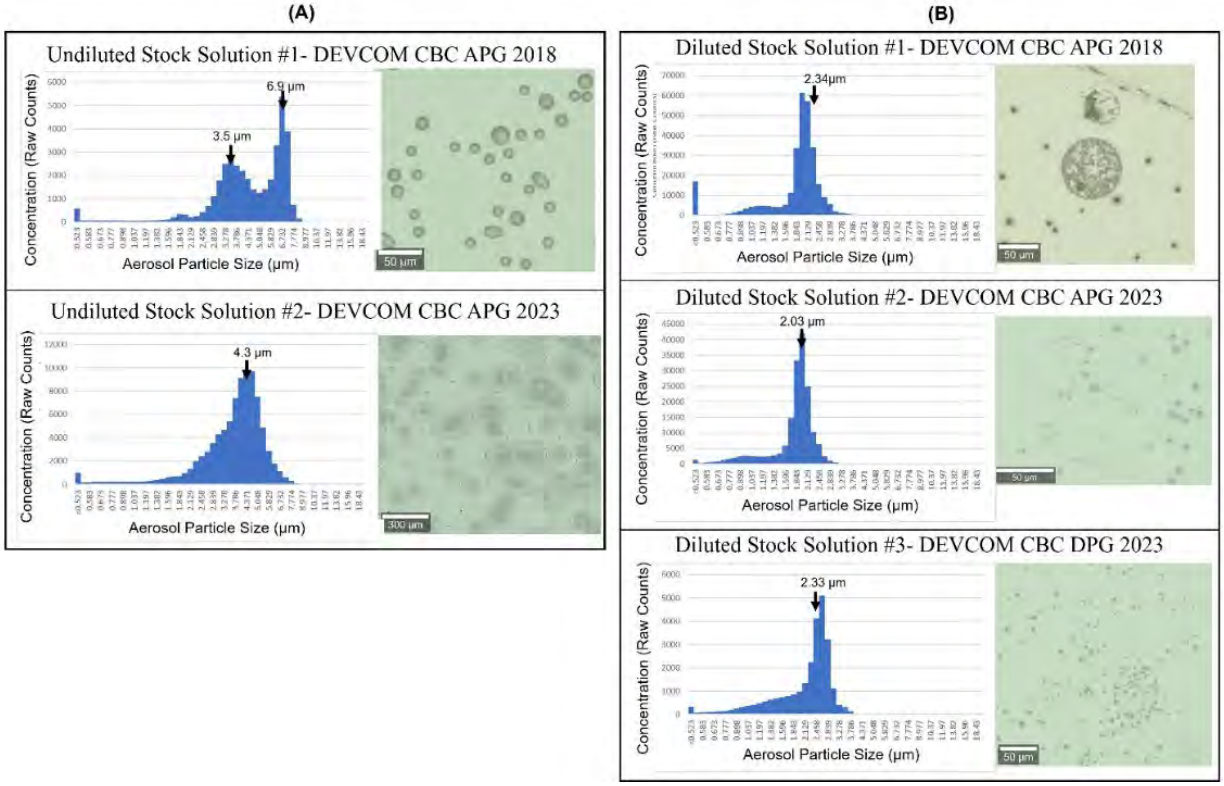


**Figure 1. CAD aerosol particle size relative to Raman microscopy measured particle sizes on aluminum slides for (A) Undiluted stock solutions and (B) Diluted stock solutions to obtain smaller particle sizes.**

In moving forward with the aerosolization generation techniques with S1–S4, the undiluted (i.e., stock solution as is) Pa solutions were aerosolized via the CAD system and particle sizes were measured. CAD nominal operation parameters for heat, airflow, and syringe feed rate were initially set from previous bioaerosol spore studies with this system. Figure 1 Column A shows the APS measured geometric mean particle size as deposited on the slides on the left and the corresponding L-RCIM images on the right. Aerosolized undiluted solutions were measured by the APS to have a geometric mean diameter of 4.7 µm (S1) and 4.3 µm (S2). As observed in the Raman microscopy images shown to the right of the APS measurements, the aerosolized particles deposited onto the slides were observed to be droplets compared to dry particles. The sizes measured were slightly larger compared to aerosolized APS measurements due to the inertial impaction on the slide as the aerosolized droplets are deposited but still comparable. Undiluted stock solutions were measured as these solutions had the highest concentration of Pa within the observed droplets in hopes the increased concentration would allow Raman spectroscopy to pick up the individual vegetative bacteria cells in the growth media. Even though the CAD system includes a heated column for drying the droplets

down to a nominal size based on the starting droplet, the aerosolized particles deposited were still considered droplets and too 'wet' for further Raman spectroscopy analysis to differentiate vegetative bacteria components from the nutrient broth/media (i.e., background components). No further iterations were attempted with S3 or S4 to proceed to the next round of testing and aerosol particle sizing.

The next round of testing involved diluting stock solutions to obtain measurements of approximately half of the aerosol particle size to presumably cut back the presence of the background components. Figure 1 Column B shows the aerosolized undiluted solutions were aerosolized by the CAD and measured by the APS to have geometric mean diameters of 2.34 µm (S1), 2.03 µm (S2), and 2.33 µm (S3) and compared with the Raman microscopy images to the right. Again, as observed in the microscopy images, the aerosolized size deposited onto the slides measured were at least smaller in size compared to the undiluted stock solutions and comparable to the measured APS sizes, but still observed and considered too 'wet' for further Raman spectroscopy analysis.

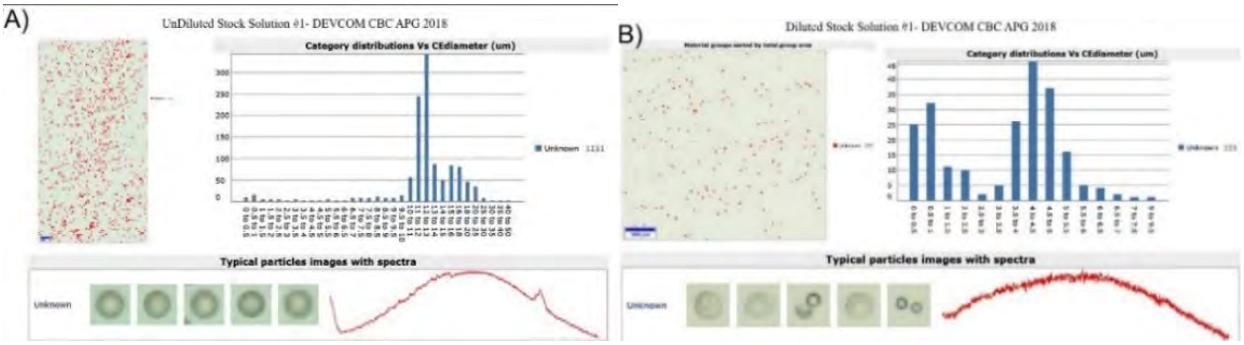


**Figure 2. Raman spectroscopy analysis of deposited aerosol particles using the CAD aerosol generation system. Top left shows aerosol Raman microscopy image obtained, revealing aerosol droplets deposited onto the slide. The top right bar graph shows binned particle size diameter distribution. The bottom spectra represented by the red line shows the Raman spectra obtain of random particles for (A) undiluted and (B) diluted by half stock solutions.**

An example of the Raman spectroscopy analysis and aerosolize droplets being too 'wet' is shown in Figure 2 with S1 undiluted (A) and diluted (B) results. Each example shown to the left the same microscopy image as in the previous Figure 1. Particles/droplets within each image were 'binned' with particle size diameter distributions. The particle distributions align similarly with the APS measured aerodynamic particle sizes as previously mentioned. In the bottom illustration of each example, at random, several particle images were scanned and analyzed via Raman spectroscopy. The spectra taken from each particle image is represented by the red line (axis). Both undiluted and diluted samples show high background noise with little-to-no notable peaks showing above the baseline, indicative of lack of signature obtained from the sample to make any type of analysis and identification of sample components. Peaks that were observed barely above baseline were only observed in the undiluted samples, notably from samples with higher Pa concentrations, but could not be differentiated from the background components to be identified.

Within this short research effort timeframe, only a handful of further iterations were performed of different dilutions of the stock solution and different CAD settings, most notably the heating for the drying column, for drying the droplets further. Eventually the settings reached a point where the droplets were dried 'too much' resulting in lack of viability of the Pa particles and therefore no Pa was deposited on the slides. One round of testing was performed with switching to another aerosol generation technique called the inkjet aerosol generator (IJAG) and obtained the results with using stock solution S4 (Figure 3). In utilizing a different aerosolization method, similar results with at least S4 were observed as shown using the CAD system for S1–S3 in which the aerosols deposited and then analyzed via Raman spectroscopy still appear to be droplets and yielding no identifiable signature peaks for identification.

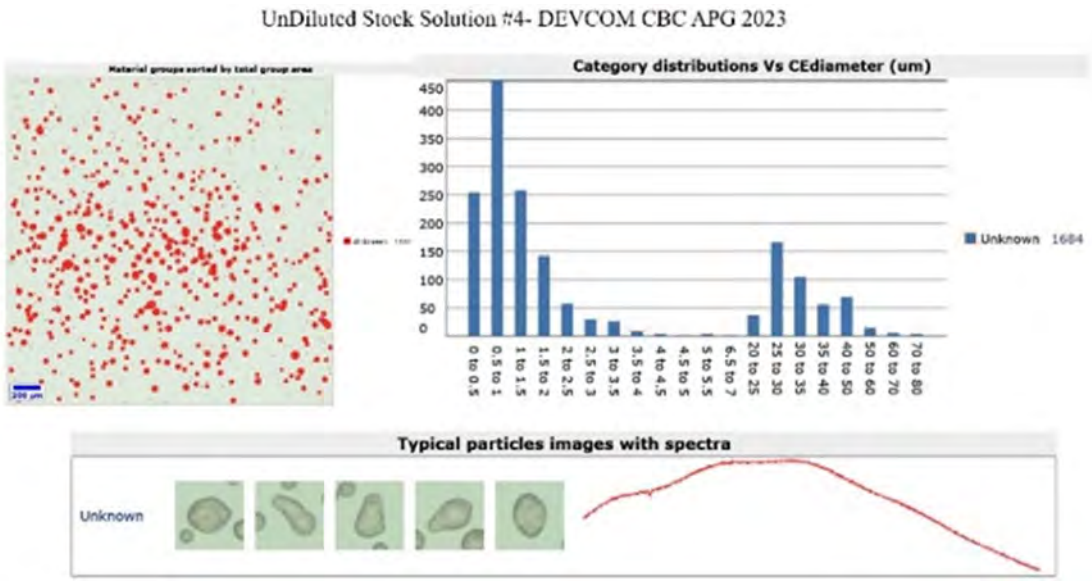


**Figure 3. Raman spectroscopy analysis of deposited aerosol particles using the inkjet aerosol generator aerosol generation system. Top left image shows aerosol Raman microscopy image obtained, revealing aerosol droplets deposited onto the slide. The top righthand bar graph shows binned particle size diameter distribution to compared to APS measured particle sizes. The bottom spectra represented by the red line shows the Raman spectra obtain of random particles for undiluted and diluted by half stock solutions.**

## 4. CONCLUSIONS

While the results of the aerosolization process and manipulation of CAD system parameters yielded droplets over the size of what is assumed to be dry aerosolized particles, data collected so far has resulted in a better understanding of the viability phenomena/problem of vegetative bacteria. The characteristics of droplet vs. dry single solid particles were determined using Raman microscopy for differentiating the aerosol deposition. Results suggest a trade space in which the viability for Pa is greater if the aerosolization technique/variables results in an aerosol droplet relative to a dry single particle, suggesting the drier the resulting particle the less nutrients available for Pa cells to feed and survive the aerosolization, transport, and deposition processes. Therefore, the CAD system may require modifications once parameters combinations are exhausted. Data so far has included characterization of the viability of the stock solution based on age. The CAD aerosolization technique was more heavily performed compared to the IJAG aerosolization generator, however both techniques had similar results. Experiments were started in another aerosol chamber to increase the path length for drying time, but not enough data had been collected at the end of this period of performance to draw any conclusions. Viability will be better understood once the aerosol technique for drier particles is achieved. It's also important to note that while there was not enough data gathered in comparing growth protocols ATCC versus the microbial fermentation method (S3), but previous experiments show differences in test results were due to the greater Pa concentration via the fermentation method, suggesting a greater number of viable cells from initial growth.

These results point out the crucial need for continued development to reach a standardized level of stable methods for testing the reproducibility of vegetative bacteria aerosolization to confirm intact dry single particles which has already been accomplished with Gram positive spores (i.e., *Bacillus atrophaeus*). Future research efforts should include additional aerosol profiling for multiple vegetative bacteria profiles to be conducted as future references, especially for a Raman based detection technology as no 'one size fits all' for profiling exists.

## ACKNOWLEDGMENTS

We'd like to thank Todd Sickler of Combat Capabilities Development Command Chemical Biological Center for the preparation of the various Pa stock solutions. Funding for this Seedling project was made available through

the Department of Defense Funding Laboratory Enhancements Across (X) Four Categories (FLEX 4) in accordance with the Army, Navy, and Air Force efforts funded under the authority in 10 U.S.C. § 4123.

## REFERENCE

[1] Rule, A.M.; Schwab, K.J.; Kesavan, J.; Buckley, T.J. Assesment of Bioaerosol and Sampling Efficiency Based on *Pantoea agglomerans*. *Aerosol Sci. Technol.* **2009**, *43* (6), pp 620–628.